The Quandary of the Sask Craton:
Origin and Evolution of the Lithospheric Mantle beneath the Sask Craton

by

Janina Czas

A thesis submitted in partial fulfillment of the requirements for the degree of

Doctor of Philosophy

Department of Earth and Atmospheric Sciences
University of Alberta

Abstract

Mantle xenoliths from the Cretaceous (~106 to ~95 Ma) kimberlites at Fort à la Corne (FALC) present a unique opportunity to study the lithospheric mantle beneath the newly recognised Sask Craton. The Sask Craton, a small terrane with Archean (3.2 - 2.5 Ga) crustal ages, is enclosed in the Paleoproterozoic (1.9 - 1.8 Ga) Trans Hudson Orogen (THO). Only limited research has been conducted on this craton, yet it hosts major diamond deposits within the FALC Kimberlite Field. This thesis presents the first study of major and trace elements, as well as isotopic data from diamondiferous and barren mantle xenoliths (peridotitic and eclogitic) from two volcanic centres (Star and Orion South) in the Fort à la Corne Kimberlite Field. To constrain the origin and evolution of the lithospheric mantle beneath this craton, the age and composition of the lithosphere are established, and diamond forming processes are assessed. Further, this study provides the opportunity to constrain the influence of the Trans Hudson Orogeny on the mantle keel and its effect on the diamond population.

Based on the geochemistry of peridotite xenoliths from FALC, the garnet-bearing lithospheric mantle is dominated by moderately depleted lherzolite. Signatures of carbonatitic and kimberlitic melt metasomatism can be identified in the majority of the xenolith suite. Pressure and temperature conditions (840 to 1250 °C and 2.7 to 5.5 GPa) of the lithospheric root are similar to other cratons, the calculated geotherm is cool and compares well with a 38 mW/m^2 reference geotherm. No Archean ages were recorded in the Os isotope composition, with the main mode of Re depletion ages spanning from 2.4 to 1.7 Ga. This provides evidence that the majority of the lithospheric mantle was depleted and stabilised in the Palaeoproterozoic, significantly later than the Archean crust. The timing of the dominant lithosphere formation is linked to the rifting (~2.2

Ga - 2.0 Ga), as well as the subsequent collision (1.9 - 1.8 Ga) of the Superior and Hearne craton during the Wilson cycle of the Trans Hudson Orogen.

FALC eclogites have major element and oxygen isotope compositions consistent with an origin from subducted, seawater-altered oceanic crust. Diamond-free eclogites commonly have signatures indicative of a gabbroic origin, while diamond-bearing xenoliths are likely derived from basaltic protoliths. Temperatures calculated for the FALC eclogites span a broad range (740 to 1390 °C), though diamondiferous samples are restricted to the higher temperatures (1180 – 1390 °C). Both modal (diamond formation) and cryptic metasomatism affected the FALC eclogite suite. Intense melt metasomatism, which occurred in temporal proximity to host kimberlite magmatism, resulted in strong chemical gradients and heterogeneities in major, trace and even oxygen isotope values within the diamondiferous eclogites. Similar to the peridotitic sample suite, both carbonatitic, and proto-kimberlitic metasomatism can be identified in the diamondiferous FALC eclogites. Eclogite formation is likely linked to the subduction of oceanic crust during the Trans Hudson Orogeny.

All diamonds in this study are intergrown with mantle minerals, with eclogitic assemblages dominating the sample suite. Three diamond suites (monocrystalline, aggregate and polycrystalline diamonds) were identified based on their morphology and chemistry. Monocrystalline diamonds from FALC have nitrogen and carbon systematics indicative of a mantle-derived source fluid, a subduction-related origin is likely for the polycrystalline diamonds. In the diamond aggregates nitrogen and carbon systematics are decoupled; mixing of mantle-like and recycled nitrogen, or the presence of nitrogen-bearing phases during diamond crystallisation could account for the observed disconnect between nitrogen and carbon isotope variations. The decoupling of carbon and nitrogen systematics suggests that diamond

crystallisation is not fluid limited and Rayleigh fractionation does not play a major role at FALC. It is more likely that diamond crystallised from a supersaturated CHO-rich fluid/melt due to isochemical cooling. Unusual diamond brecciation and annealing patterns observed in the diamond aggregates are possibly linked to the intense melt metasomatism that affected their host eclogites. Considering the absence of Archean lithospheric mantle beneath the Sask Craton it is likely that all diamonds from FALC are Palaeoproterozoic in age. Further, nitrogen aggregation and platelet peak degradation suggests that at least some of the FALC diamonds formed during the THO.

Preface

This thesis is original work carried out by Janina Czas (J.C.). It contains three separate manuscripts based on the findings of the author's Ph.D. research supervised by Profs Thomas Stachel and Graham Pearson. This project was possible due to sample donations by Star Diamond Corp. (formerly Shore Gold Inc.) The research was funded through an NSERC (Discovery) grant to T.S. and a CERC grant to D.G.P.

A modified version of Chapter 2 is intended to be submitted to LITHOS for publication as: *Czas, J., Pearson, D.G., Stachel, T., Kjarsgaard, B.A., Read, G.H. Palaeoproterozoic diamond-bearing lithospheric mantle root beneath the Archean Sask Craton, Canada.* Samples were provided by G.H.R. (Star Diamond Corp.) and sample selection was conducted by J.C. and T.S.. Sample processing and analytical work was carried out by J.C. G.H.R provided additional major element data. The initial manuscript was written by J.C., while T.S., D.G.P and B.A.K. contributed to the discussion of results and their implications, as well as provided valuable edits of the manuscript.

A modified version of Chapter 3 was published as: *Czas, J., Stachel, T., Pearson, D.G., Stern, R.A., Read, G.H. 2018. Diamond brecciation and annealing accompanying major metasomatism in eclogite xenoliths from the Sask Craton, Canada. Mineralogy and Petrology - Proceedings of the 11th International Kimberlite Conference.* J.C. and T.S. collected the barren xenolith samples, diamondiferous micro-xenoliths were provided by G.H.R. (Star Diamond Inc.). Sample selection and preparation, as well as the majority of the analytical work were carried out by J.C. R.A.S and J.C. obtained oxygen isotope analyses via SIMS. The initial manuscript was written by J.C., while T.S., D.G.P., R.A.S and G.H.R. contributed to the discussion of results and their implications, as well as provided valuable edits of the manuscript.

A modified version of Chapter 4 will be submitted for publication as: *Czas, J., Stachel, T., Pearson, D.G., Stern, R.A., Read, G.H. Diamond formation and brecciation beneath the Sask Craton, Canada – Insights from diamondiferous microxenoliths.* Samples were provided by G.H.R (Star Diamond Inc.). Diamond extraction and characterisations, as well as the majority of analytical work were conducted by J.C. Carbon and nitrogen isotope ratios, as well as nitrogen concentration data were collected by R.A.S and J.C. The initial manuscript was written by J.C.

T.S., D.G.P and R.A.S. contributed to the discussion of results and their implications and T.S., D.G.P provided valuable edits, which improved the manuscript.

Acknowledgements

This thesis would not have been possible without the support of my supervisors, colleagues, friends, and family. I am incredibly grateful for your advice and encouragement throughout my PhD journey.

First and foremost, I would like to thank my supervisors Drs. Thomas Stachel and Graham Pearson. Your guidance, insights, and comments greatly improved my work and truly made me a better researcher. Thomas, thank you for always having an open door to discuss my research, or mantle geochemistry in general – in particular during the last months of my PhD when everything was very hectic. Further, your German directness and humour were always appreciated and made Edmonton feel a bit more like home. Thank you Graham, for always making the time for discussions of all sorts and for providing insightful advice on research and academia.

I would also like to thank the entire examining committee – Drs. Robert Luth, Karlis Muehlenbachs, and Yana Fedortchouck for agreeing to be examiners during my PhD thesis defence and for providing interesting discussions, as well as constructive feedback on this thesis.

An NSERC (Discovery) grant to Thomas Stachel and a Canada Excellence Research Chair grant to Graham Pearson provided the funding for this project. All samples were kindly donated by Star Diamond Inc., formerly known as Shore Gold Corp. through George Read, Moreover, thank you George for always being excited to talk about this project.

Thanks to Dr. Bruce Kjarsgaard for all the discussions about the Sask Craton and your words of encouragement. Dr. Richard Stern is thanked for his support with obtaining stable isotope data. Dr. Yan Luo provided assistance was LA-ICPMS analyses. Thanks to Dr. Andrew Locock for providing help with obtaining EMPA data, as well as being an endless source of mineralogical knowledge. The NanoFab facility, in particular Dr. Anqiang He and Peng Li, are thanked for their help with obtaining EBSD data. Many thanks to Dr. Sarah Woodland and Kate Hogberg for the countless times they assisted in the lab. Martin von Dollen and Mark Labbe provided immeasurable help during sample preparation. Thank you to Anetta Banas for tips and tricks on how to take great diamond pictures and to Dr. Jeff Harris for helping with the characterisation of diamonds.

I am also grateful for all the colleagues that became friends throughout this PhD, Yannick, Pedro, Joe, Mike, Matt, Lauren, Mandy, Nicole, Natasha, Ben, Noga - thanks for lots of laughs and cat videos. My writing buddies, Merilie and Danielle, our coffee/tea-shop sessions provided vital writing motivation. Jesse, thank you for being the best thesis-coach. I am also grateful for my friends back home that supported me throughout this degree, in particular: Eva, Marie, Sophie, Kristina, Karsten, Christoph, and Theresa.

A special thanks goes to all the former inhabitants of the cat house, who made Canada a home away from home. Scully, you are the best companion a PhD student could ask for, thanks for keeping me company throughout endless nights of working on this thesis. Shawna, you're a wonderful friend – we are basically a match made in heaven, thanks for adopting this introvert. Lauren thanks for the countless evenings spent chatting about life and sloths on kitchen floors. Margo, thanks for unforgettable cake-breakfasts and coming to all the hilarious yoga classes with me. Jody thanks for showing me that math can be cool and for all the outdoor adventures.

Lastly, I would like to thank my family and Ryan for their endless moral support and immense patience during this PhD. Ryan, I am forever grateful for your love and constant encouragement – thanks for always believing in me. Mama, Papa und Oli, danke für all eure Unterstützung.

Table of Contents

List of Tables

List of Figures

List of Abbreviations and Symbols

%B	Percentage of nitrogen in a diamond in B centres
‰	Parts per thousand or per mille
~	Approximately
ArF	Argon fluoride
CCIM	Canadian Centre for Isotopic Microanalysis
CL	Cathodoluminescence
DA	Diamond aggregates
e.g.	For example
EPMA	Electron probe micro analysis
Eu*	Eu anomaly calculated as $Eu^*=Eu_N/[0.5Gd_N+0.5Sm_N]$
FALC	Fort à la Corne
FTIR	Fourier transform infrared
G_D	Class of garnets likely originating from the diamond stability field
G1	Class of mantle-derived megacrystic garnets
G10	Class of mantle-derived harzburgitic garnets
G11	Class of mantle-derived Ti-metasomatised garnets
G3	Class of mantle-derived eclogitic garnets
G4	Class of mantle-derived eclogitic / pyroxenitic garnets
G9	Class of mantle-derived lherzolitic garnets
Ga	Giga-annum; Billion years
GPa	Gigapascal
h	hour
HREE	Heavy rare earth element
HSE	Highly siderophile element

I-PGE	Iridium-group PGEs (Os, Ir, Ru)
i.e.	That is
LA-ICPMS	Laser-ablation inductively coupled plasma mass spectrometry
LREE	Light rare earth element
Ma	Mega-annum; Million years
MC	Monocrystalline
Mg#	100 x Mg/(Mg+Fe)
MORB	Mid-ocean ridge basalt
MREE	Middle rare earth element
N	Subscript to indicate normalised values
N-TIMS	Negative – thermal ionisation mass spectrometer
OIB	Ocean island basalt
P-PGE	Platinum-group PGEs (Pt, Pd)
PC	Polycrystalline
PGE	Platinum group element
ppm	Parts per million
ppb	Parts per billion
PT	Pressure and temperature
PUM	Primitive upper mantle
REE	Rare earth element
s	Second
SCLM	Subcontinental lithospheric mantle
SEM	Secondary electron multiplier
MC-SIMS	Multi-collector secondary ion mass spectrometry
THO	Trans Hudson Orogeny
T_{MA}	Re-Os model age (time of separation from mantle)

T_{RD}	Rhenium depletion age (minimum age)
VPDB	Vienna-Pee-Dee-belemnite
VSMOW	Vienna-standard-mean-ocean-water
wt%	Weight percent
$\delta^{13}C$	Carbon isotope composition relative to the international VPDB standard
$\delta^{18}O$	Oxygen isotope composition relative to the international VSMOW standard
σ	Sigma or one standard deviation of the mean

Chapter 1

1 Introduction

For thousands of years gem diamonds have exerted a special fascination on humankind - they have been highly sought after for jewellery and as talismans due to their unique fire and brilliance. In the 20th century diamonds also found many industrial applications (Olson, 2015), which utilise their exceptional hardness (Mohs hardness of 10), very high thermal conductivity, or high density. For the last 50 years diamond exploration, as well as the diamonds themselves have been a highly valuable source of information on mantle mineralogy and geochemistry (Meyer and Boyd, 1972; Richardson *et al.*, 1984; Boyd and Gurney, 1986; Griffin and Ryan, 1995; Grütter, 2009; Gurney *et al.*, 2010).

Most natural diamonds are hosted in kimberlites found in Earth's cratonic regions, the long-lived and stable interiors of our continents. Cratons owe their longevity to their thick and buoyant lithospheric roots (Jordan, 1975, 1988), which are considered to be the result of exceptional degrees (up to 50%) of melt depletion (Boyd, 1989; Walter, 1999; Carlson *et al.*, 2005). Hence, cratons are commonly known to be excellent locations for diamond exploration, as their thick lithospheric roots extend into the diamond stability field (Clifford, 1966; Stachel and Harris, 2008). This association is commonly known as Clifford's rule (Clifford, 1966; Janse, 1994), and has been first noted by Kennedy (1964).

Mantle xenoliths, as well as diamonds, provide a powerful tool to study the sub-continental lithospheric mantle (SCLM) beneath cratons. They offer a glimpse at the mineralogical and geochemical nature of the mantle at the time of kimberlite eruption (Boyd and Gurney, 1986; Pearson *et al.*, 2003).

The mantle beneath the Canadian Shield has been the focus of numerous studies (Hoffman, 1988; Davis *et al.*, 2003; Griffin *et al.*, 2004; Canil, 2008; Snyder *et al.*, 2017), yet research conducted on the recently discovered Sask Craton is scarce. The few previous studies on this craton have focused on heavy mineral concentrate samples from the Fort à la Corne (FALC) Kimberlite Field (Leahy and Taylor, 1997; Griffin *et al.*, 2004; Read and Janse, 2009). The nature of these samples (xenocrysts rather than xenoliths), combined with small sample suites,

result in a limited view and did not provide the opportunity for geochronology studies on the lithospheric keel. Most of the produced information centered around geotherm studies. Read and Janse (2009) reported a cold (~37 mW/m^2) geotherm for the Sask Craton, derived from single clinopyroxene geothermobarometry. This agrees with Griffin *et al.* (2004), who examined a small garnet suite from FALC and determined that the dominantly lherzolitic lithospheric mantle beneath the Sask Craton is divided into two layers, which exhibit 35 mW/m^2 (upper) and 43 mWm^2 (lower layer) geotherms. Based on garnet compositions (major elements and Zr-Y) they concluded that the lower part of the lithosphere is more depleted - similar to the SCLM of the Slave Craton, whereas the upper part of the lithosphere has experienced Proterozoic thermo-tectonic reworking. According to Leahy and Taylor (1997), a major tectonic event also played a significant role during diamond formation, as they suggested that FALC diamonds with strongly degraded platelets were formed during the Trans Hudson Orogeny (THO).

1.1 The Trans Hudson Orogeny

The Trans-Hudson Orogen is a well-exposed Himalayan-style (St-Onge *et al.*, 2006; Weller and St-Onge, 2017) Paleoproterozoic orogenic belt, extending from the northern US, through Saskatchewan and Manitoba (Canada), and as far as Greenland (Fig. 1.1; Bickford *et al.*, 1990; Lucas *et al.*, 1993; Lewry *et al.*, 1994; Ansdell and Norman, 1995; Ashton *et al.*, 1999). During the THO, the Superior and the Rae-Hearne cratons (Churchill Province) were amalgamated, creating the North American Craton (Hoffman, 1988). Uranium-Pb geochronology was applied to determine the time of collision as well as peak metamorphism (Ansdell and Norman, 1995), constraining the age of the orogen between 1.9 – 1.8 Ga (Heaman *et al.*, 1992, 1994; Rayner *et al.*, 2005). The Wilson cycle of the THO was initiated during the rifting and opening of the Manikewan Ocean (~2.2 - 2.0 Ga; Stauffer, 1984; Hoffman, 1988; Collerson *et al.*, 1989).

Seismic reflection data collected during the LITHOPROBE project reveal a buried, seismically distinct structure beneath the THO, interpreted to be an Archean fragment or microcontinent – the Sask Craton (Lucas *et al.*, 1993; Ansdell and Norman, 1995; Ellis *et al.*, 1996; Bank *et al.*, 1998; Hammer *et al.*, 2011). First evidence of this Archean craton was reported by Chiarenzelli (1989), who discovered Archean and Paleoproterozoic basement rocks exposed within the interior orogenic belt. Further Archean crustal ages, ranging between 3.2 – 2.4 Ga, have since

been reported for the craton (Nd model ages, Collerson *et al.*, 1989, 1990; U-Pb in zircons, Heaman *et al.*, 1992, 1994; Davis *et al.*, 1998; Ashton *et al.*, 1999; Rayner *et al.*, 2005).

1.2 Sask Craton

The largely buried Sask Craton is only exposed in three tectonic windows; the Nistowiak and Hunter Bay tectonic windows within the Glennie Domain, and the Pelican Window within the Flin Flon Domain (stars in Fig. 2.1; Collerson *et al.*, 1990; Ashton *et al.*, 1999; Bickford *et al.*, 2005). As such, seismic reflection data (Lucas *et al.*, 1993; Ellis *et al.*, 1996; Hajnal *et al.*, 2005; Németh *et al.*, 2005) or the geochemical composition of post-orogenic intrusions have been used to estimate the sub surface extent of the craton (Bickford *et al.*, 2005).

Recent studies have focused on determining the origin, and the tectonic and thermal history of the Sask Craton. Neodymium and lead isotopic studies of post-orogenic intrusions, as well as U-Pb age constraints, indicate clear differences between the Sask Craton and both adjacent Archean cratons (Superior and Hearne; Lewry *et al.*, 1994; Ashton *et al.*, 1999; Rayner *et al.*, 2005). Hence, an exotic origin such as the Wyoming craton has been inferred for the Archean crust, which has similar $^{208}Pb/^{204}Pb$ ratios in both cratons (Bickford *et al.*, 2005). Others have argued that the Sask Craton is a distinct microcontinent with no connection to the surrounding cratons (Rayner *et al.*, 2005). During the THO the Archean microcontinent experienced a pervasive mechanical and thermal overprint, recorded in the metamorphic rims of zircons (Rayner *et al.*, 2005). The composition and extent of the lithospheric mantle keel beneath the Sask Craton has not been studied extensively and involvement of the Trans Hudson Orogeny in the formation or alteration of the diamondiferous root have not been explored. Previous studies have suggested that during the THO, the local lithosphere experienced major reworking, potentially resulting in the creation (Leahy and Taylor, 1997; Cartigny *et al.*, 2004), or destruction of diamonds (Ellis *et al.*, 1996).

1.3 Star and Orion South - Fort à la Corne kimberlites

The Star and Orion South kimberlites are part of the Fort à la Corne kimberlite field, situated within the proposed boundaries of the Sask Craton in central Saskatchewan approximately 50 km east of Prince Albert (Fig. 1.1 & Fig. 1.2). The more than 70 kimberlite bodies of the FALC field

occur within an approximately 200 m thick Lower Cretaceous sedimentary succession, deposited close to the north-eastern margin of the North American Interior Platform (Pittari *et al.*, 2008). Kimberlite emplacement ages of ~106 to ~95 Ma were determined using U-Pb in perovskite, and Rb-Sr in phlogopite (Heaman *et al.*, 2004; Kjarsgaard *et al.*, 2009). Unlike kimberlites from South Africa, which are typically described as elongate/carrot-shapes diatremes (Hawthorne, 1975; Mitchell, 1995), FALC kimberlites are considered complexes consisting of small feeder vents, which are covered by volcanic cones/rings and tephra deposits (Zonneveld *et al.*, 2004; Harvey *et al.*, 2009) that can range up to ~2000 m in diameter (Berryman *et al.*, 2004; Lefebvre and Kurszlaukis, 2008; Kjarsgaard *et al.*, 2009). They exhibit exceptional preservation of primary pyroclastic deposits, including tuff rings, tuff cones, crater and extra crater deposits (Leahy, 1997; Leckie *et al.*, 1997; Harvey *et al.*, 2009), which were emplaced contemporaneous with near-shore facies sediments of the Mannville and Colorado Groups (Berryman *et al.*, 2004; Zonneveld *et al.*, 2004; Kjarsgaard *et al.*, 2009). The majority of FALC kimberlites (75%) were characterised as diamond bearing (Harvey *et al.*, 2009).

1.4 Exploration and diamond potential

Diamond exploration on the Sask Craton first started in 1989 with the discovery of the first kimberlite pipe in the Fort à la Corne Field (Lehnert-Thiel *et al.*, 1992; Kjarsgaard and Levinson, 2002) through Uranerz Exploration and Mining and is still ongoing to this day. Macrodiamonds were identified in 50% of FALC kimberlites (Harvey *et al.*, 2009), while gem quality diamonds make up ~70% of the recovered diamond population (Jellicoe *et al.*, 1998). Diamond exploration and future mining of the FALC kimberlites is hampered by approximately 100 m of overburden consisting of glacial till and sediments (Kjarsgaard and Levinson, 2002).

The samples examined in this thesis were derived from the Star and Orion South kimberlites, which are currently owned by Star Diamond Corp. (formerly Shore Gold Inc.). Current economic estimates average at 14 carats per hundred tonnes, which, for an estimated a 38 years project lifespan would result in a total of 66 million carats recovered (Leroux *et al.*, 2018).

1.5 Main objectives

This PhD research is the first comprehensive study of a suite of mantle xenoliths from the Fort à la Corne kimberlite field on the Sask Craton. With this research I expand on the previous studies of xenocrysts from FALC (e.g. Leahy and Taylor, 1997; Griffin *et al.*, 2004; Read and Janse, 2009), evaluating whether their findings can be confirmed, or if a larger data set of barren and diamondiferous mantle xenoliths yields different conclusions on the geochemical composition and evolution of the SCLM. The overall aim of this thesis is to characterise the age and composition of the subcratonic lithospheric mantle in the FALC area of the Sask Craton and to assess the role of the Trans Hudson Orogeny in the formation, stabilisation and evolution of the Sask SCLM.

Age and composition of the subcratonic lithospheric mantle

The primary objective is to provide an overall petrological and geochemical evaluation of the mantle xenoliths (peridotitic and eclogitic) from FALC. By studying peridotite xenoliths, the composition of the lithospheric mantle beneath the Sask Craton is characterised and conclusions on the timing of lithosphere formation and stabilisation can be drawn. In addition, the research on eclogite xenoliths provides information on the origin of the eclogite protoliths, as well as their age and their relation to the THO.

Evolution of the SCLM

Evaluating the evolution of the Sask SCLM is another major aim of this thesis. Assessing the mineralogical and geochemical changes in peridotite and eclogite FALC xenoliths enables me to trace the impact of metasomatic fluids/melts and to characterise their composition. In this regard, the role of the Trans Hudson Orogeny is critically assessed; this will involve identification of recycling events and metasomatic overprinting: which other events have modified the lithospheric mantle – what is the possible influence of other structural events or metasomatic infiltration?

Diamonds from Fort à la Corne

The study of diamondiferous mantle xenoliths from Fort à la Corne enhances our understanding of diamond formation processes beneath the Sask Craton. Using carbon and nitrogen isotope

geochemistry and nitrogen concentrations and aggregation states, the composition of the diamond bearing fluids is characterised, and mechanisms of diamond formation are assessed. The timing of diamond crystallisation, in particular in regard to the THO, is discussed. As this thesis deals with xenolith-hosted diamonds, it provides the opportunity to study the relationship between diamond and their substrates.

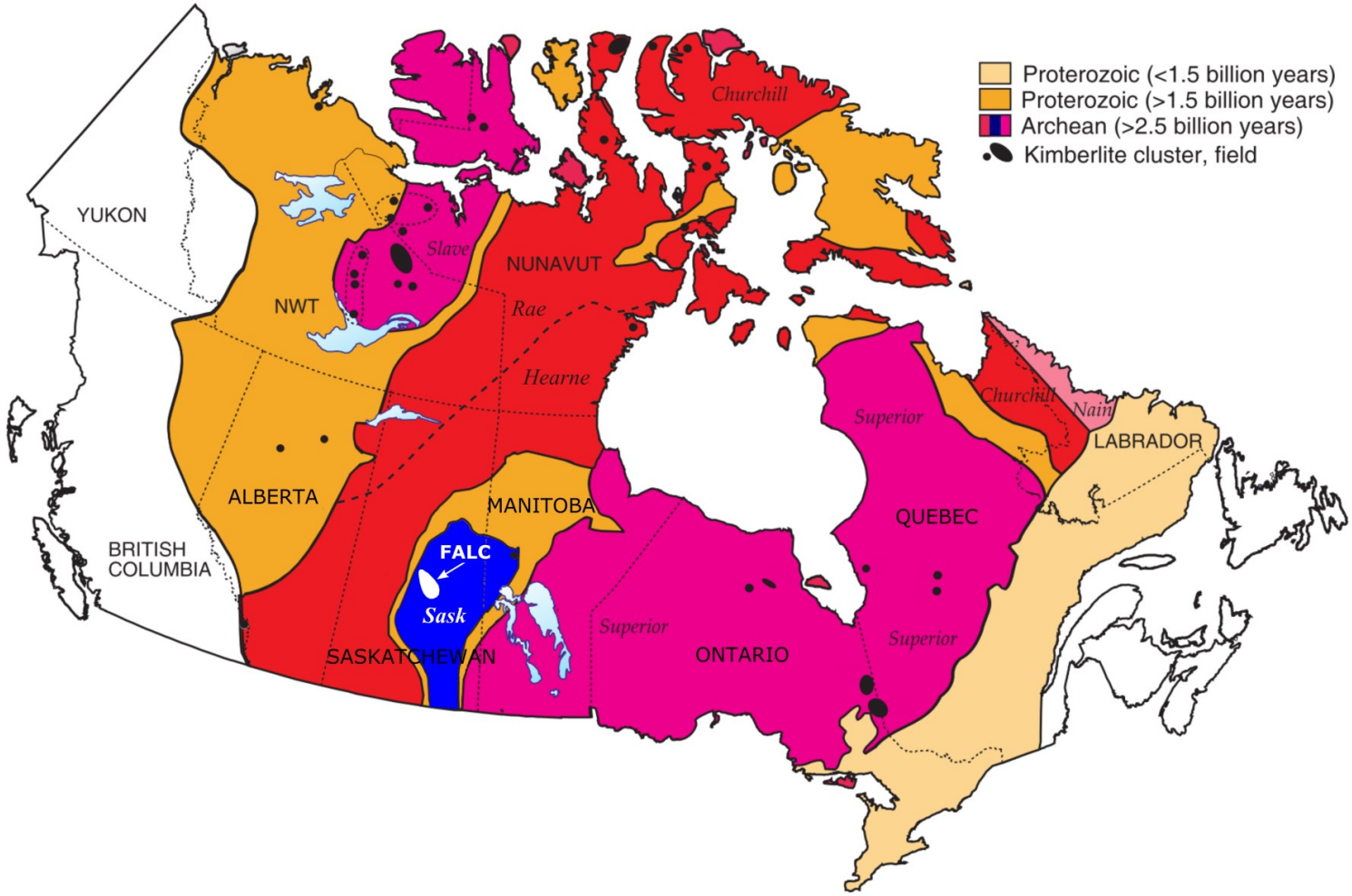

Fig. 1.1 Schematic map of cratons and mobile belts in Canada. The Sask Craton is shaded in blue, whereas the Rae and Hearne Cratons, and the Superior Craton are shown in red and pink, respectively. Orange shading indicates the Palaeoproterozoic Trans Hudson Orogen. The location of the Fort à la Corne (FALC) kimberlite field is show in white, while other kimberlite fields are indicated in black

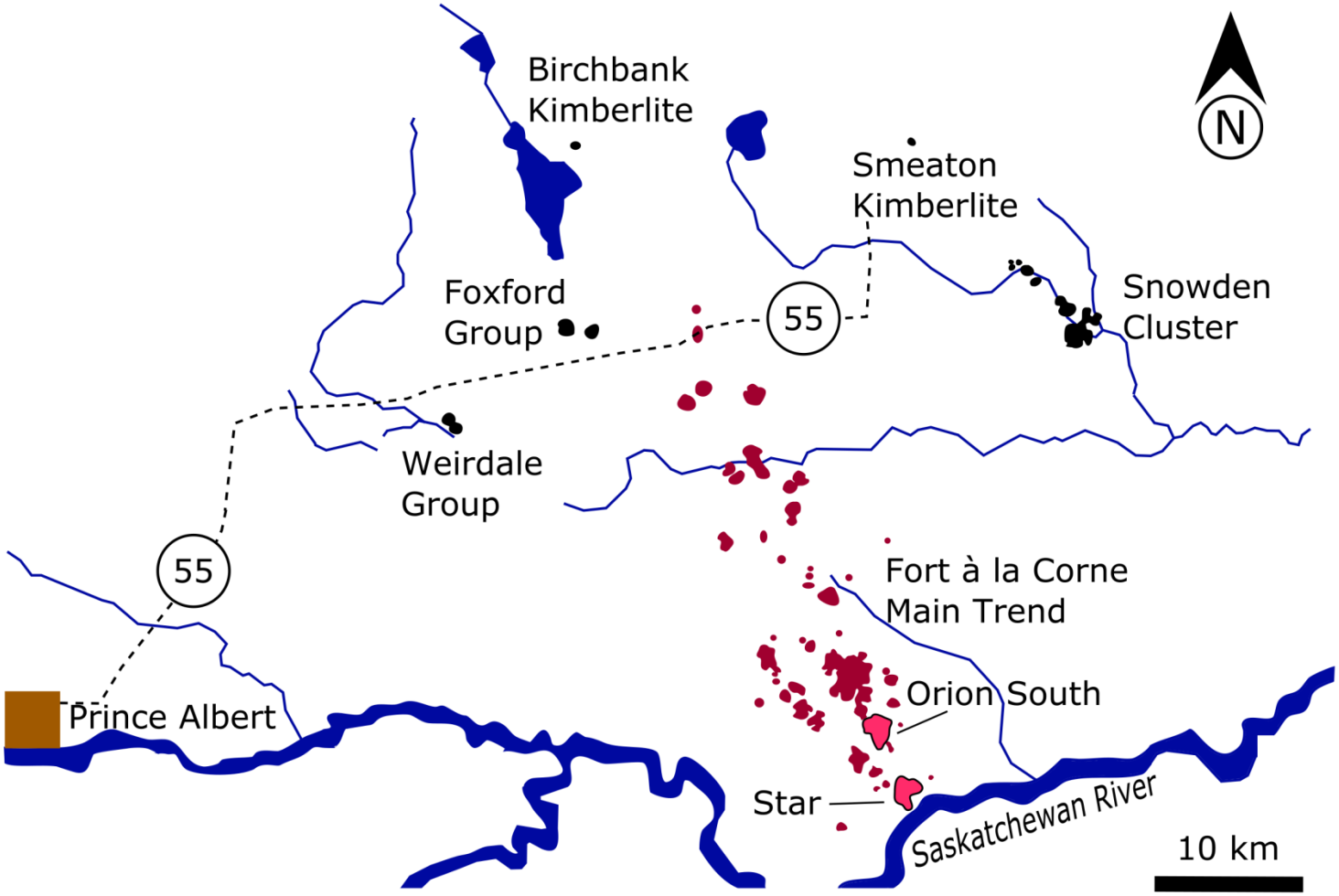

Fig. 1.2 Regional map of the Fort à la Cone Kimberlite Field (red) and other Saskatchewan kimberlite pipes (black) (after Harvey et al. 2009). The Star and Orion South pipes are highlighted in pink

Chapter 2

2 A Palaeoproterozoic lithospheric mantle root beneath the Archean Sask Craton, Canada

2.1 Introduction

The subcontinental lithospheric mantle (SCLM) beneath cratons has been extensively studied to characterise its composition and to investigate the timing and processes involved in stabilising cratonic roots (Ringwood, 1975; Boyd, 1989; de Wit *et al.*, 1992; Carlson *et al.*, 1999; Pearson, 1999). Our current understanding of when cratonic roots formed is predominantly based on Re-Os model ages, providing a minimum estimate of the time of Re depletion. The Re-Os system is the preferred method to estimate the timing of SCLM formation due to its greater resistance than lithophile-element based isotope systems to metasomatic overprinting (Walker *et al.*, 1989; Pearson *et al.*, 2002). In most cratonic settings the stabilisation of their mantle keels broadly correlates with the Archean age of the crust (e.g., Pearson, 1999), resulting in Archean crust being underlain by Archean mantle lithosphere. This age relationship can be significantly disturbed by tectonothermal and major metasomatic events affecting the SCLM. For instance, the mantle beneath the central Kaapvaal Craton, sampled by the Premier kimberlite, was significantly over-printed or replaced in the Palaeoproterozoic by Bushveld magmatism (Carlson *et al.*, 1999), but in such cases a vestige of the Archean mantle is observed.

The Sask Craton is the most recently discovered and by far the smallest of Canada's cratons. The formation and evolution of the mantle beneath the Sask Craton is scarcely studied. The few previous studies on the Sask Craton focussed on the sparsely distributed Precambrian crystalline basement (Collerson *et al.*, 1990; Rayner *et al.*, 2005). Our current knowledge of the geochemical nature of the Sask lithospheric mantle is limited to three studies, one focussing on diamonds (Leahy and Taylor, 1997) and the other two on garnet xenocrysts from kimberlite (Canil *et al.*, 2003; Griffin *et al.*, 2004). Here we present the first petrographical and geochemical characterisation of mantle xenoliths from the Fort à la Corne kimberlite field on the Sask Craton.

Re-Os dating was used to constrain the timing of melt depletion and to understand whether this part of the Sask Craton is under-pinned by classical "Archean' cratonic mantle.

2.2 Geological setting

The Sask Craton is an Archean crustal fragment located within central Saskatchewan and Manitoba (Lucas *et al.*, 1993). The terrane is enclosed within the Palaeoproterozoic Trans Hudson Orogen, which is one of the largest Palaeoproterozoic orogenic belts worldwide (Fig. 2.1) and comparable to the Himalaya (Weller and St-Onge, 2017). During the THO, the Superior Province, the Wyoming Craton, as well as the combined Hearne and Rae cratons were amalgamated, creating the extant North American Craton (Hoffman, 1988). Uranium-Pb geochronology constrains the time of collision as well as peak metamorphism of the orogen to between 1.9 – 1.8 Ga (Heaman *et al.*, 1992; Rayner *et al.*, 2005). Prior to the orogeny, rifting between the Superior and the Hearne cratons occurred from 2.2 to 2.0 Ga (Lewry *et al.*, 1994; Hajnal *et al.*, 2005; Heaman *et al.*, 2009) Seismic reflection data collected during the LITHOPROBE project reveal a buried, seismically distinct structure – the Sask Craton (Lewry *et al.*, 1994; Lucas *et al.*, 1994; Ansdell and Norman, 1995). First evidence of this Archean Craton was reported by Chiarenzelli (1989), who discovered Archean and Palaeoproterozoic basement rocks exposed within the interior of the orogenic belt. Further Archean to Palaeoproterozoic crustal ages, ranging between 3.3 – 2.07 Ga, have since been reported for other areas of the craton (Nd model ages, Collerson *et al.*, 1989; U-Pb in zircons, Rayner *et al.*, 2005 and references therein). However, exposure of the basement is limited to four small tectonic windows (Ashton *et al.*, 2005) and the reported ages are dominantly Palaeoproterozoic, 2.5 – 2.3 Ga.

As with many Archean cratons, the Sask Craton is intruded by kimberlites. The Star and Orion South kimberlites, from which our sample suite derives, are part of the Fort à la Corne (FALC) kimberlite field, situated within the proposed boundaries of the Sask Craton (Fig. 2.1). This diamondiferous kimberlite field was discovered in 1989 (Read and Janse, 2009). The more than 70 known kimberlite bodies of the FALC cluster occur within an approximately 200 m thick Lower Cretaceous sedimentary succession, deposited close to the north-eastern margin of the Western Interior Seaway (Leckie *et al.*, 1997). Kimberlite emplacement ages of circa 106 to 95 Ma have been determined using U-Pb perovskite and Rb-Sr phlogopite methods (Heaman *et al.*,

2004; Kjarsgaard *et al.*, 2017). Emplacement of the kimberlites was contemporaneous with Mannville Group and Colorado Group sedimentation (Zonneveld *et al.*, 2004). The kimberlite bodies represent extremely well-preserved primary and reworked pyroclastic deposits, including tuff rings, tuff cones, crater and extra-crater deposits (Leckie *et al.*, 1997; Zonneveld *et al.*, 2004).

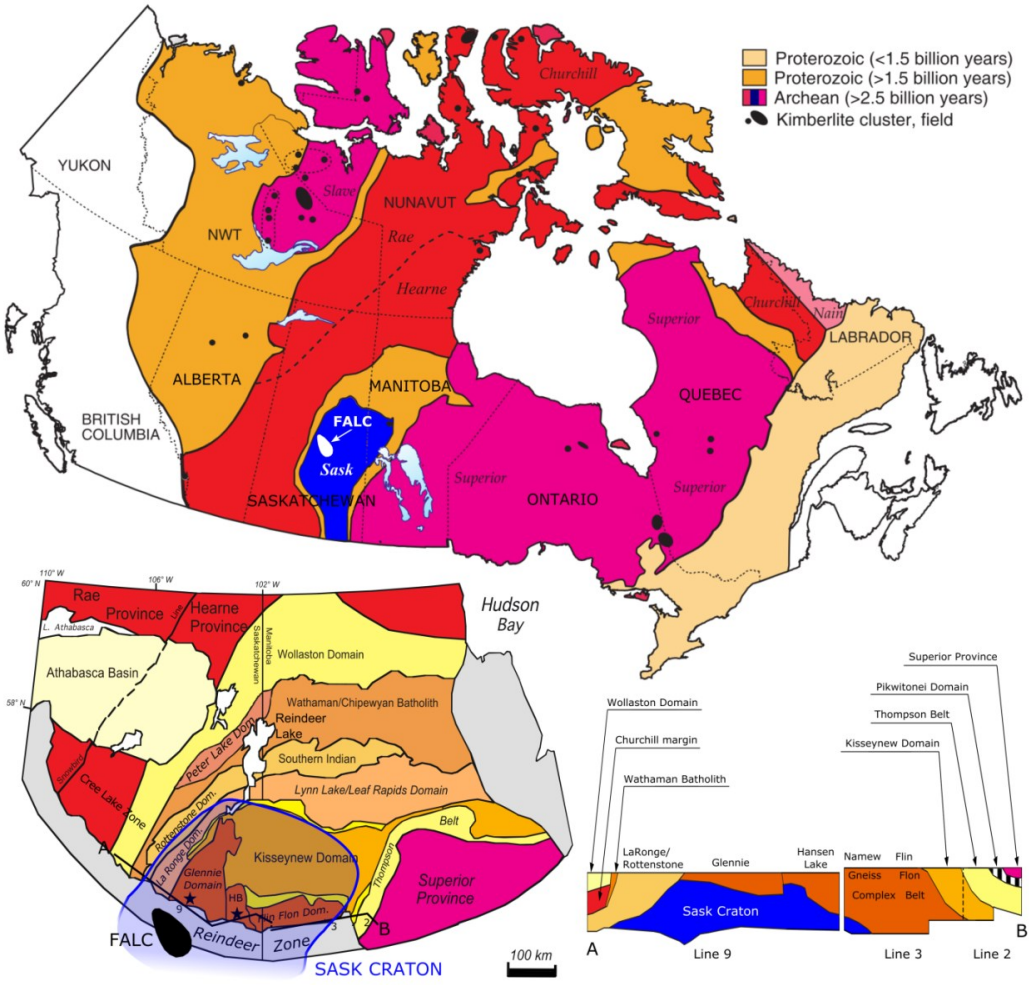

Fig. 2.1 Distribution of cratons, Proterozoic belts and kimberlite occurrences within Canada (adapted from Kjarsgaard, 2007), with a detailed map of the Trans Hudson Orogen and a cross-section of the Sask Craton and THO (LITHOPROBE Lines 9, 3, 2; adapted from Lewry *et al*., 1994 and Bickford *et al.*, 2005). Archean cratonic crust is shaded in red, pink and blue, black fields indicate kimberlite clusters, Proterozoic crust is displayed in shades of orange and yellow. White indicates Phanerozoic crust. The Sask Craton, highlighted in blue, is surrounded by the Proterozoic Trans Hudson Orogen (shaded in orange). The location of the FALC kimberlite cluster is outlined in black. The tectonic windows with exposure of Archean crust are indicated by stars

2.3 Samples and petrography

All peridotite xenoliths studied here were extracted from kimberlite drill core, as peridotite xenoliths generally did not survive crushing and subsequent heavy media separation. Twenty-six peridotite xenoliths from the Orion South and the Star kimberlite bodies, suitable in size for Re-Os analysis (diameter > 1cm), were chosen for analysis.

The xenoliths were classified as lherzolites based on the presence of clinopyroxene as well as their garnet major element chemistry. All xenoliths show minimal evidence of kimberlite melt infiltration. The majority of the samples experienced moderate to strong low-temperature alteration; a network of serpentine is often the only remaining evidence for the former presence of olivine; fresh orthopyroxene was identified in only two samples (17969 and 17698-3) and is otherwise lacking from the recognizable mineral assemblage. Clinopyroxene is more readily identified, but alteration is still common, often leaving garnet as the single remaining fresh phase. Kelyphite rims surrounding garnet grains are common, along with phlogopite replacement of garnet, suggesting late stage metasomatism, potentially related to kimberlite infiltration. Due to the intense alteration, no fresh sulphides were observed. Grain sizes vary significantly between xenoliths, with garnets ranging from 1 mm to 1 cm. In sample 17700-1, garnets and clinopyroxenes are spatially related and occur in bands. Additional textural features are difficult to identify due to the pervasive alteration of the samples and accurate modal proportions could not be determined for the sample suite. Garnets of varying colour and chemistry (see below) were observed in 7 of the 20 garnet-bearing samples. In some of these samples olivine of varying colours was identified. Olivines of uniform, light (highest Mg#) colour were picked for Os isotopic and PGE analyses when possible.

2.4 Analytical methods

Major and trace elements were measured on epoxy grain mounts. Major element analyses of mineral separates were obtained on a JEOL8900R Electron Probe Micro-Analyser (EPMA) using an accelerating voltage of 20 kV, a 20 nA probe current, and peak counting times between 30 and 60 s. The CITZAF procedure of Armstrong (1995) was used for data reduction. All analyses were carried out using a range of mineral and synthetic reference materials (Table A1, in Appendix).

Laser-ablation inductively coupled plasma mass spectrometry (LA-ICP-MS) employing a RESOlution 193 nm ArF Excimer Laser Ablation System coupled with a Thermo Element 2 XR ICP-MS was used to determine minor and trace element concentrations *in-situ* in garnet and clinopyroxene. The NIST612 reference glass was used for calibration. Reference glasses NIST614, BIR-1G, as well as in-house mineral standards PN1 (garnet) and GP-13 (clinopyroxene) were employed as secondary standards. Data reduction was conducted with the Iolite software using ^{43}Ca (for REE) and ^{29}Si (for Ni and Ti) as internal standards. Data are generally accurate to within 10% of "accepted" values for reference materials.

Radiometric dating using the Re-Os system, coupled with platinum group element (PGEs) analyses were carried out on picked olivine separates (presumably hosting Os alloys) rather than whole rock powder to avoid contamination through common kimberlite infiltration and contamination. Re-Os and platinum group element chemistry followed a protocol adapted from Pearson and Woodland (2000). Digestion is accomplished in an Anton Parr high pressure asher at 130 bar and 290 °C for 16 h, using inverse Aqua Regia followed by HBr and $CHCl_3$ back extraction and subsequent microdistillation of Os. Osmium isotopic compositions, as well as osmium abundances, were obtained using a Thermo Triton-Plus negative – thermal ionisation mass spectrometer (N-TIMS) via peak-hopping on a secondary electron multiplier (SEM). The Durham Os Standard (DrOsS) was used to determine long-term repeatability, giving an average $^{187}Os/^{188}Os$ of 0.16098 ± 0.00027 (2σ), in good agreement with the value proposed by Luguet et al. (2008).

Platinum group element and Re concentrations were determined via isotope dilution ICP-MS (Thermo Element 2 XR). Oxide production rates were determined using standard solutions (Ir and Pt: LuO/Lu <0.5%, HfO/Hf <1.5%; Pd: ZrO/Zr <2.5%, MoO/Mo <0.5%, YO/Y <1.8%; Re: YbO/Yb <0.05%, TmO/Tm <0.025%). Full procedural blanks (Os 0.71 ± 0.20 pg, Ir 2.3 ± 0.4 pg, Pt 4.1 ± 2.7 pg, Pd 6.0 ± 4.7 pg, Re 6.1 ± 3.0 pg) were used to correct samples.

2.5 Results

Average major and trace element concentrations, as well as platinum group element and isotopic compositions are reported in Tables A2, A3, and A4, respectively.

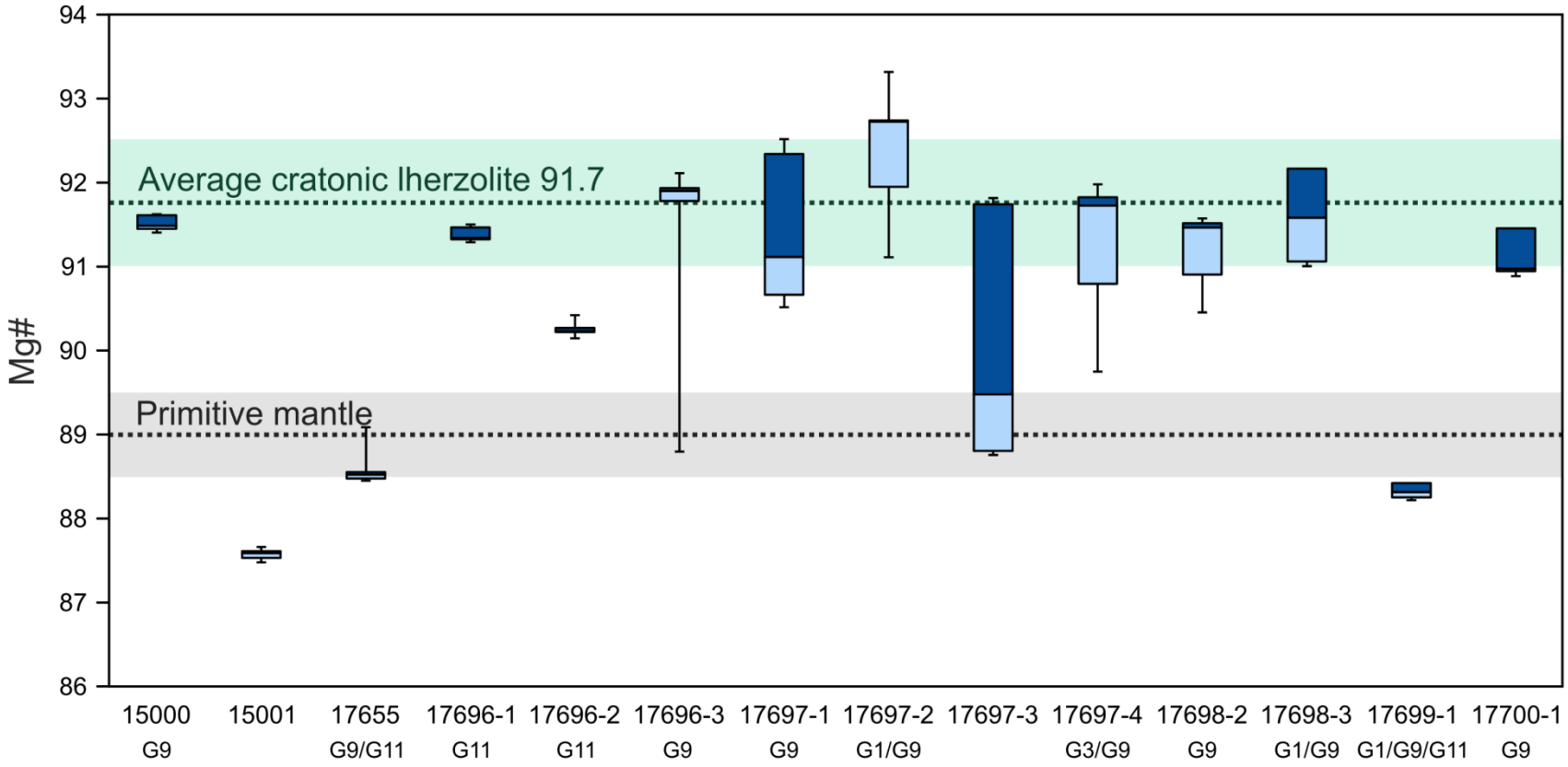

Fig. 2.2 Box and whisker plot of olivine Mg#. The majority of FALC olivine compositions overlap with the 1 sigma range of olivine from cratonic lherzolites (based on 903 published analyses of olivine from cratonic lherzolite xenoliths from a xenolith database). A small proportion of samples have compositions similar to, or lower than primitive mantle (~89, McDonough and Sun, 1995; Palme and O'Neill, 2003). Lower and upper limit of boxes represent the first and 3rd quartile, respectively. The middle line of the box indicates the median value of the sample population; the extent of the whiskers correlates to the minimum and maximum Mg#. Garnet G-classification (Grütter *et al.*, 2004) for garnet-bearing samples is shown below the sample name

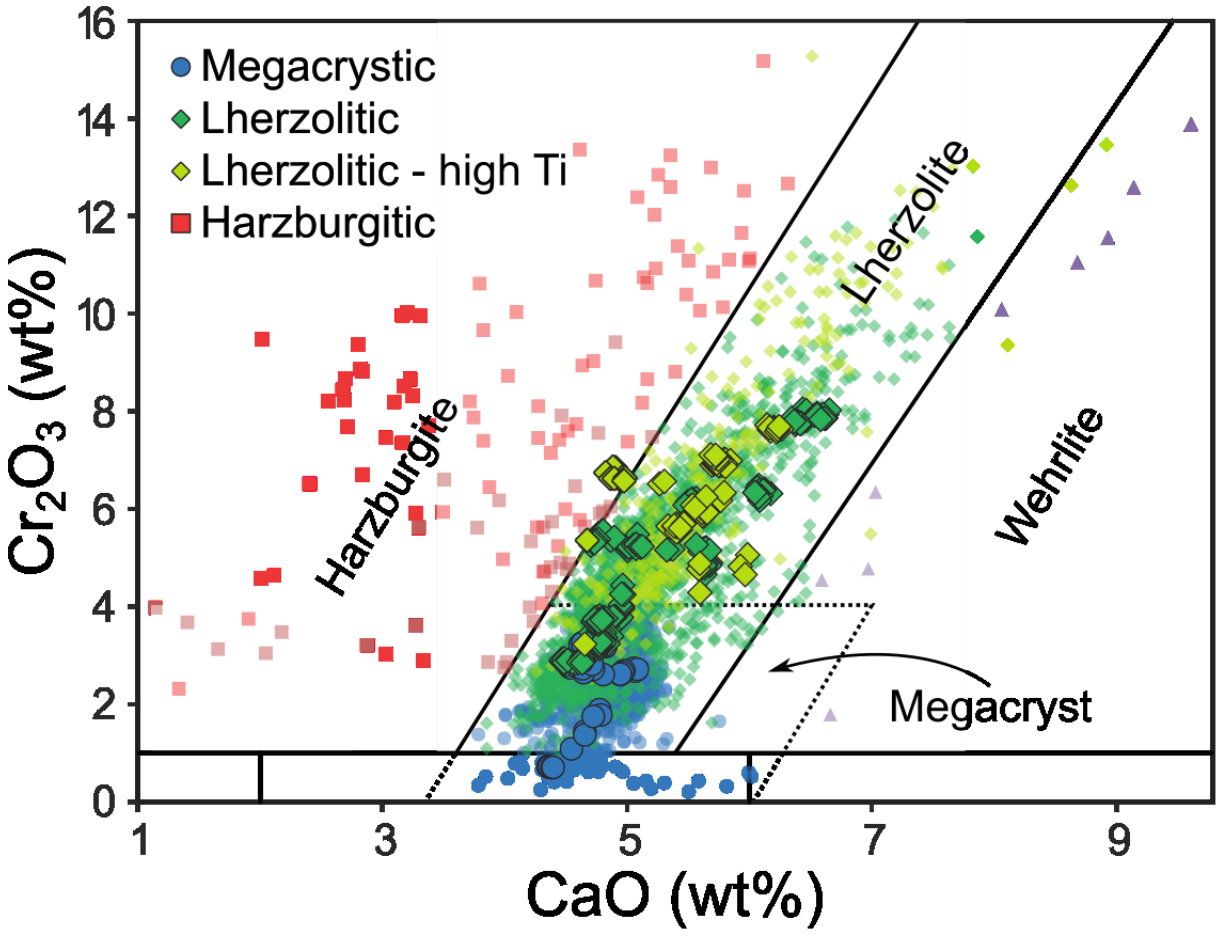

Fig. 2.3 Garnet classification using major element compositions, following Grütter *et al.* (2004). Small symbols are data for garnet from heavy mineral concentrate (Star Diamond Corp., unpublished). Large symbols represent xenolith garnet compositions from this study. Most xenolith garnets fall within the lherzolitic field and only a small subset of high-Ti peridotitic (G11) garnets plots just within the harzburgite field. The division between lherzolitic and harzburgitic garnets depends on pressure, temperature and compositional effects, with elevated Na in particular stabilising lherzolitic garnets to lower Ca contents (Sobolev *et al.*, 1973). The few high-Ti peridotitic garnets plotting in the harzburgite field co-exist with cpx with slightly enriched Na contents, consistent with the observation of Sobolev *et al.* (1973)

2.5.1 Major and trace element mineral chemistry

Olivine major element compositions were obtained for 14 peridotites. Single olivine grains are internally homogeneous, but a broad spread in Ni, Mg and Fe contents is observed among and within xenoliths. Molar Mg# (100Mg/(Mg+ Fe)) values range from 87.6 to 92.8, with a dominant mode at 91.5, which is typical for lherzolitic cratonic mantle (Fig. 2.2). Though olivines with Mg# <90 are compatible with a lherzolitic lithology, the variation of olivine Mg# in the same sample (17697-1) from 92 to 89 likely is the result of secondary Fe-enrichment (Eggler *et al.*, 1987). Large variations in Ni concentrations (0.13 to 0.37 wt%) have been recorded in olivines with anomalously low Mg#, whereas the olivines with depleted mantle peridotite signatures (Mg# >90) have higher and more restricted Ni contents (0.31 – 0.42 wt%).

Twenty xenoliths contain garnet, which shows a wide range of composition, even in one sample. Individual garnets are homogenous, the majority being of lherzolitic paragenesis (Fig. 2.3), with 15 xenoliths containing G9 (lherzolitic) and 7 xenoliths G11 (high-titanium peridotitic) garnets. Low-Cr, high-Ti garnets of megacryst-like compositions are less common (G1; 5 xenoliths). One sample (17697-4) contains garnets of both peridotitic (G9) and eclogitic (G3/G3D) composition and could be characterised as a polymict breccia (Lawless *et al.*, 1979), the first known occurrence of such xenoliths in North America. In contrast to garnets from heavy mineral concentrate (Star Diamond Corp. unpublished), no harzburgitic (G10) garnets were identified in the xenoliths studied (Fig. 2.3), in keeping with their general scarceness in xenolith suites worldwide (Boyd *et al.*, 1993).

Garnets typically show "normal" (Hoal *et al.*, 1994) REE_N patterns (N=chondrite normalised; Fig. 2.4), characterised by positively sloped $LREE_N$ and flat to enriched $MREE_N$-$HREE_N$, common in mantle lherzolites that experienced melt metasomatic re-enrichment (Stachel *et al.*, 1998). Five samples (15000, 17651-1, 17694-2, 17696-2, 17698-2) have weakly sinusoidal patterns. Zr and Y concentrations (Fig. 2.5) indicate that the secondary enrichment was dominated by high temperature melt metasomatism. Similar REE_N patterns for garnets from FALC have been reported by Canil *et al.* (2003). Only a few samples experienced low temperature (phlogopite) metasomatism (Griffin *et al.*, 1999c). Clinopyroxene (Cr-diopside) could be identified in 13 of the peridotites. Most compositions plot within the “on-craton” garnet peridotite field defined by Ramsay and Tompkins (1994), i.e., with low Al contents (Al_2O_3 < 4

wt%) and Mg# ranging from 88.7 to 93.2. Only a few analyses, from the heavily metasomatised sample 17679, have Al_2O_3 > 4 wt%. Clinopyroxenes (Fig. 4) are typically enriched in $LREE_N$ (10 – 70 x chondritic) with a negative slope in $MREE_N$ and $HREE_N$. There is no difference in pyroxene compositions coexisting with lherzolitic, high-Ti peridotitic and megacryst-like garnets. Only samples 17679 and 17698-3 contain orthopyroxene fresh enough for analysis. The enstatite compositions (Mg# 91.7 and 92.2, respectively) are slightly lower than typical cratonic harzburgite (Pearson *et al.*, 2014), but they overlap with compositions reported for lherzolitic orthopyroxene from the Slave Craton (Kopylova *et al.*, 1999). The orthopyroxene in garnet lherzolite sample 17679 has low CaO (0.2 wt%) and elevated Al_2O_3 (2.3 wt%) values, whereas 17698-3 has a high CaO content of 0.78 wt% and an Al_2O_3 value of 0.73 wt%.

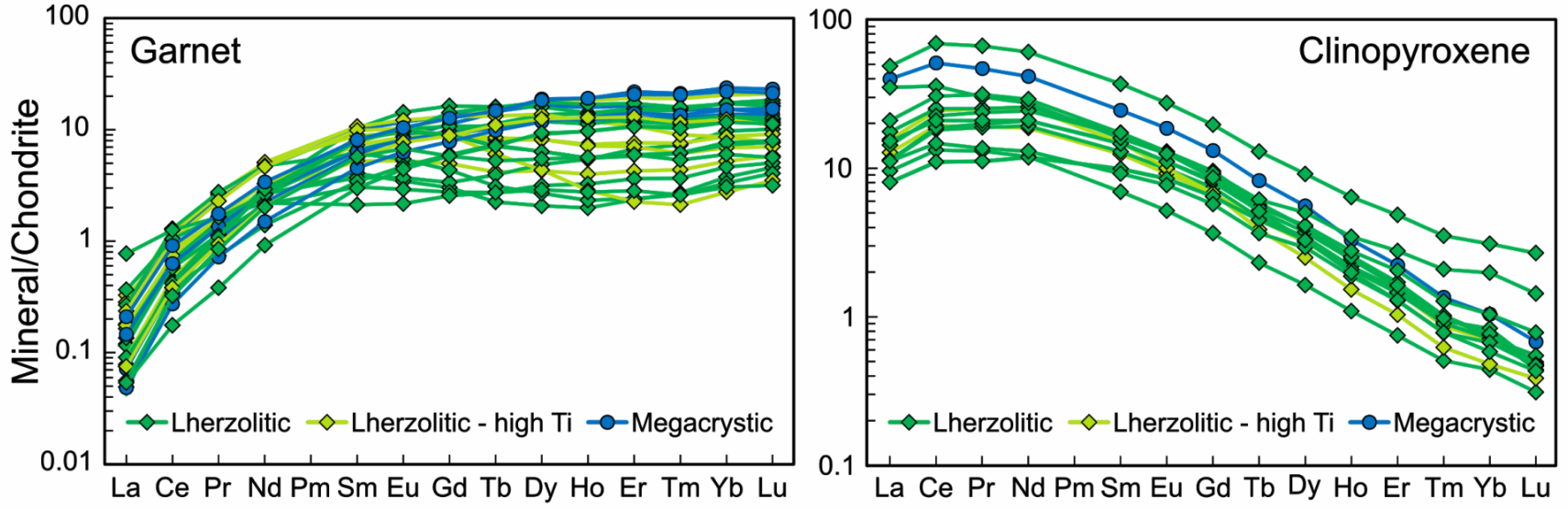

Fig. 2.4 REE composition of FALC garnets and clinopyroxenes normalised to chondrite (McDonough and Sun, 1995). For samples where more than one trace element composition was obtained, the averaged data is plotted. Sample colours correlate to the colour scheme in the garnet CaO vs Cr_2O_3 plot (Fig. 2.3)

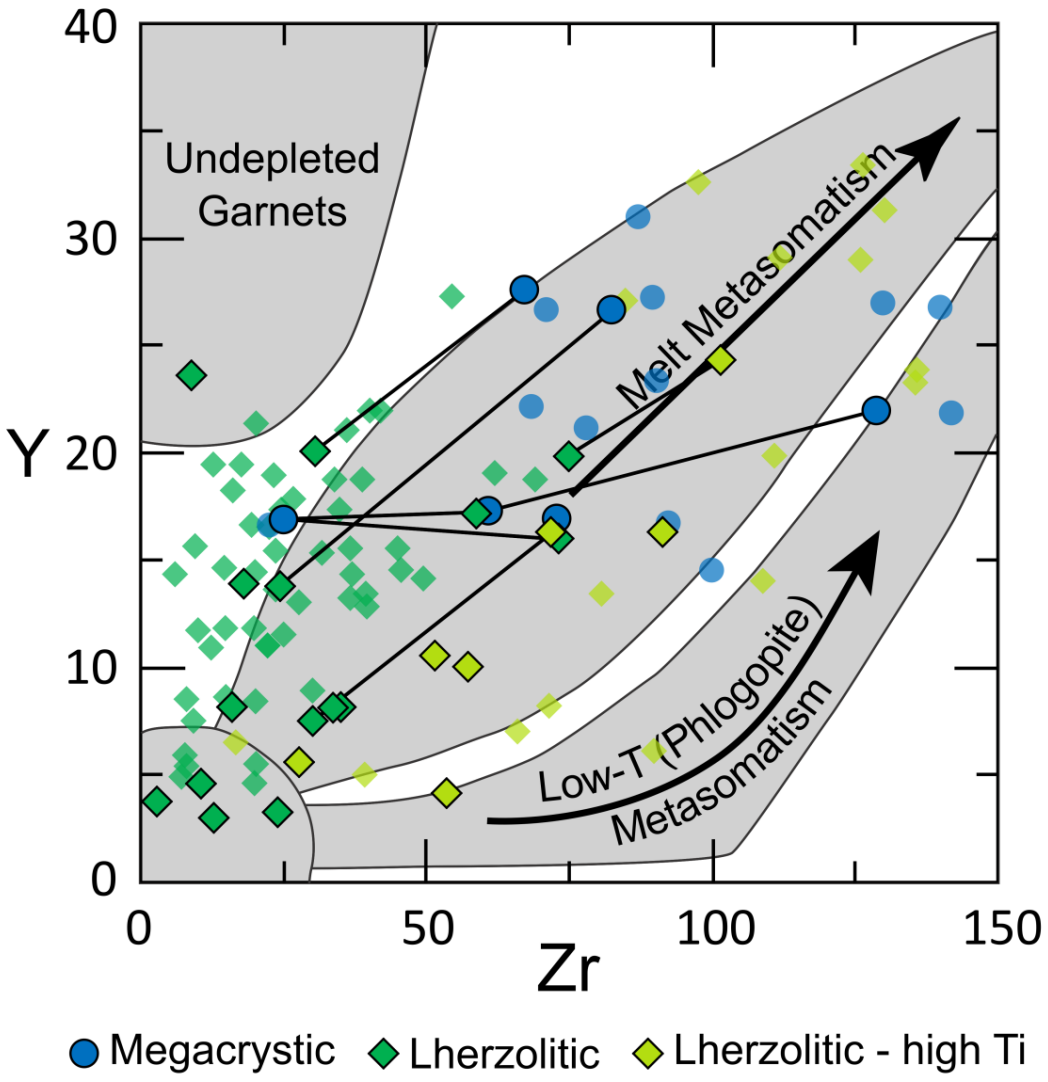

Fig. 2.5 Zr vs Y variation in peridotitic garnets, following (Griffin *et al.*, 1993). Garnets from FALC peridotite xenoliths dominantly exhibit compositions associated with high temperature melt metasomatism, which appears to have affected all identified types of garnet compositions (i.e. G1, G9, and G11). Only a small subset of samples show little metasomatised, depleted compositions, or a low temperature metasomatic signature. Xenolith compositions are shown as black-rimmed symbols, where samples that contain two significantly different types of garnet are linked by a black line. Small lighter coloured symbols indicate concentrate data (Star Diamond Corp., unpublished)

2.5.2 Geothermobarometry

Temperature and pressure estimates, as well as thermobarometers used are listed in Table A5. As xenolith-based P-T data are limited, single grain thermobarometry (T_{NT00} & P_{NT00}, Nimis and Taylor, 2000) on clinopyroxene mantle xenocrysts from heavy media concentrate was used to construct a Cretaceous palaeogeotherm for the mantle beneath FALC (Fig. 2.6). A series of compositional filters was applied to test for (1) quality of the EMPA data, (2) derivation from garnet peridotite, and (3) adherence to specific compositional brackets covered by the experimental calibration of P_{NT00} (Grütter, 2009). Further, samples with significant Na-enrichment were removed from the dataset using a similar approach as employed by Creighton and Read (2013). Over 700 clinopyroxene analyses out of 5500 from the Star Diamond Corp. database (unpublished) were used to calculate a FITPLOT geotherm following the method of Mather *et al.* (2011) and McKenzie and Bickle (1988). The resulting geotherm is "cool", similar to the Slave Craton geothermal array (Grütter, 2009) and the 38 mW/m^2 reference geotherm of Hasterok and Chapman (2011). Our FITPLOT geotherm compares well to a previously published geotherm by Read and Janse (2009). Lithosphere thickness, based on the intersection of the geotherm with a mantle adiabat for a potential temperature of 1300 °C, is estimated at 210 ± 20 km and diamond is stable at depths greater than 120 ± 20 km using the graphite-diamond transition of Day (2012), resulting in a large "diamond window" of about 100 km.

The pressure and temperature data for single clinopyroxene grains from FALC xenoliths, ranging from 840 to 1250 °C and 2.7 to 5.5 GPa, scatters around the deeper portion of the geotherm calculated from xenocrysts (Fig. 2.6). The majority of FALC peridotite xenoliths were derived from within the diamond stability field with pressures ranging from 4.6 to 5.5 GPa. Only sample 17679 equilibrated at significantly lower pressures (above diamond-graphite transition). The Cr exchange barometer (P_{NT00}) of Nimis and Taylor (2000) was used to derive pressure estimates for clinopyroxene-bearing samples; in addition for the two xenoliths containing fresh garnet and orthopyroxene (17679 and 17698-3) pressures were calculated via Al-exchange (P_{NG85}; Nickel and Green, 1985). Pressure estimates for 17698-3 are in good agreement for the two barometers, whereas for sample 17679 pressures produced by P_{NT00} (2.7 GPa) are higher than pressures for P_{NG85} (2.0 GPa).

For the two samples that contain orthopyroxene in addition to clinopyroxene, temperatures of 840 °C (17679; P_{NG85} = 2.0 GPa) and 1190 °C (17698-3; P_{NG85} = 5.3 GPa) were calculated using the two pyroxene thermometer (T_{TA98}; Taylor, 1998), which agrees well with the temperatures obtained by T_{NT00} (Table A5).

$T_{Ni\text{-}in\text{-}grt}$ was applied to xenoliths with fresh garnet. The most accurate estimates for $T_{Ni\text{-}in\text{-}grt}$ are obtained by averaging T_{Canil} (Canil, 1999) and T_{Giffin} (Griffin and Ryan, 1996), based on the observation that at high temperatures T_{Canil} underestimates and T_{Giffin} overestimates temperatures (Shu *et al.*, 2013). The temperatures for garnets of lherzolitic (G9) composition are generally in agreement (< 100 °C difference) with those derived via enstatite-in-clinopyroxene thermometers (T_{TN00} and T_{TA98}). Pressure estimates obtained by projecting the calculated temperatures onto the Sask palaeogeotherm record a similar sampling depth to the applied single pyroxene and pyroxene-garnet barometers. However, a significant proportion of FALC xenoliths (28%) contain multiple garnets of variable geochemical compositions (G1, G9, and G11) as a result of metasomatism. If all analysed garnet compositions are taken into consideration, the calculated Ni in garnet temperatures and corresponding pressures span a significantly wider range (750 to 1430 °C, 3.3 to 6.8 GPa), with the highest temperature estimates relating to garnets of megacryst-like (G1) composition. Similarly, temperatures calculated for garnets of G11 composition are elevated in comparison to temperatures derived by the single clinopyroxene thermometer of Nimis and Taylor (2000). The Ni in garnet thermometer assumes exchange between garnet and olivine (Ni concentrations of 3000 ppm were assumed). However, garnets with elevated Ti-contents (G1 and G11) were affected by melt metasomatism and are likely not in equilibrium with the assumed olivine compositions, hence, reporting elevated temperatures.

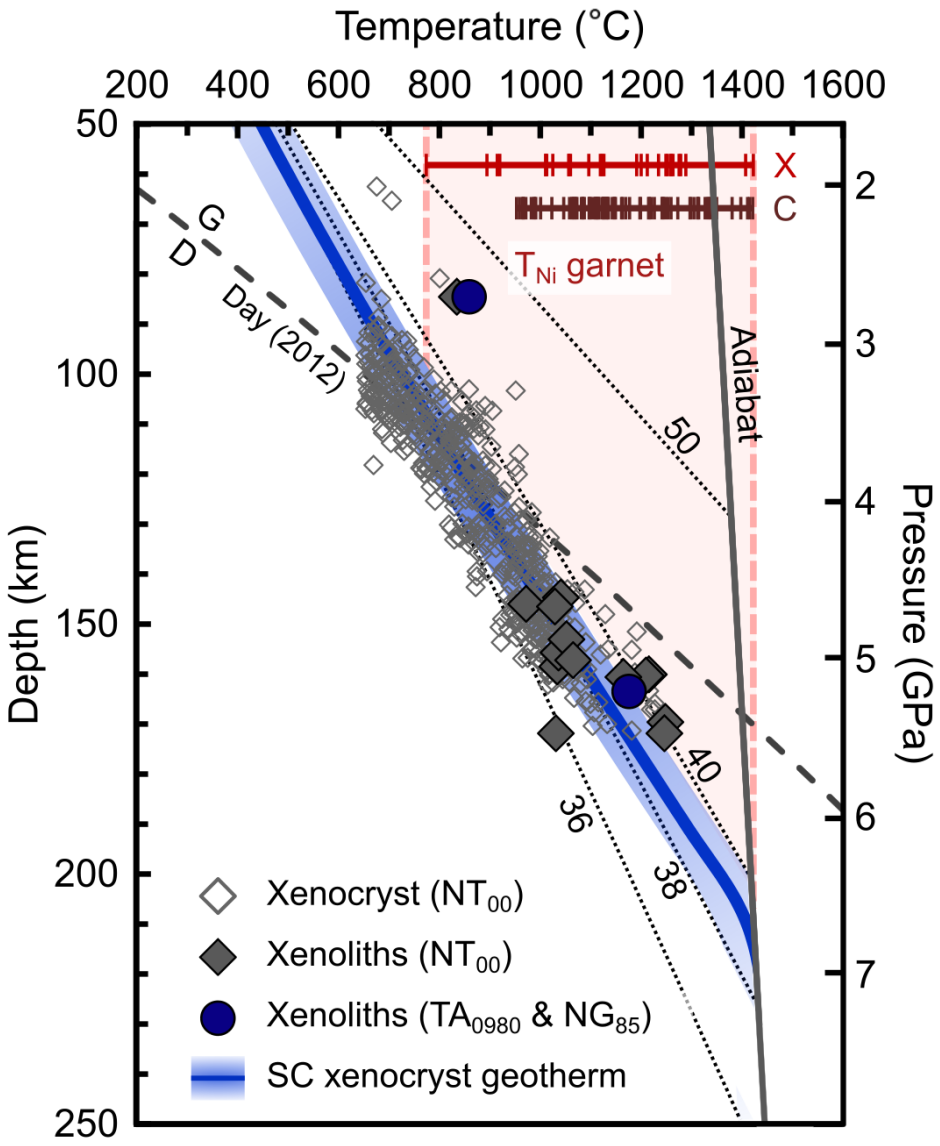

Fig. 2.6 Depth/pressure versus temperature profile of the Cretaceous Sask Craton lithospheric mantle, based on geothermobarometric data obtained from FALC clinopyroxene xenocrysts and peridotite xenoliths. A FITPLOT model geotherm (thick blue line) with error envelope (lightly blue shaded area) was calculated based on combined estimates of T_{NT00} and P_{NT00} (Nimis and Taylor, 2000) using 742 clinopyroxene xenocrysts that passed the compositional filters of Grütter (2009). The diamond-graphite transition curve (Day, 2012), as well as model geotherms of Hasterok and Chapman (2011) for 36, 38, 40 and 50 mW/m^2 surface heatflow are included for reference. For peridotite xenoliths, PT estimates based on T_{NT00} and P_{NT00} (grey filled diamonds) and T_{TA98} (Taylor, 1998) and P_{NG85} (Nickel and Green, 1985; blue circles) fit the xenocryst based geotherm. Ni in garnet temperatures (Griffin and Ryan, 1996; Canil, 1999) are shown in red at the top for xenoliths (X) and xenocrysts (C)

2.5.3 Re-Os isotope composition and age constraints

FALC peridotites exhibit a wide range of $^{187}Os/^{188}Os$ compositions, ranging from 0.1109 to 0.1507 (Table A4). The most radiogenic isotopic ratios correspond to samples with low Os concentrations (<0.35 ppb) and high $(Pd/Ir)_N$ (see below). Elevated Pd/Ir in depleted peridotites has been shown to reflect metasomatism (Rehkämper *et al.*, 1999; Pearson *et al.*, 2002) and such samples will not be considered further because they cannot be used to obtain melt depletion ages. Duplicate analyses were carried out for three samples, of which only sample 17700-1 had reproducible Os compositions and the average of the two analyses was used to calculate a model age. For the other two samples, only one of the analyses produced realistic Os ratios. Sample heterogeneity in Os isotope composition can be explained by kimberlite infiltration or as a nugget effect. T_{RD} (time of Re-depletion) model ages were calculated using initial $^{187}Os/^{188}Os$ values to exclude recent Re addition during kimberlite eruption. This approach results in minimum ages, except for undisturbed high degree melt residues, for which they approximate the time of melt depletion. The T_{RD} ages are in good general agreement with T_{MA} (time of melt depletion) ages (calculated with the measured Re/Os), with the ages typically being well within error due to low Re in most olivines. A proportion (3 samples) of T_{MA} ages are meaningless, (future ages or ages older than the age of the Earth), indicating recent disturbance of Re concentration, Os isotopes, or both (Fig. 2.7). As such, only T_{RD} ages will be plotted and discussed. The rhenium depletion ages for the FALC peridotites range from 2.4 to 0.5 Ga (Fig. 2.8), with a dominant mode at 1.8 – 2.4 Ga.

2.5.4 Platinum group element (PGE) and Re concentrations

PGE concentrations for olivine separates of the FALC xenoliths are highly variable, all being significantly lower than primitive upper mantle (PUM) abundances (Fig. 2.9). The I-PGEs Os and Ir show no strong inter-element fractionation, which is common for these elements as they behave similarly even at high degrees of partial melting (Pearson *et al.*, 2004; Aulbach *et al.*, 2016). For xenoliths recording model ages older than 1.7 Ga, platinum group-PGEs (P-PGEs) are increasingly fractionated from Pt to Re, a trend most characteristic of highly depleted peridotites, or olivines from such peridotites (Smit *et al.*, 2014b). Re-enrichment of Re is only observed in a few samples. Peridotites younger than 1.5 Ga have positive PUM normalised Pt and Pd

anomalies, as well as more fractionated P-PGEs. Phanerozoic samples and xenoliths lacking age correlation exhibit almost horizontal or irregular PGE patterns (Fig. 2.9).

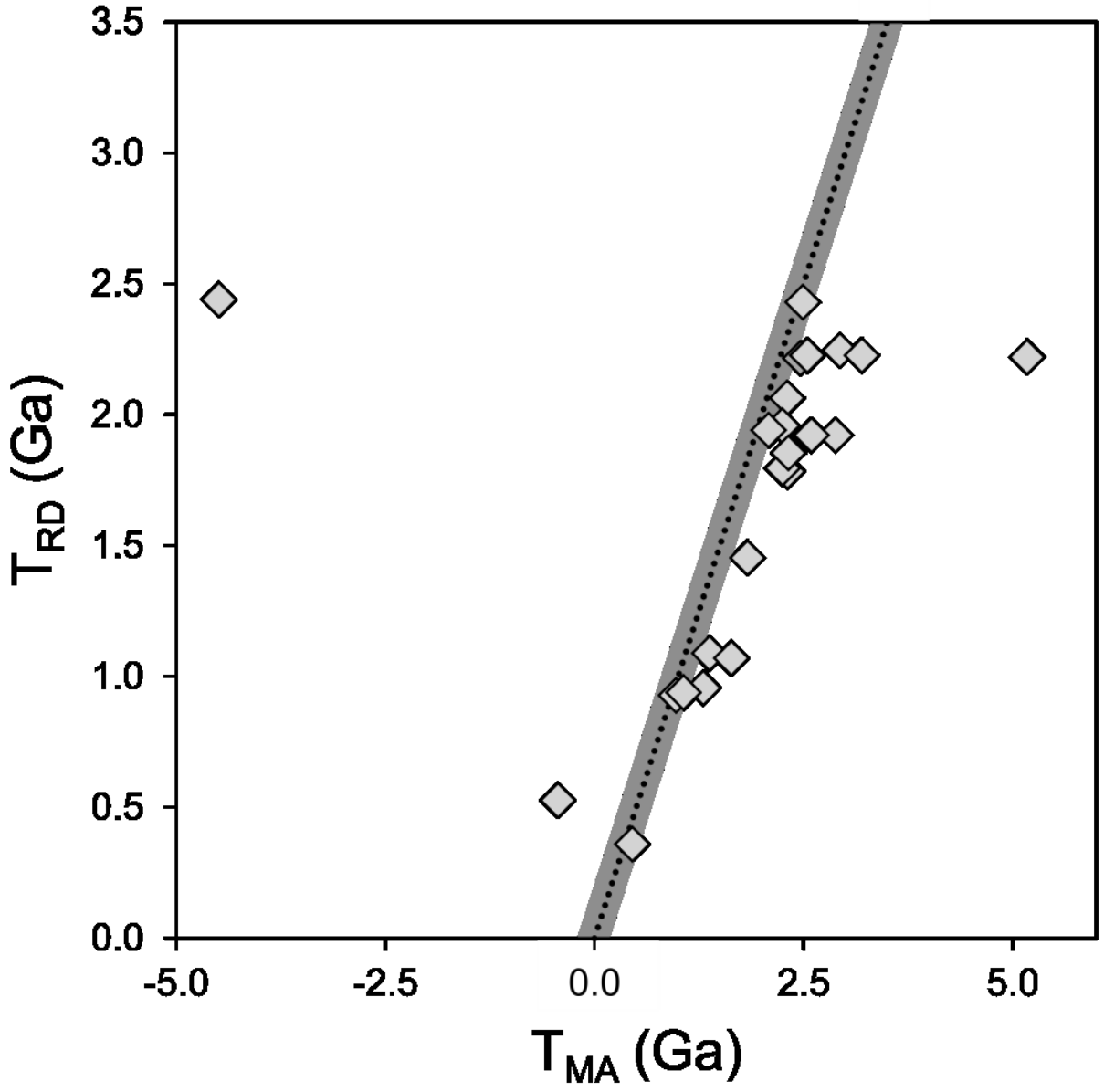

Fig. 2.7 Comparison of Re depletion (T_{RD}) and mantle separation (T_{MA}) model ages for olivine separates from FALC peridotite xenoliths. The dotted line indicates a 1:1 ratio of T_{RD} to T_{MA} ages

2.6 Discussion

Cratonic peridotites are typically interpreted as the residues of high degrees of partial melting (Boyd, 1989; Walter, 1999). Hence, harzburgites - peridotites that have experienced significant degrees of melt depletion - have been identified in the SCLM for the majority of Canadian cratons (e.g., Slave, Griffin *et al.*, 1999a, Kopylova *et al.*, 1999; Superior, Scully *et al.*, 2004, Smit *et al.*, 2014; Rae, Liu *et al.*, 2016). Mineral concentrate data from Sask Craton kimberlites (Griffin *et al.*, 2004; Star Diamond Corp., unpublished; Fig. 2.3) show a minor population of high-Cr subcalcic garnets that last equilibrated with olivine at depth of 130 – 185 km. Calculated olivine Mg# for the SCLM (90.5 - 92.5; calculated from lherzolitic and harzburgitic garnets; Griffin *et al.*, 2004) is in agreement with olivine compositions measured from the garnet-facies xenoliths examined in this study (Mg# 87.6 to 92.8), indicating that the Sask craton root is not quite as depleted as the lithospheric root beneath the Slave Craton. Canil *et al.* (2003) reported garnet compositions (e.g. low Zr/Y) indicative of prevalent high-T metasomatism.

In contrast to the concentrate data of Griffin *et al.* (2004), all garnets in xenoliths analysed in this study have lherzolitic compositions (Fig. 2.3), even for xenoliths containing no visible clinopyroxene. In samples where garnet and clinopyroxene are absent, the average Mg# of olivine (91.5; Fig. 2.2) is consistent with a moderately depleted (lherzolitic) mantle composition. We cannot rule out that the lack of harzburgite and/or dunite xenoliths may relate to sampling bias; in this regard, we also have no spinel peridotites in our sample set. However, the proportion of high-Cr G10 garnets is low overall (<10%; Griffin *et al.* 2004) and a more fertile bulk composition for the Sask Craton lithospheric mantle is consistent with, although not exclusively explained by, lower S-wave velocities compared with adjacent cratons (Superior, Churchill, and Slave; Schaeffer and Lebedev, 2014). Composition and temperature are the dominant factors affecting velocity. Comparing the Slave (average harzburgite content > 35%; Griffin et al. 1999) and Sask cratons, which have comparable geotherms (Grütter, 2009), the variation in velocity is likely related to compositionally different lithospheric mantle.

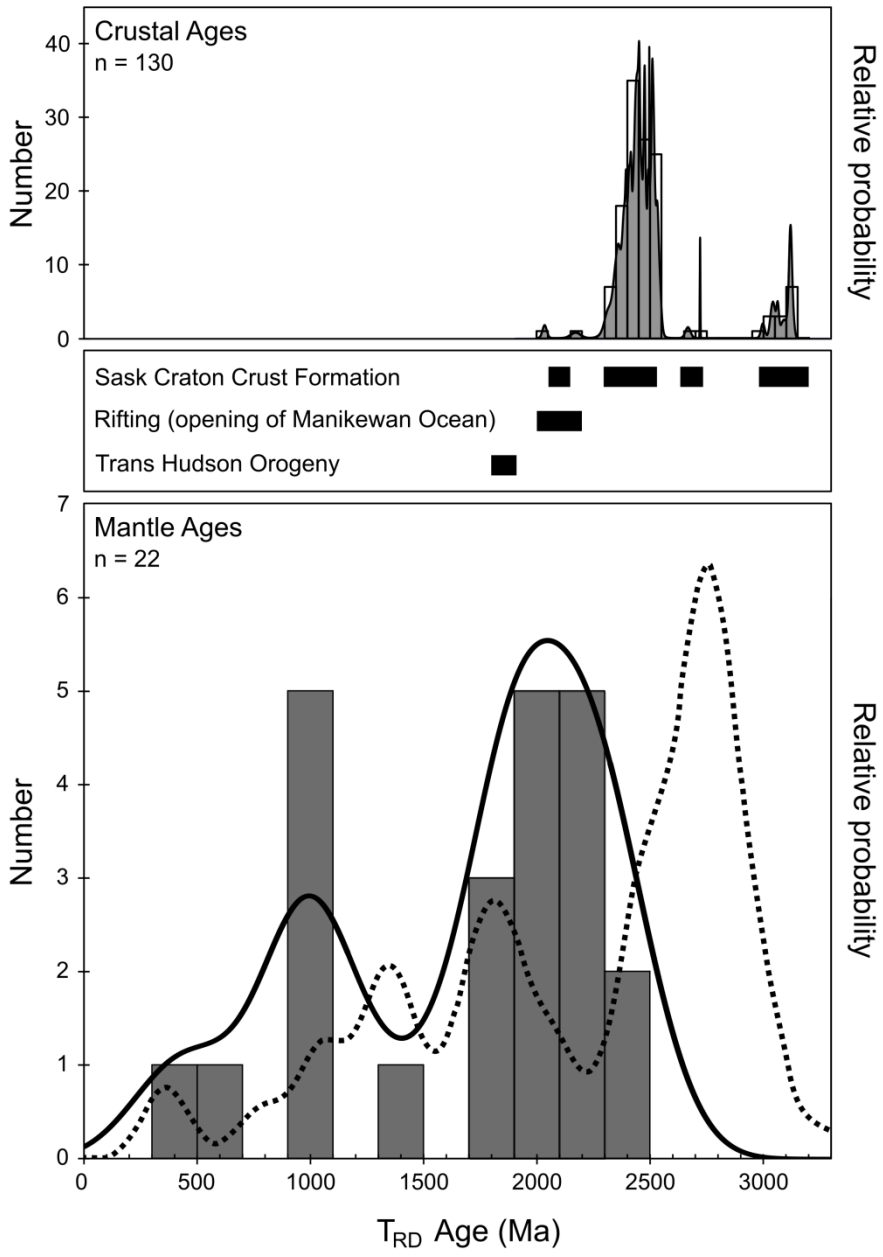

Fig. 2.8 Histogram and probability density diagram of T_{RD} model ages, corrected for Re ingrowth after kimberlite infiltration. An average uncertainty of 0.2 Ga (1σ) was applied to all ages, to avoid overrepresentation of ages with small uncertainties. For comparison, the dominant crustal ages for the Sask Craton, the timing of the opening of the Manikewan ocean and the subsequent Trans Hudson Orogeny are shown above the histogram (additional data from Collerson *et al.*, 1990; Heaman *et al.*, 1992; Davis *et al.*, 1998). In addition, a compilation of crustal zircon ages from the Sask Craton is shown for reference (Rayner, personal correspondence). A probability density plot of Slave peridotite whole-rock and sulphide T_{RD} ages is plotted as a dotted black line (Heaman and Pearson, 2010)

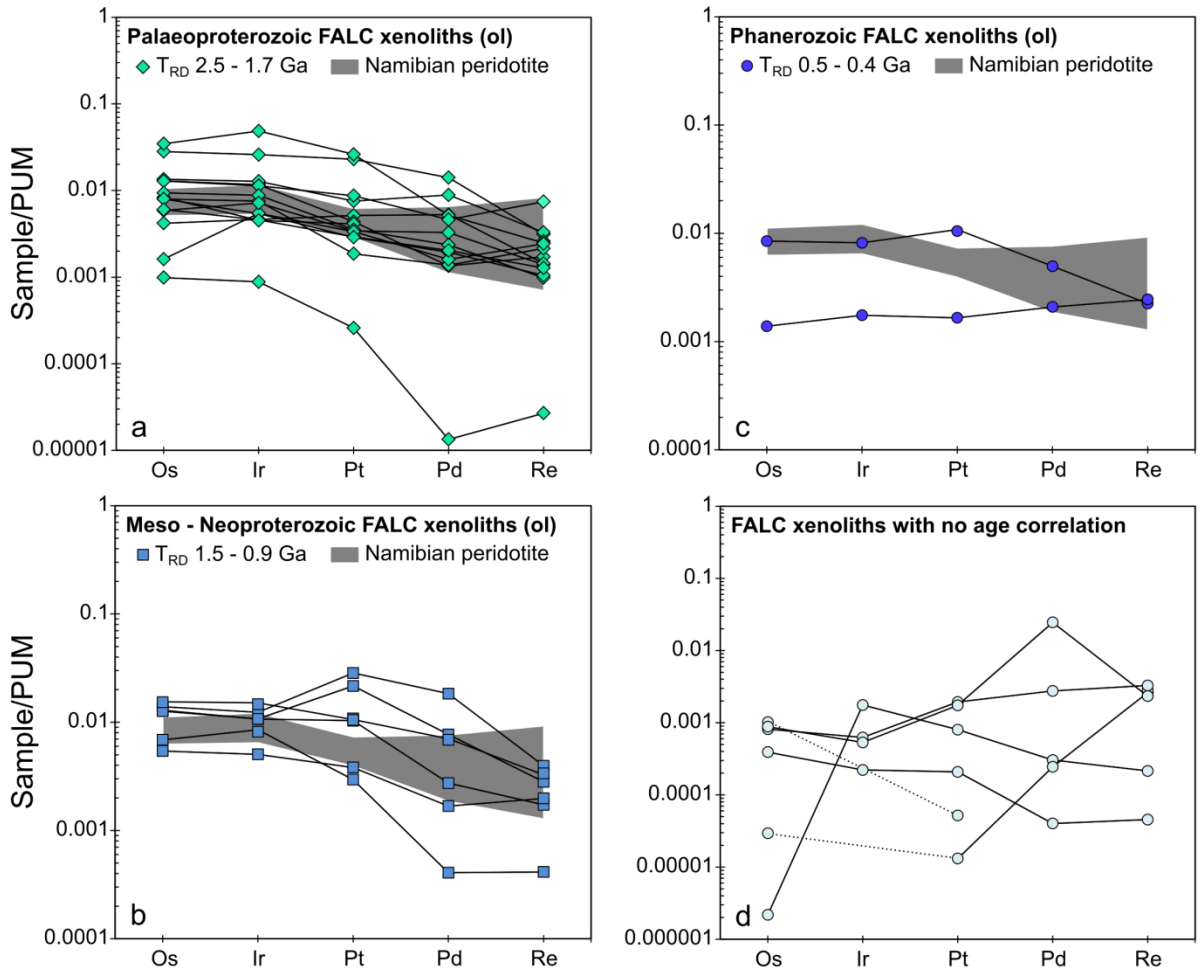

Fig. 2.9 Platinum group element (PGE) and Re concentrations from olivine separates of FALC xenoliths normalised to primitive upper mantle (Becker et al. 2006). The data are separated into four groups based on T_{RD} model ages. (a) For samples with Paleoproterozoic T_{RD} ages (green diamonds) fractionation trends are comparable to trends for Namibian peridotites (grey shaded area; Pearson *et al.*, 2004). (b) Peridotites with T_{RD} model ages (light blue squares) between 1.5 and 0.9 Ga show a mix of P-PGE (Pt to Re) depleted trends and also enrichment in Pt and Pd, indicative of a metasomatic process. (c) Two samples with Phanerozoic ages (dark blue circles) have flat PGE patterns. (d) Xenoliths that have future or negative model ages (light blue circles) show overall greatly disturbed PGE_N patterns. Rhenium re-enrichment can be observed in samples from all groups

2.6.1 Effects of mantle metasomatism and crustal alteration

Peridotite xenoliths from the FALC kimberlites are characterised by strong variations in major element composition for olivine, garnet and clinopyroxene, an observation that is commonly attributed to secondary processes. The two dominant processes affecting the sampled peridotite xenoliths are high temperature metasomatism and low temperature crustal alteration.

FALC kimberlites were emplaced in a near-shore marine setting (Zonneveld *et al.*, 2004) resulting in pervasive serpentinisation of the peridotite xenoliths. Crustal alteration, however, appears to have little effect on Os isotope compositions. Previous studies have found that there is no evidence for significant addition of radiogenic Os during crustal alteration (Rehkämper *et al.*, 1999; Liu *et al.*, 2016) and T_{RD} model ages are routinely reported for abyssal peridotites (e.g., Snow and Reisberg, 1995; Warren and Shirey, 2012), which have commonly experienced severe serpentinisation. Hence, Re – Os ages can be robust even for pervasively serpentinised xenoliths.

In comparison to values typically reported for lherzolites from the cratonic lithosphere, Mg#s of olivines from the Sask Craton show a broad range (87.6 to 92.8, Fig. 2.2), extending to values below primitive mantle (~89; McDonough and Sun, 1995; Palme and O'Neill, 2003), for which coexisting olivine should have an Mg# of ~89. However, the depleted nature of lithospheric mantle (e.g., Boyd, 1989) should result in elevated bulk rock and olivine Mg#s. Here we use a cut-off in olivine Mg# of ≥90 for primary cratonic peridotites. Samples with olivine Mg# <90 represent a minor subset (~20%) of our entire dataset. Previous studies have demonstrated that olivine with lower forsterite content (Mg# <90) can form via high temperature metasomatism, potentially related to infiltration by proto-kimberlite melts (Eggler *et al.*, 1987). In addition, in the studied xenoliths this Fe-enrichment is typically coupled with a spread in Ni concentrations, following a trend that has previously been described for polymict peridotites from South Africa (Lawless *et al.*, 1979; Giuliani *et al.*, 2014). One of the FALC peridotites (17697-4) is evidently polymict in nature, containing garnets of lherzolitic and eclogitic composition, indicating proto-kimberlite metasomatism and physical disruption and mixing of peridotites and eclogites.

Further evidence for high temperature metasomatism can be derived from garnet major and trace element compositions. FALC peridotite xenoliths have lherzolitic (G9) garnet compositions, with some being enriched in TiO_2. Weakly sinusoidal REE_N patterns are associated with either low Y and Zr concentrations characteristic for depleted garnets, or show high Zr/Y ratios typical for

hydrous fluid metasomatism, which is in agreement with their sinusoidal nature (Stachel and Harris, 2008). The "typical" normal garnet REE patterns in Fig. 2.4, with flat $MREE_N$ and $HREE_N$, show enrichment in Y and Zr (Fig. 2.5; Griffin *et al.*, 1993) consistent with melt-dominated metasomatism. The agent of melt metasomatism can be further characterised employing Ti/Eu and Zr/Hf (Shu and Brey, 2015). A combination of elevated Zr/Hf (> 40) and low Ti/Eu (< 3500) can be attributed to interaction with carbonatite (Yaxley *et al.*, 1991; Rudnick *et al.*, 1993). Metasomatism by silicate melts, such as kimberlites, is associated with enrichment in Ti (Menzies *et al.*, 1987; Griffin *et al.*, 1999c). Most lherzolitic (G9) garnets in this study have Ti/Eu < 3500 and Zr/Hf > 40, indicative of carbonatitic metasomatism. The metasomatism may be linked to Palaeoproterozoic carbonatite activity in the THO and the Superior Craton (Chakhmouradian *et al.*, 2008; Heaman *et al.*, 2009). In comparison, garnets enriched in Ti (G1 and G11), have Ti/Eu > 3500 and Zr/Hf between 30 and 50, and are more likely to document interaction with a low volume silicate melt, potentially proto-kimberlitic (Griffin *et al.*, 1989). This complex metasomatic history is consistent with findings from diamondiferous eclogites from FALC (Czas *et al.*, 2018), which also interacted with both carbonatitic and kimberlitic metasomatic agents.

Pd/Ir ratios can be used as a proxy for melt depletion and enrichment as the P-PGEs become preferably incorporated into melt, whereas the I-PGEs are retained in the residue (Alard *et al.*, 2000; Mungall and Brenan, 2014). If the residue interacted with a sulphide-rich melt, the disturbance in the PGE system can be characterised by elevated Pt/Ir and Pd/Ir ratios (Pearson *et al.*, 2002; Rudnick and Walker, 2009; Lorand *et al.*, 2010; Fig. 2.10). Samples affected by melt metasomatism should also be enriched in Re and hence record a disturbance in their time-integrated Os isotopic composition. Even though peridotites from the Sask Craton have experienced high T metasomatism, I-PGEs have remained largely undisturbed with $(Os/Ir)_N$ close to chondritic. High (super-chondritic) Pd/Ir ratios occur in FALC peridotites with both radiogenic (super-chondritic; $^{187}Os/^{188}Os > 0.1283$ (Walker *et al.*, 2002) and unradiogenic Os (sub-chondritic $^{187}Os/^{188}Os$) isotopic compositions (Fig. 2.10). Peridotites with Os isotope compositions that give T_{RD} ages between 2.5 and 1.7 Ga have Pd/Ir ranging from chondritic to generally sub-chondritic, consistent with melt depletion. The peridotite with the most P-PGE depleted olivine, with a PGE pattern identical to the most depleted of cratonic peridotites, has a T_{RD} model age of ~ 2 Ga - the dominant age mode of FALC peridotites. Whereas this PGE

pattern indicates a lack of disturbance of the HSE systematics, the low Mg# of the olivine in this sample (~88) indicates significant metasomatic re-enrichment by an agent with low Re, Os and Pd/Ir. In the case of the FALC peridotite xenoliths, PGEs are likely a more robust proxy for primary melt depletion than major elements.

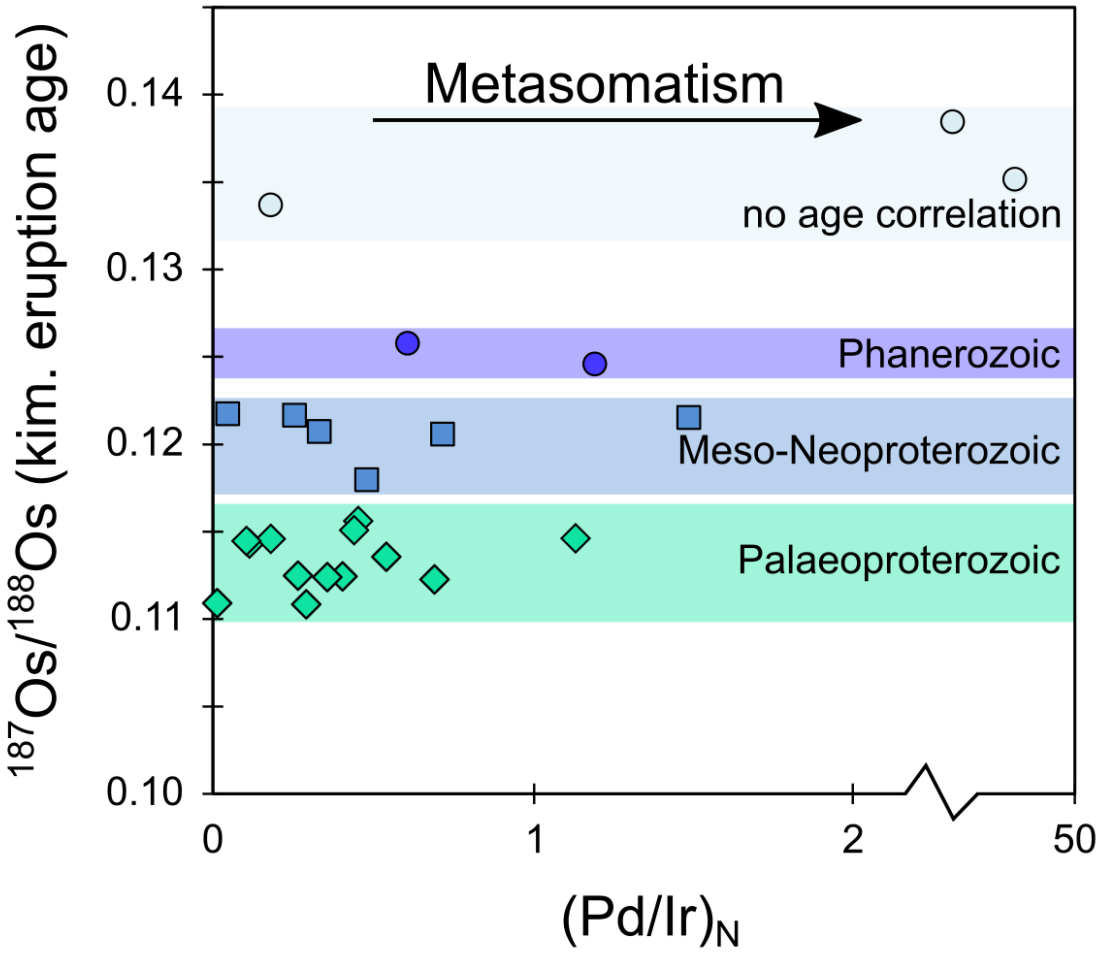

Fig. 2.10 Pd-Ir_N ratio vs. Os isotopic composition. Pd and Ir was normalised to primitive upper mantle (Becker et al. 2006). $^{187}Os/^{188}Os$ was calculated to represent the Os isotope composition at the time of kimberlite eruption. Green diamonds indicate samples with T_{RD} model ages ranging from 2.5 – 1.7 Ga, samples with ages between 1.5 and 0.9 Ga are shown as light blue squares, Phanerozoic samples are highlighted as dark blue circles and light blue circles represent radiogenic Os. Samples with Pd/Ir > 1.0 have been affected by secondary processes

In contrast, the peridotites with $^{187}Os/^{188}Os > 0.12$, equivalent to Mesoproterozoic or younger model ages, have the largest range in Pd/Ir_N ratios with values as high as 46.1, clearly indicating metasomatic enrichment, which has likely modified both their Os isotopic ratios and their P-PGE/I-PGE ratios. The significant Pt and Pd enrichment observed in the majority of these samples could be related to metasomatism by sulphide-bearing melts, perhaps associated with kimberlitic magmatism. We cannot call upon melts of basaltic character to cause this sulphide metasomatism in deeply (>150 km, Fig. 2.6) equilibrated garnet peridotites because silicate melts that exist at such depths grade from kimberlitic to komatiitic with increasing degree of partial melting (Dalton and Presnall, 1998).

2.6.2 Influence of the extent of melt depletion on the accuracy of model ages - The age of depletion of Sask Craton peridotites

T_{RD} model ages provide a minimum estimate for the time of Re depletion of the lithospheric mantle (Shirey and Walker, 1998). During mantle melting, Re is extracted from the residue as it partitions into the melt, whereas the compatible Os is retained in the mantle (Walker *et al.*, 1989; Mungall and Brenan, 2014). For high degrees of melting, monosulphide solid solution (mss) will be completely exhausted in the residue and as a result, all Re is extracted (> 30% melt removed; Aulbach *et al.*, 2016; Pearson *et al.*, 2004). Thus, the most accurate T_{RD} model ages are obtained for peridotites depleted beyond mss exhaustion. Traditionally, bulk rock Al_2O_3 and CaO are used as a proxy for the degree of melt depletion (Pearson *et al.*, 2014). However, xenolith bulk rock chemistry could not be obtained for FALC xenoliths as they have experienced significant alteration and kimberlite infiltration. Instead, the Mg# of olivine can be correlated with per cent melt extracted (F) from peridotite (Pearson and Wittig, 2008) and this proxy is used here to examine whether FALC peridotites should have experienced quantitative Re removal during melting (Fig. 2.11). The degree of melt depletion experienced by FALC peridotites is in the range of 10 to 42% (Mg# of 90.2 to 92.7). Samples with Mg# below 90 were not considered in estimates of the melt fraction F, due to their evidently metasomatic nature. However, even a number of samples with Mg# greater than 90 are interpreted to have experienced some degree of metasomatic enrichment, due to their mixed garnet chemistry (G1, G9, G11), and hence the calculated degrees of melt depletion likely reflect minimum estimates.

To quantify the effect of partial melting on the accuracy of Re depletion ages, apparent T_{RD} ages were calculated for 5, 10, 15 and 20% of melt extracted from a residue at a given age of depletion (Fig. 2.11). It is important to note that for this model melting was assumed to occur at pressures of 5 GPa and oxygen fugacities of ΔFMQ = 0 (Aulbach *et al*. 2016). Extracting a melt-fraction of 20% can be sufficient to deplete all Re from the residue at high pressures, which is in agreement with findings from Aulbach *et al.* (2016). Samples from FALC have on average experienced at least 20% melt depletion using olivine with Mg#s >90, enough to completely remove Re from the residue, and hence, in the absence of re-enrichment of Re, their T_{RD} ages should closely approximate the age of melt depletion. Further, the peridotite with the most P-PGE depleted olivine, with a PGE pattern identical to the most depleted cratonic peridotites (Pearson *et al.*, 2004), has a T_{RD} model age of ~ 2 Ga, in agreement with the dominant age mode of FALC peridotites. This indicates that undisturbed Re depletion ages constitute the main mode of SCLM formation.

The T_{RD} model ages from FALC show a wide spread, ranging from 2.5 – 0.4 Ga. Yet two dominant age groups can be identified. The majority of ages are Palaeoproterozoic with a broad mode at 2.4 – 1.8 Ga, the former overlapping with the dominant ages determined for the Sask Craton crustal rocks, and the latter the THO age (Fig. 2.8). A second, less distinct age cluster is observed at about 1 Ga (Meso – Neoproterozoic transition), which coincides with the Midcontinent Rift at 1.1 Ga (Van Schmus and Hinze, 1985). Only two samples record Phanerozoic ages (17651-2 and 17698-2). If the T_{RD} ages approximate the age of melting in these depleted peridotites then the data from our sample suite provide no evidence for unmodified Archean lithosphere below the Sask Craton.

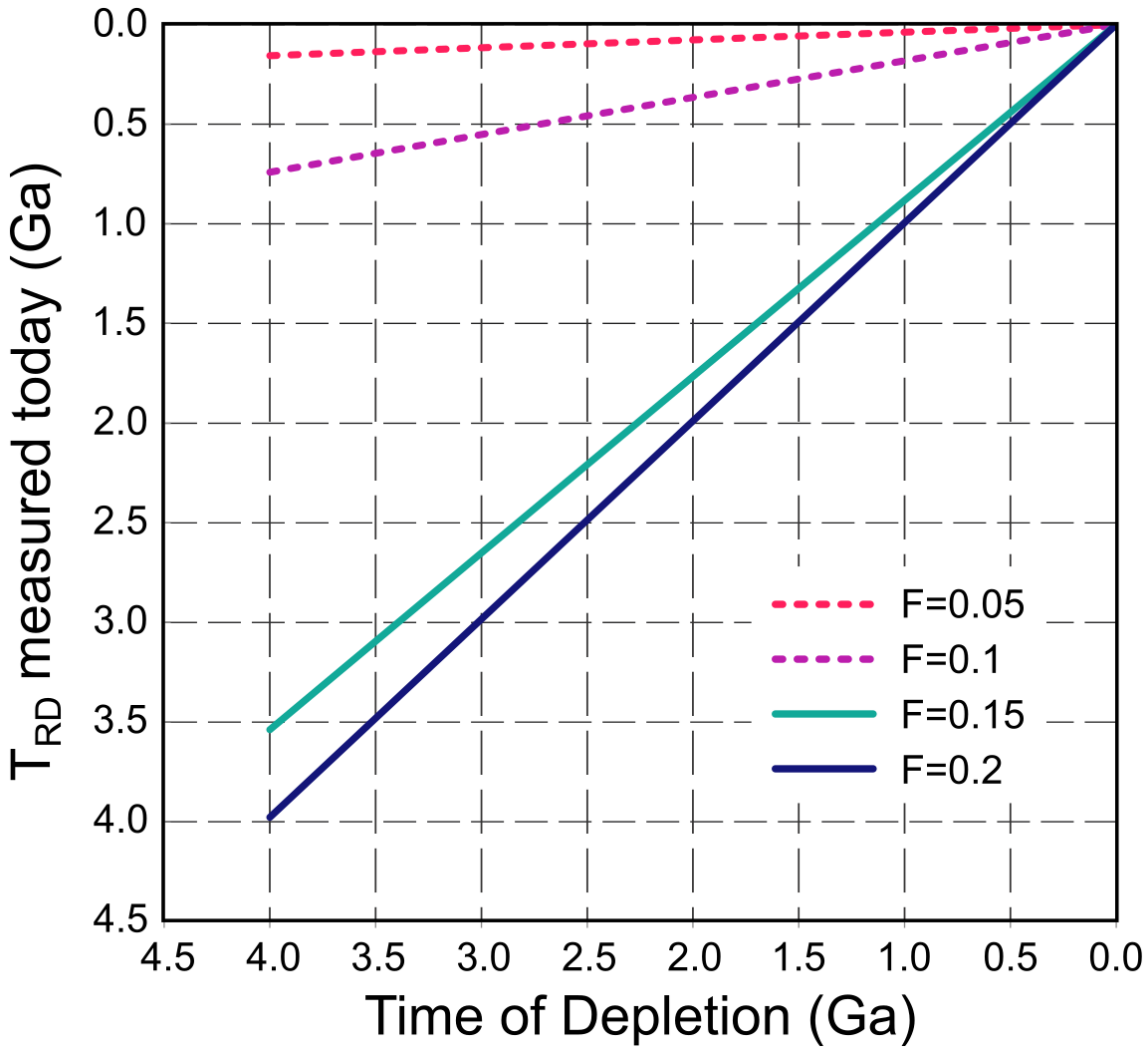

Fig. 2.11 The influence of the degree of mantle melting (F) on the accuracy of measured T_{RD} depletion ages. For 5 – 10% (F=0.05 – 0.1) melting T_{RD} ages are a poor estimate for the time of melt depletion, whereas for degrees of partial melting of >0.15 calculated model ages agree well with the time of depletion. Time of depletion was calculated using Re and Os concentrations from melt models of Aulbach *et al.* (2016), using a ^{187}Re decay constant of 1.64×10^{-11} yr^{-1} (Lindner *et al.*, 1989). Estimates of Re and Os concentrations in the residue for varying degrees of melt depletion at 5 GPa and ΔFMQ=0 are from Aulbach *et al.* (2016).

2.6.3 Dichotomy of mantle and crustal ages – A tectonic model

For cratons, Archean crust is underpinned by Archean mantle lithosphere (e.g., Pearson, 1999). Furthermore, according to "Clifford's Rule" (Clifford, 1966; Boyd and Gurney, 1986; Janse, 1994) diamond occurrences are restricted to cratonic nuclei of Archean age. Archean crust has been dated from a few locations on the Sask Craton, establishing it as a small craton (Collerson *et al.*, 1990; Heaman *et al.*, 1992). Yet, the exact origin of the micro-continent forming the Sask Craton is still unknown (Corrigan *et al.*, 2009); proposals include an origin as part of the Wyoming Craton (Bickford *et al.*, 2005), or as an exotic microcontinent (Rayner *et al.*, 2005).

A key question is whether the underlying lithospheric mantle is also Archean. The T_{RD} ages presented here are the first estimates for the timing of SCLM formation beneath the Sask Craton. Typically, Archean cratonic roots, even where significantly disturbed, such as at the Central Rae craton (Liu *et al.*, 2016), have Archean melt depletion ages reflected in their kimberlite-derived peridotite xenolith suites. In contrast, for the Sask craton, no Archean Re-depletion ages are recorded by this suite of peridotites. The FALC olivines with the most P-PGE depleted patterns yield Palaeoproterozoic T_{RD} ages of circa 2.5 – 1.7 Ga, which are interpreted to reflect the formation and stabilisation of the SCLM beneath the Sask Craton. It is important to note that using Re depletion ages, we lack the resolution to determine which specific event might be responsible, partly because of the heterogeneity in convecting mantle sources (Pearson *et al.*, 2007; Dijkstra *et al.*, 2016), and partly due to potential mixing/metasomatic disturbance. Below we summarise the complex tectonothermal history in the THO area that could have produced the main mode in T_{RD} ages.

Considering the uncertainties inherent in Os model ages, for the FALC peridotites, T_{RD} ages between 2.0 to 2.3 Ga overlap with the timing of significant crustal addition at ~2.5 to 2.3 Ga. Major magmatic activity has been reported at 2.45 Ga (Ashton *et al.*, 1999) relating to the emplacement of the Mirond Lake Igneous Suite, a long-lived intra-plate magmatic event, which is in good temporal agreement with the oldest peridotite ages obtained (Table A4). Alternatively, the oldest Palaeoproterozoic ages could be linked to magmatic activity during the Arrowsmith orogeny (~2.5 – 2.3 Ga), an orogenic event of Andean style and scale, which has been traced along the western edge of the Rae Craton (Berman *et al.*, 2013). Subsequently, during the opening of the Manikewan Ocean (~2.2 – 2.0 Ga; Ansdell, 2005; Stauffer, 1984), potentially

extant deep SCLM beneath the Sask Craton could have been weakened by metasomatism (Foley, 2008). This weakened root could then have been replaced by mantle residues formed by melting that was not as extensive as that in the Archean, producing peridotites with slightly lower Mg numbers that are characteristic of Palaeoproterozoic melt residua (Boyd *et al.*, 2004).

Initiation of regional rifting occurred at ~ 2.2 Ga, between the Hearne and Superior Cratons, which coincides with the main mode of T_{RD} ages. Additional depleted material could have been added to the Sask Craton root during the collision of the Superior Craton and the Churchill Province (THO, 1.9 – 1.8 Ga, Fig. 2.8), via subduction processes (Ansdell, 2005). Thus, the final composition and form of the cratonic root could be an integration of several processes/events, stabilised to its current thickness by THO compression. Dynamical models have shown that compression of depleted residues is a very effective mechanism of stabilising a deep, buoyant craton root (Wang *et al.*, in press). Scattered younger ages (T_{RD} < 1.5 Ga) are interpreted as a result of metasomatic disturbance related to post-Palaeoproterozoic magmatism and kimberlite infiltration (mixing ages of about 0.5 Ga).

We cannot exclude that the Sask Craton had an Archean lithospheric root that was heavily modified during rifting and closure of the Manikewan Ocean and that parts of the lithospheric mantle not sampled here may have retained Archean ages, but we have no evidence for the existence of Archean aged peridotites either. The possibility of either replacement of Archean with Palaeoproterozoic mantle, or substantial addition to, or overprinting of, existing Archean mantle is in line with examples from other cratons. The Premier (Cullinan) kimberlite samples peridotitic lithosphere from beneath the central Kaapvaal Craton that shows clear evidence of major replacement/disruption due to the formation of the ~2.0 Ga Bushveld complex (Carlson *et al.*, 1999), along with some preservation of the original Archean mantle root. Similarly, a newly enlarged Re-Os database for Siberian peridotites shows major Palaeoproterozoic lithosphere re-working and addition, as well as further re-working during the Phanerozoic (Ionov *et al.*, 2015; Pernet-Fisher *et al.*, 2015). It is, however, important to note that Archean T_{RD} model ages, reflecting remnants of the initial SCLM, are reported for each of the above-mentioned locations but are notably absent beneath the Sask Craton. Therefore, it is likely that our T_{RD} ages record the stabilisation of the lithospheric mantle in the Paleoproterozoic rather than an over-printing or replacement event. The assessment that model ages > 1.7 Ga reflect the initial stabilisation of the Sask Craton is reinforced by the PGE data. PUM normalised PGE patterns (Fig. 2.9) commonly

have a trend of increasing depletion for the P-PGEs, which has previously been interpreted as a depletion signature in peridotite protoliths (Pearson *et al.*, 2004). The Sask peridotites yielding younger Re-Os ages (T_{RD} <1.1 Ga) commonly exhibit PGE patterns with enriched Pt and Pd concentrations, suggesting secondary re-enrichment (Fig. 2.9). These signatures of reworking could be related to a failed intracontinental rifting event in the Superior Craton at 1.1 Ga (Midcontinental Rift; Van Schmus and Hinze, 1985), as well as the several episodes of metasomatic re-enrichment previously discussed.

This model has important implications for the timing of diamond formation, suggesting that all diamonds must have formed in the Proterozoic, after stabilisation of new lithospheric mantle beneath the Sask Craton. As such, the FALC kimberlites on the Sask Craton present a diamond deposit that does not adhere to "Clifford's rule".

2.7 Conclusions

1. This study is the first detailed characterisation of the lithospheric mantle beneath the Sask Craton, based on the study of peridotite xenoliths from the Fort à la Corne kimberlite field. Petrological observations and major element concentrations of mineral separates revealed that the peridotitic xenoliths are lherzolitic, with a composition similar to average cratonic lherzolite.
2. The depletion and stabilisation of a lithospheric mantle root occurred in the Palaeoproterozoic (dominant Re-Os age: 2.5 to 1.7 Ga) relating to large scale tectonothermal events such as the opening and subsequent closure of the Manikewan Ocean. There is no evidence for T_{RD} ages coeval with the oldest crustal ages.
3. FALC xenoliths show evidence for melt metasomatism that affected the olivine and garnet chemistry. However, the PGEs and hence the Os isotopic composition remained largely unaffected.
4. In the absence of Archean lithospheric mantle beneath the Sask Craton, the diamondiferous kimberlites at Fort à la Corne (FALC) represent unconventional diamond deposits. This has important implications for diamond exploration, as formation of lithospheric diamonds evidently is not restricted to Archean mantle keels.

Chapter 3

3 Major metasomatism in eclogite xenoliths from the Sask Craton, Canada

3.1 Introduction

Eclogites are only a minor component of the lithospheric mantle (Schulze, 1989; Bina and Helffrich, 2014). Yet, mantle eclogites are a key target in diamond exploration and provide valuable insights into the assembly and evolution of the subcratonic lithospheric mantle. Two competing petrogenetic models have been proposed for the formation of mantle eclogites and whether the individual suites represent subducted metamorphosed oceanic crust (Helmstaedt and Doig, 1975; Jacob *et al.*, 1994) or cumulates of high-pressure mantle melts (O'Hara and Yoder, 1967; McDade and Harte, 2000) is still debated. Oxygen isotope compositions outside of the accepted mantle range (+5.1 to +5.9 ‰) are traditionally interpreted as evidence for the low-pressure origin of the protolith of mantle eclogites (Garlick *et al.*, 1971; Jagoutz *et al.*, 1984; MacGregor and Manton, 1986; Jacob *et al.*, 1994). Studies on ophiolite complexes have linked low-temperature seawater alteration to positive shifts in the oxygen isotope composition of shallow oceanic crust and high-temperature seawater alteration (up to greenschist facies conditions) to negative deviations (Muehlenbachs and Clayton, 1976; Gregory and Taylor, 1981; Benoit *et al.*, 1996; Shanks, 2001). As the effects of pressure and temperature on the fractionation of oxygen isotope ratios are not significant (Clayton *et al.*, 1975; Eiler, 2001), $\delta^{18}O$ values outside the mantle range are assumed to be inherited from crustal protoliths (Jacob *et al.*, 1994). While the mineral chemistry, in particular trace elements and radiogenic isotopes (e.g., Jacob, 2004), is often affected by metasomatism, oxygen isotope compositions are commonly resistant to late metasomatic overprinting due to oxygen representing roughly 50 % of the rock and their low diffusion rates in garnet (Fortier and Giletti, 1989). However, recent studies have questioned the nature of non-mantle like $\delta^{18}O$ values in eclogite xenoliths (Gréau *et al.*, 2011; Huang *et al.*, 2012), as they report a correlation of $\delta^{18}O$ value with trace element concentrations affected by metasomatism.

Here, we examine both barren and diamond-bearing eclogite microxenoliths from the Fort à la Corne Kimberlite Field on the Sask Craton, Saskatchewan, Canada for their major and trace element mineral compositions, as well as their oxygen isotope compositions to determine the origin of the xenolith suite and to investigate the composition of potential metasomatic agents and their possible effects on oxygen isotope ratios.

3.1.1 Geological setting

The Fort à la Corne (FALC) kimberlite field on the Archean Sask Craton (Collerson *et al.*, 1990; Heaman *et al.*, 1992) is located in Western Canada (Fig. 3.1A) within the Paleoproterozoic (1.8 – 1.9 Ga) Trans Hudson Orogen (THO; Rayner et al. 2005). During the THO, the Superior and the Churchill provinces were amalgamated, creating the North American Craton (Hoffman, 1988). Diamonds have been discovered in 75% of the FALC kimberlites (Harvey *et al.*, 2009), which sampled principally Trans Hudson age (~2.0 – 1.9 Ga) lithospheric mantle beneath the Archean Sask Craton (see Chapter 2).

The more than 70 Cretaceous FALC kimberlites (~106 to ~95 Ma; Heaman et al. 2004; Kjarsgaard et al. 2017) occur interstratified with an approximately 200 m thick sedimentary succession (Pittari *et al.*, 2008). Eclogitic xenoliths analysed in this study were obtained from the Star and Orion South kimberlites, which are located at the Southern end of the FALC kimberlite trend (Fig. 3.1B).

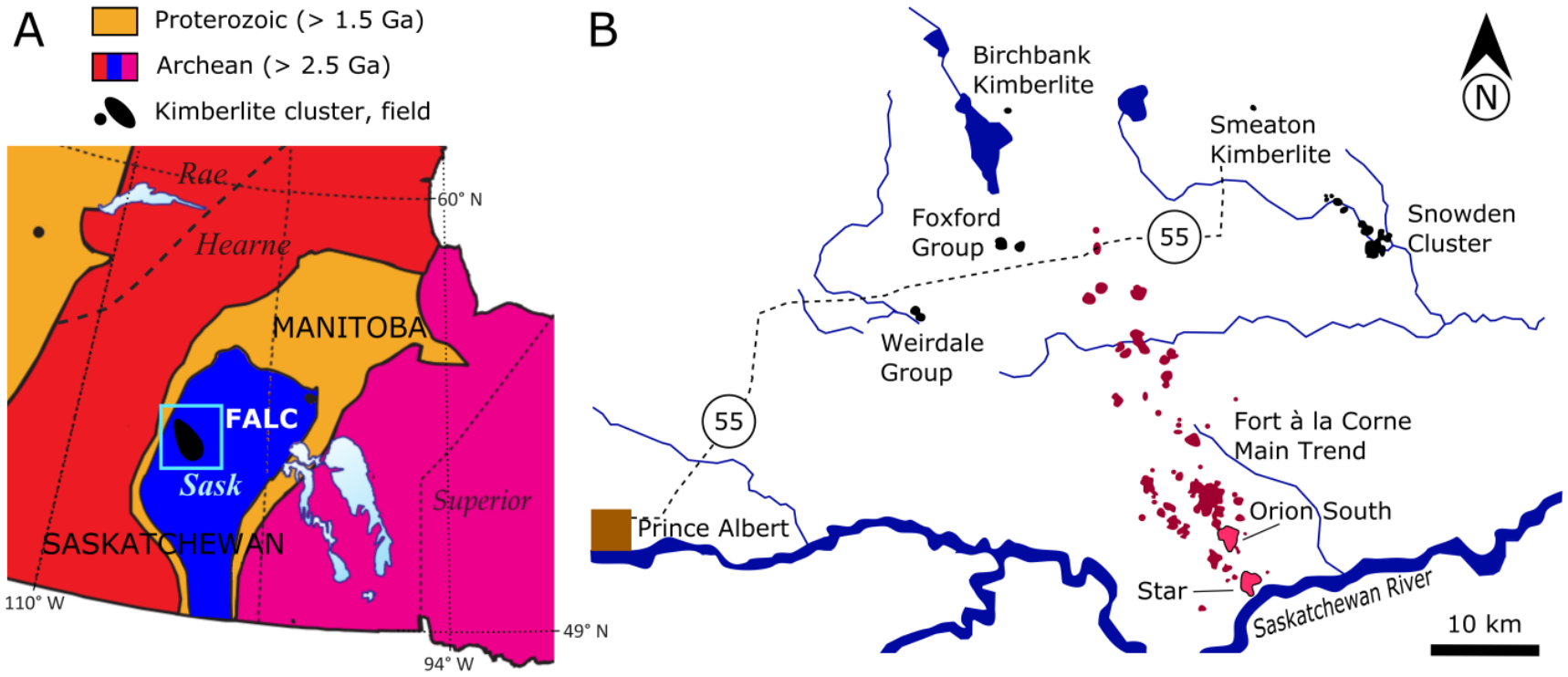

Fig. 3.1 A. Sketch map showing cratons, Proterozoic belts and kimberlites in Saskatchewan and adjacent areas (adapted from Kjarsgaard 2007). Cratons are highlighted in red, pink and blue (Sask Craton), kimberlite fields are shaded in black. B. Regional map of the Fort à la Cone Kimberlite Field shown in red and other Saskatchewan kimberlite pipes in black (Harvey *et al.*, 2009). The Star and Orion South pipes are highlighted in pink.

3.1.2 Samples and petrography

The xenoliths (diamond-free n=28; diamondiferous n=22) studied are all eclogites and were principally recovered from flow concentrate from exploration stage underground mining operations within the Star and Orion South kimberlites. Only two xenoliths (17664 and 17672) were sampled from kimberlite core.

Sample sizes for the diamond-free xenoliths vary between 1 and 5 cm, whereas diamondiferous eclogite sizes are generally limited to less than 1 cm. Diamond-free eclogites typically contain equant garnet and clinopyroxene crystals (1-5 mm in diameter). In comparison, grain sizes in diamondiferous xenoliths are smaller (0.1 – 2 mm).

All diamond-free eclogites consist of garnet and clinopyroxene (Fig. 3.2); accessory fine (~0.1 mm), anhedral rutile and/or apatite are present in less than 10 % of the samples. A large proportion (52 %) of diamondiferous micro-xenoliths are diamond-garnet intergrowth and contain no clinopyroxene or accessory phases. In the barren xenoliths and the clinopyroxene-bearing diamondiferous xenoliths, garnet and clinopyroxene typically have roughly equal proportions, as is common for eclogites (Jacob, 2004). It is important to note that due to the small xenolith size, in particular for diamondiferous xenoliths, meaningful estimates of mineral modes cannot be accurately determined. Even though clinopyroxene can be identified in all diamond-free eclogites, it is typically replaced by alteration minerals, whereas garnet has fresh cores with only minor alterations rims. Texturally, diamond-free eclogites can be classified as Group I, with subhedral garnet grains floating in a clinopyroxene matrix, as well as Group II, consisting of a network of interlocking garnet and clinopyroxene grains with 120° angles following the terminology of MacGregor and Carter (1970). Transitions between these two groups commonly occur in individual samples. The small sample size and common absence of clinopyroxene precluded a meaningful textural classification of the diamondiferous xenoliths.

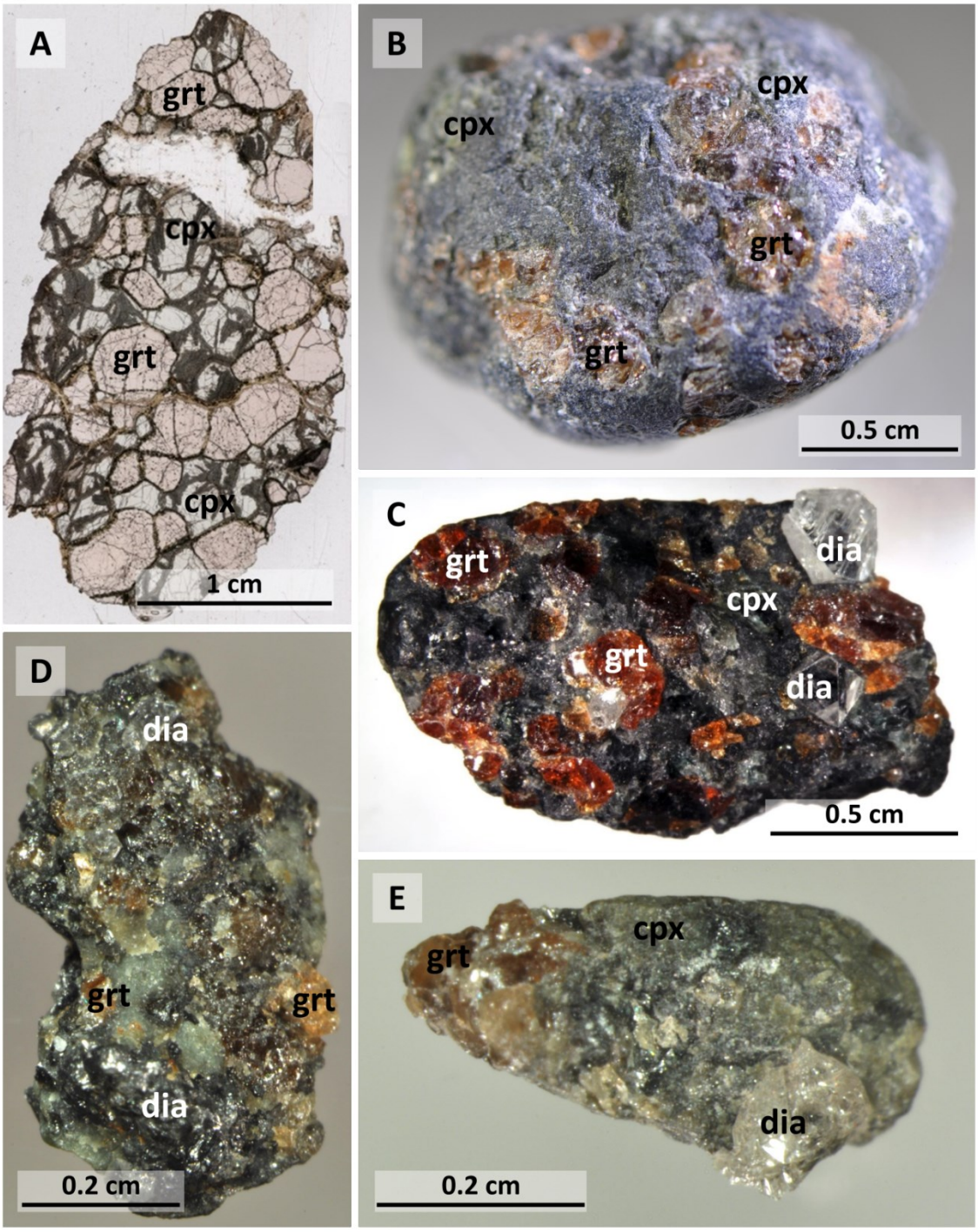

Fig. 3.2 Selected images representative of typical eclogitic xenoliths from Fort à la Corne. Minerals are indicated as garnet – grt, clinopyroxene – cpx, and diamond – dia. A and B are photographs of a barren eclogite (A: thin section 52006-5, B: 52006-17); C, D, and E show pictures of diamondiferous eclogite nodules (C: SGF-009, D: SGF-025 50224-2, E: SGF-003)

3.1.3 Analytical techniques

Major element compositions of garnet and clinopyroxene were obtained using a JEOL8900R Electron Probe Micro-Analyser (EPMA), with 20 kV accelerating voltage, a probe current of 20 nA, and peak counting times between 30 and 60 s. Limits of detection range from 0.01-0.02 wt%. The CITZAF procedure of Armstrong (1995) was used for data reduction. Kα lines were analysed. Standards are garnet for Si, Al, Mg, and Fe, diopside for Si, Ca, and Mg, sanidine for K, albite for Si, Al, and Na, labradorite for Al, fayalite for Fe, spessartine for Fe and Mn, apatite for P, nickel wire for Ni, chromium oxide for Cr, and rutile for Ti (detailed information on reference materials in Table B1).

In-situ laser-ablation inductively coupled plasma mass spectrometry (LA-ICPMS) was carried out on a RESOlution 193 nm ArF Excimer Laser Ablation System coupled with a Thermo Element 2 XR ICP-MS to obtain minor and trace element concentrations in garnet and clinopyroxene. NIST612 reference glass was used as a primary standard, reference glasses NIST614 and BIR-1G, as well as mineral standards PHN-B (garnet) and GP-13 (clinopyroxene) were employed as secondary standards and could be reproduced within 10 % of the internal lab average. Calcium and Si (for Ni) were used as internal standard for quantification of elemental abundances. Multiple analyses for mineral phases were averaged in both barren and diamondiferous xenoliths (Table B2).

The oxygen isotope ratio ($^{18}O/^{16}O$) of garnets was analysed using a Cameca IMS 1280 multi-collector ion microprobe (MC-SIMS). The primary $^{133}Cs^{+}$ beam was operated with an impact energy of 20 keV and a beam current between 2.0 – 2.5 nA. Propagated uncertainties for $\delta^{18}O$ have an average of ±0.3 ‰ (2σ), and standard deviations for reference materials range between 0.07 and 0.08 ‰. A detailed description of the analytical method was published by Ickert and Stern (2013). Oxygen isotope ratios are expressed in delta notation relative to Vienna Standard Mean Ocean Water (VSMOW; Baertschi 1976).

3.2 Results

Major and trace element concentrations for garnet and clinopyroxene, as well as garnet oxygen isotope data are reported in Tables B2, B3, and B4 in the Appendix.

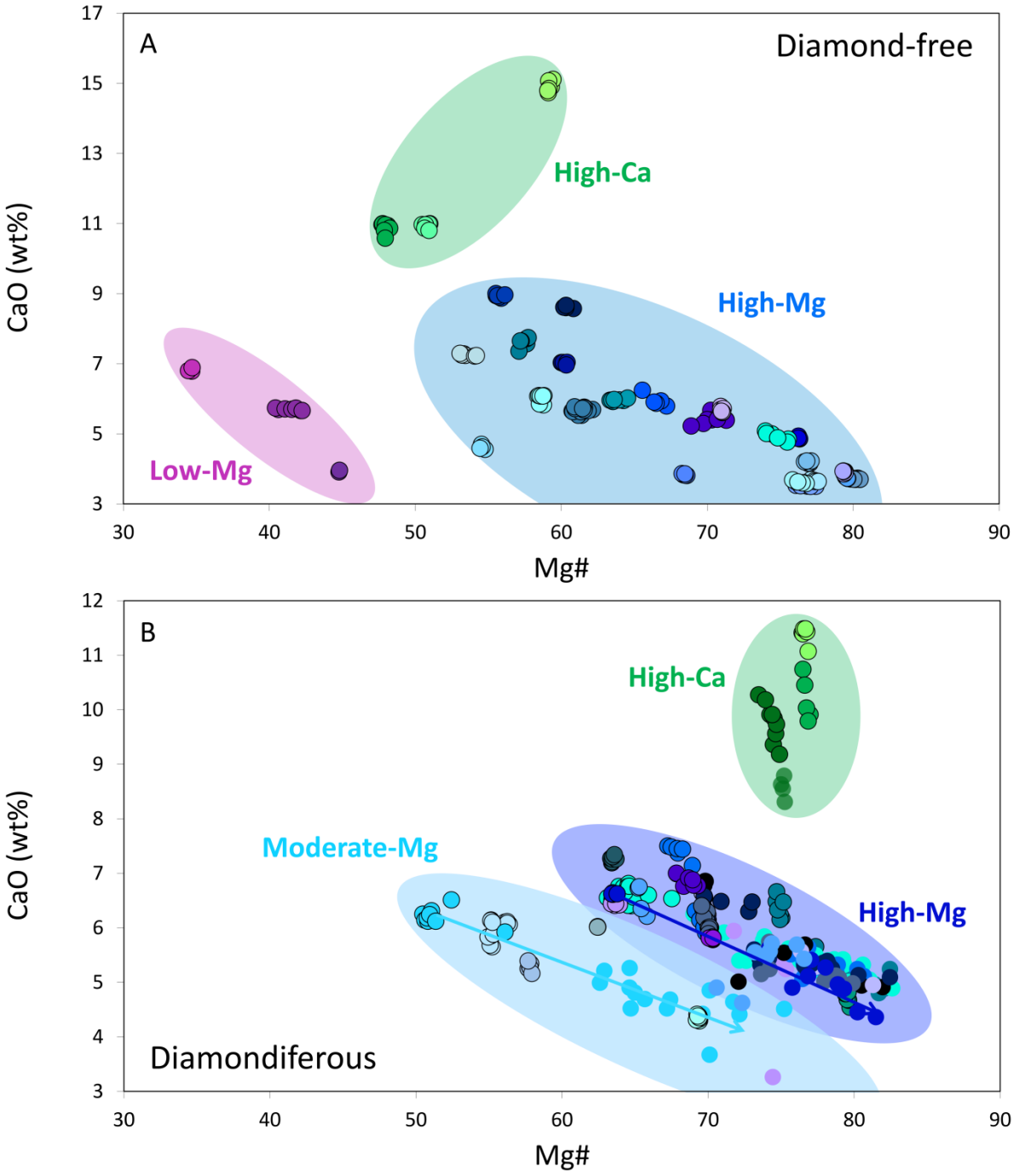

Fig. 3.3 Mg# vs. CaO in garnet for diamond-free and diamondiferous eclogite samples. Molar Mg# = 100*Mg/(Mg+Fe). Each sample is plotted in a separate colour and every data point represents an analytical spot. For the diamondiferous samples, primary compositions are outlined in black, whereas secondary ones are shaded in a lighter colour. The samples are grouped into (1) medium- to high-Mg (light blue and dark blue), (2) low-Mg (pink), and (3) high-Ca (green). Arrows indicate the general trend for moderate (light blue) and high-Mg (dark blue) eclogites**Diamond-free eclogites**

The inter-sample major element mineral chemistry of diamond-free eclogites spans a wide compositional range but is typically homogenous within individual samples (Fig. 3.3A). In general, garnets have low to moderate CaO contents (3.5 – 9.0 wt%), low Na_2O concentrations (< 0.07 wt%), and fall into a low-Mg (Mg# 33 – 45) and a moderate- to high-Mg (53 – 82) group. In addition, three samples (52006-7, -14 and -24) are classified as high-Ca (CaO > 9.0 wt%; distinctly higher than the other samples), with CaO concentrations ranging up to 15.1 wt%. Based on their clinopyroxene composition, the FALC xenoliths dominantly are classified as eclogitic ($0.2 \leq Na/(Na+Ca) < 0.8$; Coleman et al. 1965; Clark and Papike 1968). Only sample 52006-13 contains jadeite-poor clinopyroxene of diopsidic composition and hence could be classified as pyroxenite; however, we prefer a classification as eclogite based on modal mineralogy (sample is composed of garnet and clinopyroxene in approximately equal proportions). Backscattered electron images reveal spongy-textured, jadeite-poor clinopyroxene that occurs in thin veins and rims surrounding relict omphacite. Hence, clinopyroxene chemistry is often heterogeneous within single grains. Primary omphacitic clinopyroxene covers a wide range of compositions, with MgO ranging from 7.0 – 15.5 wt%, CaO from 11.2 – 19.4 wt%, Na_2O from 1.1 – 7.0 wt%, and Al_2O_3 from 3.5 – 15.7 wt%.

REE_N (C1-chondrite normalised, McDonough and Sun 1995; Fig. 3.4A) patterns for garnets are generally characterised as "normal" with depleted LREE and flat HREE (~10 x chondritic). High-Mg group garnets either display no distinct Eu anomaly, or for a large number of cases, exhibit positive Eu-anomalies (Eu* 1.1 – 1.8; $Eu^*=Eu_N/[0.5Gd_N+0.5Sm_N]$; positive anomalies Eu*>1 and negative anomalies Eu* <1). High-Ca garnets are on average more enriched in MREE (> 10 x chondritic) and have positive Eu* of 1.1 – 1.5. The low-Mg samples have overall enriched REE_N (MREE up to 100 x chondritic), elevated La values, and negative Eu anomalies (Eu* 0.5 – 0.9). Clinopyroxene REE_N patterns have flat LREE or peaks at Ce-Nd (high-Ca samples), followed by negative MREE-HREE slopes (Fig. 3.5; MREE can be up to 20 x chondritic and HREE range from chondritic to subchondritic). Positive Eu anomalies are common (Eu* > 1.1 in 50 % of samples). Garnet shows a broad polymodal distribution in $\delta^{18}O$ from +3.6 to +7.9 ‰, with a well-defined mode at 3.9 ‰, and a second broad mode (~+4.5 to +6.5 ‰) centred about the mantle range (Fig. 3.6A).

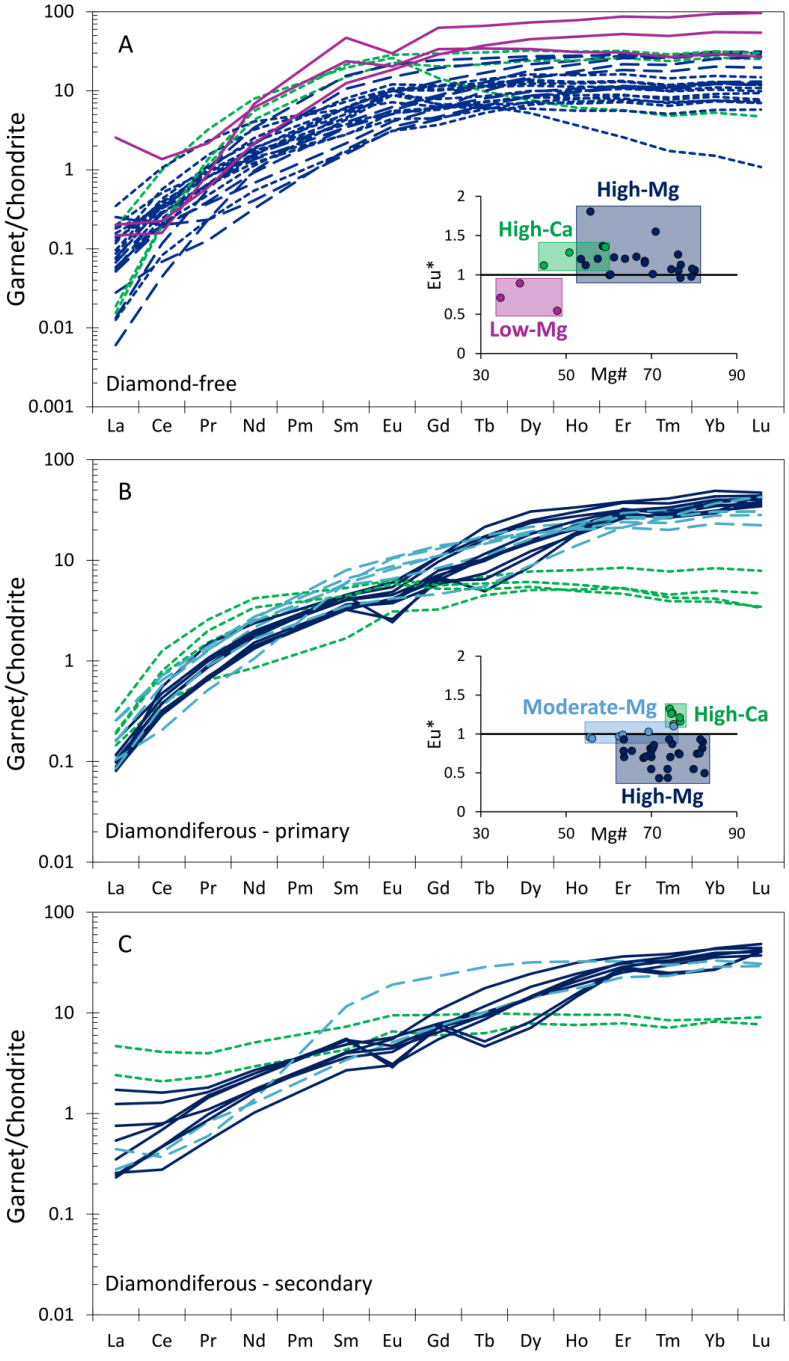

Fig. 3.4 Chondrite-normalised REE patterns for eclogitic garnets with insets of Eu anomaly (Eu*) vs. Mg#. A. Patterns for barren eclogites. B. Patterns for diamondiferous eclogites (primary). C. Patterns for diamondiferous eclogites (secondary). Analyses for the barren samples were averaged by samples, whereas in diamondiferous eclogites the samples are averaged as primary and metasomatised (see Table B2 for values). Garnets with positive Eu-anomalies are shown as dotted lines, patterns without a significant Eu anomaly as dashed lines, and analysis with negative Eu* are solid lines. Line colours, as well as colours in the inset correspond to major element compositions, with high-Ca samples shown in green, low-Mg in pink and medium- to high-Mg in light and dark blue, respectively. Black line in the inset indicates no Eu anomaly (Eu* = 1)

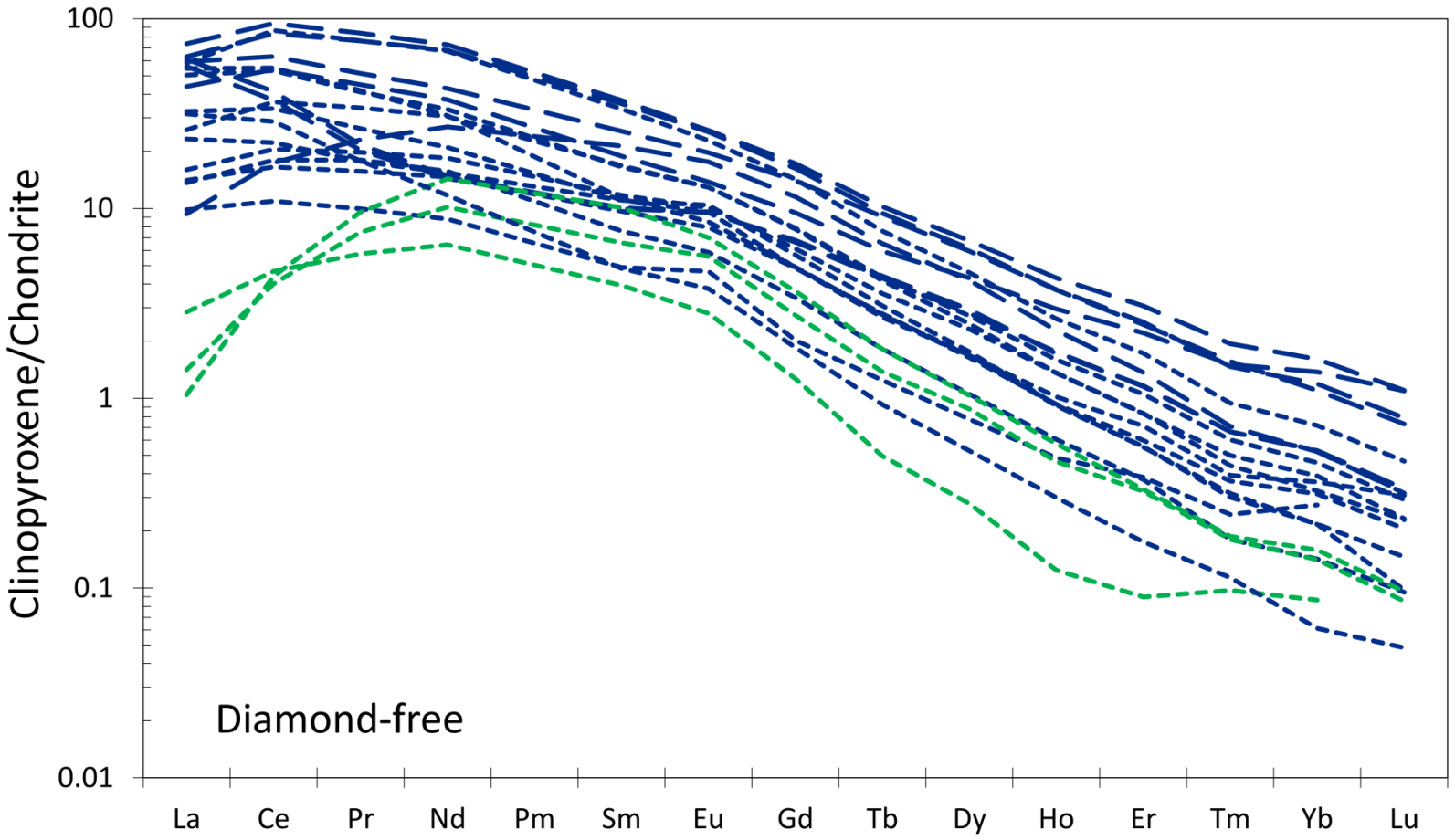

Fig. 3.5 Chondrite-normalised REE patterns for eclogitic omphacites. All samples are homogeneous, so patterns represent the sample average. Patterns are grouped according to the garnet chemistry they are associated with; high-Ca samples shown in green and high-Mg in dark blue, dotted lines indicate positive Eu* and dashed lines are used for samples with no Eu anomaly

3.2.2 Diamondiferous eclogites

Garnets from diamondiferous eclogites have a smaller compositional range than their barren counterparts (Fig. 3.3B). They are typically moderate to high in Mg# (50 to 83), have low to high CaO contents (3.3 to 11.5 wt%), and low to high (for eclogitic garnet) Cr_2O_3 values (0.06 to 0.8 wt%). The majority of garnets exhibit complex irregular textures in back-scattered electron (BSE) images (Fig. 3.7A) corresponding to large variations in Mg# (up to 19 within individual grains) and minor variations in CaO (moderate Mg# and high Mg# trends). TiO_2 is positively correlated to MgO. Intra-sample variations in CaO (up to 3.1 wt%; Fig. 3.3B) occur in a subset of high-Ca garnets (CaO > 9 wt%) with little change in Mg#. Magnesium heterogeneity on the intra-sample scale (Mg# varies by up to 25) exceeds the heterogeneity seen within individual grains (up to 19 in Mg#), while intra-grain variation in CaO is minor (CaO < 0.7 wt%) compared to intra-sample variability. Clinopyroxenes, where present, are internally homogeneous, but have broad inter-sample compositional ranges similar to the barren eclogites, with MgO contents of 9.3 – 16.4 wt%, CaO of 11.1 – 17.9 wt%, Na_2O of 2.6 – 6.1 wt%, and Al_2O_3 of 4.9 – 11.2 wt% (Table B3). Omphacites associated with high-Ca garnets are also higher in CaO content.

The primary garnets have normal REE_N patterns, with subchondritic to suprachondritic LREE and HREE varying from ~ 3 x to ~50 x chondritic (Fig. 3.4B). The majority of garnets that exhibit significant internal variations in Mg# show negative Eu-anomalies, with Eu* as low as 0.42 (Fig. 3B) and slightly positive $HREE_N$ slopes (Dy_N/Yb_N <1). The moderate-Mg samples lack Eu anomalies and have negative $HREE_N$ slopes (Dy_N/Yb_N > 1). High-Ca garnets exhibit REE_N pattern with positive Eu anomalies (Eu* of 1.12 – 1.43) and Dy_N/Yb_N >1. Secondary LREE enrichment is present in a few of the garnets in samples with strong major element variations, in comparison to the primary garnet compositions (Fig. 3.4C). No reliable trace element data could be obtained from fresh clinopyroxene grains, due to their small size.

In comparison to the barren eclogites, oxygen isotope compositions for diamondiferous samples are shifted towards higher $\delta^{18}O$ values (+4.6 to +7.6 ‰) with a dominant mode at +6.5 ‰ (Fig. 3.6A). In samples with significant major element variations, oxygen isotope compositions can vary up to 1 ‰ (Fig. 3.6B).

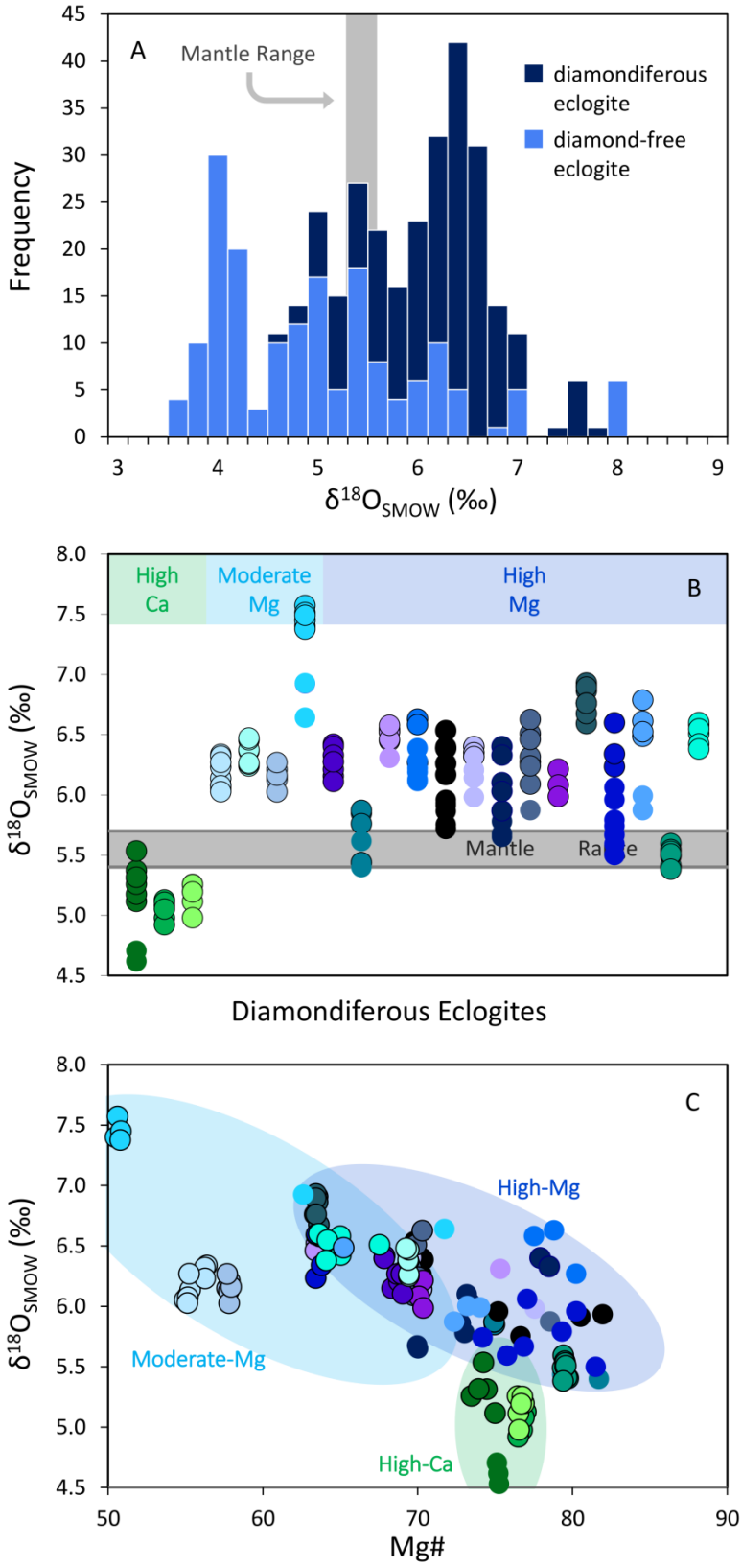

Fig. 3.6 Oxygen isotope variations in barren and diamondiferous FALC eclogites.

A. Stacked histogram of garnet $\delta^{18}O_{SMOW}$ (‰) for diamondiferous (dark blue) and diamond-free eclogites (light blue);

B. Variations in oxygen isotope compositions of garnets within diamondiferous eclogite samples, original garnet compositions are indicated with black circles. Garnet mantle range (+5.4 to +5.7‰; Ickert et al. 2013) is shown in grey for reference;

C. $\delta^{18}O_{SMOW}$ (‰) vs. Mg# in garnets from diamond-bearing eclogites, high-Ca samples are given in green, moderate- to high-Mg samples are shaded in light and dark blue respectively

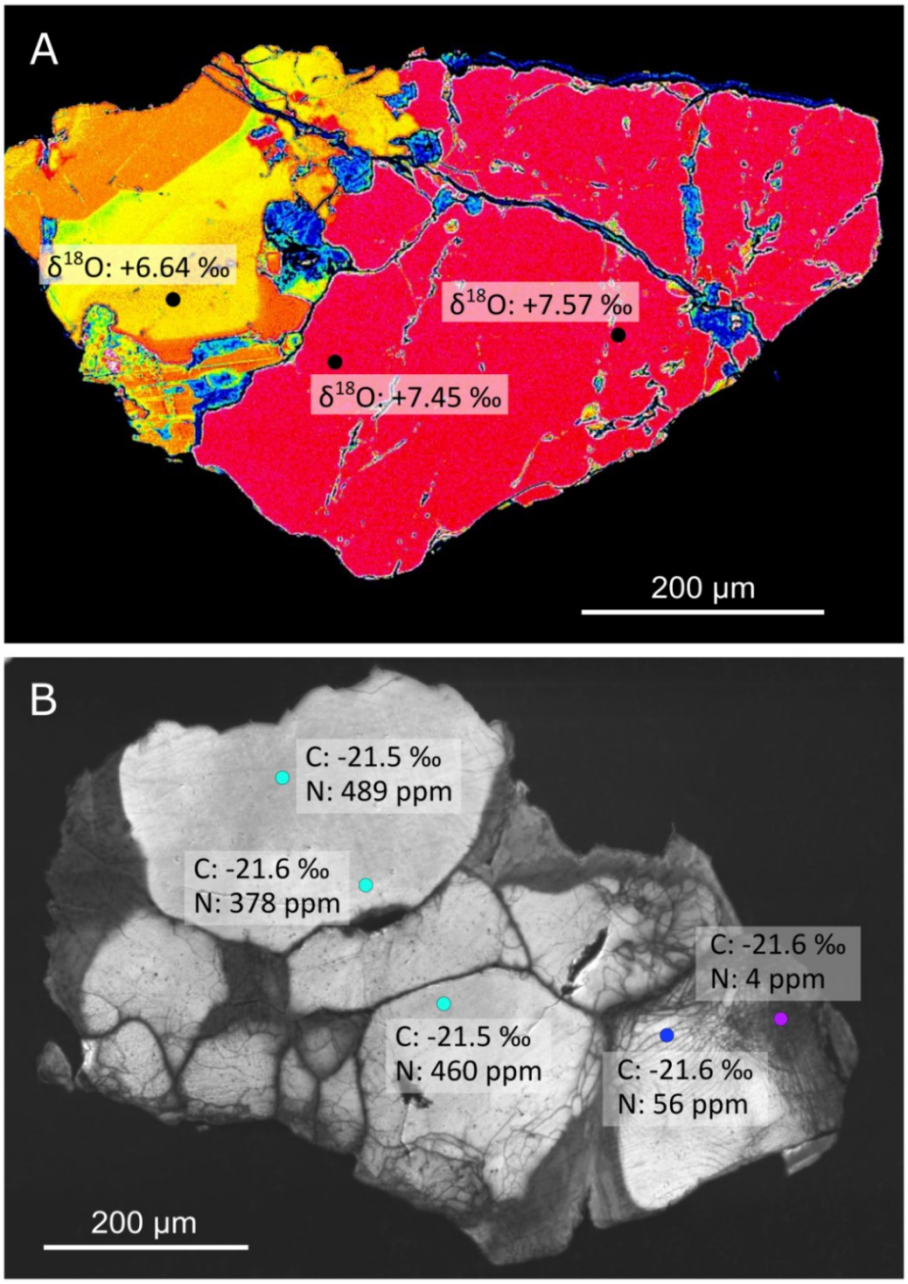

Fig. 3.7 False coloured backscattered electron (BSE) image of metasomatised garnet (A) and Cathodoluminescence (CL) image of a brecciated diamond (B). A. Garnet from diamondiferous eclogite (SGF-042 50495). Colour variations correspond to changes in major element chemistry (yellow: high Mg#), variability in $\delta^{18}O$ is indicated. B. CL image of a brecciated diamond, light areas are interpreted to be primary diamond, whereas dark bands are attributed to secondary diamond growth during or following brecciation. SIMS analytical spots are indicated by coloured circles with associated $\delta^{13}C$ (‰) value and N (at. ppm) concentration (light blue: primary diamond; dark blue mixture of primary and secondary diamond; pink: secondary diamond, dark bands

3.2.3 Geothermobarometry

Equilibration temperatures for eclogites containing garnet and fresh clinopyroxene (Table B5) were calculated using the Mg-Fe exchange thermometer of Krogh (1988). As no reliable barometer exists for eclogites (Nimis and Grütter, 2010), $T_{Krogh88}$ was projected onto the Sask Craton geotherm (Fig. 3.8; additional information on the FALC geotherm in Chapter 2). For diamondiferous eclogites, only garnets with presumed primary compositions were selected for temperature calculations. Secondary diopside (spongy rims) was excluded.

Diamond-free eclogites span a wide range in temperatures and pressures (740 – 1300 °C and 32 – 61 kbar), indicating the presence of eclogite through much of the lithospheric mantle. Temperatures in diamondiferous eclogites are restricted to higher values (1180 – 1390 °C), which implies they originated at the base of the lithospheric mantle (55-65 kbar).

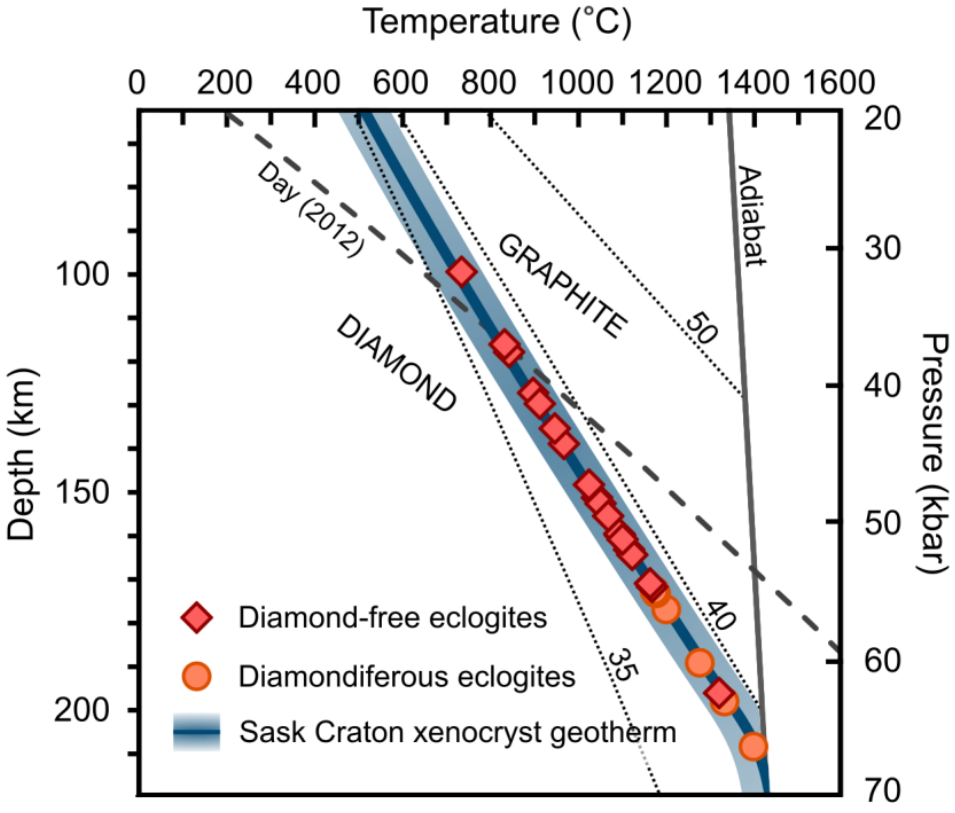

Fig. 3.8 Mg-Fe exchange temperatures (Krogh, 1988) for diamond-free (red) and diamondiferous eclogites (orange) projected onto the FITPLOT model geotherm for the Sask Craton (thick blue line). Reference geotherms for 35, 40 and 50 mW/m^2 surface heat flow (Hasterok and Chapman, 2011) are included as dotted lines and the stippled line indicates the diamond-graphite transition curve (Day, 2012)

3.3 Origin of FALC eclogites

3.3.1 Bulk rock reconstruction

Due to well-documented effects of kimberlite infiltration on the incompatible element geochemistry of eclogite xenoliths (e.g., Jacob *et al.*, 1994), bulk rock compositions are reconstructed from mineral chemistry data rather than measured directly. As accurate modal abundances cannot be obtained for most FALC xenoliths due to their small size, a 1:1 ratio of garnet and clinopyroxene was assumed. This agrees with rough modal abundances for some of the larger FALC xenoliths, which typically have approximately equal proportions of garnet and clinopyroxene with localised modal heterogeneities. Worldwide garnet and clinopyroxene modal abundances of eclogitic mantle xenoliths typically vary between 70:30 and 40:60 (Jacob 2004), though minor variations in true modal abundances (up to 30 %) have negligible effects on reconstructed trace element patterns and only moderately affect calculated major element compositions (Jerde *et al.*, 1993). Major element bulk rock chemistries and trace element concentrations are reported in Table B6 and B7. Reconstructed bulk rock REE_N patterns of diamond-free eclogites are compared to N-MORB (Sun and McDonough, 1989), and units from the Oman ophiolite (basaltic lavas and sheeted dykes of Alabaster et al. (1982), and lower, transition zone and high level gabbros of Pallister and Knight (1981), Fig. 3.9).

3.3.2 Subduction related protoliths of FALC eclogites

A high-pressure origin related to partial melting of a peridotitic source is unlikely for the FALC eclogites. Bulk rock MgO values are too low to be a result of deep mantle melting (Walter, 1998) and high pressure liquidus pyroxenes are not jadeite rich (Pearson and Nixon, 1996). Rather, FALC eclogites have geochemical signatures consistent with a subducted low-pressure origin. Reconstructed bulk rock major element compositions are similar to MORB and oceanic gabbro (Dludla *et al.*, 2006 and references therein). In addition, the majority of $\delta^{18}O$ values deviate from the mantle range for garnets (Ickert *et al.*, 2013), which is commonly attributed to seawater alteration of oceanic crust (Muehlenbachs and Clayton, 1976; Jacob *et al.*, 1994).

Based on their garnet major element chemistry, the eclogites are separated into high-Ca (with varying Mg#), moderate to high-Mg (11.2 – 21.5 wt% MgO) and low-Mg (low-Ca) groups (Fig.

3.3), with the latter only present among barren eclogites. Most samples in the FALC eclogite suite classify as moderate- to high-Mg. Reconstructed bulk rock REE_N patterns for barren eclogites are characterised by flat, supra-chondritic HREE (2- 15 x chondritic), consistent with oceanic crust (Pallister and Knight 1981; Fig. 3.9), which results from partial melting of peridotite within the spinel stability field (Presnall *et al.*, 2002). High-Mg eclogites generally have positive Eu and Sr anomalies, suggesting that their protoliths were enriched in plagioclase (Jacob, 2004 and references therein), which is a characteristic of oceanic gabbros. Barren high-Mg eclogites also have oxygen isotope compositions below the mantle range (Fig. 3.6A), typical of gabbroic oceanic crust (layer 3) that experienced high temperature seawater alteration (Muehlenbachs and Clayton, 1976; Gregory and Taylor, 1981; Benoit *et al.*, 1996). In contrast, the diamondiferous high-Mg xenoliths have no or negative Eu anomalies in garnet and $\delta^{18}O$ signatures elevated relative to mantle values, which are consistent with shallow basaltic protoliths (layer 2; Jacob *et al.*, 1994; Dludla *et al.*, 2006).

The diamondiferous and diamond-free high-Ca eclogites have markedly different Mg#. This difference, however, is not reflected in their similar trace element and $\delta^{18}O$ values (Fig. 3.4 and Fig. 3.6; Table B2 and B4). Both suites have positive Eu anomalies, indicative of plagioclase accumulation in their source, as well as $\delta^{18}O$ values below the mantle value, characteristic of hydrothermally altered gabbroic oceanic crust (Benoit *et al.*, 1996; Shanks, 2001). The high CaO contents are consistent with the formation of the protolith with plagioclase and/or clinopyroxene accumulation (Beard *et al.*, 1996). In addition, the barren xenoliths have low bulk rock $LREE_N$, which have previously been interpreted as residues after up to 20% melt removal within the eclogite stability field (McDonough, 1991; Foley *et al.*, 2002; Stachel *et al.*, 2004).

The low-Mg eclogites are only present in the diamond-free suite and contain no fresh clinopyroxene. Based on their garnet trace element patterns (Fig. 3.4), the suite has the highest MREE-HREE contents, experienced metasomatic enrichment in LREE, shows negative Eu-anomalies, and has $\delta^{18}O$ values above the mantle range, typical for derivation from a basaltic crust protolith (Beard *et al.*, 1996; Dludla *et al.*, 2006).

Based on a review of the data above, at FALC, barren and diamondiferous eclogites have distinct major and trace element compositions, reflecting different protoliths. The diamondiferous eclogites, which occur close to the base of the lithosphere, are interpreted to be derived from

shallow basaltic protoliths. Barren xenoliths reside over a much larger depth range (mid-lithosphere levels to near the base of the lithosphere) and mostly have gabbroic protoliths, with a volcanic protolith component being reflected by the low-Mg eclogite group.

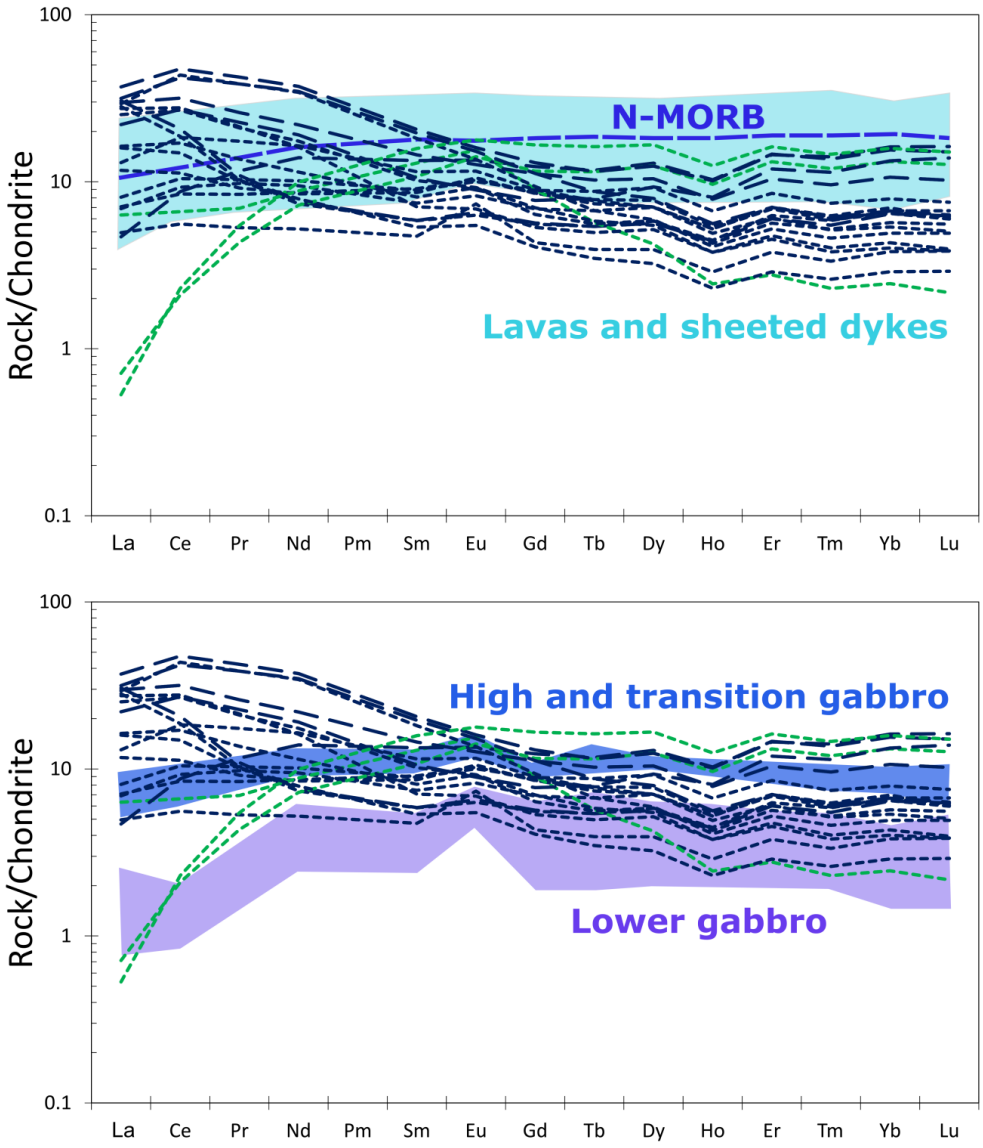

Fig. 3.9 Reconstructed trace element bulk rock composition for diamond-free eclogites. Concentrations are normalised to C1-chondrite of McDonough and Sun (1995). Eclogite data are compared to N-MORB of Sun and McDonough (1989), lava and sheeted dyke compositions (Alabaster *et al.*, 1982; shaded in light blue), as well as gabbroic chemistries (Pallister and Knight, 1981; high level and transition zone gabbros in blue and lower (layered) gabbros in purple) of the Oman ophiolite. High-Ca samples are shaded in green and moderate to high-Mg eclogites in blue; dotted lines represent eclogites containing garnets with positive Eu-anomalies, dashed lines are patterns without a significant Eu-anomaly

3.4 Timing of eclogite formation and metasomatism

Without obtaining radiogenic isotope data, the timing of eclogite formation cannot be constrained unequivocally. However, we can indirectly infer a possible eclogite age range using geo-tectonic constraints. As the petrographical and geochemical characteristics of the barren and diamond-bearing eclogites are variable and discrete groups can be identified within each suite, it is likely that the FALC eclogites are not cogenetic. Thus, it is possible that the different eclogite suites could have formed during distinct tectonic events and we are limited to infer broad windows of eclogite formation. The maximum Re depletion (T_{RD}) age of the lithospheric mantle beneath the Sask Craton is Paleoproterozoic (2.4 Ga; Chapter 2) and it appears reasonable that this also provides an upper age limit for any eclogite contained in the lithospheric mantle. All of the studied eclogites appear to have crustal protoliths, linking the eclogite formation to subduction events that occurred between the Superior and Hearne cratons. The most significant tectonic event in this area, the Trans Hudson Orogeny (THO; 1.9 – 1.8 Ga), is related to the closure of the Manikewan Ocean (Rayner *et al.*, 2005), associated with NW- and SE-ward subduction of oceanic crust beneath the Sask Craton. No other major subduction event occurred beneath the Sask Craton following the THO (Hoffman, 1988). Thus, the formation of FALC mantle eclogites is likely tied to the THO, which constrains their age to 1.9 to 1.8 Ga.

The FALC diamondiferous eclogites also provide insights into a complex metasomatic history. All diamond bearing samples have been affected by the metasomatic agent(s) responsible for diamond formation. Though, few geochemical traces of this event can be identified in the silicate geochemical composition, as this signature has been overprinted by subsequent major metasomatic events. However, elevated bulk rock $LREE_N$ in some of the high-Mg barren eclogites (up to 50 x chondritic, Fig. 3.9) could be linked to the initial diamond forming metasomatic event.

Significant compositional heterogeneities in mantle minerals are rarely preserved due to rapid elemental diffusion at mantle temperatures (e.g., Griffin *et al.*, 1989). Since, the minerals in FALC diamond-bearing eclogites record strong chemical gradients, it is possible to provide a rough estimate of the residence time following metasomatism, based on the diffusion coefficient for garnet major elements. Magnesium diffusion in garnet was modelled (diffusion coefficient D_{Mg} $8.49*10^{-15}$ cm^2/s), using experimental data of Korolyuk and Lepezin (2008). The model

assumes preserved heterogeneities on the scale of 100 μm and pressure-temperature conditions of 55 kbar and 1200 °C, which is in agreement with our geothermobarometric results for diamondiferous xenoliths. For grains with strong chemical gradients, in particular grains SGF-042 (see Fig. 3.7A), the diffusion model only permits mantle residence times of less than 200 years, which is in agreement with estimates for sheared peridotites from South Africa (Griffin *et al.*, 1989). To preserve the observed heterogeneity, mantle metasomatism must have occurred shortly before kimberlite eruption and thus is temporally linked to the Cretaceous FALC kimberlite event. However, it is unlikely that the metasomatism is caused by entrainment in the host kimberlite itself, as we would expect to see similar metasomatic overprinting in the barren eclogites as well. Therefore, this recent metasomatic event is likely localised to the base of the lithosphere, which is dominated by the diamond-bearing eclogites (Fig. 3.8).

3.5 Effects of mantle metasomatism on diamond-bearing eclogites

3.5.1 Nature of metasomatic agents

The majority of diamondiferous eclogites from FALC are compositionally heterogeneous, with garnets exhibiting irregular zonation textures in BSE images (Fig. 3.7A), corresponding to large increases in Mg# (up to 25) and decreases in CaO content (up to 3.1 wt%) from primary to secondary compositions (Fig. 3.3B). In a few samples (Fig. 3.10) these variations even resulted in a shift to low-Cr megacryst-like garnet compositions (G1; Grütter *et al.*, 2004). Garnets from diamondiferous high-Ca eclogites lack zonation within individual mineral grains but also show intra-sample compositional heterogeneity, principally in the form of decreasing CaO correlating to minor increases in Mg# (Fig. 3.3B). In both groups, increasing pyrope content is accompanied by enrichment in Ti, Nb, and Pb (Table B2 and B3) and in some of the most metasomatised samples, $LREE_N$ enrichment and depletion in $HREE_N$. While Zr/Hf ratios in the diamondiferous eclogites are typically low (< 50; Fig. 3.11), some samples of the moderate-Mg and high-Ca suites have elevated Zr/Hf ratios (up to 94.3). The diamondiferous eclogites have variable Ti concentrations on the inter- and intra-grain level, even for samples recording little to no internal increase in Mg#.

Low volume melts like carbonatites and kimberlites (Shimizu and Richardson, 1987), or diamond forming high-density fluids (HDFs; Navon *et al.*, 1988; Weiss *et al.*, 2014) have been recognised as important metasomatic agents in the lithospheric mantle. MARID-style metasomatism, which results in the formation of phlogopite, is expected to shift garnet Zr/Hf towards lower values. This is contrary to what is observed in the FALC eclogites, as Hf is preferentially incorporated into phlogopite and zircon in those rocks (Jacob *et al.*, 2009). For carbonatite metasomatism we would not expect to see enrichment in Ti, but rather, concurrent increases in Ca and Zr/Hf ratio (Rudnick *et al.*, 1993; Shu and Brey, 2015). Distinctly elevated Zr/Hf ratios are only observed for samples of the moderate–Mg and to a lesser extent for the high–Ca suite (Fig. 3.11), coinciding with a large range of Ti values (1226 – 2995 ppm). These contrasting signatures of high Zr/Hf and Ti concentrations about 2000 ppm, may indicate more than one stage of metasomatic modification or may represent a mixed signal of the crustal basaltic protolith and carbonatitic metasomatism. For the high-Mg group, the observed concurrent increases in Mg and Ti, at low Zr/Hf ratios, are consistent with metasomatism by low volume silico-carbonatitic melts, such as kimberlite (Griffin *et al.*, 1999c; Kargin *et al.*, 2016), or potentially a fractionated OIB-like melt (Harte *et al.*, 1993). This interpretation is consistent with the evolution of garnet compositions towards the low-Cr megacryst and sheared peridotite suite (Fig. 3.10 and Fig. 3.11; Aulbach *et al.*, 2004; Merry and le Roex, 2007), which have been interpreted as forming from kimberlitic or OIB-melts (Moore and Lock (2001) and references therein). Similar but less pronounced trends of increasing pyrope and in some samples Ti contents have been reported for rims around eclogitic garnet from the Central Slave Craton and were attributed to late stage kimberlite infiltration (Aulbach *et al.*, 2007). In addition, the garnet compositions overlap with eclogitic garnets included in diamonds (Fig. 3.11), potentially providing a genetic link between the metasomatic signatures and diamond forming events.

In summary, the FALC diamondiferous eclogites suite has a complex metasomatic history. While it is not possible to unequivocally invoke one melt type as the sole agent for chemical change in the moderate-Mg and high-Ca samples – as they have signatures indicative of both carbonatitic, and proto-kimberlitic metasomatism – the high-Mg suite has potentially only experienced proto-kimberlite metasomatism. The silico-carbonatitic metasomatic events even affected the oxygen isotope composition of the eclogites (Fig. 3.7B) and a large number of samples record significant (up to 1 ‰) decreases in $\delta^{18}O$ from primary to metasomatised zones.

These recent metasomatic events only affected diamondiferous eclogites, which are confined to near the base of the lithosphere. Decreasing metasomatic re-enrichment of lithospheric mantle sections with decreasing depth is a common observation (e.g., Griffin *et al.*, 1999b; Stachel *et al.*, 2003). Due to their small size and associated common restriction to garnet-diamond assemblages, modal metasomatism could not be identified in any of the diamondiferous xenoliths, but is likely to have occurred during such a strong metasomatism.

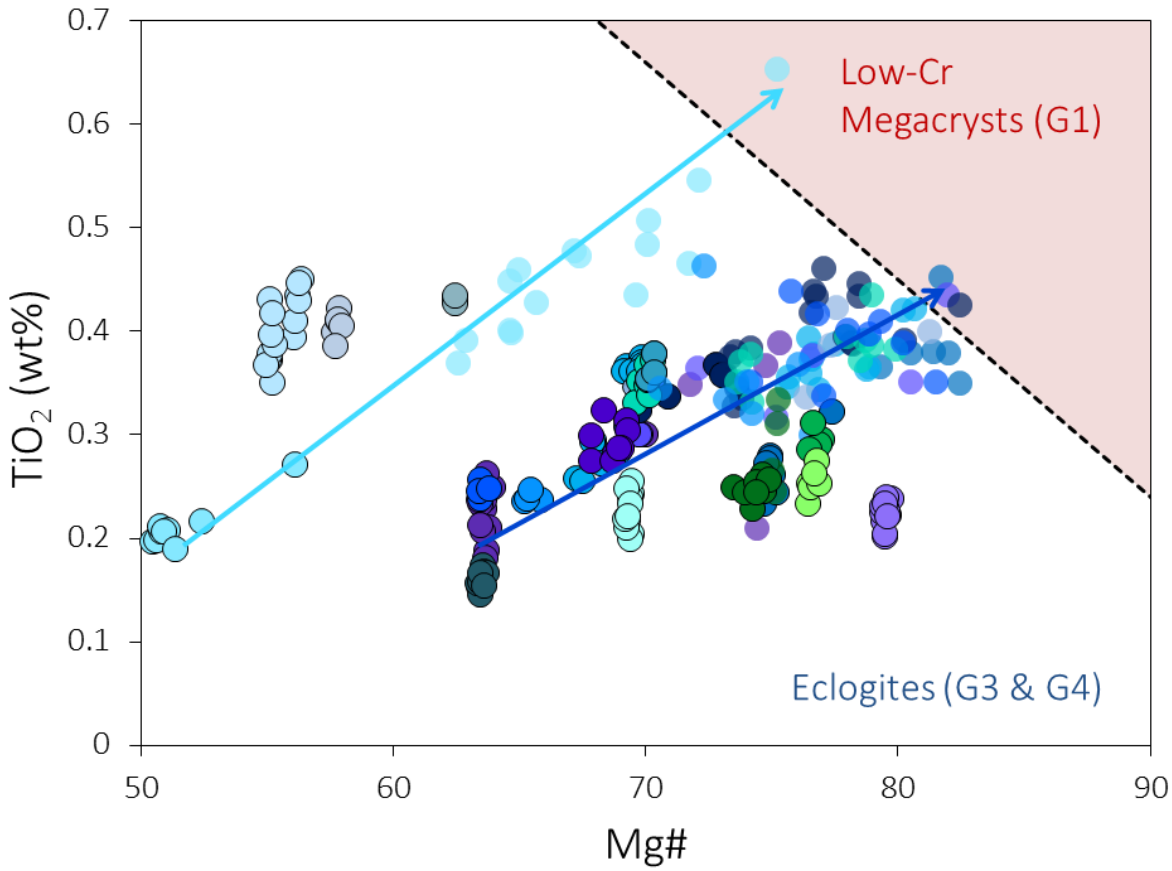

Fig. 3.10 Mg# vs. TiO_2 in diamondiferous samples indicating a shift towards megacryst-like compositions in metasomatised eclogitic garnets. Each sample is plotted in a separate colour and every data point represents an analytical spot. The primary compositions are outlined with black circles, whereas secondary ones are shaded in a lighter colour. The samples are grouped into high-Ca (green), medium (light blue) and high-Mg (dark blue). General trends for moderate and high-Mg eclogites are indicated with arrows

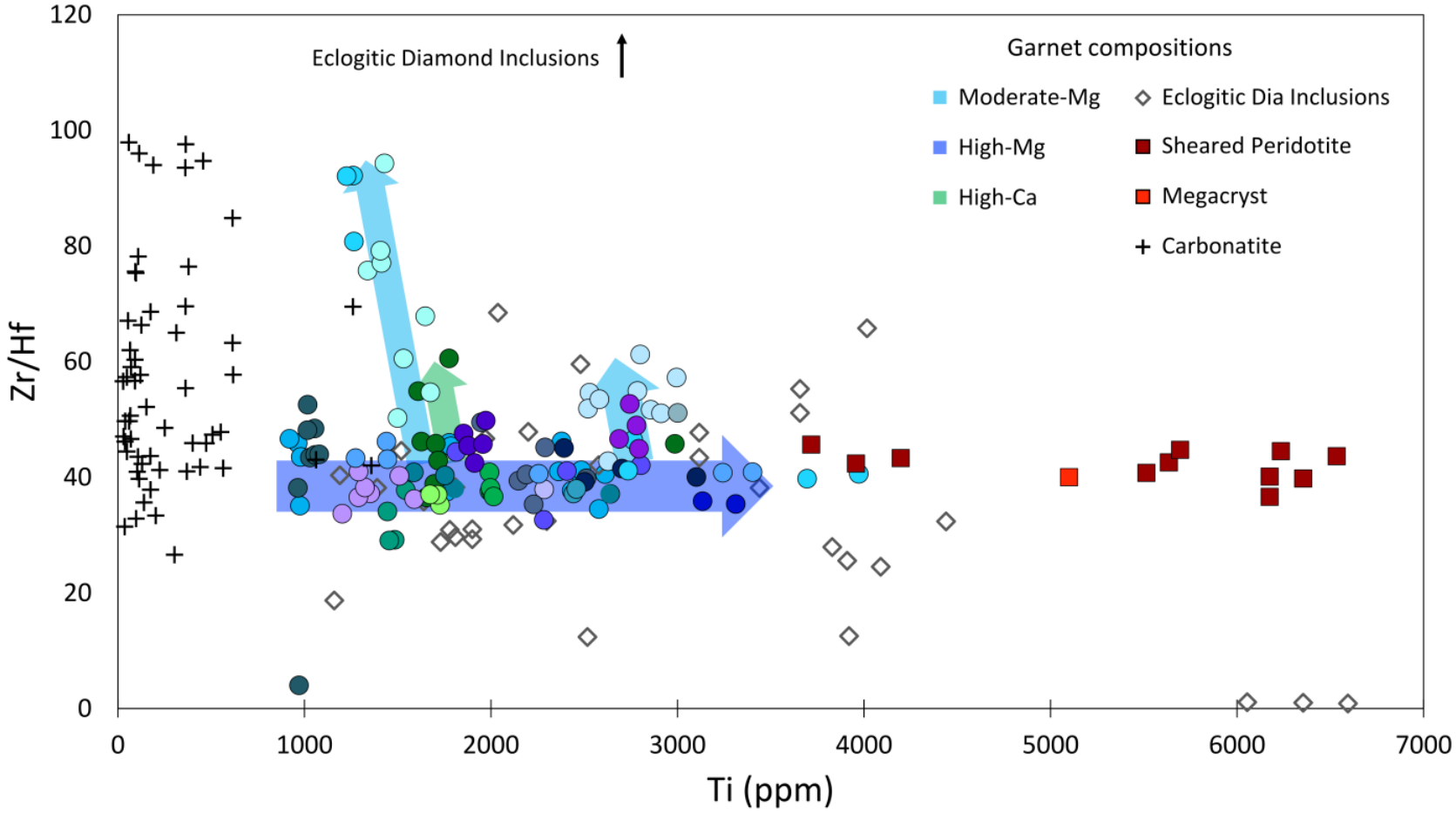

Fig. 3.11 Zr/Hf vs. Ti diagram for garnets from diamondiferous eclogites compared to eclogitic garnets included in diamond (Taylor, 1996; Davies *et al.*, 2004; De Stefano *et al.*, 2009; Viljoen *et al.*, 2010), carbonatite-metasomatised peridotitic garnets (Shu and Brey, 2015), garnets from a sheared peridotite (Aulbach *et al.*, 2004), and megacrystic garnets (Merry and le Roex, 2007). Each sample is plotted in a separate colour and each point represents a single analysis. Trends within different sample groups are indicated by arrows (moderate-Mg in light blue, high-Mg in dark blue, and high-Ca in green)

3.5.2 Origin of oxygen isotope variations beyond the mantle range

The oxygen isotope compositions of garnets from mantle eclogites are commonly used to constrain their origin, as they are interpreted to represent pristine signatures inherited from low-temperature seawater alteration of their crustal precursor (Jagoutz *et al.*, 1984; Jacob *et al.*, 1994). In contrast, recent studies have inferred a non-primary, metasomatic origin for oxygen isotope compositions outside the mantle range (Gréau *et al.*, 2011; Huang *et al.*, 2012).

$\delta^{18}O$ values in barren FALC eclogites significantly extend beyond the mantle range (Fig. 3.6A) and their intra-sample variation is within analytical uncertainty (±0.3 ‰, 2σ). In contrast, oxygen isotope compositions in diamondiferous eclogites, while spanning a similarly broad range, can vary by up to 1 ‰ within a sample (Fig. 3.6B). Eclogites with the strongest major element metasomatic signatures have the largest intra-sample shifts in oxygen isotope ratios. Within zoned garnet grains, increasing Mg# is commonly correlated with decreasing $\delta^{18}O$ (Fig. 3.6C). High temperature mantle metasomatism invariably shifts garnet $\delta^{18}O$ to lower values, regardless of their original oxygen isotopic compositions, as expected from melt-rock interaction mass balance models (e.g., Riches *et al.*, 2016). To produce these metasomatism-induced variations of $\delta^{18}O$ in the mantle, intense fluid – rock interaction (locally > 50 % melt addition) is needed according to a model proposed by Riches et al. (2016). In this model, the authors predict that oxygen isotope compositions of volumetrically minor volatile-rich fluids can be buffered under open (Rayleigh fraction) and closed system (mass balance) conditions by interacting with the peridotitic host rock. However, with significantly larger fluid-rock ratios (> 1:2) it is possible for the fluid to retain a distinct $\delta^{18}O$ value ($\delta^{18}O$ < average mantle: CO_2-rich; $\delta^{18}O$ > average mantle: H_2O-rich) and to subsequently impart their oxygen isotope composition onto the eclogitic host rock.

While the diamondiferous FALC eclogites indicate that oxygen isotope compositions can be altered due to mantle metasomatism, the direction of any change seems to be away from their crustal protolith $\delta^{18}O$ signatures towards mantle-like or lower values, while never fully equilibrating, such that vestiges of their crustal precursor compositions are preserved. This is consistent with interaction with large volumes of CO_2–rich fluids, which are predicted to have oxygen isotope signatures below the average mantle value.

3.5.3 Brecciation and annealing of diamond in FALC eclogites

Diamonds from FALC micro-eclogites have been analysed separately (Chapter 4) and also provide evidence for metasomatism. Cathodoluminescence imaging of diamonds in the eclogites affected by significant metasomatism reveals complex internal textures (dark irregular thin bands and rims; Fig. 3.7B). These unusual dark bands occur as secondary diamond growth between crystals in diamond aggregates and as filled fractures within individual diamond crystals (Fig. 3.7B). These characteristics are consistent with diamond brecciation followed by annealing. As these fractures are solely present in diamonds associated with metasomatically zoned garnets, a genetic link between melt metasomatism and brecciation is a strong possibility. The secondary diamond identified between initial diamonds and along annealed fractures has the same $\delta^{13}C$ as the original diamond crystals (Fig. 3.7; Chapter 4). However, while the secondary diamonds are solely Type II (i.e. "nitrogen-free"), the original diamonds have variable, but often significant N (12 – 1435 molar ppm) that is highly aggregated (80.8 – 100 %B). Based on these high nitrogen aggregation states, the main diamond forming event in eclogitic substrates has to be related to an earlier metasomatic event than the one responsible for brecciation and annealing.

High stresses can result in the brecciation of diamond even at mantle P-T conditions (Howell *et al.*, 2012c). During the rapid ascent of melts, such as kimberlites, high deviatoric stresses are created above the ascending diapir, which are linked to brittle deformation (Artyushkov and Soboley, 1984). A possible process at FALC could involve the intrusion and stagnation of a proto-kimberlitic melt near the base of the lithosphere, as invoked for the formation of sheared peridotites (Mercier, 1979) and low-Cr megacrysts (Moore and Lock, 2001), or polymict mantle breccias (Lawless *et al.*, 1979; Giuliani *et al.*, 2014).

The very close agreement in $\delta^{13}C$ between original nitrogen-rich diamonds and secondary nitrogen-poor fracture fillings and overgrowth (Fig. 3.7B) suggests that annealing/regrowth of diamond utilised carbon already present in the rock, involving, e.g. a diamond dissolution – re-precipitation process. Annealing via the crystallisation of secondary diamond constrains metasomatic melt infiltration to have occurred inside the diamond stability field.

3.6 Conclusion

Diamond-free eclogites in Fort a la Corne kimberlites on the Sask Craton dominantly reflect gabbroic protoliths of the lower portion of oceanic crust, whereas diamondiferous samples commonly have signatures consistent with basaltic protoliths. Eclogite formation is likely linked to the Trans Hudson orogeny and associated subduction of Manikewan oceanic crust (1.9 – 1.8 Ga).

Based on garnet-clinopyroxene geothermobarometry, FALC eclogites are distributed throughout much of the lithospheric mantle deeper than 100 km, with diamondiferous eclogites being concentrated at the base of the lithosphere.

A major melt metasomatic event in temporal proximity to kimberlite magmatism is documented in the diamondiferous eclogite xenoliths. This event (1) caused strong chemical gradients in major and trace element concentrations within xenolith garnets, (2) induced diamond brecciation and annealing and (3) drove the $\delta^{18}O$ values of garnets towards lower, generally more mantle-like compositions, away from the high $\delta^{18}O$ values of crustal precursors.

Chapter 4

4 Diamond formation and brecciation beneath the Sask Craton, Canada – Insights from diamondiferous microxenoliths

4.1 Introduction

Diamondiferous kimberlites are intimately associated with Archean cratons. This relationship, first described by Kennedy (1964), is known as "Clifford's rule" as revised by Clifford (1966) and Janse (1994), and forms a foundation for diamond exploration. Yet, the diamondiferous Fort à la Corne kimberlites do not adhere to this rule, as these unusual diamond deposits are located in a Palaeoproterozoic mobile belt, the Trans Hudson Orogen (Lewry *et al.*, 1994; Bank *et al.*, 1998). In itself, this is not unique to FALC, as mobile belt hosted diamond deposits have been described from other locations, such as Orapa and Argyle (Orapa: Proterozoic Magondi Belt, Stiefenhofer *et al.*, 1997; Argyle: Paleoproterozoic Halls Creek Orogen, Jaques *et al.*, 1990. Archean lithospheric mantle keels were however identified beneath the younger mobile belt in each of these settings (Graham *et al.*, 1999; Deines *et al.*, 2001; Luguet *et al.*, 2009). For the FALC deposits, the situation is reversed. While the FALC kimberlites are hosted on what has been called the "Sask Craton" (Lehnert-Thiel *et al.*, 1992), a crustal terrane enclosed within the THO yielding Archean ages, the lithospheric mantle age of the craton is Palaeoproterozoic (2.4 - 1.7 Ga; Chapter 2). Hence, FALC represent an unusual geological setting for diamond deposits.

Leahy and Taylor (1997) previously studied a small suite of micro- and macrodiamonds from the Fort à la Corne region on the Sask Craton, describing diamond characteristics similar to other cratonic settings, as well as unusual platelet peak degradation (absent platelet peak), which they attributed to diamond formation during the THO. Our current understanding of the FALC diamond population is limited and valuable information, such as diamond paragenesis is still unknown. This detailed study of a large suite of diamondiferous micro-xenoliths from FALC provides the opportunity to investigate diamond forming processes in eclogitic substrates beneath the Sask Craton.

4.2 Geology

The Sask Craton, which is host to the diamondiferous Fort à la Corne Kimberlite Field, is one of the most recently recognised cratons worldwide (Chiarenzelli, 1989). It is located in Western Canada, spanning the provinces of Saskatchewan and Manitoba (Fig. 4.1A). The craton is encompassed by the Palaeoproterozoic Trans Hudson Orogen (1.9 - 1.8 Ga; e.g., Bickford *et al.*, 1990; Heaman *et al.*, 1994; Ansdell and Norman, 1995; Bank *et al.*, 1998; Chiarenzelli *et al.*, 1998). The Himalayan style Trans Hudson Orogeny (Weller and St-Onge, 2017) involved the rifting and opening of the Manikewan Ocean (Stauffer, 1984; Corrigan *et al.*, 2009) and its subsequent closure leading to the collision of the Superior and the Hearne-Rae cratons (Hoffman, 1988; Corrigan, 2012). Although occasional Archean crustal ages have been reported for a few tectonic windows on the Sask Craton (Collerson *et al.*, 1989; Davis *et al.*, 1998; Rayner *et al.*, 2005), the underlying subcratonic lithospheric mantle is Palaeoproterozoic in age (< 2.5 Ga, main mode at 2.4 - 1.7 Ga; Chapter 2).

More than 70 kimberlite bodies (Kjarsgaard and Levinson, 2002) have been identified in the FALC Kimberlite Field, which is situated approximately 50km east of Prince Albert, Saskatchewan. The Cretaceous (~114.7 to ~92.5 Ma; Heaman *et al.*, 2004; Kjarsgaard *et al.*, 2017) FALC kimberlites are interstratified with marine and continental Cretaceous sediments (Zonneveld *et al.*, 2004; Harvey *et al.*, 2009; Kjarsgaard *et al.*, 2009), and are covered by a 100 m thick succession of glacial overburden (Ellis *et al.*, 1996). The first kimberlites in the Fort à la Corne area were discovered in 1989 (Lehnert-Thiel *et al.*, 1992) and diamond exploration has been continuously carried out since then (Kjarsgaard and Levinson, 2002). More than 50% of the discovered kimberlites are diamondiferous, and approximately 70% of the recovered diamonds are of gem quality (Jellicoe *et al.*, 1998). Samples examined in this study were derived from the Star and Orion South kimberlites, located at the Southern end of the FALC kimberlite field (Fig. 4.1B). Grade estimates for the two kimberlites average at 14 carats per hundred tonnes (Leroux *et al.*, 2018).

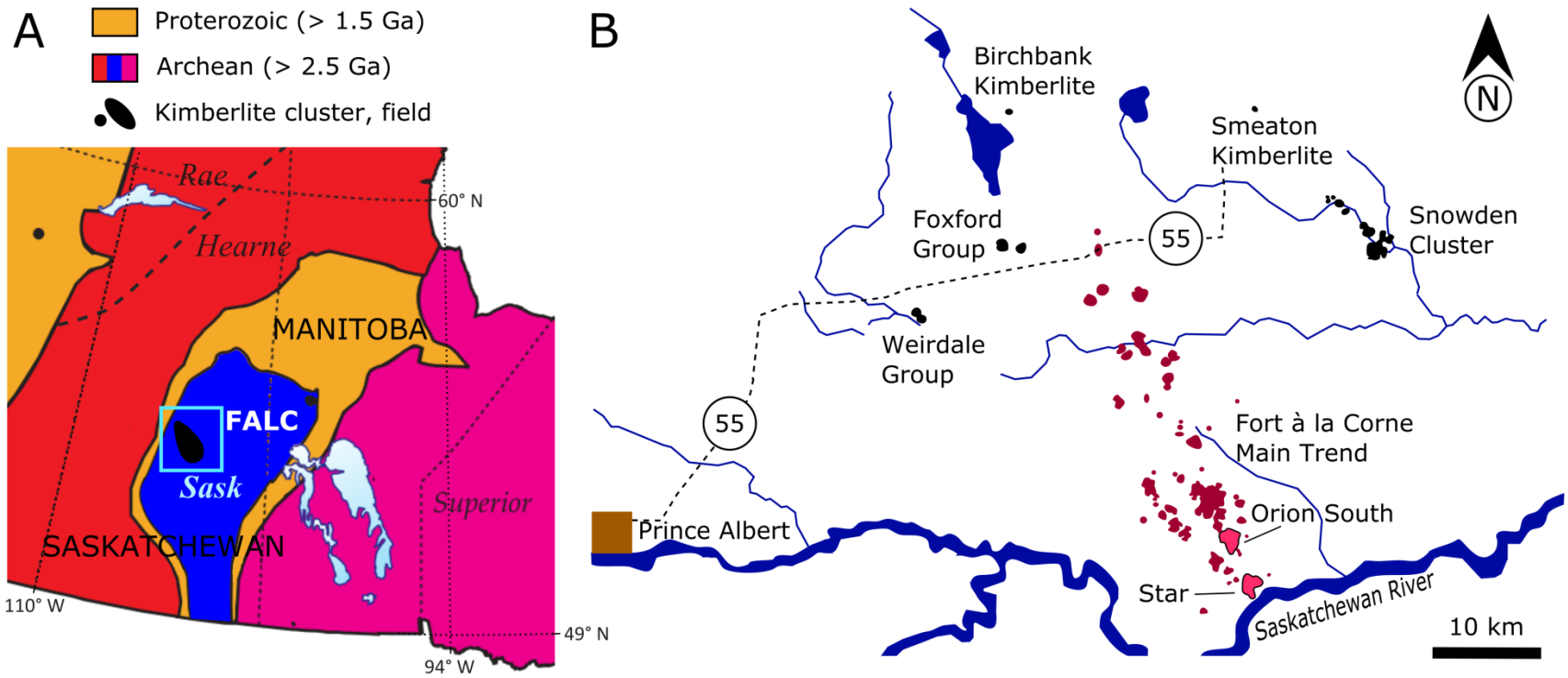

Fig. 4.1 A. Schematic map of cratons and mobile belts in and surrounding Saskatchewan, Canada. The Sask Craton is shaded in blue, whereas the Rae, Hearne, and the Superior cratons are shown in red and pink. Orange shading indicates the Palaeoproterozoic Trans Hudson Orogen. The location of the Fort à la Corne (FALC) Kimberlite Field is show in black, the surrounding blue box outlines the area of the detailed map. B. Detailed map of the FALC area of the Sask Craton. The SSE trend of kimberlite occurrences is shown in red, with the Orion South and Star pipes (sample locations) shaded in pink

4.3 Samples and petrography

A suite of 25 diamond-bearing micro-xenoliths from Fort à la Corne kimberlites was investigated in this study. All samples were recovered during underground bulk sampling of the Star and Orion South kimberlites. Therefore, the sample set is not representative of run of mine production; rather it presents a small subset of diamonds intergrown with silicates.

Eclogitic assemblages dominate the sample suite, comprising 22 xenoliths; only one sample is classified as peridotitic and consists of a purple garnet intergrown with a single octahedral diamond (Fig. 4.2). One of the eclogite xenoliths is cross-cut by a vein of diamonds (Fig. 4.3), a feature that has not been reported before. In addition to the mantle xenoliths, two polycrystalline diamonds are present and provide a non-gem end-member of diamond for this study. The xenoliths are typically less than 1 cm in size and their mineral assemblage often consist only of diamond-garnet intergrowths (Fig. 4.2) within a serpentinised kimberlite matrix. The xenoliths were disaggregated and 44 diamonds, plus a cross-section of the diamond vein were selected for further investigation. Diamonds range in size from 0.5 mm to 3 mm and display a large variety of morphologies and resorption stages (representative diamonds in Fig. 4.4). The diamonds can be separated into three groups (monocrystalline, aggregates, polycrystalline) based on their physical characteristics. All groups are dominated by octahedral and dodecahedral shapes, which are often present as fragments; no cuboid shapes were identified. Stepped growth and negative trigons are common surface features, resorption is present in a few samples. Detailed diamond characteristics are described in Table C1 in the Appendix.

Monocrystalline diamonds (MC) are colourless and have few inclusions. Cathodoluminescence (CL) images reveal homogenous, concentrically zoned or complex internal growth. The diamond aggregates, which include the diamond vein, consist of three or more intergrown octahedral to dodecahedral diamonds. The majority of these diamonds are grey or brown in colour and have cloudy zones as a result of abundant micro-inclusions. In addition to cloudy areas, the aggregates also contain frequent black inclusions, likely of graphite. All diamond aggregates show complex internal textures, typically including irregular secondary veinlets connected to secondary rims (Fig. 4.5). The polycrystalline (PC) diamonds consist of abundant irregular diamonds. They appear grey, as their surface is lightly graphitised. Yet, diamond fragments from these samples

are typically colourless. In one of the polycrystalline diamonds there are a number of intergrown purple garnets. Both polycrystalline diamond samples have irregular growth patterns in CL.

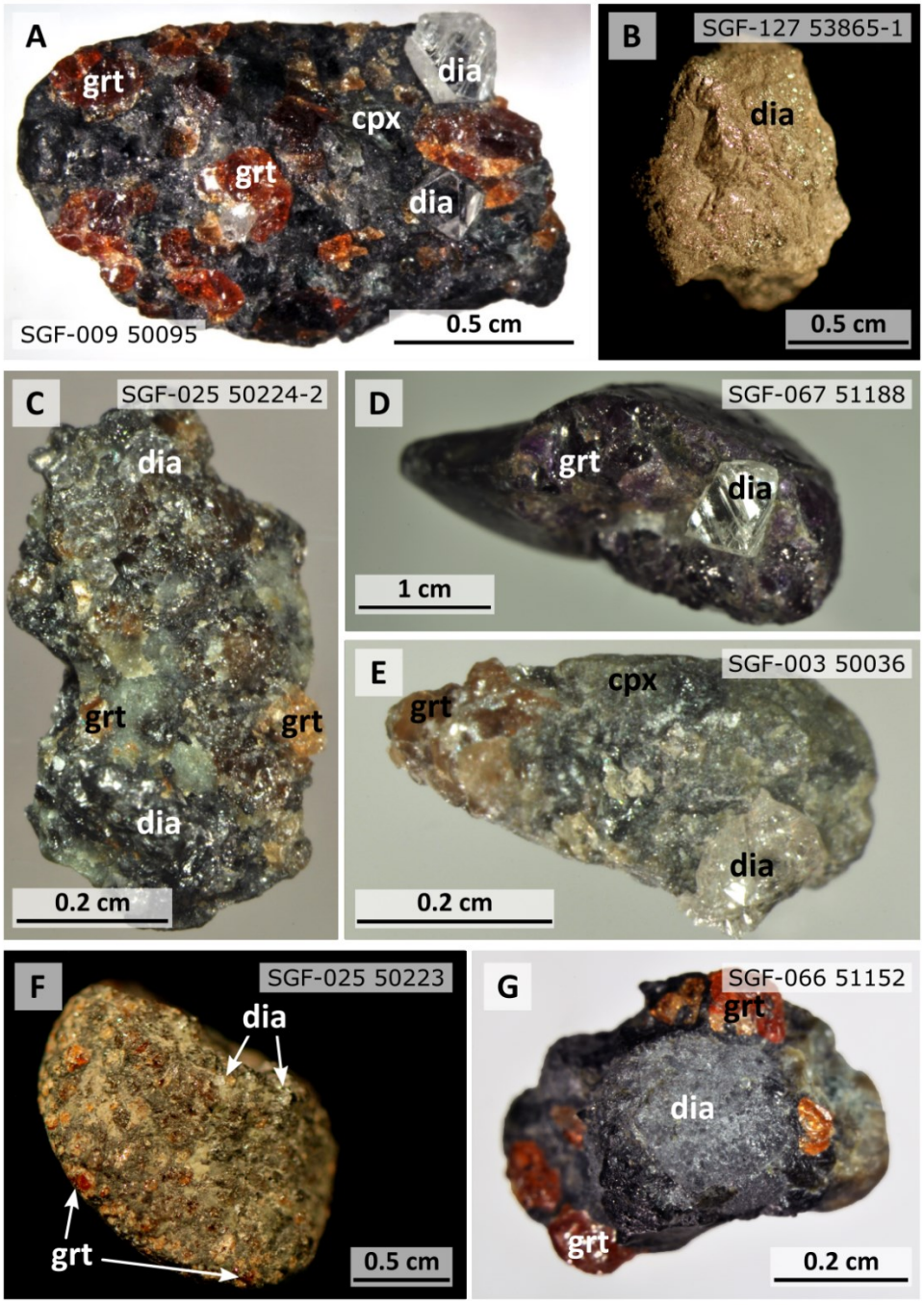

Fig. 4.2 Selected images representative of the diamondiferous micro-xenolith population from Fort à la Corne. Minerals are indicated as garnet – grt, clinopyroxene – cpx, and diamond – dia. Pictures A, C, E, F, and G show diamondiferous eclogite nodules, B depicts a polycrystalline diamond fragment, and the sample in image D is peridotitic

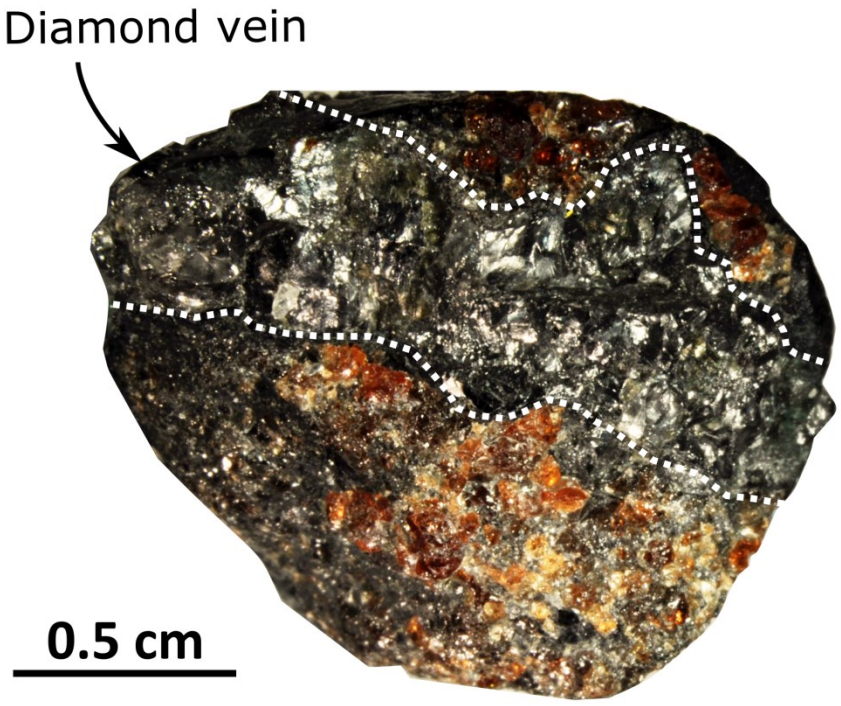

Fig. 4.3 Photographs of a unique eclogite xenolith cross-cut by a diamond vein. The diamond-eclogite contact is indicated by a dotted white line

The unique eclogite xenolith cross-cut by a diamond vein is 2 cm in diameter, with the diamond vein measuring up to 0.7 cm in width (Fig. 4.3). The vein consists of polycrystalline/aggregated diamonds, and its characteristics are similar to the ones identified in the diamond aggregates, with overall grey diamond colour, cloudy zones, and an unusual "fractured" CL pattern (Fig. 4.6). The CL image also reveals two different types of diamond growth within the vein. Polycrystalline/aggregated diamond growth appears to dominate the interior, while concentric growth zoning, similar to the zoning identified in MC diamonds, can be observed close to the diamond-eclogite contact (Fig. 4.6).

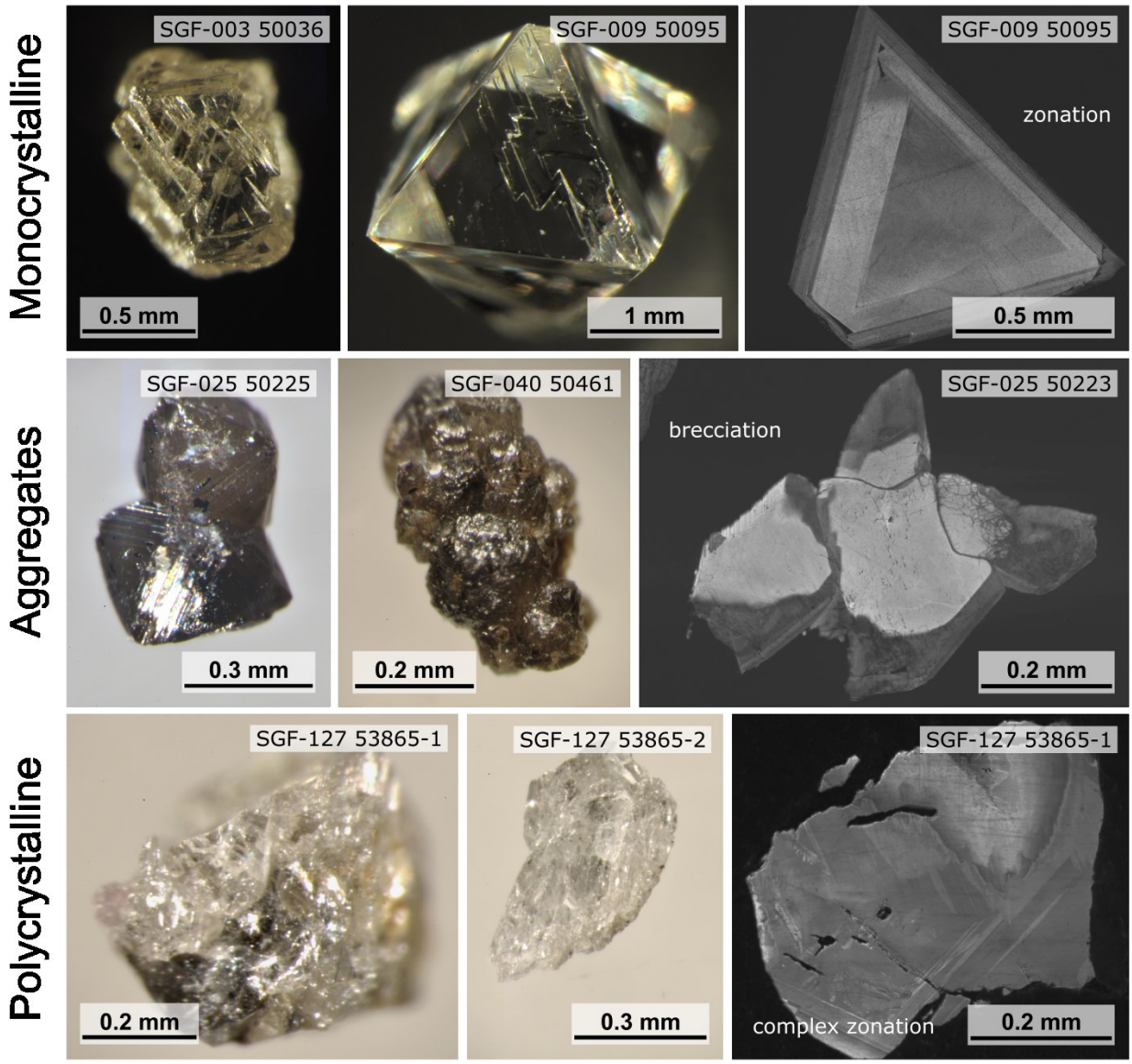

Fig. 4.4 Selected images of diamonds from FALC microxenoliths. Diamonds are grouped as monocrystalline (MC; top), aggregates (AG; middle) and polycrystalline (PC; bottom). Images on the left and centre are photographs and cathodoluminescence images are on the right. Octahedral MC (SGF-003 - macle; SGF-009) and AG (SGF-025) diamonds have stepped growth layers on the surfaces, while SGF-040 consists of intergrown diamonds with resorbed dodecahedral shapes and rough surfaces. Both pictures of PC diamonds show irregular fragments

4.4 Analytical methods

All diamondiferous microxenoliths were characterised, photographed and subsequently, diamonds were carefully extracted trying to avoid breakage, using tweezers, a small steel mortar and pestle, or a hammer. The micro-xenolith containing the diamond vein was cut in half and four diamonds were extracted. In total 44 diamonds were selected, cleaned and imaged prior to the initial geochemical characterisation.

Concentrations (at. ppm) and aggregation states (%B) of nitrogen were determined using a Thermo-Nicolet Nexus 470 Fourier Transform Infrared (FTIR) spectrometer coupled with a Nicolet Continuum infrared microscope and a KBr beam splitter at the De Beers Laboratory of Diamond Research, University of Alberta. With spot sizes of 100 μm, data obtained by FTIR by transmission mode are comparable to bulk analyses. To reduce interferences, the system and sample stage was continuously purged with a mixture of dry nitrogen and oxygen. Background measurements were recorded every 2-3 hours and subtracted from the sample spectra. Up to four spectra were collected per diamond for 200 s over the mid-infrared range (650 – 4,000 cm^{-1}), with a resolution of 4 cm^{-1}. The spectra were baseline corrected using the OMNIC software and subsequently normalised to a pure Type II diamond of 1 cm thickness. For platelet peaks (B', 1358 – 1378 cm^{-1}) a local baseline was fitted to measure the B' peak area. Deconvolution was carried out using a spreadsheet provided by David Fisher (De Beers Technologies). In addition, automatic deconvolution of 20 FTIR spectra was performed using the DiaMap program (Howell *et al.*, 2012b, 2012a). Results from the different data reduction processes are in good agreement. Dependent on sample quality detection limits range between 10-20 at. ppm and analytical uncertainty between 5 to 10% of the nitrogen concentration.

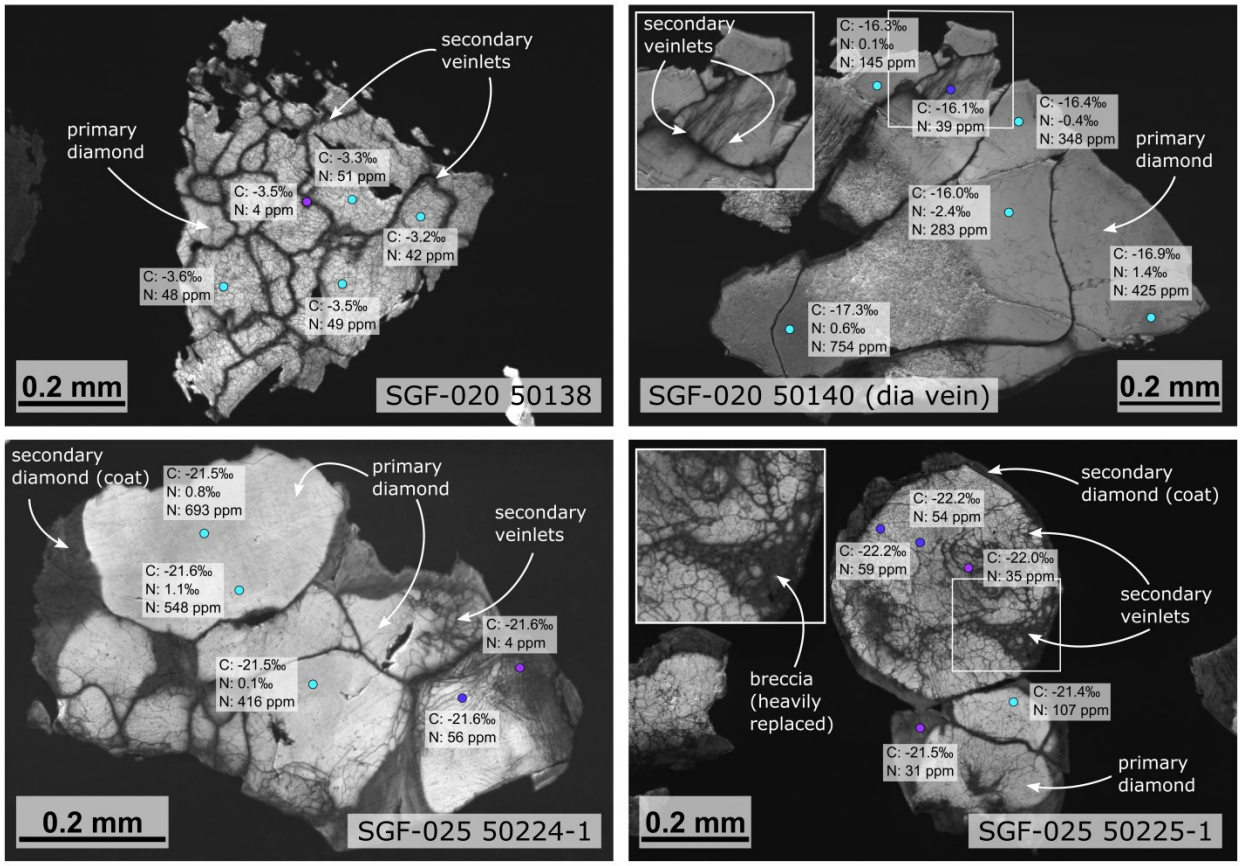

Fig. 4.5 Cathodoluminescence images of representative brecciated diamonds from FALC diamond aggregates. Diamond growths features, such as primary diamonds, secondary veinlets and coats are labelled, or highlighted by insets. Sample SGF-020 50140 is a fragment from the diamond vein. Carbon isotope values, as well as nitrogen concentration and when possible nitrogen isotope ratios for single spot analyses by SIMS are shown. Colour of analytical spots is correlated with spot location. Primary diamonds are shown in light blue, secondary diamond in purple and spots on mixed diamonds in dark blue

A subset of 33 diamonds plus the cut diamond vein were chosen for analyses via secondary ion mass spectrometry (SIMS). The diamonds and the vein fragment were mounted in epoxy, polished and imaged by cathodoluminescence (CL) using a Zeiss EVO MA15 instrument. A Cameca IMS 1280 multi-collector ion microprobe (MC-SIMS) at the Canadian Centre for Isotopic Microanalysis (CCIM) was used to obtain carbon isotope ratios ($^{13}C/^{12}C$), as well as nitrogen abundances (at. ppm) and isotope ratios ($^{15}N/^{14}N$). Detailed methods and information on reference materials were published by Stern *et al.* (2014). A 20 keV $^{133}Cs^{+}$ primary beam with a

diameter of ~12 μm, and beam currents of 2.0 – 3.0 nA was used for analyses. N concentrations (at. ppm) were determined from within the C-isotope pit, while nitrogen isotope ratios and a second measurement of N abundances (at. ppm) were collected adjacent to the C-isotope pit in the same zone. Carbon and nitrogen isotope ratios are reported relative to the Vienna Pee-Dee Belemnite (VPDB) and atmospheric nitrogen (AIR) reference materials, respectively. Propagated uncertainties are typically ±0.15 to 0.20‰ (2σ) for $\delta^{13}C_{VPDB}$ and ±0.56 to 3.6 ‰ for $\delta^{15}N_{AIR}$, the latter depending on N concentration (1400 – 30 ppm). The uncertainties in N abundance measurements range from ±3 – 37% (95% confidence), for N concentrations > 50 at. ppm uncertainties are generally below 4.5%.

Crystallographic orientation data were obtained for a subset of diamonds (n=4) with fractured CL patterns via electron backscatter diffraction (EBSD). EBSD analyses were performed on carbon coated diamond surfaces using a Zeiss SIGMA field-emission scanning electron microscope equipped with an Oxford Instruments AZtecSynergy system (NanoFAB, University of Alberta), with an accelerating voltage of 20 kV, a sample tilt of 70° and high-vacuum. The patterns are obtained on rectangular grids with the electron beam moving at a constant step size (1.6 – 8.6 μm, depending on the sample size) and are automatically indexed using Channel5 post-processing software from HKL Technology–Oxford Instruments.

4.5 Results

4.5.1 Nitrogen and other impurities

Nitrogen concentrations and aggregation states for all diamonds are reported in Table C2. In addition, the platelet peak (B') area, the "hydrogen" peak (3107 cm^{-1}) area, as well as other identified impurities, such as carbonate and CO_2, are also listed in Table C2.

Due to abundant micro-inclusions in a large portion of the studied FALC diamond suite, it is difficult to obtain high-quality infrared spectra, in particular for diamonds with low (< 50 at. ppm) nitrogen content. For three diamonds no reliable spectra could be obtained. Thirty percent of analysed FALC diamonds are Type II, meaning nitrogen is below detection limit (10 at. ppm). For the remaining diamonds the data show a large spread in nitrogen concentration, as well as aggregation state, with each group (MC, PC, aggregates) having distinct nitrogen characteristics.

For the entire dataset, nitrogen concentrations range from 18 to 1005 at. ppm, with a median of 471 at. ppm, and nitrogen aggregation varies between 0 and 100 %B, with a median of 79 %B (Fig. 4.7). As a group, monocrystalline diamonds have the largest spread in nitrogen contents (18 - 1004 at. ppm) and nitrogen aggregation states (0 - 83 %B), with both Type IaA and IaAB diamonds being present. Nitrogen shows minimal variability in polycrystalline diamonds (892 – 959 at. ppm; 18 – 21 %B). The diamond aggregates span a broad spectrum in nitrogen contents (24 - 889 at. ppm), with all nitrogen accommodated in the B-centers (100 %B).

Platelets, planar defects oriented parallel {100} that formed by the expulsion of carbon from the diamond lattice during the formation of B-centres, can be found in Type Ia diamonds (Sobolev *et al.*, 1969; Woods, 1986). In an infrared spectrum, the platelet peak (B') is usually identified between 1358–1378 cm^{-1} (Sobolev *et al.*, 1969). Approximately 60% of nitrogen-bearing FALC diamonds show a platelet peak; peak positions range between 1360 and 1378 cm^{-1} and the peak area ranges from 0.2 to 143 cm^{-2}.

The hydrogen-related peak at 3107 cm^{-1} is another impurity commonly identified in FALC diamonds (82%). Based on first principle simulations, Goss *et al.* (2014) suggested VN_3H centres (hydrogen atoms captured by a N_3 defect - three nitrogen atoms surrounding a vacancy) as the cause for the 3107 cm^{-1} absorption peak. For the studied diamond suite, the area under the 3107 cm^{-1} absorption peak ranges between 0.3 and 49 cm^{-2}. In addition, the spectra from the cloudy diamonds contained abundant peaks indicative of fluid or mineral micro-inclusions often exceeding the height of the diamond peak, such as carbonate, CO_2, silicates, or apatite (Fig. 4.8). FTIR peaks at ~1014 cm^{-1}, ~1090 cm^{-1}, and ~3676 cm^{-1} have been attributed to sheet silicates, apatite, or carbonates (Farmer, 1974; Kopylova *et al.*, 2010). Peaks ranging from 860 to 885 cm^{-1}, as well as 1420 to 1450 cm^{-1} are attributed to the presence of carbonates (in approximately 50% of the FALC diamonds). The variation in absorption of the carbonate bands has been attributed to changes in carbonate chemistry, i.e. calcite vs. dolomite (Weiss *et al.*, 2010). The presence of CO_2 is suggested by bands at 650-670 cm^{-1} and 2350-2395 cm^{-1}, where the shift in peak position is assumed to be a function of pressure (Schrauder and Navon, 1993; Guilhaumou *et al.*, 2005). Generally small IR peaks attributed to the absorption of sp^3 bonded CH_2 groups (2860 cm^{-1} and 2930 cm^{-1}, symmetric and asymmetric stretch bands, respectively; Titus *et al.*, 2005) have also been identified in more than half of the cloudy FALC diamonds.

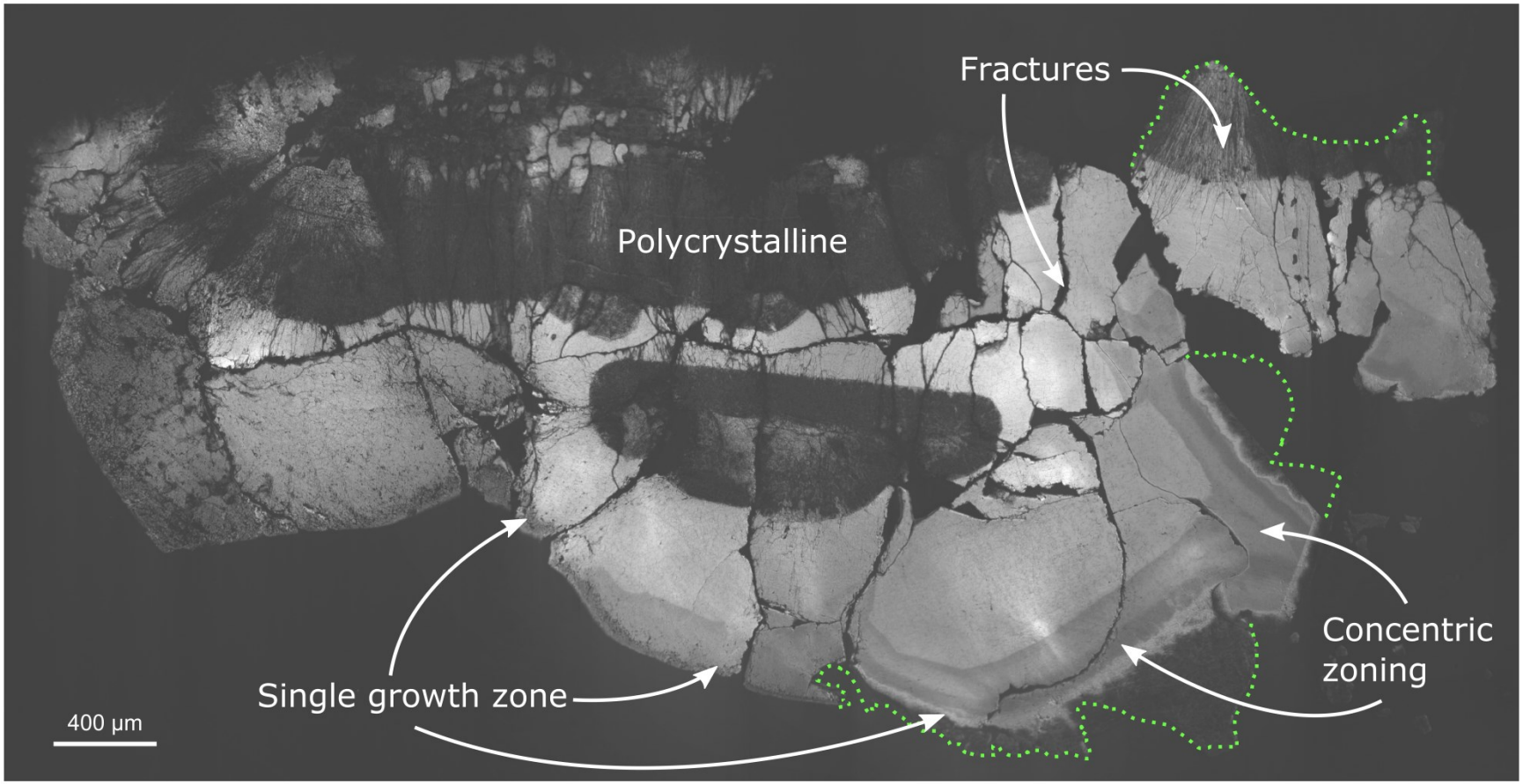

Fig. 4.6 Cathodoluminescence image of the diamond vein from FALC. Diamond growth, as well as brecciation related features are highlighted. Green dotted line outlines the edge of the vein

4.5.2 Carbon and nitrogen isotope ratios and nitrogen concentrations by SIMS

A total of 317 carbon isotope and nitrogen concentration (at. ppm) analyses, as well as 156 and 159 nitrogen isotope and concentration (at. ppm) measurements, respectively, were obtained from 33 diamonds. The $\delta^{13}C_{VPDB}$ values span a broad range (Fig. 4.9) from -29.2 to -2.9‰ (2σ <0.2‰), with three distinct modes at -21.5‰, -16.4‰ and -4.6‰, which were identified using probability density functions in Isoplot. MC diamonds, including the diamond from the peridotitic assemblage, make up the bulk of the mode at -4.6‰, which overlaps with the mantle range (Deines, 1980; Cartigny, 2005). The majority of diamond aggregates and all of the polycrystalline diamonds have carbon isotope values below the mantle range. It is important to note that the -16.4‰ mode is strongly exaggerated, as it is dominated by data points (n=127) from the diamond vein (Fig. 4.9).

Nitrogen concentrations also vary significantly across the sample suite from 0.4 to 1435 at. ppm (Fig. 4.10) at constant $\delta^{13}C_{VPDB}$. Even intra-sample variations cover up to 1419 at. ppm. In diamond aggregates, secondary diamond (veinlets, rims) has low nitrogen – typically less than 30 at. ppm – regardless of the nitrogen concentration in the primary diamond, while $\delta^{13}C_{VPDB}$ remains constant (within error) across the two generations.

More than 25% of analyses plot above the limit sector defined by Cartigny et al. (2001) in N vs. $\delta^{13}C_{VPDB}$ space. $\delta^{15}N_{AIR}$ for the FALC diamonds ranges between -5.7 and +9.4‰, with a median of -1.1‰ (2σ ~ 1.1‰), exceeding the mantle value (-5±3‰; Cartigny, 2005). No correlations between $\delta^{13}C_{VPDB}$, $\delta^{15}N_{AIR}$ or N abundance have been observed for the FALC diamonds.

4.5.3 Crystallographic orientation of FALC diamond aggregates

Electron backscatter diffraction images were obtained for four diamond aggregates, including the diamond vein. All of the analysed samples show complex internal textures in CL, including irregular veinlets and secondary rims. The crystallographic orientation for the individual diamonds comprising the diamond aggregates are distinct and vary up to 90° (Fig. 4.11). However, secondary diamond, or diamond pieces in between secondary diamond, have crystallographic orientations identical to their neighbouring original diamond and show no significant internal variation.

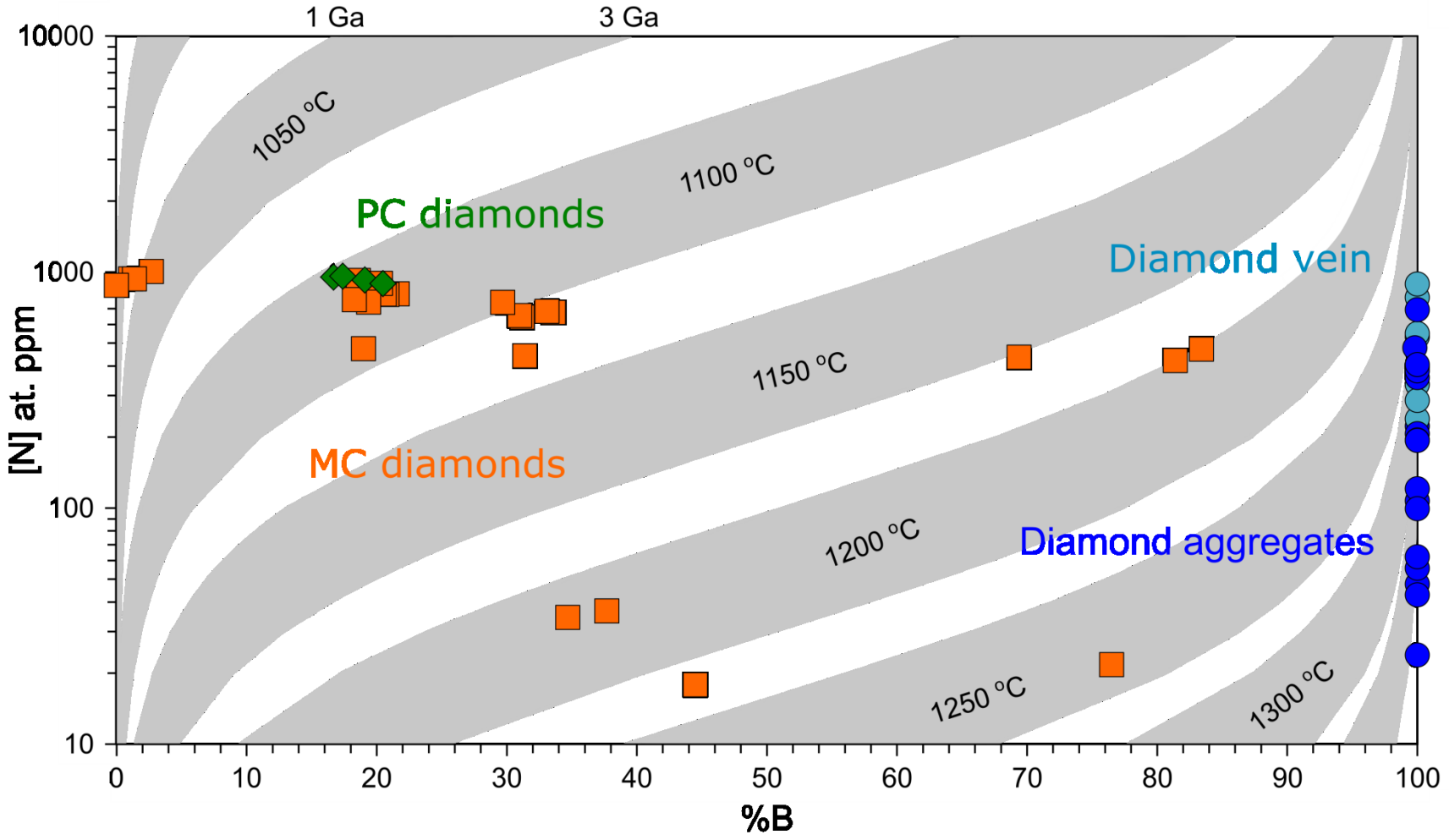

Fig. 4.7 Total nitrogen content (at. ppm) vs. %B (100B/[A+B]) for Fort à la Corne diamonds. Monocrystalline (MC) diamonds are shown as orange squares, polycrystalline (PC) diamonds as green diamonds; the aggregated diamonds, including the diamond vein, are dark and light blue circles, respectively. Isotherms range between 1 and 3 Ga mantle residence time and were calculated following Leahy and Taylor (1997) and Taylor *et al.* (1990)

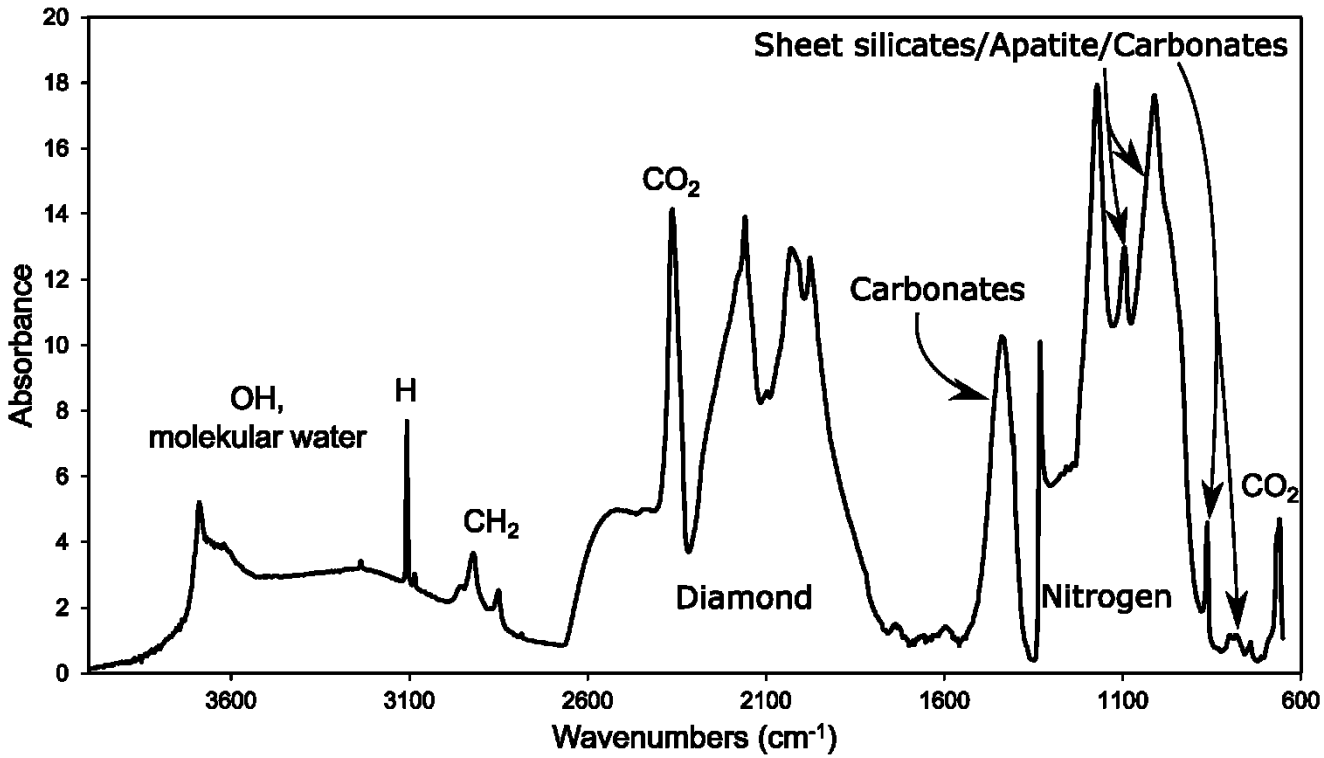

Fig. 4.8 FTIR absorption spectra of a representative cloudy diamond (SGF-025 50223-2) from Fort à la Corne. Absorption peaks for mineral and fluid inclusions are labelled

4.6 Discussion

4.6.1 Origin of FALC diamonds

The distribution of carbon isotope values ($\delta^{13}C$ -29.2 to -2.9‰) in diamonds from Fort à la Corne is consistent with their predominantly eclogitic paragenesis, with the peridotitic MC diamond having mantle-like values (Cartigny, 2005; Stachel *et al.*, 2009). Carbon isotope values are overall restricted to three main modes (Fig. 4.9), nitrogen isotope ratios ($\delta^{15}N$ -5.7 to +9.4‰), as well as nitrogen concentrations (N 0.4 to 1435 at. ppm) span a broad range, regardless of the associated carbon isotope values (Fig. 4.10). Whereas mantle-like $\delta^{13}C$ and $\delta^{15}N$ in the majority of MC diamonds can be explained by a mantle origin of the diamond-precipitating fluid (Cartigny, 2005), strongly negative $\delta^{13}C$ (average -20.7‰) coupled with positive $\delta^{15}N$ (average +7.7‰) in PC diamonds can be interpreted as diamond growth from a subduction related-fluid (Javoy *et al.*, 1986; Deines, 2002).

The apparent decoupling of isotopic ratios for the remaining samples needs further consideration. Carbon isotopes within single grains are typically homogeneous (within 2σ), while intra-sample nitrogen variations reach 1419 at. ppm. The absence of covariation between carbon isotope ratios and nitrogen concentrations indicates that the system is not fluid limited (Cartigny *et al.*, 2001; Stachel *et al.*, 2009) and the observed small variations in $\delta^{13}C$ cannot be explained by Rayleigh fractionation involving an oxidised or reduced metasomatic agent. Nitrogen isotope heterogeneities, while commonly small, can range up to 7‰ within a sample (Table C3), yet no correlations with $\delta^{13}C$ or N content are observed (Fig. 4.10).

A number of models have been proposed to explain such apparent decoupling between nitrogen and carbon. Some authors have suggested that this lack of correlation supports the absence of subducted carbon and nitrogen in diamond-forming fluids (e.g., Cartigny *et al.*, 1998). Further, fine-scaled isotopic heterogeneities in the diamond-forming fluid, as well as several growth stages from fluids of vastly different composition have been proposed to explain intense heterogeneities in $\delta^{15}N$ (ranging from mantle to sediment-like values; Mikhail *et al.*, 2014). Partitioning of nitrogen into mantle phases besides diamond (e.g., potassium-bearing minerals, Fe-carbide, or metallic Fe) has been suggested to significantly affect nitrogen abundance and possibly also isotopic composition in the diamond-forming fluid (Peats *et al.*, 2012; Smith *et al.*,

2014). Lastly, Hogberg *et al.* (2016) proposed that the significantly higher isotopic fractionation factor of nitrogen compared to carbon results in a one order of magnitude higher sensitivity of $\delta^{15}N$ to Rayleigh fractionation in comparison to $\delta^{13}C$. In this instance, clear covariations between $\delta^{15}N$ and N concentrations would be expected, which is not the case at FALC. The majority of diamonds from FALC have low carbon isotope values, indicative of recycled biogenic carbon, in combination with mantle-like, as well as recycled nitrogen isotope ratios (Fig. 4.10) with narrow intra-sample $\delta^{13}C$ and $\delta^{15}N$ variations, which is consistent with a decoupling of carbon and nitrogen systematics. Distinct fluctuations of $\delta^{15}N$ at almost constant carbon isotope values in a few of the FALC diamonds can be explained by either mixing of mantle-like and recycled nitrogen, or by co-precipitation/break-down of nitrogen bearing phases during diamond growth.

About 25% of spot analyses do not follow a trend of decreasing maximum nitrogen content with decreasing carbon isotope values and plot above the limit sector of Cartigny *et al.* (2001); (Fig. 4.10). The limit sector is the result of open system fractionation of mantle melts (Cartigny *et al.* 2001). At FALC, high N-contents at a given carbon isotope value indicate that other processes than fractionation dominate the nitrogen and carbon behaviour. Rapid growth could increase nitrogen incorporation during diamond precipitation; however fibrous diamonds, which crystallise extremely rapidly, still follow the limit sector (Cartigny *et al.* 2001). Therefore, diamond forming fluids likely have varying initial nitrogen contents (Stachel *et al.* 2009). High N contents could imply a recycled component for nitrogen.

4.6.2 Diamond-forming fluids and mode of diamond formation

Diamond formation has long been attributed to melt/fluid metasomatism in the mantle (Haggerty, 1986; Guthrie *et al.*, 1991; Stachel and Harris, 1997). Although studies agree on the metasomatic nature of diamonds, a variety of modes of diamond crystallisation have been proposed. The classical model invokes redox reactions to crystallise diamond (Deines, 1980; Frost and McCammon, 2008) involving the reduction of CO_2 or the oxidation of CH_4. However, recently changes in pH (Sverjensky *et al.*, 2014; Sverjensky and Huang, 2015), isobaric cooling of CHO-rich fluids (Stachel and Luth, 2015), or crystallisation from C-supersaturated metallic liquids (Smith *et al.*, 2016) have been suggested as a means of diamond precipitation.

Fluid inclusions can provide useful information on the nature of the diamond growth medium (Navon *et al.*, 1988; Weiss *et al.*, 2009). Some of the FALC diamonds contain high-pressure CO_2 inclusions (Schrauder and Navon, 1993; Guilhaumou *et al.*, 2005; Fig. 4.8, Table C2), possibly indicating an oxidised parental diamond fluid - at least for a subset of the sample suite. Further, carbonatitic to hydrous-silicic melts (Navon *et al.*, 1988), such as kimberlites, could present a diamond source at FALC. Carbonate inclusions, which have been linked to diamond formation from a carbonatitic/kimberlitic melt in fibrous (Chrenko *et al.*, 1967; Guthrie *et al.*, 1991; Weiss *et al.*, 2010) and polycrystalline diamonds (Kurat and Dobosi, 2000; Rege *et al.*, 2008; Sobolev *et al.*, 2016), were identified in a number of FALC diamonds (Table C1, Fig. 4.8). Host eclogites of fractured diamonds show evidence for kimberlitic and carbonatitic melt metasomatism (Czas *et al.*, 2018) and it is likely that carbonate/kimberlite melt is linked to the formation of fractures in FALC diamond aggregates. Yet, it is not possible to unequivocally link the carbonate inclusions to this metasomatic event. Alternatively, carbonate inclusions in FALC diamonds record initial diamond formation and are linked to a prior metasomatic event unrelated to the brecciation of FALC diamonds.

Experimental studies investigating the mode of diamond formation generally focus on mantle peridotites and their buffering capacity, even though these processes operate differently in eclogitic environments (Luth and Stachel, 2014). In bimineralic eclogite diamond formation via wall rock buffered redox-reactions can only occur by producing either olivine or coesite (Luth, 1993), neither of which were identified in FALC eclogite xenoliths. Further, for eclogitic xenoliths containing abundant diamonds - in particular the diamond vein with a width of up to 0.7 cm, which likely crystallised large amount of diamonds at the same time at distinct nucleation points, forming the aggregated interior (Fig. 4.6) - redox-reactions are not easily buffered by wall rock interaction (Stachel and Luth, 2015). Hence, we propose isochemical crystallisation as the dominant mode of formation for the FALC diamonds, whereby diamond crystallised from a cooling, ascending fluid (Stachel and Luth, 2015) rather than due to redox-reactions. Percolating CHO-rich fluids trigger melting of the eclogitic wall rock (Luth and Stachel, 2014), causing water to be drawn from the fluid into the melt, which in return leads to the supersaturation of the fluid in carbon and results in diamond precipitation (Luth, 2017).

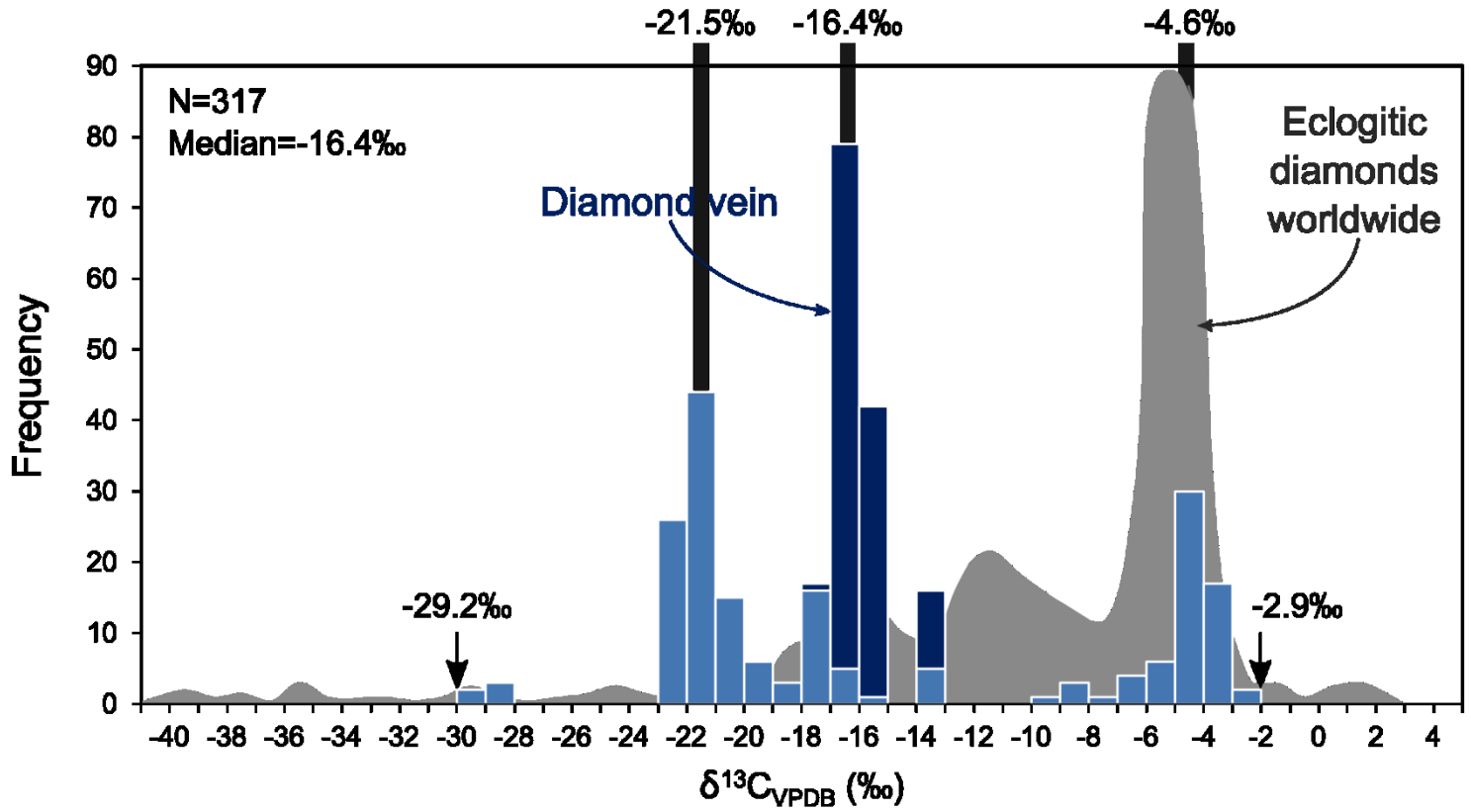

Fig. 4.9 Stacked histogram of carbon isotope spot analyses ($\delta^{13}C_{VPDB}$) of FALC diamonds. Data points from the diamond vein are indicated in dark blue, while the remaining diamonds are shown in light blue. The worldwide $\delta^{13}C_{VPDB}$ distribution of eclogitic diamond is from Stachel (2014) and plotted in grey. Three main modes in the FALC diamond data at -21.5, -16.4 and -4.6‰ are highlighted with grey bands (2σ ±0.2‰)

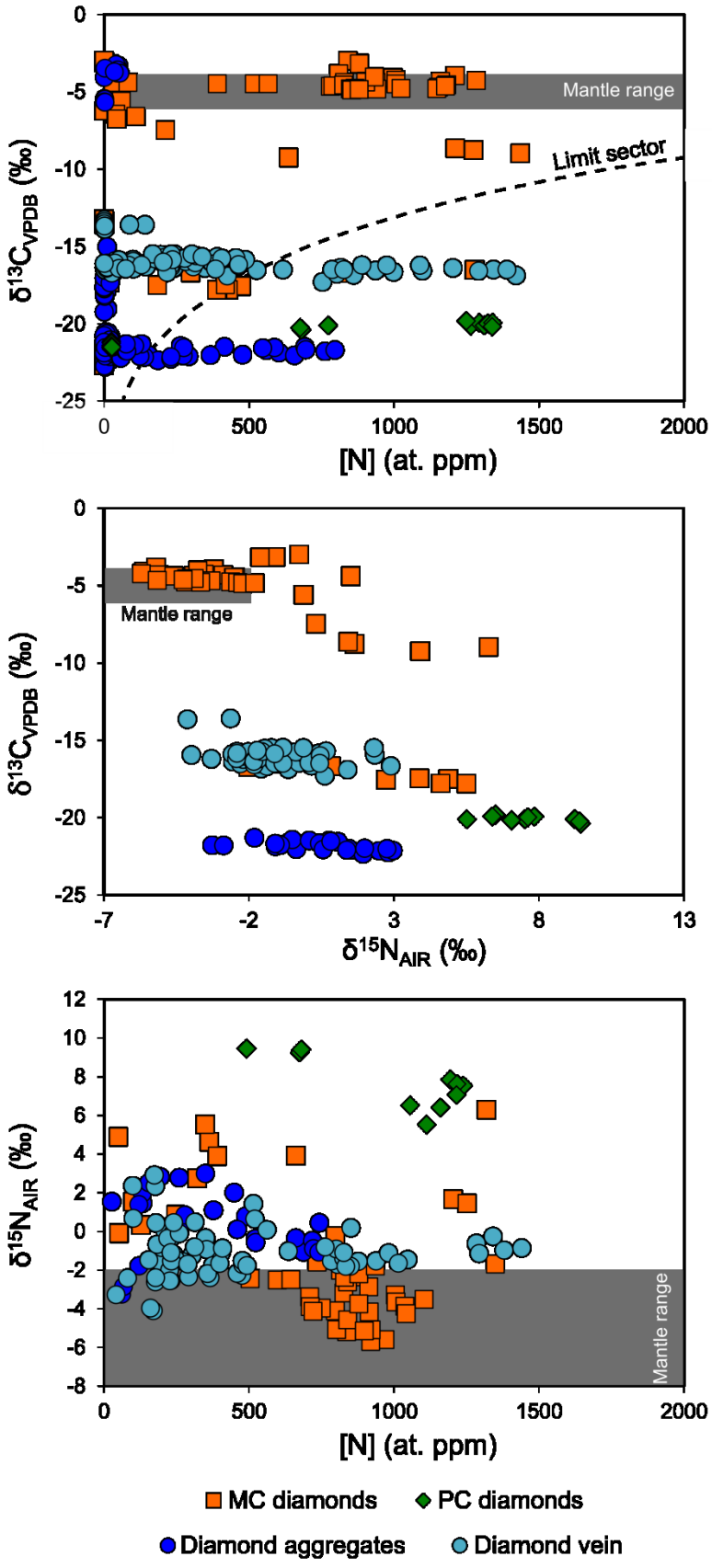

Fig. 4.10 Carbon ($\delta^{13}C_{VPDB}$) and nitrogen ($\delta^{15}N_{AIR}$) isotope ratios, as well as nitrogen concentration variations. Each data point represents an analytical spot. Monocrystalline diamonds (MC) are shown as orange squares, polycrystalline (PC) diamonds as green diamonds, and diamond aggregates as dark blue circles, with analyses from the diamond vein highlighted in light blue. Mantle ranges for carbon and nitrogen isotope ratios are shown as grey fields (Cartigny, 2005).Top: $\delta^{13}C_{VPDB}$ vs. N-concentration, some of the FALC diamonds plot at high N concentrations for low carbon isotope values, above the limit sector defined by Cartigny *et al.* (2001). Middle: $\delta^{13}C_{VPDB}$ vs $\delta^{15}N_{AIR}$, carbon isotope values show distinct clusters, while $\delta^{15}N_{AIR}$ spans broad ranges for each of the respective clusters. Bottom: $\delta^{15}N_{AIR}$ vs. N-concentration, FALC diamonds have $\delta^{15}N_{AIR}$ comparable or above the mantle range

4.6.3 Timing of diamond formation

The studied suite of diamonds from Fort à la Corne documents a long and complex formation history, with all B-centre containing diamonds recording at least two distinct diamond growth events (primary diamond and secondary nitrogen-poor veinlets/coats). Based on the overall high nitrogen aggregation states (median of 79 %B, Fig. 4.7), the initial diamond growth has to be related to a metasomatic event early in the history of the cratonic root. While it is not possible to constrain the exact timing of initial diamond crystallisation from N characteristics alone, it is reasonable to assume that the first FALC diamonds formed in the Palaeoproterozoic, following the initial stabilisation of the lithospheric mantle (~2.4 Ga, Chapter 2). During the Trans Hudson Orogeny (1.9 - 1.8 Ga, e.g., Heaman *et al.*, 1994) the subcratonic lithospheric mantle was thickened, which could lead to the crystallisation of diamond (Leahy and Taylor, 1997; Cartigny *et al.*, 2004). Considering that the bulk of the analysed diamonds were extracted from eclogitic substrates, which likely formed during the THO, a correlation between orogeny, lithospheric thickening and diamond growth seems plausible.

In the FALC diamond aggregates, secondary diamond growth can be observed within fractures, interstitial to individual diamond crystals, or as coats. The formation of fractures within diamonds is attributed to the percolation of kimberlitic or carbonatitic melts in the Sask lithospheric mantle, as a close association is inferred between intense late-stage (~200 years prior kimberlite eruption) metasomatic-induced zoning of garnets in the host eclogites and brecciated diamond (Czas *et al.*, 2018). Subsequent growth of secondary diamond filling these fractures could have occurred via dissolution and reprecipitation. Hence, we propose that the crystallisation of secondary diamond in FALC diamond aggregates is temporally linked to kimberlite eruption.

With nitrogen aggregation of up to 21 %B (Fig. 4.7), polycrystalline diamonds likely crystallised during an earlier metasomatic event, potentially related to the growth of MC and aggregated diamonds. Hence, at FALC the formation of PC diamonds is not temporally linked to the host kimberlites (Gurney and Boyd, 1982; Jacob *et al.*, 2000; Kurat and Dobosi, 2000).

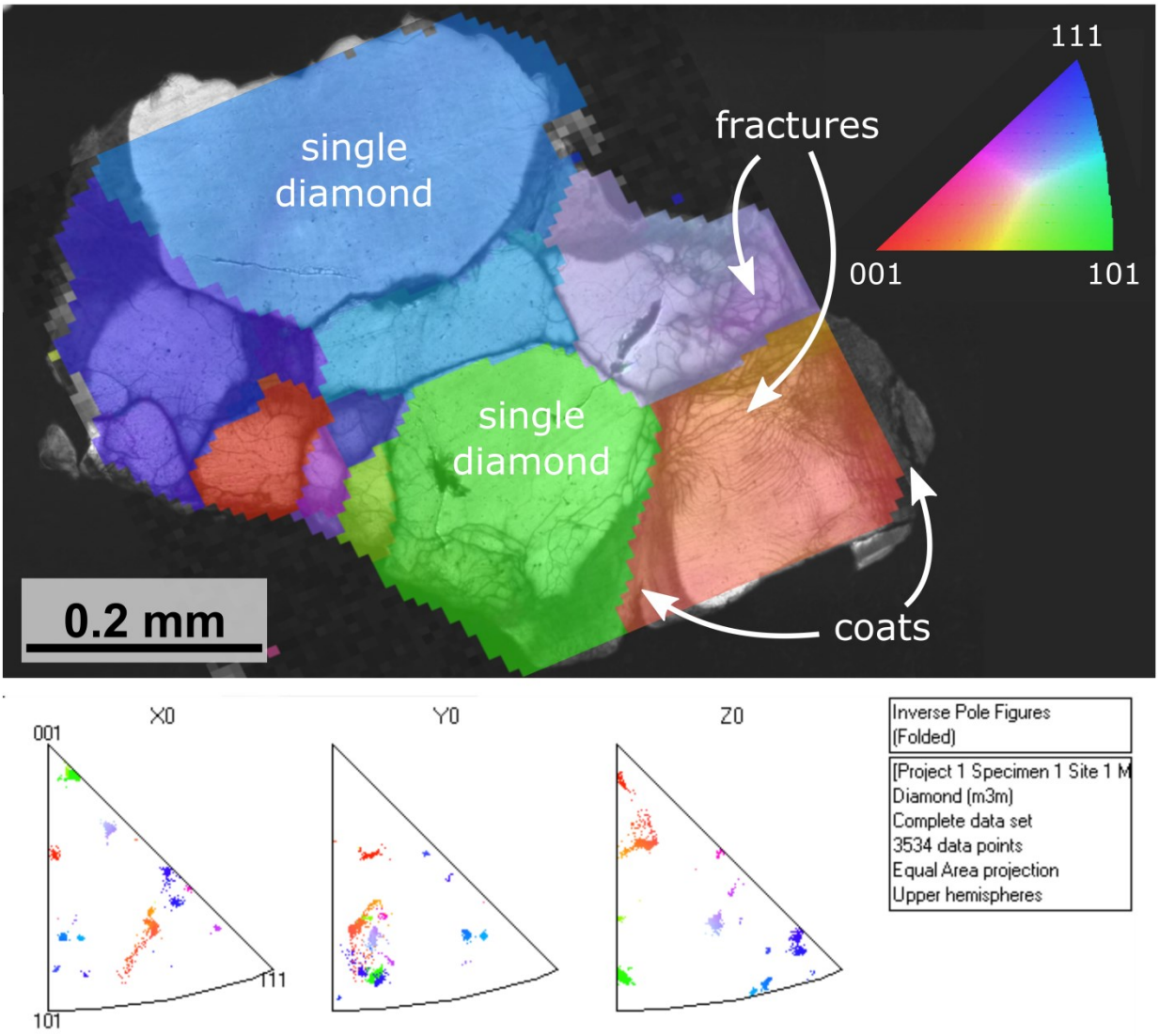

Fig. 4.11 Electron backscatter diffraction (EBSD) images of a representative brecciated diamond (SGF-025 50224-1 2); the sample is also shown in Fig. 4.5. Crystallographic orientation is colour-coded. The individual diamonds making up the diamond aggregates have different orientation, yet the brecciation has not caused any rotation within the diamond grains. Inverse pole figures indicating the orientation of the individual diamonds are shown above and below their respective EBSD images

4.6.4 Nitrogen thermometry

Nitrogen is the most common impurity in diamond. Its aggregation state is dependent on the mantle residence time and temperature (Evans and Harris, 1989; Taylor *et al.*, 1990). Nitrogen first enters the crystal lattice as single N atoms (C-centres; Type Ib diamond), which are not stable at mantle conditions and hence are not commonly identified in natural diamonds (Taylor *et al.*, 1996). From C-centres the aggregation sequence continues to nitrogen pairs (A-centre, Type IaA) and finally B-centres (Type IaB), which consist of four N atoms surrounding a vacancy and are associated with the formation of platelets (Evans *et al.*, 1981; Bursill and Glaisher, 1985). Using the conversion from A- to B-centres, time-averaged mantle residence temperatures can be obtained (Taylor *et al.*, 1990; Leahy and Taylor, 1997). Long residence times and/or high temperatures are assumed when nitrogen is fully aggregated (Type IaB; Evans and Harris, 1989; Taylor *et al.*, 1995).

As Type IaB diamonds are common at FALC, temperature estimates for diamonds with 100 %B were calculated for 99.5 %B following the suggested detection limit for A-centres of Stachel *et al.* (2018), resulting in minimum temperature estimates. $T_{Nitrogen}$ is calculated on the basis that the oldest FALC diamonds formed in the Palaeoproterozoic, during or following the THO, which constrains the mantle residence time to ~2 Ga. It is possible that FALC diamonds formed before the THO at ~2.4 Ga, which constitutes the oldest reported age of the lithospheric mantle, or more recently, as a small portion of peridotite xenolith T_{RD} model ages from the same kimberlite (Chapter 2) overlap with the Midcontinent Rift at ~1 Ga (Van Schmus and Hinze, 1985). However, changing the mantle residence time to 2.4 or 1 Ga only results in a small shift of $T_{Nitrogen}$ of max 15 °C and the overall temperature distribution remains unchanged.

Time-averaged mantle residence temperatures for the FALC diamonds range between 1010 and 1380 °C (Fig. 4.12, Table C2). The dataset shows a bimodal distribution with two modes at 1100 °C and 1300 °C, which coincide with different groups of diamond morphology. Monocrystalline and polycrystalline diamonds (Type IaA and IaAB) record mantle residence temperatures below 1260 °C, while $T_{Nitrogen}$ from diamond aggregates (Type IaB) coincides with the high-T mode (>1260 °C). Low-T samples typically form in a cool, undisturbed lithosphere, whereas diamonds from a high-T regime are likely to have experienced a thermo-tectonic event, and/or were derived from the base of the lithosphere.

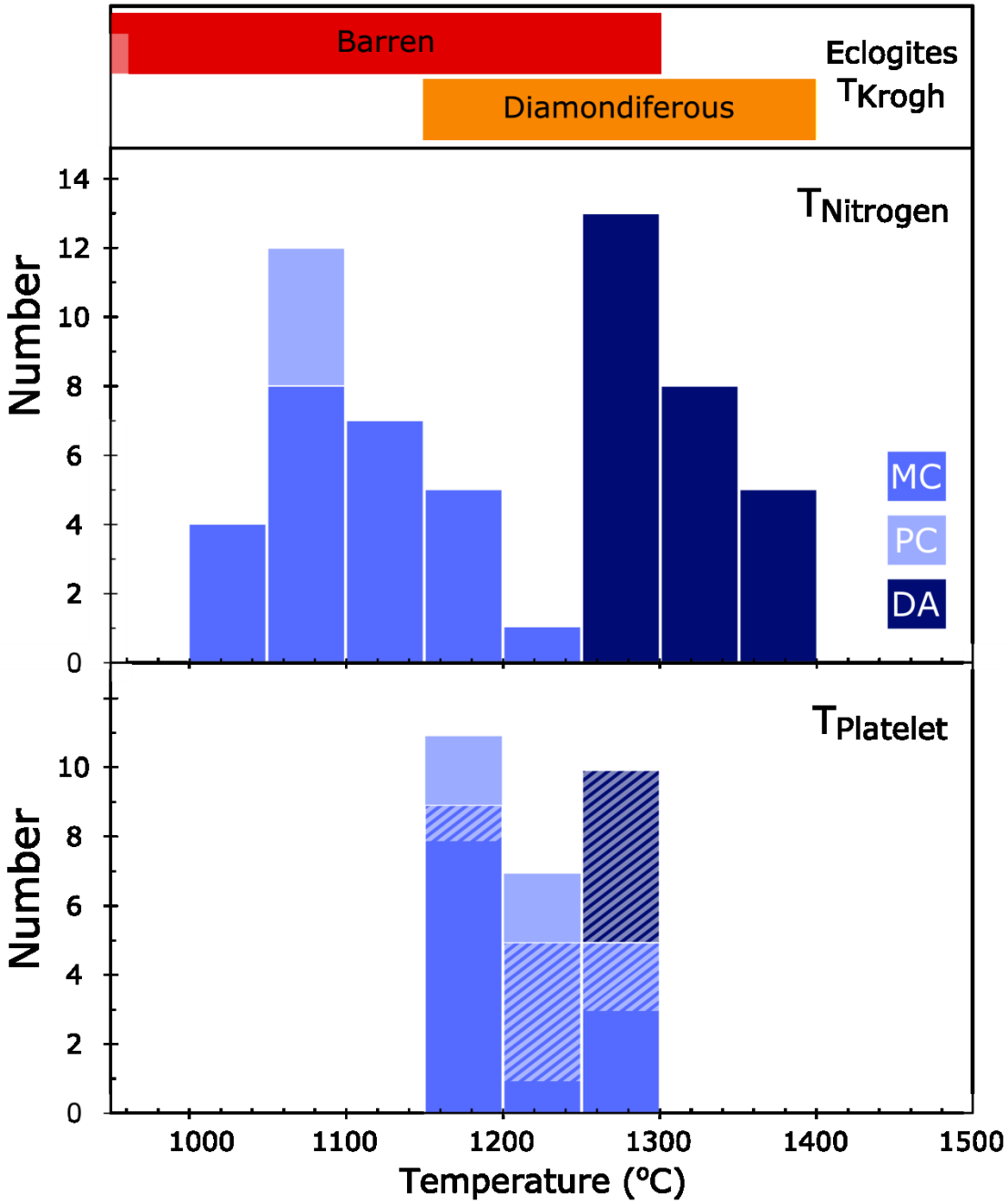

Fig. 4.12 Histograms of time averaged mantle residency temperatures ($T_{Nitrogen}$) and platelet degradation temperatures ($T_{Platelet}$) for FALC diamonds. Temperature distribution is bimodal with modes at 1100 °C and 1280 °C. Data for polycrystalline (PC), monocrystalline (MC) diamonds and diamond aggregates (DA) are shown in light, medium and dark blue, respectively. $T_{Platelet}$ temperatures corresponding to $T_{Nitrogen}$ > 1120 °C are highlighted with white stripes. Diamond temperatures are compared to Fe-Mg exchanged temperatures ($T_{Krogh88}$) for barren (red) and diamondiferous (orange) eclogite xenoliths from FALC (Czas *et al.*, 2018)

Platelet formation is linked to the aggregation of nitrogen from A- to B-centres. A linear correlation between the area beneath the platelet peak (I(B') cm^{-2}) and the absorption coefficient of the B-centre was initially observed by Woods (1986). Undisturbed diamonds follow this "regular" linear trend, while diamonds plotting below the line are classified as irregular and suggest platelet degradation (Woods, 1986). Transient thermal events (Evans *et al.*, 1995), and plastic deformation (Woods, 1986) have been suggested as causes for platelet degradation.

A link between mantle residence temperatures and the rate of platelet degradation has recently been proposed by Speich *et al.* (2018). Using this relationship, we calculated $T_{Platelet}$ (1175 - 1276 °C; Fig. 4.12, Table C2) for diamonds containing measurable platelet peaks. While these temperatures are in good agreement with $T_{Nitrogen}$ for 50% of the samples, a shift of $T_{Platelet}$ to higher temperatures (up to 170 °C higher than $T_{Nitrogen}$) is observed in the remaining samples (Fig. 4.13). Speich *et al.* (2018) reported a similar shift for subregular diamonds (Fig. 4.13 and Fig. 4.14). They suggest that in these diamonds the small platelet size is connected to incomplete platelet growth rather than degradation. For 9 out of 11 samples with $T_{Nitrogen}$ > 1120 °C, $T_{Platelet}$ and $T_{Nitrogen}$ agree within 50 °C. The good agreement between $T_{Nitrogen}$ and $T_{Platelet}$ for four of the five Type IaB diamonds (diamond aggregates) indicates that the minimum values for $T_{Nitrogen}$ (based on 99.5 %B) are realistic, whilst for one sample an ~70 °C higher temperature is derived via platelet degradation.

The nitrogen aggregation based temperatures in the analysed diamonds show the same range as temperatures derived from both FALC eclogites (Fig. 4.11; Czas *et al.*, 2018) and peridotites (Chapter 2). Temperatures < 1150 °C derived via nitrogen-in-diamond are, however, not observed in the diamondiferous eclogite suite but are only present in the barren eclogites. The prerequisite fresh clinopyroxene for geothermometry is not present in many of the diamond-bearing eclogites and hence this difference could simply be the result of sampling bias. In addition, temperatures calculated for diamonds and their host xenoliths are rarely in agreement. There could be several reasons for this. First, mineral exchange thermometry yields the temperature of last equilibration, whereas $T_{Nitrogen}$ is a time averaged residence temperature over the entire > 1 Ga residence period. Short term heating directly before the kimberlite emplacement thus would affect mineral exchange temperatures only. Second, the intense metasomatic overprinting (Chapter 3; Czas *et al.* 2018) experienced by these xenoliths could result in disequilibrium between garnet and clinopyroxene explaining this discrepancy.

Similarly to $T_{Nitrogen}$ from this study, mantle residence temperatures of FALC diamonds from Leahy and Taylor (1997), as well as Ni-in-garnet temperatures from FALC concentrate (Griffin *et al.*, 2004), also exhibit a bimodal temperature distribution. The temperature range identified in the Leahy and Taylor (1997) study is smaller though - including no diamonds with $T_{Nitrogen}$ > 1250 °C - while the peridotitic garnet-based temperature range from Griffin *et al.* (2004) agrees well. The absence of high-T samples in the Leahy and Taylor (1997) dataset reflects the lack of Type IaB diamonds in their study, which may relate to the low sample number (n=21), the exclusive analysis of micro-diamonds, and the sampling of different kimberlites in the FALC kimberlite field.

4.6.5 Plastic deformation in diamonds from FALC

Measurable platelet peaks have been identified in ~60% of nitrogen bearing FALC diamonds (Table C2). Excluding diamond aggregates, which all are Type IaB (100 %B), platelet degradation occurred in all but one of the diamonds from FALC (Fig. 4.13). For fully aggregated diamonds platelets are typically absent, with less than 30% of these IaB diamonds exhibiting measurable platelet peaks. “Sloan-type” diamonds, i.e. nitrogen-poor diamonds lacking platelet peaks, were identified in a previous study of FALC diamonds by Leahy and Taylor (1997). They propose that the Sloan-type diamonds formed during the Palaeoproterozoic Trans Hudson Orogeny in the lower lithospheric mantle, where temperatures are highest, as a result of thickening during continent collision. In this model diamond formation likely occurred simultaneous to the stabilisation and thickening of the Sask cratonic keels, which has previously been attributed to accretion during orogenies (Jordan, 1988; Wang *et al.*, in press). This mode of diamond formation is supported by findings of Cartigny *et al.* (2004), who identified orogenic diamonds in the Akluilâk dykes, from the northern extension of the Trans Hudson Orogen. Mantle residency for diamonds from Akluilâk is, however, estimated to be less than 200 Ma and hence nitrogen is frequently unaggregated (Type Ib - IaA) and no platelets have been reported. Czas *et al.* (2018) proposed that diamondiferous eclogite xenoliths formed by subduction during the THO, which agrees with the orogenic diamond formation suggested by Leahy and Taylor (1997). Mantle residency at high temperatures following diamond formation could have resulted in the observed platelet degradation. The majority of FALC diamonds, including Type IaAB samples, show intense platelet degradation (Fig. 4.13 and Fig. 4.14), which could be - at least in

part - the result of a later thermo-tectonic event related to the fracturing of the FALC diamonds (see below).

4.6.6 Diamond deformation beneath the Sask Craton

The FALC diamond aggregates described here exhibit some unique features of deformation that relate to their complex evolutionary history. Experimental studies have suggested that, at mantle pressures and temperatures, diamond behaves in a ductile manner and undergoes plastic deformation (Evans and Wild, 1965; DeVries, 1975; Howell *et al.*, 2012c). Features of plastic deformation, such as appearance of birefringence, have long been observed in natural diamonds (Phaal, 1964; Lang, 1967). As plastic deformation has been linked to the generation of diamond colour, such as brown and more importantly pink (Collins, 1982; Fisher, 2009; Gaillou *et al.*, 2012; Howell *et al.*, 2015), understanding the ductile behaviour of diamond is also of economic importance. Studies on brittle deformation, which is present in natural samples (e.g. fractures in diamonds; Taylor *et al.*, 1995; Pearson *et al.*, 1999), are rare. In general, such studies focus on the relation of fractures to diamond inclusions (e.g., Gurney, 1989; Taylor *et al.*, 1995) or investigate diamond fracturing at atmospheric pressures (Field and Pickles, 1996).

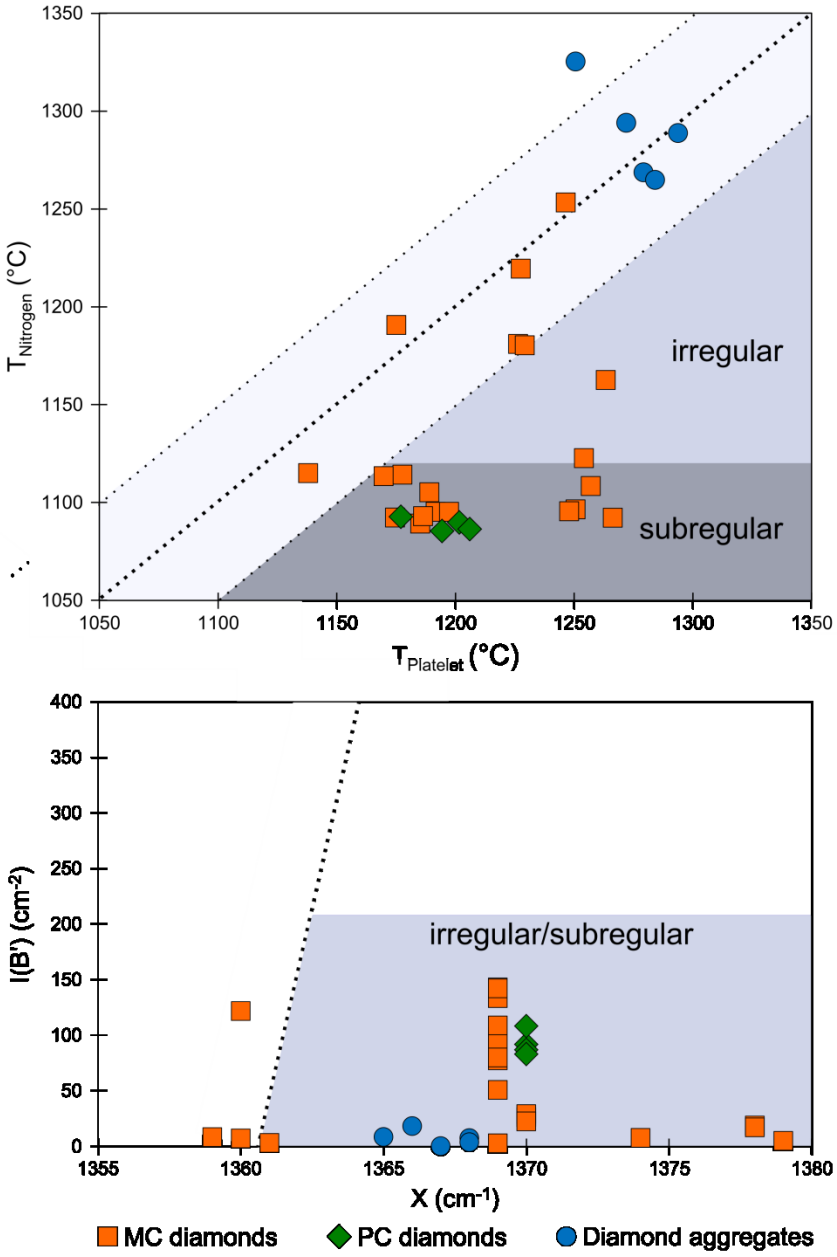

Fig. 4.13 Platelet behaviour and temperatures of FALC diamonds. Classification as regular, subregular and irregular following Woods (1986) and Speich *et al.* (2018). Top: Comparison of platelet degradation temperatures to nitrogen aggregation temperatures. For some irregular diamonds $T_{Platelet}$ is shifted to higher temperatures; Bottom: Platelet peak area (I(B'); cm^{-2}) vs. position of platelet peak maximum (X; cm^{-1}), regular diamonds follow the dotted line (from Speich *et al.,* 2018), while irregular and subregular diamonds plot in the grey field. Diamonds with $T_{Nitrogen}$ < 1120 °C show subregular platelet growth, to which $T_{Platelet}$ is not applicable

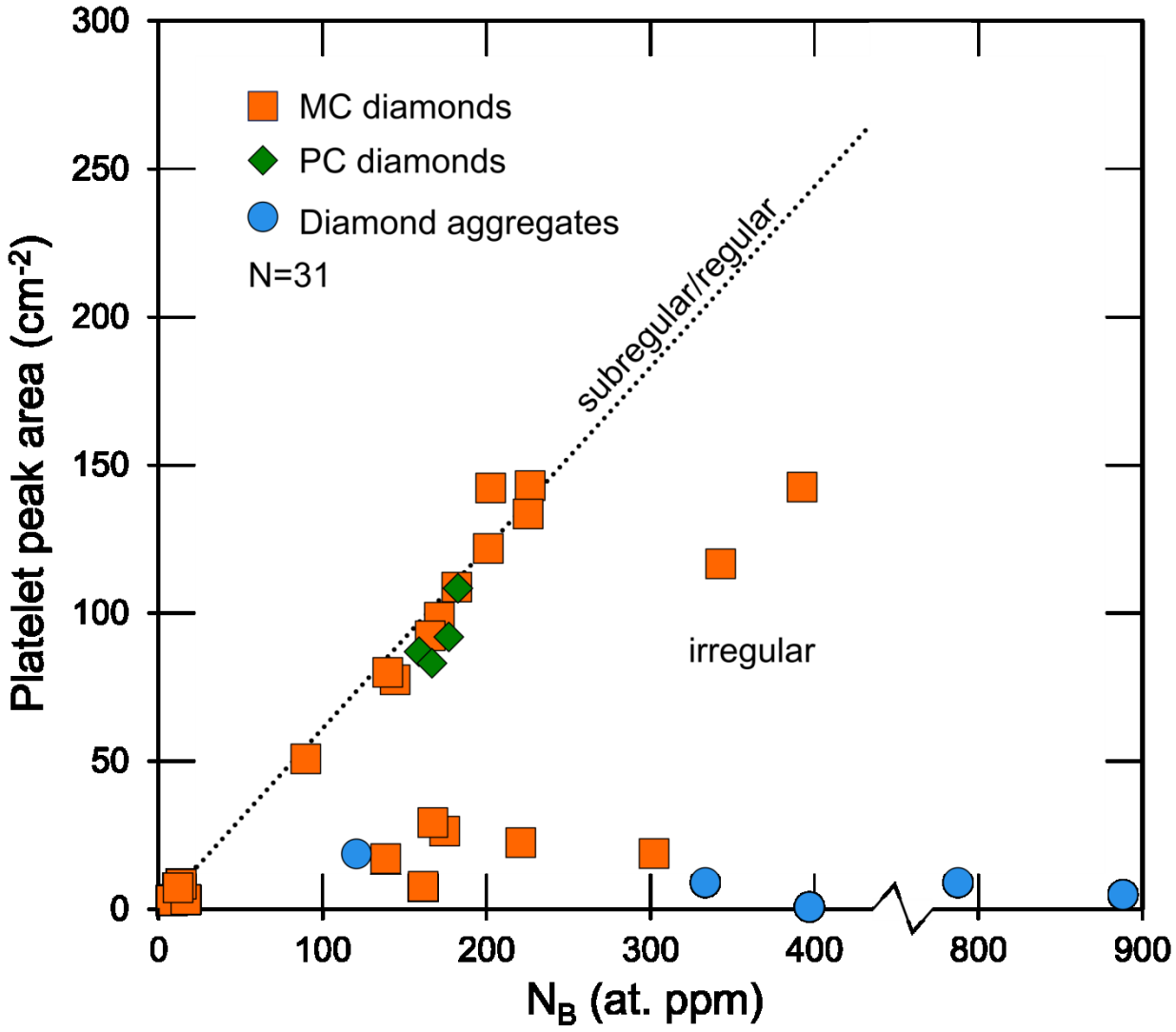

Fig. 4.14 Platelet peak area (I(B'); cm^{-2}) vs. concentration of nitrogen in B-centres (at. ppm) for FALC diamonds. The relationship between I(B') and N_B is considered irregular for diamonds below the dotted trend line (Woods, 1986)

4.6.7 Brecciation of FALC diamonds

Cathodoluminescence images of the studied diamond aggregates reveal unusual, complex internal textures; thin irregular bands (veinlets) that are connected to interstitial diamonds in the aggregates, or diamond coats (Fig. 4.5). These bands are attributed to secondary diamond growth forming rims and filling/annealing fracture systems. To produce these filled fractures, diamond deformation and annealing has to occur within the diamond stability field at depth greater than

120 km (Chapter 2). Texturally, these diamonds are similar to breccias described in fault systems (Sibson, 1977; Woodcock *et al.*, 2006), or ore deposits, in particular fluid-driven brecciation (Sillitoe and Sawkins, 1971). The majority of these unusual FALC diamonds are similar to undisplaced shatter breccias (Fig. 4.11, Sillitoe and Sawkins, 1971), with little or no rotation and limited fluid infiltration, while the most deformed diamond SGF-025 50225-1 (Fig. 4.5) has characteristics comparable to heavily replaced parts of breccias (Sillitoe and Sawkins, 1971).

If diamond deformation at mantle conditions is ductile, how can we explain the evidence for brittle behaviour in FALC diamonds? To fracture diamonds at mantle conditions, high strain rates are needed (Brookes *et al.*, 1999). Increasing differential stresses and high pore fluid pressure shift the position of the Mohr's stress circle towards the failure envelope (Phillips, 1972), which results in the formation of fractures and creates brecciation. In rapidly ascending melts, such as kimberlites, high differential stresses are created above the ascending diapir, which have been linked to brittle deformation (Artyushkov and Soboley, 1984; Wilson and Head III, 2007). At FALC, the brecciation could be caused by the intrusion of a proto-kimberlitic melt near the base of the lithosphere, in an environment similar to formation of sheared peridotites (Mercier, 1979), low-Cr megacrysts (Moore and Lock, 2001), or polymict mantle breccias (Lawless *et al.*, 1979). An origin from the base of the lithosphere is supported by the chemistry and thermometry of the eclogitic host xenoliths (Chapter 3), as well as the presence of polymict breccias in the peridotite xenolith suite (Chapter 2). Fractures are solely present in diamonds associated with intensely metasomatised garnets (Czas *et al.*, 2018) hence, it is likely that melt metasomatism and brecciation are genetically linked. Pressure and temperature conditions derived from the host eclogites point towards a deep lithosphere origin (Fig. 4.12).

It is important to note that brittle deformation is limited to diamonds from the aggregate population, while monocrystalline and polycrystalline diamonds are fracture-free. Based on their high time-averaged mantle residence temperatures (Fig. 4.12), diamond aggregates could be derived from the base of the lithosphere and therefore were more readily affected by the ascending melts.

$\delta^{13}C$ in the secondary diamond that cements the breccias together is typically within error of the carbon isotope value of the original diamond crystals (Fig. 4.5). However, secondary and original diamonds differ greatly in their nitrogen content; while secondary diamonds are

generally Type II (up to ~30 at ppm in mixed zones, Fig. 4.5), original diamonds typically have significant, though variable, nitrogen concentrations (12 – 1435 at ppm, Table C3). This close agreement in $\delta^{13}C$ between the two diamond growth phases suggests that the precipitation of secondary diamond utilised existing carbon in the rock, in a process involving diamond dissolution followed by reprecipitation, at which stage the original nitrogen was already largely lost. It is difficult to explain the homogenous $\delta^{13}C$ values, if the brecciating agent was a carbon-rich melt, such as a carbonatite or kimberlite, as the carbon isotope ratios in the secondary diamond should have shifted towards those of the melt composition. Rather, diamond dissolution and reprecipitation was likely caused by a hydrous melt, which did not affect the $\delta^{13}C$ values.

4.7 Conclusion

Diamonds in micro-xenoliths from the Fort à la Corne Kimberlite Field of the Sask Craton are dominated by eclogitic assemblages, with one peridotitic sample. Of two additional polycrystalline diamonds, one was intergrown with peridotitic garnet; the petrogenetic association of the second is unknown. Three dominant suites of diamond morphologies are identified: monocrystalline, aggregated and polycrystalline diamonds. These morphological groups also differ in their chemical characteristics. While MC diamonds are Type IaA and IaAB and have carbon and nitrogen isotope compositions similar to the average mantle value, PC diamonds, with 31 - 40 %B, show isotopic characteristics indicative of a recycled crustal carbon source. All diamond aggregates are Type IaB, are depleted in $\delta^{13}C$ and have variable $\delta^{15}N$ as well as nitrogen contents, indicating a decoupling of nitrogen and carbon systematics.

Nitrogen-based time-averaged mantle residence temperatures for diamonds from FALC range between 1050 and 1360 °C, Fe-Mg exchange temperatures derived from FALC eclogite xenoliths and T_{Ni} for peridotitic garnets cover similar ranges. The two temperature modes at 1100 °C and 1280 °C are dominated by monocrystalline/polycrystalline diamond and diamond aggregates, respectively.

Cathodoluminescence images of the diamond aggregates reveal secondary diamond growth, annealing complex fracture systems and forming rims surrounding individual diamonds. This indicates brecciation and subsequent annealing of the diamonds. This brittle deformation is likely associated with the intense metasomatic modification of the eclogitic diamond substrates

(Chapter 3) and could be the result of increasing differential stresses created above rapidly ascending melts, such as proto-kimberlites, at the base of the lithosphere. Platelet peak degradation occurred in the majority of FALC diamonds, which could either be a result of diamond genesis during the Trans Hudson Orogeny, or related to the thermo-tectonic event responsible for diamond brecciation.

Based on their carbon and nitrogen characteristics, the majority of monocrystalline FALC diamonds likely crystallised from a mantle-derived fluid, while the carbon of polycrystalline diamonds has a recycled origin. $\delta^{13}C$, $\delta^{15}N$, and N contents in diamond aggregates and a few MC diamonds are indicative of involvement of both subducted and mantle sources, in agreement with the observed decoupling of carbon and nitrogen systematics. While diamond growth from CO_2-rich fluids, or carbonatitic/kimberlitic melts can be inferred from micro-inclusions, it is unlikely that wall rock buffered redox-reactions are involved in eclogitic diamond formation. Rather, we propose that diamonds from FALC crystallised during isochemical cooling of CHO-rich fluid.

Chapter 5

5 Conclusions

The main aims of this thesis were threefold. First, characterise the composition of the lithospheric mantle beneath the Sask Craton and to estimate the timing of craton formation. Second, examine the effects of mantle metasomatism on the Sask Craton lithospheric root. Third, identify the mode of diamond formation and to characterise the composition of the diamond forming fluid. A particular focus in this study was placed on the effects of the Trans Hudson Orogeny.

5.1 The lithospheric mantle beneath the Sask Craton

Based on a detailed petrological and geochemical characterisation of peridotite xenoliths (Chapter 2) from the Star and Orion South kimberlites from FALC, the composition of the garnet-stable lithospheric mantle beneath the Sask Craton is dominated by moderately depleted lherzolite. This is evident from their olivine Mg# (mean of 91.5), their dominantly lherzolitic garnet compositions (G9 and G11) and their moderately depleted PGE patterns. All eclogite xenoliths in this study (Chapter 3) have geochemical signatures consistent with subducted low-pressure protoliths. The composition of barren eclogites is overall gabbroic, indicating that their protoliths were derived from the lower portion of oceanic crust, while basaltic protoliths dominate the diamondiferous eclogite suite.

The calculated geotherm, using the FITPLOT approach on single clinopyroxene (n > 700) geothermobarometry, is cool and compares well with the 38 mW/m^2 reference geotherm of Hasterok and Chapman (2011). Overall this geotherm is similar to the PT conditions of the lithospheric root beneath the Slave Craton and conforms to a typical cratonic geothermal array. The geotherm reveals that the Sask Craton has a lithosphere thickness of ~210 km, resulting in a large "diamond window" of ~100 km. Sask Craton peridotite xenolith geothermobarometry overlaps well with the calculated geotherm (PT_{NT00}: 840 to 1250 °C and 2.7 to 5.5 GPa; T_{TA98} and P_{NG85}: 840 to 1190°C and 2.0 to 5.3 GPa). Similarly, Fe-Mg exchange temperatures and projected pressures for eclogite xenoliths are in good agreement with the geotherm, with

diamondiferous eclogites dominating the lower lithosphere (1180 – 1390 °C and 5.5-6.5 GPa). while barren eclogites are present throughout the lithospheric mantle (740 – 1300 °C and 3.2 – 6.1 GPa). Nitrogen-based time-averaged mantle residence temperatures for diamonds from FALC span the entire range of the FALC diamond window (1050 and 1360 °C).

Based on Re-Os chemistry obtained from olivine separates of peridotitic xenoliths (Chapter 2), the depletion and stabilisation of a lithospheric mantle root occurred in the Palaeoproterozoic between 2.5 and 1.7 Ga - not during the Archean, as commonly observed in other cratons, but in-keeping with the 2 Ga ages found for thick diamondiferous roots found beneath other Paleoproterozoic terranes in Canada (Liu *et al.*, in press). Younger Re-Os ages (< 1.1 Ga) obtained for the Sask Craton are interpreted to reflect reworking events, rather than additional material added to the craton. This also has important implications for diamond exploration, as the diamond formation is not restricted to Archean cratonic roots. Therefore, diamondiferous kimberlites from the Palaeoproterozoic Sask Craton present unconventional diamond deposits.

5.2 Effects of metasomatism

At FALC, mantle metasomatism is present in the form of modal metasomatism where the ascent of metasomatic fluids/melts is linked to the formation of diamond (Chapter 4), as well as cryptic metasomatism, which affected the chemical composition of both peridotitic and eclogitic minerals (Chapter 2 and 3). Mantle xenoliths from the Sask Craton report a complex metasomatic history. Mineral geochemistry, in particular trace elements in garnet (REE, Ti, Y, Zr) in peridotites reveal evidence for hydrous fluid metasomatism, as well as metasomatism by low volume silicate melts, such as kimberlites, or carbonatitic melts. Similarly, signatures indicative of both carbonatitic, and proto-kimberlitic metasomatism are identified in the diamondiferous eclogite xenoliths. In this suite, melt metasomatism caused strong chemical gradients (chemical zoning) within the garnets, even shifting their $\delta^{18}O$ values up to 1‰. The major metasomatic event responsible for chemical zonation in eclogitic garnets must have occurred in temporal proximity to kimberlite magmatism, as the diffusion rate in garnet operates rapidly (homogenisation in less than 200 years) at mantle temperatures. The presence of FALC diamonds is also evidence for mantle metasomatism. Cathodoluminescence images of some diamonds reveal complex growths (MC) and fracture systems (AG), indicating multiple stages of

diamond growth. The complex system of annealed fractures and rims surrounding individual diamonds - indicative of brecciation - is unique to diamonds from FALC. This brittle deformation is only identified in diamonds intergrown with zoned garnet, indicating that brecciation was associated with the same metasomatic event. Rapidly ascending melts, such as proto-kimberlites are attributed to the cause of the increase in differential stresses above the diapir, which result in brecciation, temporally linking the diamond fractures to the host kimberlite eruption. It is important to note that due to the complex nature of the metasomatic overprinting it is not possible to unequivocally constrain a metasomatic history or identify one type as the sole agent.

5.3 Diamond formation at FALC

The chemistry and formation history of FALC diamonds in mantle xenoliths are summarised in Chapter 4. The diamonds are commonly intergrown with eclogitic minerals, while peridotitic assemblages are less frequent. Morphologically and chemically the diamonds can be separated into three suites: monocrystalline, aggregate and polycrystalline diamonds. Based on their carbon and nitrogen characteristics, the majority of monocrystalline FALC diamonds likely crystallised from a mantle-derived fluid, while the diamond-forming agent for polycrystalline diamonds had a recycled origin. Diamond aggregates record a more complex origin indicative of a decoupling of nitrogen and carbon systematics, while variations of nitrogen isotope values at almost constant $\delta^{13}C$ could be the result of the presence of nitrogen bearing phases during diamond crystallization or the mixing of mantle-like and recycled nitrogen. At FALC the traditional model of wall rock buffered redox reactions is unlikely to apply, as carbon and nitrogen systematics are decoupled. Rather, diamond precipitation likely occurred during isochemical cooling of a CHO-rich fluid, which resulted in the supersaturation of carbon and subsequent diamond crystallisation.

5.4 The role of the Trans Hudson Orogeny

This thesis suggests that the Trans Hudson Orogeny played a major role in the formation and stabilisation of the lithospheric mantle beneath the Sask Craton. The main mode of Re-depletion ages obtained for the FALC peridotite xenoliths is Palaeoproterozoic, with most ages ranging

from 2.5 - 1.7 Ga. The oldest T_{RD} ages predate the Wilson cycle of the THO and may be the result of magmatic activity linked to the Mirond Lake Igneous Suite (2.45 Ga), or the Arrowsmith Orogeny (~2.5 – 2.3 Ga). The dominant timing of lithosphere formation is linked to the opening of Manikewan Ocean (~2.2 Ga - 2.0 Ga) and its subsequent closure during the Trans Hudson Orogeny (1.9 - 1.8 Ga). Even though no direct formation ages through radiometric dating have been obtained, FALC eclogite formation likely occurred during the Trans Hudson orogeny - the only known major thermo-tectonic event in this area - and its associated subduction of Manikewan oceanic crust. Further, considering that the majority of FALC diamonds in this study was extracted from eclogite hosts, diamond formation may also have occurred during the THO. A prediction from this model is that the eclogite ages should be similar to the main phase of lithosphere building.

5.5 Future directions

Until recently only a limited dataset existed from the lithospheric mantle of the Sask Craton. This thesis provides a new foundation for understanding the formation and evolution of the diamondiferous mantle root beneath the Sask Craton. Despite this, a number of questions remained unanswered, as they were beyond the scope of this study. Further research on mantle xenoliths and the diamond population of the Sask Craton is needed to better understand this unusual craton.

For one, the peridotite xenolith suite studied here is limited to the garnet stability field of the Sask SCLM. These samples cover the full range of the lithosphere where diamond is stable and therefore enabled me to assess this part of the mantle keel, while the upper lithospheric mantle remains unexplored. A study targeting spinel-bearing peridotite xenoliths suite could provide additional information on the composition of the Sask cratonic root and provide a more complete picture of the formation and evolution of the Sask Craton.

Among the questions remaining unanswered regarding the eclogite suite is the exact timing of eclogite formation. In this study, I only provided a broad timeframe for the formation of the FALC eclogites, as their age was inferred from regional tectonic events, rather than calculated using isotope geochemistry. Radiogenic isotope systems such as Rb-Sr, Sm-Nd, Pb-Pb, or Re-Os have previously been used to date eclogite xenoliths from other cratons (Jagoutz *et al.*, 1984;

Pearson *et al.*, 1995; Viljoen *et al.*, 1996; Jacob and Foley, 1999; Smit *et al.*, 2014a), and could provide a more precise age of eclogite emplacement. The model developed on the basis of the peridotite ages provides a clear framework for testing the eclogite ages; I would predict an overlap in the main mode in Re-Os ages, at 2.4 -1.7 Ga. Isotopic values from FALC eclogites could also offer additional insight into other processes affecting the eclogites, such as melt loss or metasomatic overprinting (Jacob, 2004 and references therein).

The FALC kimberlites are host to diamondiferous eclogite xenoliths that record intense metasomatism in combination with unique diamond brecciation patterns (Chapter 3 and 4), neither of which have previously been identified in any eclogitic suite. A systematic study of intensely metasomatised diamondiferous eclogite xenoliths, ideally samples from kimberlites that also sampled polymict breccias, or sheared peridotites, could potentially result in the identification of more brecciated diamonds. Although, it is possible that these intensely metasomatised eclogites recording diamond brecciation will remain unique to the FALC kimberlites.

All diamonds in this study constitute a sub-population of diamonds hosted in micro-xenoliths of dominantly eclogitic paragenesis, which constitute a unique sample set rather than run of mine production. To better assess the typical diamond population, systematic morphological and geochemical studies of macro- and micro-diamonds need to be carried out. None of the studied diamonds from FALC (Leahy and Taylor, 1997 and this study) contained mineral inclusions that could be characterised. Hence, the paragenesis of the FALC diamonds is still unknown. In addition, the quantitative study of fluid inclusions from the cloudy diamonds, in combination with further research on mineral inclusions, would provide additional information on the composition of diamond forming fluids crystallising the FALC diamonds. This would enable us to further characterise the diamond formation in this unusual cratonic setting and aid in our understanding of diamond formation.

In general, the mode of diamond formation in mantle rocks is still highly debated (e.g. Frost and McCammon, 2008; Sverjensky *et al.*, 2014; Stachel and Luth, 2015; Smith *et al.*, 2016). Further in-depth studies of the unique eclogite xenolith cross-cut by a diamond vein, as well as melt evolution modelling, in addition to experimental petrology trying to produce diamond veins,

could advance our understanding of diamond formation and fluid/melt – wall rock interaction during diamond precipitation.

References

Alabaster, T., Pearce, J. A. & Malpas, J. (1982). The volcanic stratigraphy and petrogenesis of the Oman ophiolite complex. *Contributions to Mineralogy and Petrology* **81**, 168–183.

Alard, O., Griffin, W. L., Lorand, J.-P., Jackson, S. E. & O'Reilly, S. Y. (2000). Non-chondritic distribution of the highly siderophile elements in mantle sulphides. *Nature* **407**, 891–894.

Ansdell, K. M. (2005). Tectonic evolution of the Manitoba-Saskatchewan segment of the Paleoproterozoic Trans-Hudson Orogen, Canada. *Canadian Journal of Earth Sciences* **42**, 741–759.

Ansdell, K. & Norman, A. (1995). U - Pb geochronology and tectonic development of the southern flank of the Kisseynew Domain, Trans-Hudson Orogen, Canada. *Precambrian Research* **72**, 147–167.

Armstrong, J. (1995). CITZAF: A package of correction programs for the quantitative electron microbeam X-ray-analysis of thick polished materials, thin-films, and particles. *Microbeam Analysis* **4**, 177–200.

Artyushkov, E. V. & Soboley, S. V. (1984). Physics of the kimberlite magmatism. In: J, K. (ed.) *Kimberlites I: Kimberlites and Related Rocks Proceedings of the Third International Kimberlite Conference*, 309–322.

Ashton, K., Heaman, L., Lewry, J., Hartlaub, R. P. & Shi, R. (1999). Age and origin of the Jan Lake Complex: A glimpse at the buried Archean craton of the Trans-Hudson Orogen. *Canadian Journal of Earth Sciences* **36**, 185–208.

Ashton, K. E., Lewry, J. F., Heaman, L. M., Hartlaub, R. P., Stauffer, M. R. & Tran, H. T. (2005). The Pelican Thrust Zone: Basal detachment between the Archean Sask Craton and Paleoproterozoic Flin Flon - Glennie Complex, western Trans-Hudson Orogen. *Canadian Journal of Earth Sciences* **42**, 685–706.

Aulbach, S., Griffin, W. L., O'Reilly, S. Y. & McCandless, T. E. (2004). Genesis and evolution of the lithospheric mantle beneath the Buffalo Head Terrane, Alberta (Canada). *Lithos* **77**, 413–451.

Aulbach, S., Pearson, N. J., O'Reilly, S. Y. & Doyle, B. J. (2007). Origins of xenolithic eclogites and pyroxenites from the Central Slave Craton, Canada. *Journal of Petrology* **48**, 1843–1873.

Aulbach, S., Mungall, J. E. & Pearson, D. G. (2016). Distribution and processing of highly siderophile elements in cratonic mantle lithosphere. *Reviews in Mineralogy and Geochemistry* **81**, 239–304.

Baertschi, P. (1976). Absolute 18O content of standard mean ocean water. *Earth and Planetary Science Letters* **31**, 341–344.

Bank, C., Bostock, M., Ellis, R., Hajnal, Z. & VanDecar, J. (1998). Lithospheric mantle structure beneath the Trans-Hudson Orogen and the origin of diamondiferous kimberlites. *Journal of Geophysical Research* **103**, 10103–10114.

Beard, B. L., Fraracci, K. N., Taylor, L. A., Snyder, G. A., Clayton, R. A., Mayeda, T. K. & Sobolev, N. V (1996). Petrography and geochemistry of eclogites from the Mir kimberlite, Yakutia, Russia. *Contributions to Mineralogy and Petrology* **125**, 293–310.

Benoit, M., Polvé, M. & Ceuleneer, G. (1996). Trace element and isotopic characterization of mafic cumulates in a fossil mantle diapir (Oman ophiolite). *Chemical Geology* **134**, 199–214.

Berman, R. G., Pehrsson, S., Davis, W. J., Ryan, J. J., Qui, H. & Ashton, K. E. (2013). The Arrowsmith orogeny: Geochronological and thermobarometric constraints on its extent and tectonic setting in the Rae craton, with implications for pre-Nuna supercontinent reconstruction. *Precambrian Research*. Elsevier B.V. **232**, 44–69.

Berryman, A. K., Scott Smith, B. H. & Jellicoe, B. C. (2004). Geology and diamond distribution of the 140/141 kimberlite, Fort à la Corne, central Saskatchewan, Canada. *Lithos* **76**, 99–114.

Bickford, M. E., Collerson, K. D., Lewry, J. F., Van Schmus, W. R. & Chiarenzelli, J. R. (1990). Proterozoic collisional tectonism in the Trans-Hudson orogen, Saskatchewan. *Geology* **18**, 14–18.

Bickford, M. E., Mock, T. D., Steinhart III, W. E., Collerson, K. D. & Lewry, J. F. (2005). Origin of the Archean Sask craton and its extent within the Trans-Hudson orogen: Evidence from Pb and Nd isotopic compositions of basement rocks and post-orogenic intrusions. *Canadian Journal of Earth Sciences* **42**, 659–684.

Bina, C. R. & Helffrich, G. (2014). Geophysical constraints on mantle composition. In: Holland, H. & Turekian, K. (eds) *Treatise on Geochemistry*. Elsevier, 41–65.

Boyd, F. R. (1989). Compositional distinction between oceanic and cratonic lithosphere. *Earth*

and Planetary Science Letters **96**, 15–26.

Boyd, F. R. & Gurney, J. J. (1986). Diamonds and the African lithosphere. *Science* **232**, 472–477.

Boyd, F. R., Pearson, D. G., Nixon, P. H. & Mertzman, S. A. (1993). Low Ca garnet harzburgites from Southern Africa: Their relation to cratonic structure and diamond crystallization. *Contributions to Mineralogy and Petrology* **113**, 352–366.

Boyd, F. R., Pearson, D. G., Hoal, K. O., Hoal, B. G., Nixon, P. H., Kingston, M. J. & Mertzman, S. A. (2004). Garnet lherzolites from Louwrensia, Namibia: Bulk composition and P/T relations. *Lithos* **77**, 573–592.

Brookes, E. J., Greenwood, P. & Xing, G. (1999). The plastic deformation and strain-induced fracture of natural and synthetic diamond. *Diamond and Related Materials* **8**, 1536–1539.

Bursill, L. A. & Glaisher, R. W. (1985). Aggregation and dissolution of small and extended defect structures in Type Ia diamond. *American Mineralogist* **70**, 608–618.

Canil, D. (1999). The Ni-in-garnet geothermometer: Calibration at natural abundances. *Contributions to Mineralogy and Petrology* **136**, 240–246.

Canil, D. (2008). Canada's craton: A bottoms-up view. *GSA Today* **18**, 4–10.

Canil, D., Schulze, D. J., Hall, D., Hearn Jr., B. C. & Milliken, S. M. (2003). Lithospheric roots beneath western Laurentia: the geochemical signal in mantle garnets. *Canadian Journal of Earth Sciences* **40**, 1027–1051.

Carlson, R. W., Pearson, D. G., Boyd, F. R., Shirey, S. B., Irvine, G., Menzies, A. H. & Gurney, J. J. (1999). Re-Os Systematics of Lithospheric Peridotites: Implications for Lithosphere Formation and Preservation. In: Gurney, J. J., Gurney, J. L., Pascoe, M. D. & Richardson, S. H. (eds) *7th International Kimberlite Conference*, 99–108.

Carlson, R. W., Pearson, D. G. & James, D. E. (2005). Physical , Chemical , and Chronological Characteristics of Continental Mantle. 1–24.

Cartigny, P. (2005). Stable isotopes and the origin of diamond. *Elements* **1**, 79–84.

Cartigny, P., Harris, J. W. & Javoy, M. (1998). Eclogitic diamond formation at Jwaneng: No room for a recycled component. *Science* **280**, 1421–1424.

Cartigny, P., Harris, J. & Javoy, M. (2001). Diamond genesis, mantle fractionations and mantle nitrogen content: A study of δ13 C–N concentrations in diamonds. *Earth and Planetary Science Letters* **185**, 85–98.

Cartigny, P., Chinn, I., Viljoen, K. S. & Robinson, D. (2004). Early Proterozoic ultrahigh pressure metamorphism: Evidence from microdiamonds. *Science* **304**, 853–855.

Chakhmouradian, A. R., Mumin, A. H., Demény, A. & Elliott, B. (2008). Postorogenic carbonatites at Eden Lake, Trans-Hudson Orogen (northern Manitoba, Canada): Geological setting, mineralogy and geochemistry. *Lithos* **103**, 503–526.

Chiarenzelli, J. (1989). The Nistowiak and Guncoat Gneisses: Implications for the tectonics of the Glennie and La Ronge domains, northern Saskatchewan, Canada. University of Kansas, Lawrence.

Chiarenzelli, J., Aspler, L., Villeneuve, M. & Lewry, J. (1998). Early Proterozoic evolution of the Saskatchewan Craton and its allochthonous cover, Trans-Hudson Orogen. *The Journal of Geology* **106**, 247–268.

Chrenko, R., McDonald, R. & Darrow, K. (1967). Infra-red spectra of diamond coat. *Nature* **213**, 474–476.

Clark, J. R. & Papike, J. J. (1968). Crystal-chemical characterization of omphacites. *The American Mineralogist* **53**, 840–868.

Clayton, R. N., Goldsmith, J. R., Karel, K. J., Mayeda, T. K. & Robert C., N. (1975). Limits on the effect of pressure on isotopic fractionation. *Geochimica et Cosmochimica Acta* **39**, 1197–1201.

Clifford, T. N. (1966). Tectono-metallogenic units and metallogenic provinces of Africa. *Earth and Planetary Science Letters* **1**, 421–434.

Coleman, R. G., Lee, D. E., Beatty, L. B. & Brannock, W. W. (1965). Eclogites and Eclogites: Their Differences and Similarities. *Geological Society Of America Bulletin* **76**, 483–508.

Collerson, K. D., Lewry, J. F., Schmus, R. W. Van & Bickford, M. E. (1989). Sm-Nd isotopic constraints on the age of the buried basement in Central and Southern Saskatchewan : implications for diamond exploration. *Summary of Investigations 1989. Saskatchewan Geol. Surv, Misc. Rep.* **89**, 168–171.

Collerson, K. D., Lewry, J. F., Bickford, M. E. & Van Schmus, W. R. (1990). Crustal evolution of the buried Precambrian of southern Saskatchewan: Implications for diamond exploration. In: Beck, L. S. & Harper, C. T. (eds) *Modern Exploration Techniques: Saskatchewan Geological Society*, 150–165.

Collins, A. T. (1982). A spectroscopic survey of naturally-occurring vacancy-related colour

centres in diamond. *Journal of Physics D: Applied Physics* **15**, 1431–1438.

Corrigan, D. (2012). Paleoproterozoic crustal evolution and tectonic processes: Insights from the Lithoprobe program in the Trans-Hudson Orogen, Canada. *Canadian Journal of Earth Sciences* 239–286.

Corrigan, D., Pehrsson, S., Wodicka, N. & de Kemp, E. (2009). The Palaeoproterozoic Trans-Hudson Orogen: a prototype of modern accretionary processes. *Geological Society, London, Special Publications* **327**, 457–479.

Creighton, S. & Read, G. H. (2013). Metasomatic overprinting of the lithospheric mantle of the Archean Sask Craton. *GAC-MAC*. Winnipeg.

Czas, J., Stachel, T., Pearson, D. G., Stern, R. A. & Read, G. H. (2018). Diamond brecciation and annealing accompanying major metasomatism in eclogite xenoliths from the Sask Craton, Canada. *Mineralogy and Petrology*. doi:10.1007/s00710-018-0590-y

Dalton, J. A. & Presnall, D. C. (1998). The Continuum of Primary Carbonatitic–Kimberlitic Melt Compositions in Equilibrium with Lherzolite: Data from the System CaO–MgO–Al2O3–SiO2–CO2 at 6 GPa. *Journal of Petrology* **39**, 1953–1964.

Davis, W. J., Stern, R. A. & Kjarsgaard, B. A. (1998). Geochronology of crustal xenoliths from Saskatchewan kimberlites; a glimpse at the buried Trans-Hudson Orogen. *Geological Society of America, 1998 Annual Meeting, Toronto, ON, Canada Oct. 26–29, Abstracts with Programs-Geological Society of America,* vol. 30; 7, 110.

Davis, W., Jones, A., Bleeker, W. & Grütter, H. (2003). Lithosphere development in the Slave craton: a linked crustal and mantle perspective. *Lithos* **71**, 575–589.

Davies, R. M., Griffin, W. L., O'Reilly, S. Y. & McCandless, T. E. (2004). Inclusions in diamonds from the K14 and K10 kimberlites, Buffalo Hills, Alberta, Canada: Diamond growth in a plume? *Lithos* **77**, 99–111.

Day, H. W. (2012). A revised diamond-graphite transition curve. *American Mineralogist* **97**, 52–62.

De Stefano, A., Kopylova, M. G., Cartigny, P. & Afanasiev, V. (2009). Diamonds and eclogites of the Jericho kimberlite (Northern Canada). *Contributions to Mineralogy and Petrology* **158**, 295–315.

de Wit, M. J., de Ronde, C. E. J., Tredoux, M., Roering, C., Hart, R. J., Armstrong, R. a., Green, R. W. E., Peberdy, E. & Hart, R. a. (1992). Formation of an Archaean continent. *Nature*

357, 553–562.

Deines, P. (1980). The carbon isotopic composition of diamonds: relationship to diamond shape, color, occurrence and vapor composition. *Geochimica et Cosmochimica Acta* **44**, 943–961.

Deines, P. (2002). The carbon isotope geochemistry of mantle xenoliths. *Earth-Science Reviews* **58**, 247–278.

Deines, P., Viljoen, F. & Harris, J. (2001). Implications of the carbon isotope and mineral inclusion record for the formation of diamonds in the mantle underlying a mobile belt: Venetia, South Africa. *Geochimica et Cosmochimica Acta* **65**, 813–838.

DeVries, R. C. (1975). Plastic deformation and "work-hardening" of diamond. *Materials Research Bulletin* **10**, 1193–1199.

Dijkstra, A. H., Dale, C. W., Oberthür, T., Nowell, G. M. & Graham Pearson, D. (2016). Osmium isotope compositions of detrital Os-rich alloys from the Rhine River provide evidence for a global late Mesoproterozoic mantle depletion event. *Earth and Planetary Science Letters*. Elsevier B.V. **452**, 115–122.

Dludla, S., le Roex, A. P. & Gurney, J. J. (2006). Eclogite xenoliths from the Premier kimberlite, South Africa: Geochemical evidence for a subduction origin. *South African Journal of Geology* **109**, 353–368.

Eggler, D. H., McCallum, M. E. & Kirkley, M. B. (1987). Kimberlite-transported nodules from Colorado-Wyoming; A record of enrichment of shallow portions of an infertile lithosphere. *Geological Society of America* 77–90.

Eiler, J. M. (2001). Oxygen isotope variations of basaltic lavas and upper mantle rocks. *Reviews in Mineralogy and Geochemistry* **43**, 319–364.

Ellis, R. M., Hajnal, Z. & Bostock, M. G. (1996). Seismic studies on the Trans-Hudson Orogen of western Canada. *Tectonophysics* **262**, 35–50.

Evans, T. & Wild, R. K. (1965). Plastic bending of diamond plates. *Philosophical Magazine* **12**, 479–489.

Evans, T. & Harris, J. (1989). Nitrogen aggregation, inclusion equilibration temperatures and the age of diamonds. In: Ross, J., Jaques, A., Ferguson, J., Green, D., O'Reilly, S., Danchin, R. & Janse, A. A. (eds) *Kimberlites and Related Rocks—Proceedings of the Fourth International Kimberlite Conference*. Sydney: Geological Society of Australia, 1001–1006.

Evans, T., Qi, Z. & Maguire, J. (1981). The stages of nitrogen aggregation in diamond. *Journal*

of Physics C: Solid State Physics **14**.

Evans, T., Kiflawi, I., Luyten, W., Tendeloo, G. V. & Woods, G. S. (1995). Conversion of Platelets into Dislocation Loops and Voidite Formation in Type IaB Diamonds. *Proceedings of the Royal Society A: Mathematical, Physical and Engineering Sciences* **449**, 295–313.

Farmer, V. (1974). *The Infrared Spectra of Minerals*. Londan: Mineralogical Society of Great Britain and Ireland.

Field, J. E. & Pickles, C. S. J. (1996). Strength, fracture and friction properties of diamond. *Diamond and Related Materials* **5**, 625–634.

Fisher, D. (2009). Brown diamonds and high pressure high temperature treatment. *Lithos*. Elsevier B.V. **112**, 619–624.

Foley, S. F. (2008). Rejuvenation and erosion of the cratonic lithosphere. *Nature Geoscience* **1**, 503–510.

Foley, S., Tiepolo, M. & Vannucci, R. (2002). Growth of early continental crust controlled by melting of amphibole in subduction zones. *Nature* **417**, 837–840.

Fortier, S. M. & Giletti, B. (1989). An empirical model for predicting diffusion coefficients in silicate minerals. *Science* **245**, 1481–1484.

Frost, D. J. & McCammon, C. A. (2008). The Redox State of Earth's Mantle. *Annu. Rev. Earth Planet. Sci* **36**, 389–420.

Gaillou, E., Post, J. E., Rose, T. & Butler, J. E. (2012). Cathodoluminescence of natural, plastically deformed pink diamonds. *Microscopy and Microanalysis* **18**, 1292–302.

Garlick, G. D., MacGregor, I. D. & Vogel, D. E. (1971). Oxygen isotope ratios in eclogites from kimberlites. *Science* **172**, 1025–1027.

Giuliani, A., Phillips, D., Kamenetsky, V. S., Kendrick, M. A., Wyatt, B. A., Goemann, K. & Hutchinson, G. (2014). Petrogenesis of Mantle Polymict Breccias: Insights into Mantle Processes Coeval with Kimberlite Magmatism. *Journal of Petrology* **55**, 831–858.

Goss, J. P., Briddon, P. R., Hill, V., Jones, R. & Rayson, M. J. (2014). Identification of the structure of the 3107 cm-1 H-related defect in diamond. *Journal of Physics Condensed Matter* **26**.

Graham, S., Lambert, D. D., Shee, S. R., Smith, C. B. & Reeves, S. (1999). Re-Os isotopic evidence for Archean lithospheric mantle beneath the Kimberley block, Western Australia.

Geology **27**, 431.

Gréau, Y., Huang, J. X., Griffin, W. L., Renac, C., Alard, O. & O'reilly, S. Y. (2011). Type I eclogites from Roberts Victor kimberlites: Products of extensive mantle metasomatism. *Geochimica et Cosmochimica Acta* **75**, 6927–6954.

Gregory, R. T. & Taylor, H. P. (1981). An oxygen isotope profile in a section of Cretaceous oceanic crust, Samail Ophiolite, Oman: Evidence for δ 18 O buffering of the oceans by deep (>5 km) seawater-hydrothermal circulation at mid-ocean ridges. *Journal of Geophysical Research: Solid Earth* **86**, 2737–2755.

Griffin, W. L. & Ryan, C. G. (1995). Trace elements in indicator minerals: area selection and target evaluation in diamond exploration. *Journal of Geochemical Exploration* **53**, 311–337.

Griffin, W. & Ryan, C. (1996). An experimental calibration of the "nickel in garnet" geothermometer with applications, by D. Canil: discussion. *Contributions to Mineralogy and Petrology* **124**, 216–218.

Griffin, W. L., Smith, D., Boyd, F. R., Cousens, D. R., Ryan, C. G., Sie, S. H. & Suter, G. F. (1989). Trace element zoning in garnets from sheared mantle xenoliths. *Geochimica et Cosmochimica Acta* **53**, 561–567.

Griffin, W., Sobolev, N., Ryan, C., Pokhilenko, N. P., Win, T. & Yefimova, E. (1993). Trace elements in garnets and chromites: diamond formation in the Siberian lithosphere. *Lithos* **29**, 235–256.

Griffin, W. L., Doyle, B. J., Ryan, C. G., Pearson, N. J., O'Reilly, S. Y., Davies, R., Kivi, K., Van Achterbergh, E. & Natapov, L. M. (1999a). Layered mantle lithosphere in the Lac de Gras area, Slave Craton: Composition, structure and origin. *Journal of Petrology* **40**, 705–727.

Griffin, W., O'Reilly, S. & Ryan, C. (1999b). The composition and origin of subcontinental lithospheric mantle. In: Fei, Y., Bertka, C. & Mysen, B. (eds) *Mantle Petrology: Field Observations and High Pressure Experimentation: A tribute to Francis R (Joe) Boyd, Special Publication No. 6.* Houston: The Geochemical Society, 13–45.

Griffin, W., Shee, S., Ryan, C., Win, T. & Wyatt, B. (1999c). Harzburgite to lherzolite and back again: metasomatic processes in ultramafic xenoliths from the Wesselton kimberlite, Kimberley, South Africa. *Contributions to Mineralogy and Petrology* **134**, 232–250.

Griffin, W. L., O'Reilly, S. Y., Doyle, B. J., Pearson, N. J., Coopersmith, H., Kivi, K.,

Malkovets, V. & Pokhilenko, N. (2004). Lithosphere mapping beneath the North American plate. *Lithos* **77**, 873–922.

Grütter, H. S. (2009). Pyroxene xenocryst geotherms: Techniques and application. *Lithos*. Elsevier B.V. **112**, 1167–1178.

Grütter, H. S., Gurney, J. J., Menzies, A. H. & Winter, F. (2004). An updated classification scheme for mantle-derived garnet, for use by diamond explorers. *Lithos* **77**, 841–857.

Guilhaumou, N., Sautter, V. & Dumas, P. (2005). Synchrotron FTIR microanalysis of volatiles in melt inclusions and exsolved particles in ultramafic deep-seated garnets. *Chemical Geology* **223**, 82–92.

Gurney, J. J. (1989). Diamonds. In: J. Ross et al., E. (ed.) *Kimberlites and Related Rocks—Proceedings of the Fourth International Kimberlite Conference*. Carlton: Blackwell, 935–965.

Gurney, J. J. & Boyd, F. R. (1982). Mineral intergrowths with polycrystalline diamonds from the Orapa Mine, Botswana. *Year Book - Carnegie Institution of Washington* **81**, 267–273.

Gurney, J. J., Helmstaedt, H. H., Richardson, S. H. & Shirey, S. B. (2010). Diamonds through time. *Economic Geology* **105**, 689–712.

Guthrie, G. D., Veblen, D. R., Navon, O. & Rossman, G. R. (1991). Submicrometer fluid inclusions in turbid-diamond coats. *Earth and Planetary Science Letters* **105**, 1–12.

Haggerty, S. E. (1986). Diamond genesis in a multiply-constrained model. *Nature* **320**, 34–38.

Hajnal, Z., Lewry, J., White, D., Ashton, K., Clowes, R., Stauffer, M., Gyorfi, I. & Takacs, E. (2005). The Sask Craton and Hearne Province margin: seismic reflection studies in the western Trans-Hudson Orogen. *Canadian Journal of Earth Sciences* **42**, 403–419.

Hammer, P., Clowes, R., Cook, F., Vasudevan, K. & van der Velden, A. (2011). The big picture: A lithospheric cross section of the North American continent. *GSA Today* **21**, 4–10.

Harte, B., Hunter, R. & Kinny, P. (1993). Melt geometry, movement and crystallization, in relation to mantle dykes, veins and metasomatism. *The Royal Society* **342**, 1–21.

Harvey, S., Kjarsgaard, B., McClintock, M., Shimell, M., Fourie, L., Plessis, P. Du & Read, G. (2009). Geology and evaluation strategy of the Star and Orion South kimberlites, Fort à la Corne, Canada. *Lithos*. Elsevier B.V. **112**, 47–60.

Hasterok, D. & Chapman, D. S. (2011). Heat production and geotherms for the continental lithosphere. *Earth and Planetary Science Letters*. Elsevier B.V. **307**, 59–70.

Hawthorne, J. B. (1975). Model of a kimberlite pipe. *Physics and Chemistry of the Earth* **9**.

Heaman, L. M., Kamo, S. L., Ashton, K. E., Reilly, B. A., Slimmon, W. L. & Thomas, D. J. (1992). U–Pb Geochronological Investigations in the Trans-Hudson Orogen, Saskatchewan. *Summary of Investigations 1992, Saskatchewan Geological Survey, Saskatchewan Energy and Mines, Miscellaneous Report* **92–4**, 120–123.

Heaman, L. M., Maxeiner, R. O. & Slimmon, W. L. (1994). U–Pb Geochronological Investigations in the Trans-Hudson Orogen, Saskatchewan. *Summary of Investigations 1994, Saskatchewan Geological Survey, Saskatchewan Energy and Mines, Miscellaneous Report* **92–4**, 96–99.

Heaman, L. M., Kjarsgaard, B. A. & Creaser, R. A. (2004). The temporal evolution of North American kimberlites. *Lithos* **76**, 377–397.

Heaman, L. M., Peck, D. & Toope, K. (2009). Timing and geochemistry of 1.88 Ga Molson Igneous Events, Manitoba: Insights into the formation of a craton-scale magmatic and metallogenic province. *Precambrian Research* **172**, 143–162.

Heaman, L. M. & Pearson, D. G. (2010). Nature and evolution of the Slave Province subcontinental lithospheric mantle. *Canadian Journal of Earth Sciences* **47**, 369–388.

Helmstaedt, H. & Doig, R. (1975). Eclogite nodules from kimberlite pipes of the Colorado Plateau—samples of subducted Franciscan-type oceanic lithosphere. *Physics and Chemistry of the Earth* **9**, 95–111.

Hoal, K., Hoal, B., Erlank, A. & Shimizu, N. (1994). Metasomatism of the mantle lithosphere recorded by rare earth elements in garnets. *Earth and Planetary Science Letters* **126**, 303–313.

Hoffman, P. F. (1988). United Plates of America, the Birth of a Craton: Early Proterozoic Assembly and Growth of Laurentia. *Annual Review of Earth and Planetary Sciences* **16**, 543–603.

Hogberg, K., Stachel, T. & Stern, R. A. (2016). Carbon and nitrogen isotope systematics in diamond: Different sensitivities to isotopic fractionation or a decoupled origin? *Lithos*. Elsevier B.V. **265**, 16–30.

Howell, D., O'Neill, C. J., Grant, K. J., Griffin, W. L., O'Reilly, S. Y., Pearson, N. J., Stern, R. A. & Stachel, T. (2012a). Platelet development in cuboid diamonds: Insights from micro-FTIR mapping. *Contributions to Mineralogy and Petrology* **164**, 1011–1025.

Howell, D., O'Neill, C. J., Grant, K. J., Griffin, W. L., Pearson, N. J. & O'Reilly, S. Y. (2012b). μ-FTIR mapping: Distribution of impurities in different types of diamond growth. *Diamond and Related Materials* **29**, 29–36.

Howell, D., Piazolo, S., Dobson, D. P., Wood, I. G., Jones, A. P., Walte, N., Frost, D. J., Fisher, D. & Griffin, W. L. (2012c). Quantitative characterization of plastic deformation of single diamond crystals: A high pressure high temperature (HPHT) experimental deformation study combined with electron backscatter diffraction (EBSD). *Diamond and Related Materials* **30**, 20–30.

Howell, D., Fisher, D., Piazolo, S., Griffin, W. L. & Sibley, S. J. (2015). Pink color in Type I diamonds: Is deformation twinning the cause? *American Mineralogist* **100**, 1518–1527.

Huang, J. X., Gréau, Y., Griffin, W. L., O'Reilly, S. Y. & Pearson, N. J. (2012). Multi-stage origin of Roberts Victor eclogites: Progressive metasomatism and its isotopic effects. *Lithos* **142–143**, 161–181.

Ickert, R. B. & Stern, R. A. (2013). Matrix corrections and error analysis in high-precision SIMS 18O/16O measurements of Ca-Mg-Fe garnet. *Geostandards and Geoanalytical Research* **37**, 429–448.

Ickert, R. B., Stachel, T., Stern, R. A. & Harris, J. W. (2013). Diamond from recycled crustal carbon documented by coupled δ18O-δ13C measurements of diamonds and their inclusions. *Earth and Planetary Science Letters*. Elsevier **364**, 85–97.

Ionov, D. a., Carlson, R. W., Doucet, L. S., Golovin, A. V. & Oleinikov, O. B. (2015). The age and history of the lithospheric mantle of the Siberian craton: Re–Os and PGE study of peridotite xenoliths from the Obnazhennaya kimberlite. *Earth and Planetary Science Letters*. Elsevier B.V. **428**, 108–119.

Jacob, D. E. (2004). Nature and origin of eclogite xenoliths from kimberlites. *Lithos* **77**, 295–316.

Jacob, D. E. & Foley, S. F. (1999). Evidence for Archean ocean crust with low high field strength element signature from diamondiferous eclogite xenoliths. *Lithos* **48**, 317–336.

Jacob, D., Jagoutz, E., Lowry, D., Mattey, D. & Kudrjavtseva, G. (1994). Diamondiferous eclogites from Siberia: Remnants of Archean oceanic crust. *Geochimica et Cosmochimica Acta* **58**, 5191–5207.

Jacob, D. E., Viljoen, K. S., Grassineau, N. V. & Jagoutz, E. (2000). Remobilization in the

Cratonic Lithosphere Recorded in Polycrystalline Diamond. *Science* **289**, 1182–1185.

Jacob, D. E., Viljoen, K. S. & Grassineau, N. V. (2009). Eclogite xenoliths from Kimberley, South Africa — A case study of mantle metasomatism in eclogites. *Lithos* **112**, 1002–1013.

Jagoutz, E., Dawson, J. B., Hoernes, S., Spettel, B. & Wanke, H. (1984). Anorthositic oceanic crust in the Archean Earth. *Lunar and Planetary Science* **15**, 395–396.

Janse, A. J. A. (1994). Is Clifford's rule still valid? Affirmative examples from around the world. In: Meyer, H. & Leonardos, O. (eds) *Diamonds: characterization, genesis and exploration*. Brasilia: CPRM Special Publication, 215–235.

Jaques, A. L., O'Neill, H. S. C., Smith, C. B., Moon, J. & Chappell, B. W. (1990). Diamondiferous peridotite xenoliths from the Argyle (AK1) lamproite pipe, Western Australia. *Contributions to Mineralogy and Petrology* **104**, 255–276.

Javoy, M., Pineau, F. & Delorme, H. (1986). Carbon and nitrogen isotopes in the mantle. *Chemical Geology* **57**, 41–62.

Jellicoe, R. B., Robertshaw, P., Williamson, P. & Murphy, J. (1998). Summary of exploration activities and results for the Fort à la Corne diamond project, Saskatchewan. *Summary of Investigations 1998, Saskatchewan Geological Survey, Sask. Energy Mines Misc. Report 98-4* 144–157.

Jerde, E. A., Taylor, L. A., Crozaz, G., Sobolev, N. V. & Sobolev, V. N. (1993). Diamondiferous eclogites from Yakutia, Siberia: evidence for a diversity of protoliths. *Contributions to Mineralogy and Petrology* **114**, 189–202.

Jordan, T. H. (1975). The continental tectosphere. *Reviews of Geophysics* **13**, 1.

Jordan, T.H. (1988). Structure and formation of the continental tectosphere. *Journal of Petrology* **1**, 11–37.

Kargin, A. V., Sazonova, L. V., Nosova, A. A. & Tretyachenko, V. V. (2016). Composition of garnet and clinopyroxene in peridotite xenoliths from the Grib kimberlite pipe, Arkhangelsk diamond province, Russia: Evidence for mantle metasomatism associated with kimberlite melts. *Lithos*. Elsevier B.V. **262**, 442–455.

Kennedy, W. Q. (1964). The structural differentiation of Africa in the Pan-African (+or-500 m.y.) tectonic episode. *Research Institute of African Geology, 8th Annual Report* **8**, 48–49.

Kjarsgaard, B. A. (2007). Kimberlite diamond deposits. In: Goodfellow, W. D. (ed.) *Mineral Deposists of Canada: A Synthesis of Major Deposit-Types, District Metallogeny, the*

Evolution of Geological Provinces, and Exploration Methods. Geological Association of Canada, Mineral Deposits Division, Special Publication, 245–272.

Kjarsgaard, B. A. & Levinson, A. A. (2002). Diamonds in Canada. *Gems & Gemology* **38**, 208–238.

Kjarsgaard, B. A., Harvey, S., McClintock, M., Zonneveld, J. P., Du Plessis, P., McNeil, D. & Heaman, L. (2009). Geology of the Orion South kimberlite, Fort à la Corne, Canada. *Lithos*. Elsevier B.V. **112**, 600–617.

Kjarsgaard, B. A., Heaman, L. M., Sarkar, C. & Pearson, D. G. (2017). The North America mid-Cretaceous kimberlite corridor: Wet, edge-driven decompression melting of an OIB-type deep mantle source. *Geochemistry, Geophysics, Geosystems* **18**, 2727–2747.

Kopylova, M. G., Russell, J. K. & Cookenboo, H. (1999). Petrology of peridotite and pyroxenite xenoliths from the Jericho kimberlite: implications for the thermal state of the mantle beneath the Slave craton, northern Canada. *Journal of Petrology* **40**, 79–104.

Kopylova, M., Navon, O., Dubrovinsky, L. & Khachatryan, G. (2010). Carbonatitic mineralogy of natural diamond-forming fluids. *Earth and Planetary Science Letters*. Elsevier B.V. **291**, 126–137.

Korolyuk, V. N. & Lepezin, G. G. (2008). Analysis of experimental data on the diffusion coefficients of Fe, Mn, Mg, and Ca in garnets. *Russian Geology and Geophysics* **49**, 557–569.

Krogh, E. J. (1988). The garnet-clinopyroxene Fe-Mg geothermometer - a reinterpretation of existing experimental data. *Contributions to Mineralogy and Petrology* **99**, 44–48.

Kurat, G. & Dobosi, G. (2000). Garnet and diopside-bearing diamondites (framesites). *Mineralogy and Petrology* **69**, 143–159.

Lang, A. R. (1967). Causes of Birefringence in Diamond. *Nature* **213**, 248–251.

Lawless, P. J., Gurney, J. J. & Dawson, J. B. (1979). Polymict Peridotites from the Bultfontein and de Beers Mines, Kimberly, South Africa. In: Boyd, F. R. & Meyer, H. O. A. (eds) *The Mantle Sample: Inclusions in Kimberlites and Other Volcanics.* American Geophysical Union, Washington, DC, 144–155.

Leahy, K. (1997). Discrimination of reworked pyroclastics from primary tephra-fall tuffs: a case study using kimberlites of Fort a la Corne, Saskatchewan, Canada. *Bulletin of Volcanology* **59**, 65–71.

Leahy, K. & Taylor, W. R. (1997). The influence of the Glennie domain deep structure on the diamonds in Saskatchewan kimberlites. *Russian Geology and Geophysics* **38**, 451–460.

Leckie, D. A., Kjarsgaard, B. A., Bloch, J., McIntyre, D., McNeil, D., Stasiuk, L. & Heaman, L. (1997). Emplacement and reworking of Cretaceous, diamond-bearing, crater facies kimberlite of central Saskatchewan, Canada. *Geological Society of America Bulletin* **109**, 1000–1020.

Lefebvre, N. & Kurszlaukis, S. (2008). Contrasting eruption styles of the 147 Kimberlite, Fort à la Corne, Saskatchewan, Canada. *Journal of Volcanology and Geothermal Research* **174**, 171–185.

Lehnert-Thiel, K., Loewer, R., Orr, R. G. & Robertshaw, P. (1992). Diamond-bearing kimberlites in Saskatchewan, Canada: The Fort à la Corne case history. *Exploration and Mining Geology* **1**, 391–403.

Leroux, D., Roy, W., van Niekerk, L., Wilkie, G. & McGarry, L. (2018). *Preliminary economic assessment of the Star - Orion South diamond project, Fort a la Corne, Saskatchewan*. .

Lewry, J., Hajnal, Z., Green, A., Lucas, S., White, D., Stauffer, M. R., Ashton, K. E., Weber, W. & Clowes, R. (1994). Structure of a Paleoproterozoic continent-continent collision zone: a LITHOPROBE seismic reflection profile across the Trans-Hudson Orogen, Canada. *Tectonophysics* **232**, 143–160.

Lindner, M., Leich, D. A., Price Russ, G., Bazan, J. M. & Borg, R. J. (1989). Direct determination of the half-life of ^{187}Re. *Geochimica et Cosmochimica Acta* **53**, 1597–1606.

Liu, J., Riches, A. J. V., Pearson, D. G., Luo, Y., Kienlen, B., Kjarsgaard, B. A., Stachel, T. & Armstrong, J. P. (2016). Age and evolution of the deep continental root beneath the central Rae craton, northern Canada. *Precambrian Research*. Elsevier B.V. **272**, 168–184.

Liu, J., Brin, L., Pearson, D. G., Bretschneider, L., Luguet, A., Acken, D. van, Kjarsgaard, B., Riches, A. & Mišković, A. (2018 – in press). Diamondiferous Proterozoic mantle roots beneath Arctic Canada: A study of mantle xenoliths from Parry Peninsula and Central Victoria Island. *Geochimica et Cosmochimica Acta*.

Lorand, J. P., Alard, O. & Luguet, A. (2010). Platinum-group element micronuggets and refertilization process in Lherz orogenic peridotite (northeastern Pyrenees, France). *Earth and Planetary Science Letters*. Elsevier B.V. **289**, 298–310.

Lucas, S., Green, A., Hajnal, Z., White, D., Lewry, J., Ashton, K., Weber, W. & Clowes, R.

(1993). Deep seismic profile across a Proterozoic collision zone: surprises at depth. *Nature* **363**, 339–342.

Lucas, S. *et al.* (1994). Three-dimensional collisional structure of the Trans-Hudson Orogen, Canada. *Tectonophysics* **232**, 161–178.

Luguet, A., Nowell, G. M. & Pearson, D. G. (2008). 184Os/188Os and 186Os/188Os measurements by Negative Thermal Ionisation Mass Spectrometry (N-TIMS): Effects of interfering element and mass fractionation corrections on data accuracy and precision. *Chemical Geology* **248**, 342–362.

Luguet, A., Jaques, A. L., Pearson, D. G., Smith, C. B., Bulanova, G. P., Roffey, S. L., Rayner, M. J. & Lorand, J.-P. (2009). An integrated petrological, geochemical and Re–Os isotope study of peridotite xenoliths from the Argyle lamproite, Western Australia and implications for cratonic diamond occurrences. *Lithos*. Elsevier B.V. **112**, 1096–1108.

Luth, R. (1993). Diamonds, eclogites, and the oxidation state of the Earth's mantle. *Science* **261**, 66–68.

Luth, R. (2017). Diamond formation in the Earth's mantle. *Geological Society of America Annual Meeting*. Seattle, Washington, Final Paper Number 20-6.

Luth, R. W. & Stachel, T. (2014). The buffering capacity of lithospheric mantle: implications for diamond formation. *Contributions to Mineralogy and Petrology* **168**, 1–12.

MacGregor, I. D. & Carter, J. L. (1970). The chemistry of clinopyroxenes and garnets of eclogite and peridotite xenoliths from the Roberts Victor mine, South Africa. *Physics of the Earth and Planetary Interiors* **3**, 391–397.

MacGregor, I. D. & Manton, W. I. (1986). Roberts victor eclogites: Ancient oceanic crust. *Journal of Geophysical Research* **91**, 14063.

Mather, K. A., Pearson, D. G., McKenzie, D., Kjarsgaard, B. A. & Priestley, K. (2011). Constraints on the depth and thermal history of cratonic lithosphere from peridotite xenoliths, xenocrysts and seismology. *Lithos*. Elsevier B.V. **125**, 729–742.

McDade, P. & Harte, B. (2000). Roberts Victor Eclogites with a Spinel-Facies Mantle Signature. *Goldschmidt 2000 Journal of Conference Abstracts* **5**, 690.

McDonough, W. F. (1991). Partial melting of subducted oceanic crust and isolation of its residual eclogitic lithology. *Philosophical Transactions of the Royal Society of London. Series A: Physical and Engineering Sciences*, 407–418.

McDonough, W. F. & Sun, S.-S. (1995). The composition of the Earth. *Chemical Geology* **120**, 223–253.

McKenzie, D. & Bickle, M. J. (1988). The volume and composition of melt generated by extension of the lithosphere. *Journal of Petrology* **29**, 625–679.

Menzies, M. A., Rogers, N., Tindle, A. & Hawkesworth, C. J. (1987). Metasomatic and enrichment processes in lithospheric peridotites, an effect of asthenosphere-lithosphere interaction. In: Menzies, M. A. & Hawkesworth, C. J. (eds) *Mantle Metasomatism*. London: Academic Press, 313–364.

Mercier, J.-C. C. (1979). Peridotite xenoliths and the dynamics of kimberlite intrusion. In: Boyd, F. R. & Meyer, H. (eds) *The Mantle Sample: Inclusion in Kimberlites and Other Volcanics*. Washington, D. C.: American Geophysical Union, 197–212.

Merry, M. & le Roex, A. (2007). Megacryst suites from the Lekkerfontein and Uintjiesberg kimberlites, southern Africa: Evidence for a non-cognate origin. *South African Journal of Geology* **110**, 597–610.

Meyer, H. & Boyd, F. (1972). Composition and origin of crystalline inclusions in natural diamonds. *Geochimica et Cosmochimica Acta* **86**, 1255–1273.

Mikhail, S., Verchovsky, A. B., Howell, D., Hutchison, M. T., Southworth, R., Thomson, A. R., Warburton, P., Jones, A. P. & Milledge, H. J. (2014). Constraining the internal variability of the stable isotopes of carbon and nitrogen within mantle diamonds. *Chemical Geology*. Elsevier B.V. **366**, 14–23.

Mitchell, R. H. (1995). *Kimberlites, Orangeites and Related Rocks*. New York: Plenum.

Moore, A. E. & Lock, N. P. (2001). The origin of mantle-derived megacrysts and sheared peridotites-evidence from kimberlites in the northern Lesotho - Orange Free State (South Africa) and Botswana pipe clusters. *South African Journal of Geology* **104**, 23–38.

Muehlenbachs, K. & Clayton, R. N. (1976). Oxygen isotope composition of the oceanic crust and its bearing on seawater. *Journal of Geophysical Research* **81**, 4365.

Mungall, J. & Brenan, J. (2014). Partitioning of platinum-group elements and Au between sulfide liquid and basalt and the origins of mantle-crust fractionation of the chalcophile elements. *Geochimica et Cosmochimica Acta*. Elsevier Ltd **125**, 265–289.

Navon, O., Hutcheon, I. D., Rossman, G. R. & Wasserburg, G. J. (1988). Mantle-derived fluids in diamond micro-inclusions. *Nature*, 784–789.

Németh, B., Clowes, R. & Hajnal, Z. (2005). Lithospheric structure of the Trans-Hudson Orogen from seismic refraction-wide-angle reflection studies. *Canadian Journal of Earth Sciences* **42**, 435–456.

Nickel, K. G. & Green, D. H. (1985). Empirical geothermobarometry for garnet peridotites and implications for the nature of the lithosphere, kimberlites and diamonds. *Earth and Planetary Science Letters* **73**, 158–170.

Nimis, P. & Taylor, W. R. (2000). Single clinopyroxene thermobarometry for garnet peridotites. Part I. Calibration and testing of a Cr-in-Cpx barometer and an enstatite-in-Cpx thermometer. *Contributions to Mineralogy and Petrology* **139**, 541–554.

Nimis, P. & Grütter, H. (2010). Internally consistent geothermometers for garnet peridotites and pyroxenites. *Contributions to Mineralogy and Petrology* **159**, 411–427.

O'Hara, M. J. & Yoder, H. S. (1967). Formation and fractionation of basic magmas at high pressures. *Scottish Journal of Geology* **3**, 67–117.

Olson, D. W. (2015). 2013 Minerals Yearbook - Diamond, Industrial. *U.S. Geological Survey* 21.1-21.12.

Pallister, J. S. & Knight, R. J. (1981). Rare-earth element geochemistry of the Samail Ophiolite near Ibra, Oman. *Journal of Geophysical Research: Solid Earth* **86**, 2673–2697.

Palme, H. & O'Neill, H. S. C. (2003). Cosmochemical estimates of mantle composition BT - Treatise on Geochemistry. *Treatise on Geochemistry* **2**, 1–38.

Pearson, D. G. (1999). The age of continental roots. *Lithos* **48**, 171–194.

Pearson, D. G & Woodland, S. (2000). Solvent extraction/anion exchange separation and determination of PGEs (Os, Ir, Pt, Pd, Ru) and Re–Os isotopes in geological samples by isotope dilution ICP-MS. *Chemical Geology* **165**, 87–107.

Pearson, D. G & Wittig, N. (2008). Formation of Archaean continental lithosphere and its diamonds: the root of the problem. *Journal of the Geological Society* **165**, 895–914.

Pearson, D. G., Snyder, G. A., Shirey, S. B., Taylor, L., Carlson, R. W. & Sobolev, N. V. (1995). Archean Re-Os age for Siberian eclogites and constraints on Archean tectonics. *Nature* **374**, 711–713.

Pearson, D. G. & Nixon, P. H. (1996). Diamonds in young orogenic belts: graphitised diamonds from Beni Bousera, N. Morocco, a comparison with kimberlite-derived diamond occurences and implications for diamond genesis and exploration. *African Geoscience Review* **3**, 295–

316.

Pearson, D. G., Shirey, S. B., Bulanova, G. P., Carlson, R. W. & Mllledge, H. J. (1999). Re-Os isotope measurements of single sulfide inclusions in a Siberian diamond and its nitrogen aggregation systematics. *Geochimica et Cosmochimica Acta* **63**, 703–711.

Pearson, D. G., Irvine, G. J., Carlson, R. W., Kopylova, M. G. & Ionov, D. A. (2002). The development of lithospheric keels beneath the earliest continents: time constraints using PGE and Re-Os isotope systematics. *The Early Earth: Physical, Chemical and Biological Development*. The Geological Society of London **199**, 65–90.

Pearson, D. G, Canil, D. & Shirey, S. (2003). Mantle samples included in volcanic rocks: xenoliths and diamonds. *Treatise On Geochemistry* **2**, 171–275.

Pearson, D. G., Irvine, G. J., Ionov, D. A., Boyd, F. R. & Dreibus, G. E. (2004). Re–Os isotope systematics and platinum group element fractionation during mantle melt extraction: a study of massif and xenolith peridotite suites. *Chemical Geology* **208**, 29–59.

Pearson, D. G., Parman, S. W. & Nowell, G. M. (2007). A link between large mantle melting events and continent growth seen in osmium isotopes. *Nature* **449**, 202–5.

Pearson, D. G., Canil, D. & Shirey, S. B. (2014). Mantle Samples Included in Volcanic Rocks. In: Holland, H. & Turekian, K. (eds) *Treatise on Geochemistry*. Elsevier, 169–253.

Peats, J., Stachel, T., Stern, R. A., Muehlenbachs, K. & Armstrong, J. (2012). Aviat diamonds: A window into the deep lithospheric mantle beneath the northern Churchill Province, Melville Peninsula, Canada. *Canadian Mineralogist* **50**, 611–624.

Pernet-Fisher, J. F., Howarth, G. H., Pearson, D. G., Woodland, S., Barry, P. H., Pokhilenko, N. P., Pokhilenko, L. N., Agashev, A. M. & Taylor, L. A. (2015). Plume impingement on the Siberian SCLM: Evidence from Re-Os isotope systematics. *Lithos*. Elsevier B.V. **218–219**, 141–154.

Phaal, C. (1964). Plastic deformation of diamond. *The Philosophical Magazine: A Journal of Theoretical Experimental and Applied Physics* **10**, 887–891.

Phillips, W. J. (1972). Hydraulic fracturing and mineralization. *Journal of the Geological Society* **128**, 337–359.

Pittari, A., Cas, R. A. F., Lefebvre, N., Robey, J., Kurszlaukis, S. & Webb, K. (2008). Eruption processes and facies architecture of the Orion Central kimberlite volcanic complex, Fort à la Corne, Saskatchewan; kimberlite mass flow deposits in a sedimentary basin. *Journal of*

Volcanology and Geothermal Research **174**, 152–170.

Presnall, D. C., Gudfinnsson, G. H. & Walter, M. J. (2002). Generation of mid-ocean ridge basalts at pressures from 1 to 7 GPa. *Geochimica et Cosmochimica Acta* **66**, 2073–2090.

Ramsay, R. R. & Tompkins, L. A. (1994). The geology, heavy mineral concentrate mineralogy, and diamond propectivity of the Boa Esperanca and Cana Verde pipes, Corrego D'anta, Minas Gerais, Brasil. *Fifth International Kimberlite Conference, Minas Gerais, Brazil. Vol. 1B Minas Gerais, Brazil: Companhia de Pesquisa de Recursos Minerais, Special Publication*, 329–345.

Rayner, N. M., Stern, R. A. & Bickford, M. E. (2005). Tectonic implications of new SHRIMP and TIMS U-Pb geochronology of rocks from the Sask Craton, Peter Lake Domain, and Hearne margin, Trans-Hudson Orogen, Saskatchewan. *Canadian Journal of Earth Sciences* **42**, 635–657.

Read, G. H. & Janse, A. J. A. (2009). Diamonds: Exploration, mines and marketing. *The Global Diamond Industry: Economics and Development Volume I*. Elsevier B.V. 71–94.

Rege, S., Griffin, W. L., Kurat, G., Jackson, S. E., Pearson, N. J. & O'Reilly, S. Y. (2008). Trace-element geochemistry of diamondite: Crystallisation of diamond from kimberlite–carbonatite melts. *Lithos* **106**, 39–54.

Rehkämper, M., Halliday, A. N., Alt, J., Fitton, J. G., Zipfel, J. & Takazawa, E. (1999). Non-chondritic platinum-group element ratios in oceanic mantle lithosphere: Petrogenetic signature of melt percolation? *Earth and Planetary Science Letters* **172**, 65–81.

Richardson, S. H., Gurney, J. J., Erlank, A. J. & Harris, J. W. (1984). Origin of diamonds in old enriched mantle. *Nature* **310**, 198–202.

Riches, A. J. V., Ickert, R. B., Pearson, D. G., Stern, R. A., Jackson, S. E., Ishikawa, A., Kjarsgaard, B. A. & Gurney, J. J. (2016). In situ oxygen-isotope, major-, and trace-element constraints on the metasomatic modification and crustal origin of a diamondiferous eclogite from Roberts Victor, Kaapvaal Craton. *Geochimica et Cosmochimica Acta*. Elsevier Ltd **174**, 345–359.

Ringwood, A. E. (1975). *Composition and Petrology of the Earth's Mantle*. McGraw-Hill Inc.

Rudnick, R. L., McDonough, W. F. & Chappell, B. W. (1993). Carbonatite metasomatism in the northern Tanzanian mantle: petrographic and geochemical characteristics. *Earth and Planetary Science Letters* **114**, 463–475.

Rudnick, R. L. & Walker, R. J. (2009). Interpreting ages from Re-Os isotopes in peridotites. *Lithos*. Elsevier B.V. **112**, 1083–1095.

Schaeffer, A. J. & Lebedev, S. (2014). Imaging the North American continent using waveform inversion of global and USArray data. *Earth and Planetary Science Letters*. Elsevier B.V. **402**, 26–41.

Schrauder, M. & Navon, O. (1993). Solid carbon dioxide in a natural diamond. *Nature* **365**, 42–44.

Schulze, D. J. (1989). Constraints on the abundance of eclogite in the upper mantle. *Journal of Geophysical Research: Solid Earth* **94**, 4205–4212.

Scully, K. R., Canil, D. & Schulze, D. J. (2004). The lithospheric mantle of the Archean Superior Province as imaged by garnet xenocryst geochemistry. *Chemical Geology* **207**, 189–221.

Shanks, W. C. (2001). Stable isotopes in seafloor hydrothermal systems. *Reviews in Mineralogy and Geochemistry* **43**, 469–526.

Shimizu, N. & Richardson, S. H. (1987). Trace elemept abundance patterns of garnet inclusions in peridotite-suite diamonds. *Geochimica et Cosmochimica Acta* **51**, 755–758.

Shirey, S. & Walker, R. (1998). The Re-Os isotope system in cosmochemistry and high-temperature geochemistry. *Annual Review of Earth and Planetary Sciences* **26**, 423–500.

Shu, Q. & Brey, G. P. (2015). Ancient mantle metasomatism recorded in subcalcic garnet xenocrysts: Temporal links between mantle metasomatism, diamond growth and crustal tectonomagmatism. *Earth and Planetary Science Letters*. Elsevier B.V. **418**, 27–39.

Shu, Q., Brey, G. P., Gerdes, A. & Hoefer, H. E. (2013). Geochronological and geochemical constraints on the formation and evolution of the mantle underneath the Kaapvaal craton: Lu–Hf and Sm–Nd systematics of subcalcic garnets from highly depleted peridotites. *Geochimica et Cosmochimica Acta*. Elsevier Ltd **113**, 1–20.

Sibson, R. H. (1977). Fault rocks and fault mechanisms. *Journal of the Geological Society* **133**, 191–213.

Sillitoe, R. H. & Sawkins, F. J. (1971). Geologic, Mineralogic and Fluid Inclusion Studies Relating to the Origin of Copper-bearing Tourmaline Breccia Pipes, Chile. *Economic Geology* **66**, 1028–1041.

Smit, K. V., Stachel, T., Creaser, R. A., Ickert, R. B., DuFrane, S. A., Stern, R. A. & Seller, M. (2014a). Origin of eclogite and pyroxenite xenoliths from the Victor kimberlite, Canada,

and implications for Superior craton formation. *Geochimica et Cosmochimica Acta*. Elsevier Ltd **125**, 308–337.

Smit, K. V., Pearson, D. G., Stachel, T. & Seller, M. (2014b). Peridotites from Attawapiskat, Canada: Mesoproterozoic Reworking of Palaeoarchaean Lithospheric Mantle beneath the Northern Superior Superterrane. *Journal of Petrology* **55**, 1829–1863.

Smith, E. M., Kopylova, M. G. & Peck, W. (2014). Implications of metallic iron for diamonds and nitrogen in the sublithospheric mantle. *Canadian Journal of Earth Sciences* **51**, 510–516.

Smith, E. M., Shirey, S. B., Nestola, F., Bullock, E. S., Wang, J., Richardson, S. H. & Wang, W. (2016). Large gem diamonds from metallic liquid in Earth's deep mantle. *Science* **354**, 1403–1405.

Snow, J. E. & Reisberg, L. (1995). Os isotopic systematics of the MORB mantle: results from altered abyssal peridotites. *Earth and Planetary Science Letters* **133**, 411–421.

Snyder, D. B., Humphreys, E. & Pearson, D. G. (2017). Construction and destruction of some North American cratons. *Tectonophysics*. Elsevier B.V. **694**, 464–485.

Sobolev, E. V., Lenskaya, S. V. & Lisoivan, V. I. (1969). Lamellar formations in the structure of natural diamonds. *Journal of Structural Chemistry* **9**, 917–920.

Sobolev, N. V., Lavrent'ev, Y. G., Pokhilenko, N. P. & Usova, L. V. (1973). Chrome-rich garnets from the kimberlites of Yakutia and their parageneses. *Contributions to Mineralogy and Petrology* **40**, 39–52.

Sobolev, N. V., Shatsky, V. S., Zedgenizov, D. A., Ragozin, A. L. & Reutsky, V. N. (2016). Polycrystalline diamond aggregates from the Mir kimberlite pipe, Yakutia: Evidence for mantle metasomatism. *Lithos*. Elsevier B.V.

Speich, L., Kohn, S. C., Bulanova, G. P. & Smith, C. B. (2018). The behaviour of platelets in natural diamonds and the development of a new mantle thermometer. *Contributions to Mineralogy and Petrology*. Springer Berlin Heidelberg **173**, 1–21.

St-Onge, M. R., Searle, M. P. & Wodicka, N. (2006). Trans-Hudson orogen of North America and Himalaya-Karakoram-Tibetan orogen of Asia: Structural and thermal characteristics of the lower and upper plates. *Tectonics* **25**, 1–22.

Stachel, T. (2014). Diamonds. *Geology of Gem Deposits*, 1–28.

Stachel, T. & Harris, J. W. (1997). Diamond precipitation and mantle metasomatism - evidence

from the trace element chemistry of silicate inclusions in diamonds from Akwatia, Ghana. *Contributions to Mineralogy and Petrology* **129**, 143–154.

Stachel, T. & Harris, J. W. (2008). The origin of cratonic diamonds — Constraints from mineral inclusions. *Ore Geology Reviews* **34**, 5–32.

Stachel, T. & Luth, R. W. (2015). Diamond formation — Where, when and how? *Lithos*. Elsevier B.V. **220**–**223**, 200–220.

Stachel, T., Viljoen, K. S., Brey, G. & Harris, J. W. (1998). Metasomatic processes in lherzolitic and harzburgitic domains of diamondiferous lithospheric mantle: REE in garnets from xenoliths and inclusions in diamonds. *Earth and Planetary Science Letters* **159**, 1–12.

Stachel, T., Harris, J., Tappert, R. & Brey, G. P. (2003). Peridotitic diamonds from the Slave and the Kaapvaal cratons—similarities and differences based on a preliminary data set. *Lithos* **71**, 489–503.

Stachel, T., Aulbach, S., Brey, G. P., Harris, J. W., Leost, I., Tappert, R. & Viljoen, K. S. (Fanus. (2004). The trace element composition of silicate inclusions in diamonds: a review. *Lithos* **77**, 1–19.

Stachel, T., Harris, J. W. & Muehlenbachs, K. (2009). Sources of carbon in inclusion bearing diamonds. *Lithos*. Elsevier B.V. **112**, 625–637.

Stachel, T., Harris, J. W., Hunt, L., Muehlenbachs, K., Kobussen, A. & EIMF (2018). Argyle diamonds – How subduction along the Kimberley Craton edge generated the World's biggest diamond deposit. *SEG Special Publication* **20**, 145–167.

Stauffer, M. R. (1984). Manikewan: An early proterozoic ocean in central Canada, its igneous history and orogenic closure. *Precambrian Research* **25**, 257–281.

Stern, R. A., Palot, M., Howell, D., Stachel, T., Pearson, D. G., Cartigny, P. & Oh, A. (2014). Methods and reference materials for sims diamond C- and N- isotope analysis. *Canadian Centre for Isotopic Microanalysis, Research Report* **14-01**, University of Alberta, Education and Research Arch.

Stiefenhofer, J., Viljoen, K. S. & Marsh, J. S. (1997). Petrology and geochemistry of peridotite xenoliths from the Letlhakane kimberlites, Botswana. *Contributions to Mineralogy and Petrology* **127**, 147–158.

Sun, S.-S. & McDonough, W. F. (1989). Chemical and isotopic systematics of oceanic basalts: implications for mantle composition and processes. *Geological Society Special Publications*

42, 313–345.

Sverjensky, D. A. & Huang, F. (2015). Diamond formation due to a pH drop during fluid–rock interactions. *Nature Communications*. Nature Publishing Group **53**, 1689–1699.

Sverjensky, D. a., Stagno, V. & Huang, F. (2014). Important role for organic carbon in subduction-zone fluids in the deep carbon cycle. *Nature Geoscience* **7**, 909–913.

Taylor, L. (1996). Eclogitic inclusions in diamonds: Evidence of complex mantle processes over time. *Earth and Planetary Science Letters* **142**, 535–551.

Taylor, W. R. (1998). An experimental test of some geothermometer and geobarometer formulations for upper mantle peridotites with application to the thermobarometry of fertile lherzolite and garnet websterite. *N Jb Miner Abh*. Schweizerbart'sche Verlagsbuchhandlung **172**, 381–408.

Taylor, W. R., Jaques, A. L. & Ridd, M. (1990). Nitrogen-defect aggregation characteristics of some Australasian diamonds: time-temperature constraints on the source regions of pipe and alluvial diamonds. *American Mineralogist* **75**, 1290–1310.

Taylor, W. R., Bulanova, G. P. & Milledge, H. J. (1995). Quantitative nitrogen aggregation study of some Yakutian diamonds: Constraints on the growth, thermal and deformation history of peridotitic and eclogitic diamonds. *Extended Abstracts 6th International Kimberlite Conference*. Novosibirsk, 608–610.

Taylor, W. R., Canil, D. & Milledge, H. J. (1996). Kinetics of Ib to IaA nitrogen aggregation in diamond. *Geochimica et Cosmochimica Acta* **60**, 4725–4733.

Titus, E. *et al.* (2005). Quantitative analysis of hydrogen in chemical vapor deposited diamond films. *Diamond and Related Materials* **14**, 476–481.

Van Schmus, W. & Hinze, W. J. (1985). The midcontinent rift system. *Annual Review of Earth and Planetary Sciences* **13**, 345–383.

Viljoen, F., Dobbe, R., Harris, J. & Smit, B. (2010). Trace element chemistry of mineral inclusions in eclogitic diamonds from the Premier (Cullinan) and Finsch kimberlites, South Africa: Implications for the evolution of their mantle source. *Lithos*. Elsevier B.V. **118**, 156–168.

Viljoen, K. S., Smith, C. B. & Sharp, Z. D. (1996). Stable and radiogenic isotope study of eclogite xenoliths from the Orapa kimberlite, Botswana. *Chemical Geology* **131**, 235–255.

Walker, R. ., Carlson, R. ., Shirey, S. . & F.R, B. (1989). Os, Sr, Nd, and Pb isotope systematics

of southern African peridotite xenoliths: Implications for the chemical evolution of subcontinental mantle. *Geochimica et Cosmochimica Acta* **53**, 1583–1595.

Walker, R. J., Horan, M. F., Morgan, J. W., Becker, H., Grossman, J. N. & Rubin, A. E. (2002). Comparative 187Re-187Os systematics of chondrites: Implications regarding early solar system processes. *Geochimica et Cosmochimica Acta* **66**, 4187–4201.

Walter, M. J. (1998). Melting of garnet peridotite and the origin of komatiite and depleted lithosphere. *Journal of Petrology* **39**, 29–60.

Walter, M. J. (1999). Melting residues of fertile peridotite and the origin of cratonic lithosphere. *Mantle petrology: field observations and high-pressure experimentation. Spec Publ Geochem Soc* **6**, 225–239.

Wang, H., van Hunen, J. & Pearson, D. G. (2016 – in press). Making Archean cratonic roots by lateral compression: A two-stage thickening and stabilization model. *Tectonophysics*. Elsevier B.V. 1–10.

Warren, J. M. & Shirey, S. B. (2012). Lead and osmium isotopic constraints on the oceanic mantle from single abyssal peridotite sulfides. *Earth and Planetary Science Letters*. Elsevier **359–360**, 279–293.

Weiss, Y., Kessel, R., Griffin, W. L., Kiflawi, I., Klein-BenDavid, O., Bell, D. R., Harris, J. W. & Navon, O. (2009). A new model for the evolution of diamond-forming fluids: Evidence from microinclusion-bearing diamonds from Kankan, Guinea. *Lithos* **112**, 660–674.

Weiss, Y., Kiflawi, I. & Navon, O. (2010). IR spectroscopy: Quantitative determination of the mineralogy and bulk composition of fluid microinclusions in diamonds. *Chemical Geology* **275**, 26–34.

Weiss, Y., Kiflawi, I., Davies, N. & Navon, O. (2014). High-density fluids and the growth of monocrystalline diamonds. *Geochimica et Cosmochimica Acta*. Elsevier Ltd **141**, 145–159.

Weller, O. M. & St-Onge, M. R. (2017). Record of modern-style plate tectonics in the Palaeoproterozoic Trans-Hudson orogen. *Nature Geoscience* **10**, 305–311.

Wilson, L. & Head III, J. W. (2007). An integrated model of kimberlite ascent and eruption. *Nature*. Nature Publishing Group **447**, 53.

Woodcock, N. H., Omma, J. E. & Dickson, J. A. D. (2006). Chaotic breccia along the Dent Fault, NW England: implosion or collapse of a fault void? *Journal of the Geological Society* **163**, 431–446.

Woods, G. S. (1986). Platelets and the infrared Absorption of Type Ia Diamonds. *Proceedings of the Royal Society A: Mathematical, Physical and Engineering Sciences* **407**, 219–238.

Yaxley, G. M., Crawford, A. J. & Green, D. H. (1991). Evidence for carbonatite metasomatism in spinel peridotite xenoliths from western Victoria, Australia. *Earth and Planetary Science Letters* **107**, 305–317.

Zonneveld, J.-P., Kjarsgaard, B. a., Harvey, S. E., Heaman, L. M., McNeil, D. H. & Marcia, K. Y. (2004). Sedimentologic and stratigraphic constraints on emplacement of the Star Kimberlite, east–central Saskatchewan. *Lithos* **76**, 115–138.

Appendix A – Geochemical data for Fort à la Corne peridotite xenoliths

Data reported in Appendix A are averaged; for the complete dataset see the UAL Dataverse dataset: “Geochemical data for Fort à la Corne peridotite xenoliths” at https://doi.org/10.7939/DVN/EJWJHD

Table A1 Natural and synthetic materials used for calibration, and as secondary standard.

Reference Material	Element	Crystals	Mineral	Origin	References	
Frank Smith Pyrope Garnet	SiO_2	TAP	Gt, Cpx, Opx	Frank Smith kimberlite, South Africa	Royal Ontario Museum collection. Composition from bulk XRF analysis	
	Al_2O_3	TAP	Ol, Gt, Cpx, Opx			
	MgO	TAP	Gt			
$Ca_5(PO_4)_3F$ Apatite	P_2O_5	PET	Ol, Gt, Cpx, Opx	Dwyer Mine, Wilberforce, Ontario, Canada	Apatite from alkaline source	Tacker RC (2004) Hydroxyl ordering in igneous apatite. Am Mineral 89:1411–1421
$KAlSi_3O_8$ Sanidine	K_2O	PET	Ol, Gt, Cpx, Opx	Itrongay, Madagascar	Fe-bearing K-feldspar	Ackermann S, Kunz M, Armbruster T, Schefer J and Hanni H (2005) Cation distribution in a Fe-bearing K-feldspar from Itrongay, Madagascar. A combined neutron-and X-ray single crystal diffraction study. Schweiz Miner Petrog 84:345-354. doi.org/10.5169/seals-63754
$NaAlSi_3O_8$ Albite	Na_2O	TAP	Ol, Gt, Cpx, Opx	Virginia, USA	Albite Harvard 131705, from the Harvard Mineralogical Museum	McGuire AV, Francis CA, Dyar MD (1992) Minerals standards for electron microprobe analyses of oxygen. Am Mineral 77:1087-1091 (http://iageo.com/microanalytical-reference-materials/)
$CaMgSi_2O_6$ Diopside	CaO	PET	Ol, Gt, Cpx, Opx	Wakefield, Quebec, Canada	Astimex, palest blue	http://astimex.com/com/catalog/min.html
	MgO	TAP	Cpx, Opx			
	SiO_2	TAP	Gt, Cpx, Opx			
Labradorite	Al_2O_3	TAP	Cpx	Lake County, Oregon, USA	USNM 115900	Jarosewich E, Nelen JA, Norberg JA (1980) Reference samples for electron microprobe analysis. Geostanard Newslett 4:43-47 (https://mineralsciences.si.edu/facilities/standards.htm)
Fayalite	FeO	LIF	Ol, Gt, Cpx, Opx	Rockport, Massachusetts, USA	USNM 85276	
Fo93	SiO_2	TAP	Ol	Balsam Gap,	Similar to Yund	Yund RA (1997) Rates of grain boundary diffusion

	MgO	TAP	Ol, Gt	North Carolina, USA	(1997)	through enstatite and forsterite reaction rims. Contrib Mineral Petrol 126:224-236
Rhodonite	MnO	LIF	Ol, Gt, Cpx, Opx	Sterling Hill, Franklin, New Jersey, USA	Bald Knob; Similar to Huebner and Woodruff (1985)	Huebner JS, Woodruff ME (1985) Chemical composition and critical evaluation of microprobe standards available in the reston microprobe facility. US Geological Survey Open File Report 85-718 (http://www.geology.wisc.edu/~johnf/ofr_85_718.pdf)
Ni (Nickel Wire)	NiO	LIF	Ol, Gt, Cpx, Opx	Synthetic	Alfa Aesar, 43132, Nickel wire, 0.5 mm dia, annealed, 99.98 % (metals basis)	https://www.alfa.com/en/catalog/043132/
Cr_2O_3 (Chromium Oxide)	Cr_2O_3	PET	Ol, Gt, Cpx, Opx	Synthetic	Alfa Aesar, 36258, Chromium(III) oxide, 99.6 % purity (metals basis)	
TiO_2 (Rutile)	TiO_2	PET	Ol, Gt, Cpx, Opx	Synthetic	synthetic TiO_2 from MTI	http://www.mtixtl.com/tio2substrates.aspx
Secondary Standards						
Gore Garnet				Gore Mountain Mine, New York, USA	Similar to UWG-2 from Vielzeuf et al. (2005).	Vielzeuf D, Champenois M, Valley JW, Brunet F, and Devidal JL (2005) SIMS analyses of oxygen isotopes; matrix effects in Fe-Mg-Ca garnets. Chem Geol 223:208-226. doi:10.1016/j.chemgeo.2005.07.008
Frank Smith Pyrope Garnet				Frank Smith kimberlite, South Africa	Royal Ontario Museum collection. Composition from bulk XRF analysis	

Cr-Diopside	Megacrystic from Russian kimberlite	In-house Standard	
Augite	Kakanui, New Zealand	USNM 122142	Jarosewich E, Nelen JA, Norberg JA (1980) Reference samples for electron microprobe analysis. Geostanard Newslett 4:43-47 (https://mineralsciences.si.edu/facilities/standards.htm)
Omphacite	Roberts Victor Mine, South Africa	USNM 110607	
Fo93	Balsam Gap, North Carolina, USA	Similar to Yund (1997)	Yund RA (1997) Rates of grain boundary diffusion through enstatite and forsterite reaction rims. Contrib Mineral Petrol 126:224-236

Table A2 Averaged major element concentrations in peridotite xenoliths from FALC given in wt%. (n = number of analytical spots)

Sample	**LLD**	**15000**		**15001**	**17651-1**		**17651-2**		**17652**	**17654-1**	**17654-2**	
Mineral		olivine	garnet	olivine	cpx	garnet	garnet	garnet	cpx	cpx	cpx	garnet
Description			G9^			G11	G1	G9				G9
n		9	20	9	25	15	3	3	7	8	9	14
SiO_2[+]	0.01	40.59	41.63	40.35	54.74	41.48	41.58	41.52	55.16	54.60	54.58	42.11
2σ		0.26	0.45	0.10	0.66	0.12	0.01	0.11	0.20	0.38	0.31	0.28
TiO_2	0.02	-	0.07	0.03	0.27	0.41	1.03	0.26	0.28	0.25	0.24	0.19
2σ		-	0.04	0.01	0.03	0.19	0.01	0.02	0.02	0.02	0.10	0.07
Al_2O_3	0.01	0.02	20.04	0.02	1.77	18.22	19.74	20.53	1.92	2.33	1.80	20.51
2σ		0.01	0.26	0.01	0.21	0.16	0.08	0.10	0.01	0.04	0.12	0.29
Cr_2O_3	0.02	0.02	5.00	-	2.07	6.67	2.71	3.52	0.76	1.53	1.11	3.86
2σ		0.02	0.36	-	0.50	0.18	0.05	0.10	0.24	0.05	0.05	0.20
FeO_{tot}	0.01	8.30	7.88	11.90	2.74	5.90	7.25	7.58	3.36	3.63	3.25	7.47
2σ		0.05	0.09	0.10	0.07	0.09	0.01	0.08	0.11	0.03	0.26	0.11
MnO	0.01	0.10	0.41	0.13	0.11	0.31	0.28	0.43	0.11	0.11	0.11	0.31
2σ		0.02	0.02	0.02	0.02	0.02	0.01	0.00	0.02	0.01	0.01	0.02
MgO	0.01	49.60	18.83	47.01	18.41	21.03	20.97	20.24	16.88	16.05	18.42	20.08
2σ		0.14	0.36	0.13	0.39	0.19	0.08	0.09	0.15	0.19	0.12	0.26
NiO	0.03	0.40	-	0.25	0.06	-	-	-	0.05	-	0.06	-
2σ		0.02	-	0.01	0.02	-	-	-	0.01	-	0.01	-
CaO	0.01	0.03	5.63	0.06	17.72	4.96	5.06	4.75	20.17	18.82	18.46	4.92
2σ		0.01	0.05	0.01	0.50	0.26	0.02	0.07	0.16	0.12	0.47	0.06
Na_2O	0.01	0.01	0.03	0.02	1.66	0.06	0.08	0.06	1.54	2.01	1.31	0.04
2σ		0.01	0.02	0.01	0.30	0.02	0.03	0.01	0.07	0.05	0.07	0.02
K_2O	0.01	-	-	-	0.05	-	-	-	0.04	0.02	0.04	-
2σ		-	-	-	0.01	-	-	-	0.00	0.01	0.00	-
P_2O_5	0.02	-	0.02	-	-	-	0.04	0.03	-	-	0.02	-
2σ		-	0.02	-	-	-	0.01	0.03	-	-	0.02	-
Total		99.08	99.55	99.80	99.62	99.06	98.76	98.93	100.26	99.39	99.41	99.51
2σ		0.15	0.79	0.17	0.87	0.25	0.07	0.16	0.20	0.38	0.32	0.46
Mg#*		91.41	80.99	87.57	92.3	86.4	83.76	82.64	89.95	88.73	91.00	82.74

[+]all values in wt%; *Mg# = 100xMg/(Mg+Fe); ^G-classification following Grütter et al. (2004)

Table A2 continued

Sample	**LLD**	**17655**				**17656**		**17679**				
Mineral		olivine	cpx	garnet	garnet	cpx	garnet	opx	cpx	garnet	garnet	garnet
Description				G11	G9		G11			G1	G9 low Cr	G9 high Cr
n		9	8	3	15	8	14	2	7	4	21	4
SiO_2	0.01	40.35	54.96	41.21	41.40	55.31	41.51	56.87	54.58	41.84	41.82	41.67
2σ		0.22	0.38	0.15	0.27	0.28	0.19	0.08	0.92	0.12	0.19	0.30
TiO_2	0.02	0.03	0.28	0.59	0.30	0.25	0.67	0.06	0.24	0.48	0.12	0.20
2σ		0.01	0.02	0.05	0.15	0.02	0.13	0.01	0.07	0.04	0.16	0.09
Al_2O_3	0.01	0.02	1.99	18.91	19.25	1.80	18.18	2.39	3.28	21.09	21.84	19.86
2σ		0.01	0.15	0.16	0.27	0.03	0.42	0.05	2.42	0.12	1.10	0.67
Cr_2O_3	0.02	-	1.13	4.85	5.24	1.42	5.98	0.51	1.46	2.84	2.41	4.89
2σ		-	1.29	0.33	0.16	0.04	0.28	0.01	0.26	0.06	1.18	0.81
FeO_{tot}	0.01	11.05	3.37	9.13	7.91	2.90	6.03	5.38	2.04	7.70	8.64	7.21
2σ		0.07	0.10	0.10	0.99	0.03	0.12	0.02	1.28	0.05	1.20	0.15
MnO	0.01	0.13	0.10	0.42	0.41	0.11	0.28	0.13	0.08	0.36	0.46	0.38
2σ		0.01	0.02	0.02	0.03	0.01	0.02	0.00	0.04	0.02	0.15	0.04
MgO	0.01	47.70	16.78	18.31	19.57	19.11	20.67	33.47	15.80	20.52	19.38	20.04
2σ		0.27	0.58	0.18	0.80	0.06	0.20	0.07	1.49	0.17	1.52	0.20
NiO	0.03	0.24	0.03	-	-	0.06	-	0.07	0.04	-	-	-
2σ		0.02	0.02	-	-	0.02	-	0.00	0.02	-	-	-
CaO	0.01	0.04	19.75	5.95	5.12	17.86	5.64	0.20	20.87	4.54	4.88	5.01
2σ		0.01	0.94	0.05	0.25	0.12	0.15	0.06	1.74	0.13	0.66	0.48
Na_2O	0.01	0.02	1.70	0.07	0.06	1.47	0.07	0.02	1.80	0.06	0.04	0.05
2σ		0.02	0.46	0.01	0.02	0.03	0.02	0.01	0.09	0.01	0.03	0.01
K_2O	0.01	-	0.04	-	-	0.07	-	-	0.02	-	-	-
2σ		-	0.01	-	-	0.01	-	-	0.04	-	-	-
P_2O_5	0.02	-	-	0.03	0.04	-	-	-	-	-	-	-
2σ		-	-	0.00	0.01	-	-	-	-	-	-	-
Total		99.61	100.14	99.46	99.31	100.36	99.04	99.10	100.21	99.46	99.56	99.31
2σ		0.42	0.23	0.26	0.34	0.31	0.24	0.08	0.23	0.06	0.48	0.15
Mg#		88.50	89.87	78.14	81.52	92.16	85.94	91.73	93.24	82.62	79.98	83.21

Table A2 continued

Sample	**LLD**	**17681**			**17686**	**17694-2**	**17695-1**	**17696-1**		**17696-2**		**17696-3**
Mineral		cpx	cpx	garnet	garnet	garnet	cpx	olivine	garnet	olivine	garnet	olivine
Description				G9	G11	G9			G11		G11	
n		33	25	15	15	15	8	9	15	20	23	11
SiO_2	0.01	54.90	55.15	41.32	41.24	41.74	54.99	40.68	41.73	40.71	41.44	40.79
2σ		0.37	0.39	0.63	0.45	0.12	0.47	0.20	0.34	0.46	0.19	0.20
TiO_2	0.02	0.11	0.11	0.15	0.79	0.29	0.27	0.03	0.67	0.02	0.48	-
2σ		0.02	0.02	0.02	0.05	0.17	0.01	0.01	0.06	0.02	0.13	-
Al_2O_3	0.01	2.02	1.76	18.85	16.60	18.19	1.81	0.03	18.79	0.02	17.54	0.02
2σ		0.08	0.49	0.38	0.23	0.32	0.77	0.01	0.20	0.02	0.31	0.01
Cr_2O_3	0.02	2.87	1.64	6.35	7.65	6.14	1.10	0.04	5.64	0.03	6.97	0.05
2σ		0.55	0.46	0.15	0.07	0.13	0.14	0.02	0.10	0.03	0.13	0.02
FeO_{tot}	0.01	2.56	2.71	7.62	6.47	6.30	2.87	8.37	6.95	9.02	6.76	7.82
2σ		0.12	0.09	0.08	0.23	0.11	0.20	0.07	0.06	1.70	0.26	0.12
MnO	0.01	0.12	0.12	0.42	0.31	0.29	0.10	0.12	0.31	0.12	0.32	0.12
2σ		0.02	0.02	0.02	0.03	0.02	0.02	0.01	0.02	0.02	0.02	0.02
MgO	0.01	15.51	16.49	18.61	19.82	20.60	17.36	49.48	19.93	48.85	19.84	49.83
2σ		0.77	1.07	0.53	0.21	0.14	0.47	0.31	0.24	1.25	0.38	0.23
NiO	0.03	0.04	0.04	-	-	-	0.05	0.38	-	0.35	-	0.36
2σ		0.02	0.01	-	-	-	0.02	0.02	-	0.02	-	0.02
CaO	0.01	18.62	19.53	6.08	6.20	5.53	20.10	0.06	5.41	0.05	5.75	0.07
2σ		0.35	0.64	0.07	0.07	0.08	1.83	0.01	0.07	0.04	0.08	0.01
Na_2O	0.01	2.48	1.90	0.04	0.07	0.04	1.50	0.03	0.06	0.03	0.06	0.02
2σ		0.31	0.56	0.02	0.02	0.02	0.69	0.01	0.02	0.02	0.02	0.01
K_2O	0.01	0.03	0.02	-	-	-	0.04	-	-	-	-	-
2σ		0.01	0.03	-	-	-	0.03	-	-	-	-	-
P_2O_5	0.02	0.03	0.03	-	0.02	0.02	-	-	0.02	-	0.02	-
2σ		0.03	0.03	-	0.01	0.02	-	-	0.02	-	0.02	-
Total		99.29	99.51	99.46	99.17	99.15	100.21	99.22	99.53	99.21	99.18	99.10
2σ		0.53	0.50	0.83	0.52	0.27	0.33	0.32	0.59	0.88	0.29	0.34
Mg#		91.52	91.56	81.34	84.53	85.35	91.51	91.33	83.63	90.62	83.95	91.91

Table A2 continued

Sample	**LLD**	**17696-3**		**17697-1**				**17697-2**				
Mineral		olivine	garnet	olivine	olivine	cpx	garnet	olivine	cpx	garnet	garnet	garnet
Description			G9				G9			G1 low Fe	G1 high Fe	G9
n		3	13	10	4	8	15	11	8	9	8	3
SiO_2	0.01	40.30	41.78	40.82	41.31	55.09	41.95	40.87	55.13	42.22	41.91	42.07
2σ		0.19	0.25	0.36	0.13	0.17	0.20	0.20	0.11	0.27	0.13	0.09
TiO_2	0.02	0.03	0.13	0.03	-	0.28	0.18	-	0.27	0.36	0.70	0.27
2σ		0.01	0.03	0.02	-	0.00	0.05	-	0.02	0.02	0.03	0.05
Al_2O_3	0.01	0.03	17.62	0.01	-	2.05	20.83	0.02	2.02	20.79	20.44	20.15
2σ		0.02	0.21	0.00	-	0.04	0.18	0.02	0.09	0.14	0.16	0.20
Cr_2O_3	0.02	-	7.84	-	-	1.08	3.28	-	0.85	3.22	2.66	4.32
2σ		-	0.19	-	-	0.14	0.17	-	0.12	0.05	0.10	0.17
FeO_{tot}	0.01	10.45	6.26	8.77	7.05	2.94	7.54	7.45	3.76	6.71	7.84	6.89
2σ		0.67	0.07	0.55	0.05	0.06	0.10	1.32	0.07	0.12	0.08	0.07
MnO	0.01	0.13	0.31	0.11	0.09	0.10	0.37	0.10	0.12	0.32	0.31	0.35
2σ		0.02	0.02	0.02	0.01	0.02	0.03	0.02	0.01	0.02	0.02	0.01
MgO	0.01	47.77	19.39	49.03	50.55	17.21	20.22	50.15	18.78	21.02	20.32	20.52
2σ		0.36	0.29	0.49	0.09	0.10	0.14	1.07	0.18	0.14	0.10	0.07
NiO	0.03	0.33	-	0.39	0.33	0.06	-	0.35	0.05	-	-	-
2σ		0.07	-	0.04	0.02	0.01	-	0.02	0.02	-	-	-
CaO	0.01	0.05	6.40	0.04	0.01	19.57	4.80	0.03	17.70	4.69	4.87	4.96
2σ		0.03	0.07	0.01	0.00	0.07	0.06	0.06	0.31	0.19	0.21	0.02
Na_2O	0.01	0.03	0.01	0.02	-	1.71	0.04	0.01	1.46	0.13	0.07	0.05
2σ		0.03	0.01	0.01		0.05	0.02	0.02	0.09	0.20	0.02	0.01
K_2O	0.01	-	-	-	-	0.04	-	-	0.05	-	-	-
2σ		-	-	-	-	0.01	-	-	0.01	-	-	-
P_2O_5	0.02	-	-	-	-	-	0.03	-	-	-	0.03	0.04
2σ		-	-	-	-	-	0.02	-	-	-	0.02	0.01
Total		99.15	99.75	99.24	99.38	100.12	99.23	99.01	100.17	99.46	99.15	99.64
2σ		0.11	0.52	0.45	0.22	0.32	0.30	0.33	0.30	0.40	0.26	0.18
Mg#		89.07	84.67	90.88	92.75	91.26	82.71	92.31	89.90	84.82	82.20	84.15

Table A2 continued

Sample	**LLD**	**17697-3**		**17697-4**							**17698-2**	
Mineral		olivine	olivine	olivine	olivine	olivine	olivine	garnet	garnet	garnet	olivine	garnet
Description								G9	G3	G3D		G9
n		5	4	4	5	5	3	18	7	3	10	14
SiO_2	0.01	40.57	40.90	41.14	40.84	40.74	40.59	41.38	39.44	40.69	40.82	41.95
2σ		0.18	0.12	0.10	0.33	0.20	0.28	0.15	0.16	0.04	0.18	0.17
TiO_2	0.02	0.03	-	-	-	-	0.03	0.12	0.11	0.17	0.02	0.18
2σ		0.01	-	-	-	-	0.02	0.02	0.03	0.01	0.02	0.01
Al_2O_3	0.01	0.02	0.03	0.02	0.02	0.03	0.03	17.27	21.94	22.56	0.03	20.96
2σ		0.01	0.00	0.01	0.02	0.00	0.01	0.12	0.10	0.03	0.01	0.09
Cr_2O_3	0.02	0.02	0.07	0.08	0.06	0.06	0.03	7.90	0.06	0.07	0.06	3.23
2σ		0.02	0.02	0.01	0.05	0.02	0.00	0.09	0.02	0.02	0.05	0.09
FeO_{tot}	0.01	10.61	7.94	6.92	7.93	8.68	9.82	5.87	22.87	17.70	8.49	7.59
2σ		0.53	0.08	0.06	0.11	0.30	0.01	0.09	0.23	0.07	0.76	0.09
MnO	0.01	0.13	0.11	0.10	0.12	0.12	0.13	0.31	0.54	0.38	0.11	0.36
2σ		0.02	0.02	0.01	0.01	0.01	0.02	0.02	0.02	0.01	0.02	0.01
MgO	0.01	47.80	49.66	50.36	49.71	49.15	48.29	19.68	6.83	12.72	49.30	20.41
2σ		0.30	0.16	0.05	0.29	0.24	0.06	0.15	0.06	0.07	0.48	0.21
NiO	0.03	0.31	0.36	0.36	0.37	0.36	0.33	-	-	-	0.37	-
2σ		0.07	0.01	0.01	0.01	0.04	0.01	-	-	-	0.05	-
CaO	0.01	0.05	0.06	0.05	0.05	0.07	0.06	6.59	9.11	6.24	0.06	4.78
2σ		0.10	0.12	0.09	0.10	0.14	0.13	0.06	0.21	0.03	0.12	0.06
Na_2O	0.01	0.02	0.03	0.03	0.03	0.03	0.03	0.02	0.04	0.09	0.03	0.04
2σ		0.00	0.03	0.01	0.02	0.02	0.03	0.02	0.02	0.02	0.01	0.02
K_2O	0.01	-	-	-	-	-	-	-	-	-	-	-
2σ		-	-	-	-	-	-	-	-	-	-	-
P_2O_5	0.02	-	-	-	-	-	-	-	0.04	0.08	-	0.03
2σ		-	-	-	-	-	-	-	0.01	0.01	-	0.02
Total		99.57	99.16	99.06	99.16	99.26	99.35	99.16	100.99	100.72	99.30	99.54
2σ		0.14	0.14	0.05	0.52	0.17	0.25	0.31	0.17	0.12	0.44	0.32
Mg#		88.93	91.77	92.84	91.79	90.99	89.76	85.67	34.75	56.16	91.19	82.74

Table A2 continued

Sample	**LLD**	**17698-3**					**17699-1**				**17700-1**		
Mineral		olivine	opx	cpx	garnet	garnet	olivine	garnet	garnet	garnet	olivine	cpx	garnet
Description					G1	G9		G1	G11	G9			G9
n		9	3	52	14	19	7	6	3	15	9	25	15
SiO_2	0.01	40.95	57.70	54.66	42.29	42.28	40.27	41.97	41.59	41.42	40.80	54.79	41.89
2σ		0.22	0.25	0.36	0.35	0.21	0.19	0.22	0.29	0.30	0.27	0.74	0.22
TiO_2	0.02	0.02	0.12	0.23	0.58	0.32	0.03	0.60	0.66	0.37	0.03	0.21	0.25
2σ		0.01	0.01	0.06	0.59	0.03	0.01	0.05	0.03	0.03	0.02	0.02	0.02
Al_2O_3	0.01	0.02	0.73	1.89	21.37	21.24	0.02	21.72	19.31	19.54	0.02	2.01	21.04
2σ		0.01	0.02	0.12	0.33	0.42	0.01	0.57	0.12	0.31	0.02	0.06	0.16
Cr_2O_3	0.02	0.03	0.21	0.95	2.18	2.89	-	1.55	4.65	5.41	0.05	1.44	3.72
2σ		0.01	0.02	0.04	1.86	0.08	-	0.56	0.52	0.19	0.09	0.08	0.09
FeO_{tot}	0.01	8.28	5.16	2.96	7.45	7.06	11.30	9.68	9.67	9.04	8.55	2.76	7.86
2σ		1.00	0.07	0.09	1.40	0.39	0.10	0.05	0.14	0.55	0.55	0.06	0.07
MnO	0.01	0.11	0.12	0.11	0.30	0.31	0.13	0.39	0.40	0.36	0.12	0.10	0.39
2σ		0.02	0.01	0.02	0.05	0.02	0.01	0.02	0.00	0.03	0.01	0.01	0.02
MgO	0.01	49.53	33.99	18.14	20.85	20.82	47.61	19.26	18.23	18.85	49.42	16.54	19.71
2σ		0.78	0.10	0.42	0.50	0.47	0.18	0.25	0.18	0.45	0.40	0.44	0.29
NiO	0.03	0.37	0.12	0.06	-	-	0.15	-	-	-	0.36	0.05	-
2σ		0.03	0.01	0.02	-	-	0.02	-	-	-	0.02	0.02	-
CaO	0.01	0.04	0.78	18.95	4.55	4.56	0.05	4.69	5.59	4.76	0.04	19.59	4.76
2σ		0.09	1.57	0.36	0.25	0.15	0.09	0.17	0.01	0.11	0.09	0.19	0.06
Na_2O	0.01	0.02	0.16	1.41	0.07	0.05	0.02	0.07	0.07	0.06	0.02	1.76	0.05
2σ		0.01	0.02	0.14	0.05	0.02	0.01	0.01	0.01	0.01	0.03	0.20	0.02
K_2O	0.01	-	-	0.05	-	-	-	-	-	-	-	0.02	-
2σ		-	-	0.02	-	-	-	-	-	-	-	0.01	-
P_2O_5	0.02	-	-	-	-	0.02	-	0.02	0.03	0.03	-	0.02	-
2σ		-	-	-	-	0.02	-	0.01	0.01	0.02	-	0.02	-
Total		99.38	99.10	99.42	99.66	99.55	99.59	99.95	100.22	99.83	99.42	99.28	99.71
2σ		0.30	0.48	0.39	0.74	0.44	0.27	0.34	0.35	0.31	0.34	0.72	0.40
Mg#		91.43	92.15	91.62	83.31	84.02	88.25	78.01	77.06	78.80	91.15	91.45	81.72

Table A3 Trace element concentrations in ppm of peridotitic garnets and clinopyroxenes from Fort à la Corne. Garnets are classified using the G-classification scheme of Grütter et al. (2004).

Sample	**15000**	**17651-1**		**17651-2**		**17652**	**17654-1**	**17654-2**		**17655**		
Mineral	gt	gt	cpx	gt	gt	cpx	cpx	gt	cpx	gt	gt	cpx
Description	G9	G11		G9	G1			G9		G11	G9	
n	10	13	6	2	4	5	4	7	4	2	14	4
Ti	412	2625	1632	1593	6297	1660	1550	1142	1436	3872	1943	1679
2σ	94	45	27	27	104	27	26	10	17	68	34	26
Ni	40.3	98.5	493.0	48.5	132.4	361.7	186.1	77.2	535.5	39.7	43.9	325.9
2σ	0.7	2.7	9.0	1.0	2.4	5.3	2.1	0.7	5.0	0.7	0.8	5.7
Sr	0.16	1.06	194.9	0.27	0.71	186.6	319.0	0.33	108.4	0.36	0.35	204.4
2σ	0.01	0.10	2.0	0.02	0.02	1.7	3.5	0.01	0.8	0.01	0.02	2.2
Y	3.08	5.67	2.78	17.22	21.99	2.81	4.25	8.23	1.46	24.34	19.87	3.10
2σ	0.06	0.11	0.06	0.35	0.39	0.06	0.07	0.09	0.03	0.16	0.24	0.06
Zr	12.9	27.8	10.0	58.8	128.8	23.0	60.2	16.1	6.4	101.6	75.0	26.9
2σ	0.2	0.5	0.2	1.3	2.2	0.3	0.6	0.2	0.1	0.6	0.8	0.3
Nb	0.28	0.30	0.32	0.24	0.20	0.32	0.48	0.30	0.20	0.23	0.18	0.36
2σ	0.01	0.02	0.02	0.01	0.01	0.02	0.02	0.01	0.01	0.01	0.01	0.02
Ba	0.03	4.47	0.56	-	-	0.91	1.03	0.02	1.62	-	-	0.62
2σ	0.03	0.69	0.05	-	-	0.19	0.08	0.01	0.18	-	-	0.07
La	0.03	0.08	3.04	0.03	0.06	2.69	9.49	0.04	2.28	0.02	0.02	2.71
2σ	0.00	0.01	0.05	0.00	0.00	0.04	0.10	0.00	0.03	0.00	0.00	0.05
Ce	0.36	0.51	11.93	0.40	0.70	11.18	31.44	0.42	8.16	0.28	0.26	11.57
2σ	0.01	0.02	0.19	0.02	0.02	0.15	0.39	0.01	0.09	0.01	0.01	0.18
Pr	0.13	0.14	1.78	0.12	0.22	1.76	4.36	0.14	1.22	0.11	0.11	1.85
2σ	0.01	0.01	0.03	0.01	0.01	0.03	0.05	0.01	0.02	0.01	0.01	0.03
Nd	1.18	1.28	8.58	1.17	2.05	8.83	19.03	1.19	5.49	1.23	1.37	9.57
2σ	0.06	0.06	0.18	0.05	0.07	0.15	0.28	0.05	0.12	0.05	0.05	0.18
Sm	0.59	0.76	1.85	0.93	1.44	1.92	3.65	0.54	1.03	1.11	1.49	2.21
2σ	0.04	0.04	0.09	0.05	0.07	0.07	0.12	0.04	0.05	0.05	0.06	0.09
Eu	0.19	0.29	0.52	0.45	0.65	0.56	1.05	0.20	0.29	0.57	0.79	0.63
2σ	0.01	0.01	0.02	0.02	0.02	0.02	0.03	0.01	0.01	0.02	0.02	0.02
Gd	0.59	0.96	1.36	1.74	2.59	1.48	2.63	0.65	0.73	2.44	3.18	1.61

2σ	0.04	0.06	0.07	0.08	0.08	0.07	0.11	0.04	0.05	0.09	0.10	0.08
Tb	0.08	0.15	0.16	0.37	0.52	0.17	0.30	0.14	0.08	0.54	0.57	0.19
2σ	0.01	0.01	0.01	0.02	0.02	0.01	0.01	0.01	0.01	0.01	0.02	0.01
Dy	0.50	1.03	0.79	2.95	3.98	0.85	1.38	1.17	0.41	4.37	3.84	0.92
2σ	0.03	0.04	0.04	0.10	0.11	0.04	0.06	0.04	0.03	0.09	0.10	0.05
Ho	0.11	0.21	0.11	0.63	0.85	0.12	0.18	0.29	0.06	0.98	0.76	0.13
2σ	0.01	0.01	0.01	0.02	0.02	0.01	0.01	0.01	0.01	0.02	0.02	0.01
Er	0.37	0.67	0.24	1.84	2.56	0.25	0.36	1.05	0.12	3.01	2.30	0.26
2σ	0.02	0.03	0.02	0.06	0.08	0.02	0.02	0.03	0.01	0.06	0.06	0.02
Tm	0.07	0.11	0.02	0.27	0.36	0.02	0.03	0.18	0.01	0.46	0.36	0.03
2σ	0.01	0.01	0.00	0.01	0.01	0.00	0.00	0.01	0.00	0.01	0.01	0.00
Yb	0.59	0.82	0.11	1.93	2.41	0.14	0.17	1.53	0.07	3.23	2.74	0.12
2σ	0.04	0.04	0.02	0.08	0.07	0.02	0.02	0.05	0.01	0.09	0.08	0.02
Lu	0.11	0.14	0.01	0.30	0.34	0.01	0.02	0.24	0.01	0.50	0.44	0.01
2σ	0.01	0.01	0.00	0.02	0.01	0.00	0.00	0.01	0.00	0.02	0.02	0.00
Hf	0.22	0.60	0.62	0.83	3.31	1.57	3.39	0.37	0.34	2.25	1.37	1.83
2σ	0.02	0.03	0.04	0.04	0.09	0.06	0.08	0.02	0.02	0.06	0.05	0.06
[Zr/Hf]	56	46	-	70	39	-	-	43	-	45	55	-
[Ti/Eu]	2164	9041	-	3564	9737	-	-	5594	-	6804	2461	-

Table A3 continued

Sample	**15656**	**17679**					**17681**		**17686**	**17694-2**	**17695-1**	**17696-1**
Mineral	gt	cpx	gt	gt	gt	cpx	gt	cpx	gt	gt	cpx	gt
Description	G11		G1	G9 low Cr	G9 high Cr		G9		G11	G9		G11
n	14	5	3	8	15	5	7	6	13	15	5	6
Ti	4219	1447	2828	411	1244	1466	879	624	5236	1806	1654	4053
2σ	71	19	89	11	34	19	8	7	89	33	26	31
Ni	96.2	509.4	62.8	10.3	44.3	323.6	40.4	355.8	95.4	91.4	502.2	98.8
2σ	1.7	6.1	2.1	0.4	1.2	4.1	0.5	3.2	1.6	1.6	8.5	0.8
Sr	0.78	233.9	0.31	0.04	0.31	111.7	0.18	398.6	0.74	0.58	239.8	0.53
2σ	0.02	2.2	0.02	0.01	0.02	1.0	0.01	3.7	0.02	0.02	2.2	0.02
Y	10.62	2.08	27.60	38.91	20.10	2.83	4.67	8.24	16.35	3.35	3.26	10.10
2σ	0.09	0.05	0.30	0.35	0.22	0.05	0.06	0.11	0.12	0.05	0.06	0.10
Zr	51.6	9.0	67.2	17.7	30.6	18.9	10.7	95.8	91.4	24.1	29.8	57.4
2σ	0.4	0.1	0.7	0.2	0.4	0.2	0.1	0.9	0.5	0.3	0.5	0.4
Nb	0.34	0.27	0.22	0.02	0.29	0.44	0.12	0.96	0.43	0.39	1.03	0.26
2σ	0.01	0.01	0.02	0.01	0.02	0.02	0.01	0.05	0.02	0.01	0.08	0.01
Ba	-	0.85	-	-	-	4.88	0.02	4.07	-	-	11.06	0.01
2σ	-	0.08	-	-	-	0.23	0.01	0.63	-	-	1.36	0.01
La	0.07	3.72	0.02	-	0.03	1.92	0.04	11.59	0.07	0.06	4.19	0.04
2σ	0.00	0.06	0.00	-	0.01	0.03	0.00	0.14	0.00	0.00	0.07	0.00
Ce	0.77	15.01	0.23	0.01	0.36	6.80	0.34	42.47	0.71	0.78	15.52	0.45
2σ	0.02	0.17	0.02	0.00	0.02	0.09	0.01	0.45	0.02	0.02	0.24	0.01
Pr	0.25	2.34	0.09	0.00	0.12	1.04	0.10	6.19	0.24	0.25	2.35	0.15
2σ	0.01	0.04	0.01	0.00	0.01	0.02	0.01	0.07	0.01	0.01	0.04	0.01
Nd	2.25	11.71	1.00	0.12	1.24	5.44	0.96	27.74	2.28	2.13	11.87	1.46
2σ	0.07	0.20	0.09	0.02	0.07	0.12	0.05	0.32	0.07	0.06	0.20	0.06
Sm	1.29	2.22	0.86	0.42	0.95	1.47	0.44	5.49	1.55	0.88	2.58	1.06
2σ	0.06	0.09	0.09	0.05	0.07	0.07	0.03	0.14	0.06	0.04	0.09	0.05
Eu	0.51	0.57	0.47	0.31	0.45	0.48	0.16	1.55	0.67	0.30	0.73	0.47
2σ	0.02	0.02	0.03	0.02	0.03	0.02	0.01	0.03	0.02	0.01	0.03	0.02
Gd	1.74	1.36	2.19	1.89	1.89	1.29	0.54	3.92	2.54	0.85	1.92	1.78
2σ	0.07	0.07	0.14	0.11	0.11	0.06	0.04	0.12	0.08	0.05	0.09	0.07

Tb	0.28	0.14	0.50	0.56	0.40	0.16	0.10	0.47	0.47	0.11	0.21	0.30
2σ	0.01	0.01	0.02	0.02	0.02	0.01	0.01	0.02	0.01	0.01	0.01	0.01
Dy	1.96	0.62	4.53	5.52	3.27	0.82	0.76	2.26	3.31	0.65	0.99	1.97
2σ	0.06	0.04	0.16	0.14	0.12	0.04	0.03	0.07	0.07	0.03	0.05	0.06
Ho	0.39	0.08	1.02	1.51	0.75	0.11	0.17	0.35	0.64	0.12	0.14	0.38
2σ	0.01	0.01	0.04	0.04	0.03	0.01	0.01	0.01	0.02	0.01	0.01	0.01
Er	1.19	0.17	3.42	5.43	2.41	0.23	0.57	0.78	1.69	0.38	0.28	1.10
2σ	0.04	0.02	0.12	0.14	0.09	0.02	0.03	0.04	0.05	0.02	0.02	0.03
Tm	0.18	0.02	0.51	0.92	0.37	0.02	0.09	0.09	0.22	0.06	0.03	0.15
2σ	0.01	0.00	0.03	0.03	0.02	0.00	0.01	0.01	0.01	0.01	0.00	0.01
Yb	1.38	0.08	3.73	7.21	2.70	0.12	0.73	0.50	1.36	0.52	0.12	1.09
2σ	0.05	0.01	0.17	0.19	0.12	0.02	0.03	0.04	0.05	0.03	0.02	0.04
Lu	0.22	0.01	0.56	1.19	0.41	0.01	0.12	0.07	0.18	0.10	0.01	0.17
2σ	0.01	0.00	0.03	0.04	0.02	0.00	0.01	0.01	0.01	0.01	0.00	0.01
Hf	1.10	0.51	1.31	0.20	0.53	0.87	0.29	3.98	2.21	0.50	1.88	1.39
2σ	0.04	0.03	0.09	0.03	0.05	0.04	0.02	0.08	0.06	0.03	0.07	0.04
[Zr/Hf]	48	-	51	90	55	-	36	-	41	48	-	41
[Ti/Eu]	8333	-	5992	1316	2770	-	5461	-	7811	6028	-	8568

Table A3 continued

Sample	**17696-2**	**17696-3**	**17697-1**		**17697-2**				**17697-4**		**17698-2**	
Mineral	gt	gt	gt	cpx	gt	gt	gt	cpx	gt	gt	gt	cpx
Description	G11	G9	G9		G1 high Fe	G1 low Fe	G9		G9	G3	G9	
n	12	5	14	6	7	7	3	4	10	4	10	1
Ti	3090	756	1127	1632	4416	2243	1790	1630	907	751	1057	1662
2σ	55	6	23	21	94	47	35	21	55	20	23	31
Ni	88.8	91.3	61.1	485.8	85.2	75.0	55.2	445.6	58.4	92.5	60.3	466.8
2σ	1.6	0.8	1.3	6.1	1.8	1.6	1.1	5.7	1.4	2.4	1.3	7.8
Sr	0.61	0.44	0.34	235.3	0.47	0.18	0.31	201.0	0.43	0.69	0.34	213.1
2σ	0.02	0.01	0.02	2.2	0.02	0.01	0.01	1.8	0.03	0.03	0.02	3.5
Y	4.24	3.84	8.23	3.13	17.33	16.92	16.05	3.67	23.62	5.36	8.19	4.73
2σ	0.05	0.05	0.08	0.06	0.13	0.14	0.13	0.07	0.20	0.09	0.10	0.18
Zr	53.7	3.0	35.1	28.9	60.9	25.1	73.2	9.9	9.0	5.2	33.8	15.6
2σ	0.3	0.1	0.3	0.4	0.4	0.2	0.8	0.2	0.7	0.1	0.3	0.7
Nb	0.34	0.51	0.20	0.47	0.22	0.19	0.21	0.60	0.44	0.72	0.20	4.94
2σ	0.01	0.01	0.01	0.03	0.01	0.01	0.01	0.06	0.02	0.03	0.01	0.42
Ba	-	0.01	-	2.69	-	-	-	4.76	-	-	-	41.60
2σ	-	0.00	-	0.49	-	-	-	0.66	-	-	-	3.90
La	0.05	0.08	0.01	3.40	0.03	0.01	0.02	3.63	0.18	0.12	0.01	8.33
2σ	0.00	0.01	0.00	0.06	0.00	0.00	0.00	0.09	0.06	0.01	0.00	0.58
Ce	0.62	0.63	0.21	13.86	0.38	0.10	0.25	12.89	0.76	1.06	0.21	21.98
2σ	0.02	0.01	0.01	0.18	0.01	0.01	0.01	0.26	0.17	0.03	0.01	0.85
Pr	0.21	0.15	0.10	2.22	0.12	0.04	0.10	1.95	0.15	0.27	0.10	2.81
2σ	0.01	0.01	0.01	0.04	0.01	0.00	0.01	0.04	0.02	0.01	0.01	0.09
Nd	2.08	0.99	1.27	11.19	1.24	0.51	1.22	9.63	1.17	1.86	1.31	12.61
2σ	0.06	0.04	0.05	0.18	0.05	0.03	0.05	0.20	0.09	0.09	0.06	0.39
Sm	1.43	0.31	1.21	2.49	0.93	0.57	1.14	2.17	1.17	0.60	1.19	2.37
2σ	0.06	0.02	0.06	0.09	0.05	0.04	0.05	0.08	0.06	0.06	0.07	0.11
Eu	0.57	0.12	0.54	0.73	0.45	0.31	0.55	0.63	0.53	0.20	0.53	0.71
2σ	0.02	0.01	0.02	0.03	0.02	0.02	0.02	0.02	0.02	0.02	0.02	0.03
Gd	1.73	0.50	1.75	1.82	1.81	1.40	2.09	1.66	2.76	0.71	1.74	1.86
2σ	0.07	0.03	0.07	0.08	0.07	0.07	0.08	0.07	0.11	0.06	0.09	0.09

Tb	0.21	0.10	0.25	0.20	0.37	0.30	0.38	0.20	0.56	0.13	0.26	0.22
2σ	0.01	0.01	0.01	0.01	0.01	0.01	0.01	0.01	0.02	0.01	0.01	0.01
Dy	1.05	0.70	1.54	0.99	2.95	2.67	2.85	1.02	4.27	0.98	1.53	1.25
2σ	0.04	0.03	0.05	0.05	0.08	0.08	0.08	0.05	0.11	0.05	0.07	0.07
Ho	0.15	0.15	0.30	0.14	0.65	0.63	0.60	0.15	0.90	0.22	0.30	0.19
2σ	0.01	0.01	0.01	0.01	0.02	0.02	0.02	0.01	0.03	0.01	0.02	0.01
Er	0.35	0.44	0.91	0.26	2.03	2.08	1.95	0.33	2.70	0.62	0.93	0.45
2σ	0.02	0.02	0.04	0.02	0.06	0.06	0.05	0.02	0.07	0.03	0.04	0.04
Tm	0.05	0.06	0.15	0.02	0.31	0.33	0.29	0.03	0.38	0.10	0.15	0.05
2σ	0.00	0.00	0.01	0.00	0.01	0.01	0.01	0.00	0.02	0.01	0.01	0.01
Yb	0.43	0.48	1.15	0.12	2.17	2.34	2.10	0.17	2.70	0.66	1.21	0.32
2σ	0.03	0.02	0.05	0.02	0.07	0.07	0.07	0.02	0.09	0.05	0.07	0.04
Lu	0.08	0.08	0.19	0.01	0.33	0.36	0.30	0.02	0.39	0.10	0.19	0.04
2σ	0.01	0.00	0.01	0.00	0.01	0.01	0.01	0.00	0.02	0.01	0.01	0.01
Hf	1.07	0.13	0.81	1.83	1.46	0.59	1.23	0.64	0.17	0.17	0.78	0.74
2σ	0.04	0.01	0.04	0.06	0.05	0.04	0.05	0.04	0.03	0.02	0.05	0.05
[Zr/Hf]	52	23	44	-	42	43	59	-	48	30	43	-
[Ti/Eu]	5447	6322	2069	-	9831	7243	3227	-	1700	3753	1990	-

Table A3 continued

Sample	**17698-3**			**17699-1**			**17700-1**	
Mineral	gt	gt	cpx	gt	gt	gt	gt	cpx
Description	G1	G9		G1	G11	G9	G9	
n	4	18	3	5	2	8	8	5
Ti	6560	2052	1380	3467	4259	2042	1540	1258
2σ	155	34	18	28	43	15	14	13
Ni	136.3	80.0	508.6	26.0	26.6	23.5	47.8	397.0
2σ	2.8	1.3	6.9	0.4	0.5	0.3	0.5	3.6
Sr	0.58	0.28	129.9	0.24	0.32	0.28	0.11	247.1
2σ	0.02	0.02	1.3	0.01	0.01	0.01	0.01	2.5
Y	26.67	13.82	2.57	16.97	16.36	7.58	13.95	2.62
2σ	0.26	0.14	0.05	0.17	0.15	0.09	0.13	0.05
Zr	82.5	24.4	10.4	72.9	71.9	30.2	18.2	25.2
2σ	0.7	0.3	0.2	0.6	0.5	0.3	0.2	0.4
Nb	0.19	0.21	0.27	0.14	0.18	0.17	0.19	0.62
2σ	0.01	0.01	0.01	0.01	0.01	0.01	0.01	0.03
Ba	-	-	0.53	0.03	0.03	-	0.01	2.58
2σ	-	-	0.05	0.01	0.01	-	0.01	0.28
La	0.05	0.02	2.66	0.01	0.02	0.01	0.01	5.00
2σ	0.01	0.00	0.04	0.00	0.00	0.00	0.00	0.07
Ce	0.55	0.23	9.07	0.16	0.23	0.19	0.11	18.82
2σ	0.02	0.01	0.14	0.01	0.01	0.01	0.01	0.23
Pr	0.16	0.07	1.27	0.07	0.09	0.08	0.03	2.92
2σ	0.01	0.01	0.02	0.01	0.00	0.01	0.00	0.04
Nd	1.52	0.62	5.98	0.67	0.93	0.91	0.41	13.35
2σ	0.07	0.04	0.13	0.04	0.04	0.05	0.03	0.20
Sm	1.17	0.50	1.37	0.66	0.81	0.82	0.43	2.57
2σ	0.08	0.04	0.07	0.05	0.04	0.05	0.03	0.09
Eu	0.57	0.26	0.44	0.35	0.42	0.37	0.24	0.71
2σ	0.03	0.02	0.02	0.02	0.02	0.02	0.01	0.02
Gd	2.47	1.16	1.15	1.52	1.72	1.13	1.13	1.73
2σ	0.11	0.07	0.06	0.08	0.07	0.06	0.05	0.08

Tb	0.52	0.26	0.13	0.35	0.39	0.19	0.25	0.19
2σ	0.02	0.01	0.01	0.01	0.01	0.01	0.01	0.01
Dy	4.44	2.19	0.73	2.84	3.01	1.32	2.24	0.81
2σ	0.12	0.07	0.04	0.09	0.08	0.05	0.06	0.04
Ho	1.02	0.52	0.10	0.69	0.68	0.30	0.52	0.11
2σ	0.03	0.02	0.01	0.02	0.02	0.01	0.02	0.01
Er	3.25	1.69	0.21	2.21	2.03	0.93	1.66	0.21
2σ	0.09	0.06	0.02	0.06	0.06	0.04	0.05	0.02
Tm	0.50	0.26	0.02	0.33	0.28	0.13	0.25	0.02
2σ	0.02	0.01	0.00	0.01	0.01	0.01	0.01	0.00
Yb	3.48	1.87	0.11	2.38	1.95	0.95	1.83	0.09
2σ	0.10	0.07	0.02	0.08	0.07	0.05	0.06	0.01
Lu	0.51	0.28	0.01	0.37	0.26	0.14	0.27	0.01
2σ	0.02	0.01	0.00	0.02	0.01	0.01	0.01	0.00
Hf	1.91	0.58	0.48	1.82	1.71	0.63	0.39	1.21
2σ	0.08	0.04	0.03	0.06	0.04	0.03	0.02	0.04
[Zr/Hf]	43	42	-	40	42	48	46	-
[Ti/Eu]	11424	7916	-	9993	10033	5474	6301	-

Table A4 PGE, Re-Os isotope ratios, Re-depletion (T_{RD}) and Re-Os model (T_{MA}) ages for olivine separates from Fort à la Corne peridotite xenoliths.

Sample	**15000**	**15001**	**17551-1**		**17651-2**	**17652**	**17654-1**	**17654-2**	**17655**	
Description				Re-run						Re-run
In ppb										
Os	1.633	0.397	0.011	10.997	0.541	0.317	5.033	5.428	0.152	3.105
Abs. 2σ	0.016	0.003	0.000	0.194	0.005	0.003	0.060	0.080	0.001	0.032
Ir	1.621	-	-	9.069	0.614	0.219	4.084	4.324	0.078	2.648
Abs. 2σ	0.048	-	-	0.795	0.017	0.017	0.207	0.221	0.002	0.092
Pt	3.910	0.040	0.010	17.465	1.261	1.473	3.314	21.647	0.158	1.413
Abs. 2σ	0.180	0.003	0.011	2.504	0.038	0.120	0.148	3.104	0.006	0.054
Pd	3.734	-	0.173	10.000	1.486	1.959	0.957	13.050	0.029	0.979
Abs. 2σ	0.186	-	0.033	2.215	0.263	0.166	0.281	1.996	0.004	0.048
Re	0.050	-	0.092	0.109	0.086	0.115	0.060	0.138	0.002	0.075
Abs. 2σ	0.005	-	0.011	0.013	0.010	0.011	0.010	0.012	0.002	0.008
$^{187}Os/^{188}Os$	0.14814	0.11472	0.15071	0.11361	0.12584	0.14138	0.11440	0.12173	0.13378	0.11476
Abs. 2σ	0.01384	0.00024	0.00325	0.00020	0.00021	0.00045	0.00023	0.00027	0.00018	0.00022
$^{187}Re/^{188}Os$	0.14814	-	38.21485	0.04760	0.76463	1.74493	0.05750	0.12278	0.05039	0.11633
Abs. 2σ	0.01384	-	4.72871	0.00567	0.08496	0.17154	0.00958	0.01059	0.05969	0.01291
In Ga										
$T_{RDerupt}$	1.9	-	5.5	2.1	0.5	-1.5	2.0	1.0	-0.8	1.9
Abs. 2σ	0.52	-	1.39	0.53	0.48	0.53	0.52	0.49	0.50	0.52
T_{MA}	2.9	-	0.0	2.3	-0.4	0.6	2.2	1.3	-0.9	2.6
Abs. 2σ	0.89	-	0.01	0.61	0.61	0.17	0.62	0.70	0.59	0.77

Table A4 continued

Sample Description	**17656**	**17679**	**17681**	**17686**	**17694-2**	**17695-1**	**17696-1**	**17696-2**	**17696-3**	**17697-1**
In ppb										
Os	5.265	3.246	13.498	4.931	5.008	3.659	3.110	2.294	2.682	2.115
Abs. 2σ	0.052	0.052	0.266	0.089	0.080	0.039	0.030	0.020	0.024	0.022
Ir	4.474	1.579	17.040	3.756	3.967	3.079	1.895	2.511	2.986	1.767
Abs. 2σ	0.205	0.185	2.369	0.280	0.373	0.113	0.068	0.097	0.103	0.059
Pt	5.744	3.131	19.880	16.449	6.612	2.693	2.190	2.597	2.243	2.905
Abs. 2σ	0.293	3.010	2.830	3.808	0.843	0.111	0.091	0.107	0.081	0.116
Pd	6.296	-	3.672	5.476	3.277	1.671	1.379	2.320	0.290	1.194
Abs. 2σ	1.121	-	0.381	1.263	0.860	0.144	0.092	0.369	0.036	0.097
Re	0.115	0.091	0.087	0.099	0.260	0.034	0.037	0.049	0.014	0.069
Abs. 2σ	0.013	0.009	0.008	0.015	0.049	0.004	0.005	0.007	0.004	0.008
$^{187}Os/^{188}Os$	0.11239	0.11257	0.11448	0.12073	0.11281	0.11251	0.11244	0.11574	0.12177	0.12097
Abs. 2σ	0.00020	0.00034	0.00020	0.00016	0.00022	0.00021	0.00023	0.00024	0.00019	0.00020
$^{187}Re/^{188}Os$	0.10515	0.13504	0.03093	0.09633	0.25000	0.04522	0.05672	0.10209	0.02603	0.15788
Abs. 2σ	0.01198	0.01323	0.00279	0.01484	0.04676	0.00577	0.00834	0.01409	0.00648	0.01824
In Ga										
$T_{RDerupt}$	2.2	2.2	1.9	1.1	2.2	2.2	2.2	1.8	0.9	1.1
Abs. 2σ	0.53	0.54	0.52	0.49	0.53	0.53	0.53	0.51	0.49	0.49
T_{MA}	2.9	3.2	2.1	1.4	5.2	2.5	2.5	2.3	1.0	1.6
Abs. 2σ	0.77	0.88	0.57	0.65	2.25	0.61	0.64	0.72	0.52	0.82

Table A4 continued

Sample Description	**17697-2**	**17697-3**	**17697-4**	**17698-2**	**17698-3**	**17699-1**	**17700-1**	Re-run
In ppb								
Os	0.343	0.629	5.039	3.307	6.082	0.385	2.349	2.368
Abs. 2σ	0.003	0.005	0.074	0.051	0.068	0.003	0.037	0.041
Ir	0.186	1.908	3.740	2.858	5.247	0.309	1.603	1.603
Abs. 2σ	0.019	0.071	0.244	0.188	0.280	0.008	0.072	0.072
Pt	1.323	2.547	7.854	8.240	8.140	0.197	2.217	2.217
Abs. 2σ	0.139	0.111	1.553	0.904	0.597	0.009	0.137	0.137
Pd	17.433	1.135	1.947	3.530	5.122	0.009	1.440	1.440
Abs. 2σ	7.750	0.294	0.103	0.685	0.534	0.008	0.196	0.196
Re	0.082	0.085	0.060	0.079	0.119	0.001	0.045	0.045
Abs. 2σ	0.008	0.009	0.007	0.011	0.010	0.005	0.004	0.004
$^{187}Os/^{188}Os$	0.13709	0.11187	0.12174	0.12595	0.11811	0.11088	0.11560	0.11521
Abs. 2σ	0.00032	0.00020	0.00024	0.00024	0.00019	0.00039	0.00050	0.00045
$^{187}Re/^{188}Os$	1.14712	0.65018	0.05778	0.11465	0.09387	0.01176	0.09124	0.09050
Abs. 2σ	0.11836	0.07255	0.00667	0.01575	0.00801	0.05738	0.00782	0.00778
In Ga								
$T_{RDerupt}$	-1.0	2.4	0.9	0.4	1.5	2.4	1.8	1.9
Abs. 2σ	0.51	0.54	0.49	0.48	0.50	0.55	0.52	0.52
T_{MA}	0.7	-4.5	1.1	0.5	1.8	2.5	2.3	2.3
Abs. 2σ	0.31	2.04	0.57	0.66	0.67	0.66	0.69	0.69

Table A5 Thermobarometry of peridotite xenoliths from Fort à la Corne.

		Temperature (°C)			Pressure (GPa)	
Calculated iteratively using		Taylor (1998)	Average: Canil (1999) & Griffin et al. (1989)	Nimis & Taylor (2000)	Nimis & Taylor (2000)	Nickel & Green (1985)
		P_{NG85}		P_{NT00}	T_{NT00}	T_{TA98}
		T_{TA98}	T_{Ni}	T_{NT00}	P_{NT00}	P_{NG85}
		Enstatite in cpx	Ni in grt and ol	Enstatite in cpx	Cr (cpx-grt)	Al (grt - opx)
Sample	Paragenesis					
15000	ol, grt (G9)		1012			
17651-1	cpx, grt (G11)		1255	1221	5.1	
17651-2	grt (G1)		1411			
	grt (G9)		1062			
17652	cpx			1038	5.0	
17654-1	cpx			1045	4.6	
17654-2	cpx, grt (G9)		1203	1215	5.1	
17655	ol,cpx, grt (G11)		1012	1040	5.0	
	ol,cpx, grt (G9)		1058	1040	5.0	
17656	cpx, grt (G11)		1281	1254	5.4	
17679	opx, cpx, grt (G1)	843	1122	842	2.7	2.0
	opx, cpx, grt (G9 low Cr)	843	774	842	2.7	2.0
	opx, cpx, grt (G9 high Cr)	843	1027	842	2.7	2.0
17681	cpx1, grt (G9)		1014	976	4.6	
	cpx2, grt (G9)			1035	5.5	
17686	grt (G11)		1278			
17694-2	grt (G9)		1263			
17695-1	cpx			1056	4.9	

17696-1	ol, grt (G11)		1292			
17696-2	ol, grt (G11)		1252			
17696-3	ol, grt (G9)		1262			
17697-1	ol, cpx, grt (G9)		1128	1070	5.0	
	ol, cpx, grt (G1 low Fe)		1193	1252	5.5	
17697-2	ol, cpx, grt (G1 high Fe)		1237	1252	5.5	
	ol, cpx, grt (G9)		1099	1252	5.5	
17697-4	ol, grt (G9)		1266			
17698-2	ol, grt (G9)		1125			
17698-3	ol, opx, cpx, grt (G1)	1187	1426	1170	5.1	5.3
	ol, opx, cpx, grt (G9)	1185	1215	1170	5.1	5.3
	ol, grt (G1)		916			
17699-1	ol, grt (G11)		921			
	ol, grt (G9)		895			
17700-1	ol, cpx, grt (G9)		1059	1033	4.7	

Appendix B – Geochemical data for Fort à la Corne eclogite micro-xenolith

Data reported in Appendix B are averaged; for the complete dataset see the UAL Dataverse dataset: “Geochemical data for Fort à la Corne eclogite microxenoliths” at https://doi.org/10.7939/DVN/GP4BJT

Table B1 Natural and synthetic materials used for calibration, and as secondary standard.

Reference Material	Element	Crystal	Mineral	Origin		Reference
Frank Smith Pyrope Garnet	SiO_2	TAP	Grt	Frank Smith kimberlite, South Africa	Royal Ontario Museum collection. Composition from bulk XRF analysis	
	Al_2O_3	TAP	Grt, Cpx			
	MgO	TAP	Grt			
Gore Garnet	Al_2O_3	TAP	Grt	Gore Mountain Mine, New York, USA	Similar to UWG-2 from Vielzeuf et al. (2005).	Vielzeuf D, Champenois M, Valley JW, Brunet F, and Devidal JL (2005) SIMS analyses of oxygen isotopes; matrix effects in Fe-Mg-Ca garnets. Chem Geol 223:208-226. doi:10.1016/j.chemgeo.2005.07.008
	FeO	LIF	Grt			
$Ca_5(PO_4)_3F$ Apatite	P_2O_5	PET	Grt, Cpx	Dwyer Mine, Wilberforce, Ontario, Canada	Apatite from alkaline source	Tacker RC (2004) Hydroxyl ordering in igneous apatite. Am Mineral 89:1411–1421
$KAlSi_3O_8$ Sanidine	K_2O	PET	Grt, Cpx	Itrongay, Madagascar	Fe-bearing K-feldspar	Ackermann S, Kunz M, Armbruster T, Schefer J and Hanni H (2005) Cation distribution in a Fe-bearing K-feldspar from Itrongay, Madagascar. A combined neutron-and X-ray single crystal diffraction study. Schweiz Miner Petrog 84:345-354. doi.org/10.5169/seals-63754
$NaAlSi_3O_8$ Albite	Na_2O	TAP	Grt, Cpx	Virginia, USA	Albite Harvard 131705, from the Harvard Mineralogical Museaum	McGuire AV, Francis CA, Dyar MD (1992) Minerals standards for electron microprobe analyses of oxygen. Am Mineral 77:1087-1091 (http://iageo.com/microanalytical-reference-materials/)
	SiO_2	TAP	Cpx			
	Al_2O_3	TAP	Cpx			
$CaMgSi_2O_6$ Diopside	CaO	PET	Grt, Cpx	Wakefield, Quebec, Canada	Astimex, palest blue	http://astimex.com/com/catalog/min.html
	MgO	TAP	Grt, Cpx			
	SiO_2	TAP	Cpx			
Labradorite	Al_2O_3	TAP	Cpx	Lake County, Oregon, USA	USNM 115900	Jarosewich E, Nelen JA, Norberg JA (1980) Reference samples for electron microprobe

Fayalite	FeO	LIF	Grt, Cpx	Rockport, Massachusetts, USA	USNM 85276	analysis. Geostanard Newslett 4:43-47 (https://mineralsciences.si.edu/facilities/standards.htm)
Spessartine	MnO FeO	LIF LIF	Grt, Cpx Cpx	Navegadora Mine, Minas Gerais, Brazil		www.minsocam.org/msa/Special/Pig/PIG_Articles/etched_spssrtn.pdf
Ni (Nickel Wire)	NiO	LIF	Grt, Cpx	Synthetic	Alfa Aesar, 43132, Nickel wire, 0.5 mm dia, annealed, 99.98 % (metals basis)	https://www.alfa.com/en/catalog/043132/
Cr_2O_3 (Chromium Oxide)	Cr_2O_3	PET	Grt, Cpx	Synthetic	Alfa Aesar, 36258, Chromium(III) oxide, 99.6 % purity (metals basis)	
TiO_2 (Rutile)	TiO_2	PET	Grt, Cpx	Synthetic	synthetic TiO_2 from MTI	http://www.mtixtl.com/tio2substrates.aspx
Secondary Standard Cr-Diopside				Megacrystic from Russian kimberlite	In-house Standard	

Table B2 - Part A Averaged trace element concentrations (ppm) for garnet (grt) and clinopyroxene (cpx) crystals in barren eclogites. Only omphacitic clinopyroxenes have been analysed for trace elements.

Sample #	**52006-1**		**52006-2**		**52006-3**		**52006-4**		**52006-5**		**52006-6**	
Mineral	grt	cpx	grt	cpx	grt	cpx	grt	cpx	grt	cpx	grt	cpx
n	7	9	7	4	5	10	6	8	6	4	5	7
Sc	62.97	21.49	57.79	17.42	72.14	22.06	56.44	20.49	46.80	15.84	52.01	14.28
Ti	1085.4	2099.4	1047.0	1454.0	770.4	1461.3	1647.0	2059.0	1252.8	2587.5	603.7	1149.2
V	90.78	527.1	63.75	272.3	113.7	337.8	129.9	531.7	88.63	447.9	81.54	278.5
Co	53.37	21.90	85.74	37.26	73.50	33.73	55.13	22.88	88.95	34.41	87.38	35.03
Ni	37.06	449.2	41.89	557.2	21.24	276.4	38.38	461.5	33.31	439.4	35.74	582.6
Zn	23.20	14.44	66.44	50.53	79.58	67.30	24.52	15.41	85.22	60.45	86.90	66.37
Ga	8.47	11.77	8.76	14.86	9.62	16.61	10.21	12.10	9.44	20.90	9.67	22.26
Rb	0.0135	0.418	0.0087		-	3.344	-	0.073	0.0092	0.0443	0.0181	1.551
Sr	0.179	184.1	0.327	283.0	0.423	240.9	0.0686	189.3	0.366	186.5	0.448	247.3
Y	14.46	2.29	19.02	1.23	17.93	1.25	13.83	2.29	18.63	0.81	10.05	0.66
Zr	8.27	15.73	10.60	17.05	6.48	22.08	10.95	15.21	10.47	19.49	2.97	12.66
Nb	0.0437	0.384	0.0021	0.0029	0.0103	1.25	0.0444	0.441	0.466	0.284	0.0048	1.31
Ba	0.204	1.06	0.493	0.322	0.0012	73.90	0.0086	2.13	0.115	0.114	0.0188	130.55
La	0.0599	13.30	0.0330	5.51	0.0176	3.34	0.0066	14.45	0.0279	3.24	0.0129	2.33
Ce	0.123	22.78	0.177	13.63	0.214	10.13	0.0419	25.33	0.346	11.01	0.148	6.70
Pr	0.0216	1.88	0.0583	1.64	0.0953	1.46	0.0119	2.01	0.1425	1.67	0.0618	0.925
Nd	0.187	6.56	0.691	7.04	1.15	6.70	0.147	6.79	1.47	7.17	0.749	4.02
Sm	0.234	1.50	0.916	1.63	1.19	1.43	0.267	1.47	1.08	1.13	0.674	0.724
Eu	0.177	0.534	0.603	0.586	0.680	0.447	0.197	0.539	0.597	0.331	0.568	0.262
Gd	0.866	1.35	2.25	1.13	2.32	0.964	0.934	1.32	2.06	0.673	1.32	0.402
Tb	0.232	0.159	0.453	0.111	0.412	0.101	0.235	0.155	0.419	0.0657	0.239	0.0448
Dy	2.13	0.721	3.38	0.432	3.03	0.403	2.09	0.689	3.20	0.258	1.74	0.191

Ho	0.530	0.0938	0.706	0.0503	0.674	0.0507	0.522	0.0957	0.699	0.0331	0.377	0.0265
Er	1.82	0.186	2.11	0.0883	2.08	0.0960	1.74	0.184	2.14	0.0596	1.15	0.0613
Tm	0.273	0.0165	0.285	0.0078	0.285	0.0091	0.255	0.0165	0.293	0.0045	0.159	0.0060
Yb	2.07	0.0852	2.04	0.0348	2.06	0.0504	1.98	0.0846	2.10	0.0229	1.19	0.0440
Lu	0.322	0.0082	0.292	0.0024	0.288	0.0051	0.300	0.0078	0.303	0.0023	0.172	0.0169
Hf	0.114	0.767	0.123	0.695	0.0683	0.721	0.194	0.744	0.126	0.698	0.0402	0.575
Pb	0.0278	0.771	0.0159	1.00	-	0.689	0.0026	0.834	0.0052	0.325	0.0019	0.288
Th	0.0125	0.463	0.0136	0.183	0.0011	0.228	0.0022	0.503	0.0076	0.0639	0.0028	0.138
U	0.0149	0.0788	0.0168	0.0337	0.0074	0.04172	0.0109	0.104	0.0307	0.0149	0.0094	0.0366

Table B2 - Part A continued

Sample #	52006-7			52006-9		52006-11		52006-12		52006-13		52006-14	
Mineral	grt	grt	cpx	grt	cpx	grt	cpx	grt	cpx	grt	cpx	grt	cpx
n	2	4	1	7	4	6	7	7	8	5	4	6	2
Sc	32.68	34.58	5.58	50.38	18.17	46.49	15.80	56.08	19.33	95.46	42.65	69.39	21.05
Ti	750.5	863.5	1229.0	1377.8	2614.5	1584.9	1876.9	875.5	1349.4	739.0	4345.3	367.4	1378.0
V	48.33	54.74	193.8	90.21	427.3	121.3	416.4	89.50	358.9	137.0	486.0	104.9	407.4
Co	75.45	78.05	21.80	65.34	21.57	95.75	41.31	83.35	35.27	53.89	16.66	55.30	19.43
Ni	28.62	29.23	266.6	30.21	300.5	50.57	651.8	19.48	250.6	6.42	103.0	3.43	67.40
Zn	58.30	60.08	10.66	29.91	15.13	75.50	77.31	85.66	66.26	32.74	20.15	95.08	65.25
Ga	6.09	7.84	16.57	11.90	15.33	12.58	43.42	11.30	17.28	7.87	12.99	9.81	23.73
Rb	-	0.0061	0.290	-	1.310	0.178	6.299	0.0257	0.0737	-	0.0371	0.0081	-
Sr	0.963	1.12	44.13	0.115	320.6	0.434	275.1	0.425	347.7	0.0604	169.6	0.724	324.4
Y	9.63	9.23	0.402	23.97	5.00	14.28	1.33	23.38	1.78	35.39	2.98	35.49	0.67
Zr	47.12	16.72	21.00	14.26	47.36	7.26	21.71	5.39	14.66	14.48	42.86	6.91	25.27
Nb	1.18	1.20	0.867	0.0331	1.08	0.0328	1.25	0.0189	0.0261	0.0006	0.0440	0.0002	-
Ba	0.0750	-	16.40	0.0081	0.427	0.0790	1102.39	0.0594	0.151	-	1.17	-	-
La	0.0970	0.0440	0.761	0.0122	14.09	0.0471	7.69	0.0372	3.79	0.0014	2.22	0.0037	0.335
Ce	0.637	0.601	3.12	0.114	38.73	0.313	20.60	0.209	12.58	0.0269	10.67	0.118	2.46
Pr	0.287	0.299	0.556	0.0367	4.78	0.0893	2.44	0.0751	1.83	0.0216	2.14	0.108	0.697
Nd	3.69	3.63	2.96	0.422	19.60	0.868	9.58	0.839	8.42	0.441	12.30	1.97	4.65
Sm	3.53	2.89	0.634	0.508	3.78	0.752	1.64	0.902	1.74	0.812	3.15	2.21	0.975
Eu	1.70	1.47	0.174	0.318	1.11	0.498	0.540	0.560	0.569	0.529	0.991	1.28	0.314
Gd	4.12	2.88	0.355	1.65	2.79	1.57	0.970	2.32	1.22	2.61	2.29	4.06	0.544
Tb	0.463	0.355	0.0326	0.413	0.327	0.308	0.0964	0.504	0.128	0.611	0.236	0.778	0.0498
Dy	2.29	1.87	0.162	3.66	1.47	2.46	0.414	3.97	0.568	5.33	1.03	5.91	0.216

Ho	0.336	0.334	0.0156	0.895	0.203	0.543	0.0555	0.860	0.0742	1.31	0.124	1.32	0.0253
Er	0.799	0.911	0.0185	2.93	0.391	1.70	0.114	2.60	0.133	4.46	0.219	4.17	0.0517
Tm	0.0954	0.119	-	0.435	0.0386	0.248	0.0097	0.355	0.0124	0.659	0.0176	0.588	0.0045
Yb	0.649	0.849	0.0139	3.25	0.177	1.77	0.0583	2.48	0.0628	4.91	0.0840	4.23	0.0227
Lu	0.0870	0.117	-	0.483	0.0180	0.266	0.0076	0.365	0.0057	0.735	0.0078	0.622	0.0021
Hf	0.562	0.171	1.03	0.166	1.58	0.106	0.780	0.0644	0.646	0.225	1.55	0.0978	1.33
Pb	0.0036	0.0015	0.0486	0.0036	1.28	0.0040	0.594	0.0017	0.711	0.0025	0.180	0.0020	0.501
Th	0.0129	0.0028	0.0180	0.0057	0.395	0.0097	0.167	0.0099	0.0402	0.0017	0.0800	-	0.0033
U	0.0925	0.0827	0.00680	0.0172	0.0777	0.0363	0.0304	0.0052	0.0106	0.0019	0.0185	0.0002	0.00042

Table B2 -Part A continued

Sample #	52006-15		52006-16		52006-17		52006-18		52006-19	52006-20	52006-21	
Mineral	grt	cpx	grt	cpx	grt	cpx	grt	cpx	grt	grt	grt	cpx
n	6	8	7	3	5	5	6	5	7	6	5	7
Sc	52.25	18.15	73.27	26.29	48.62	19.45	44.71	15.92	68.08	61.06	66.74	21.50
Ti	1555.7	2439.8	102.3	1592.5	79.9	1671.0	65.9	2630.4	147.6	3156.5	882.4	1815.0
V	106.2	405.1	122.3	429.5	95.14	359.8	76.53	361.0	171.3	155.0	93.15	349.1
Co	76.54	23.66	28.29	17.23	29.90	20.36	42.37	33.67	13.54	49.52	70.26	30.69
Ni	32.45	332.4	29.13	309.9	29.88	324.2	42.07	525.3	14.23	8.62	30.50	360.2
Zn	33.40	16.65	8.85	11.36	10.16	16.12	10.03	40.50	12.88	52.83	18.46	49.03
Ga	11.30	13.89	10.58	8.46	12.11	10.44	11.67	15.04	15.00	13.48	10.08	23.19
Rb	-	0.239	-	0.0101	0.014	0.151	-	0.205	-	-	-	1.301
Sr	0.222	313.4	0.165	442.4	0.229	365.0	0.315	246.6	0.463	0.755	0.197	329.4
Y	12.59	1.14	31.81	5.78	11.55	3.45	16.17	1.71	40.18	40.59	11.73	2.02
Zr	3.09	11.56	16.26	66.09	6.15	60.71	10.17	30.34	29.63	18.41	6.86	25.32
Nb	0.0133	0.358	0.109	1.12	0.123	1.27	0.0131	0.921	0.0051	0.0333	0.137	0.865
Ba	-	0.822	-	0.1983	0.593	1.99	-	1.66	-	-	0.0136	198.27
La	0.0302	12.97	0.0182	17.49	0.0429	13.83	0.0229	6.15	0.0032	0.0129	0.0207	11.94
Ce	0.241	33.71	0.211	57.91	0.199	53.16	0.262	22.31	0.0709	0.186	0.235	32.66
Pr	0.0763	3.88	0.0751	7.78	0.0589	7.10	0.102	3.14	0.0519	0.0975	0.0854	3.81
Nd	0.659	14.08	0.710	33.35	0.560	30.82	1.03	13.97	0.964	1.56	0.797	15.22
Sm	0.411	1.68	0.592	5.49	0.416	4.95	0.903	2.49	1.57	2.29	0.556	2.45
Eu	0.296	0.478	0.350	1.45	0.248	1.28	0.574	0.728	0.844	1.21	0.313	0.727
Gd	1.15	0.976	1.74	3.43	0.895	2.83	2.01	1.55	3.87	4.88	1.21	1.57
Tb	0.259	0.0994	0.463	0.369	0.211	0.274	0.404	0.150	0.802	0.931	0.264	0.156
Dy	2.13	0.414	4.44	1.66	1.78	1.13	2.86	0.607	6.24	6.72	2.03	0.668

Ho	0.479	0.0498	1.18	0.235	0.429	0.143	0.613	0.0743	1.47	1.52	0.441	0.0870
Er	1.43	0.0888	4.15	0.4897	1.39	0.276	1.81	0.133	4.69	4.55	1.28	0.168
Tm	0.191	0.0074	0.649	0.0478	0.204	0.0233	0.243	0.0109	0.682	0.642	0.173	0.0149
Yb	1.35	0.0349	4.95	0.258	1.47	0.116	1.67	0.0523	5.04	4.59	1.22	0.0736
Lu	0.191	0.0036	0.772	0.0270	0.231	0.0114	0.243	0.0056	0.754	0.681	0.183	0.0072
Hf	0.0670	0.384	0.256	1.98	0.0698	1.74	0.108	0.943	0.578	0.261	0.0584	0.683
Pb	0.0014	0.603	-	0.860	0.0049	0.913	0.0027	0.424	0.0026	0.0033	-	1.01
Th	0.0176	0.267	0.0066	0.342	0.0092	0.203	0.0061	0.122	0.0008	0.0030	0.0054	0.265
U	0.0604	0.0390	0.0288	0.0663	0.0135	0.0442	0.0277	0.0256	0.0015	0.0118	0.0254	0.04806

Table B2 -Part A continued

Sample #	52006-22		52006-23		52006-24		52006-25	52006-26	
Mineral	grt	cpx	grt	cpx	grt	cpx	grt	grt	cpx
n	7	4	7	6	8	5	6	10	2
Sc	60.86	27.82	44.00	25.14	72.88	23.13	102.8	91.51	16.22
Ti	894.4	1701.2	1179.3	2907.2	270.3	881.4	384.7	1109.1	2104.0
V	98.72	389.6	99.97	368.0	101.1	357.4	387.9	225.3	371.0
Co	49.40	16.60	58.57	19.38	53.91	20.67	36.55	74.45	33.74
Ni	19.79	206.9	30.86	280.1	3.15	63.20	0.50	39.97	452.7
Zn	19.49	11.49	19.16	11.11	97.86	75.00	133.75	33.95	28.76
Ga	10.72	7.98	13.10	10.62	11.47	21.19	12.70	8.62	13.78
Rb	-	0.769	-	0.383	-	0.0093	0.0156	0.0753	0.0035
Sr	0.151	426.3	0.112	237.6	0.585	287.2	0.0200	0.494	242.3
Y	16.08	4.82	26.10	4.03	45.83	0.530	117.4	8.04	0.276
Zr	11.03	84.30	6.43	44.57	7.58	25.90	13.47	8.16	5.72
Nb	0.1155	0.990	0.0234	2.14	0.0243	0.0708	0.0332	0.128	1.03
Ba	0.0220	0.185	-	3.47	0.0029	0.0277	-	-	0.201
La	0.0159	14.94	0.0139	10.41	0.0044	0.247	0.0350	0.0825	7.47
Ce	0.170	51.24	0.123	33.10	0.126	2.69	0.0973	0.648	17.59
Pr	0.0609	7.09	0.0345	4.17	0.126	0.889	0.0824	0.216	1.65
Nd	0.618	31.16	0.311	17.12	2.54	6.55	3.10	1.86	5.36
Sm	0.510	5.28	0.321	2.80	3.19	1.50	6.96	0.870	0.714
Eu	0.286	1.42	0.230	0.776	1.61	0.395	1.68	0.403	0.213
Gd	1.23	3.23	1.19	1.89	5.88	0.729	12.48	1.25	0.368
Tb	0.289	0.340	0.357	0.215	1.11	0.0655	2.40	0.218	0.0334
Dy	2.40	1.51	3.52	1.06	7.92	0.254	18.03	1.46	0.130

Ho	0.581	0.204	0.966	0.161	1.71	0.0314	4.27	0.306	0.0164
Er	1.85	0.403	3.47	0.354	5.13	0.0529	13.91	0.896	0.0280
Tm	0.268	0.0362	0.526	0.0372	0.717	0.0046	2.09	0.126	0.0028
Yb	1.96	0.192	4.08	0.221	5.08	0.0255	15.17	0.922	0.0099
Lu	0.292	0.0194	0.656	0.0269	0.738	0.0024	2.38	0.142	0.0012
Hf	0.129	2.57	0.0886	1.72	0.0853	1.39	0.235	0.182	0.185
Pb	-	0.715	0.0035	0.457	0.0030	0.386	0.0215	0.0031	0.582
Th	0.0040	0.246	0.0063	0.246	-	0.0018	0.0220	0.0247	0.145
U	0.0235	0.03793	0.0295	0.03837	0.0008	0.00073	0.0062	0.0849	0.0222

Table B2 -Part A continued

Sample #	**53001-1**	**53001-2**	**17664**	**17672**
Mineral	grt	grt	grt	grt
n	7	5	7	5
Sc	57.09	15.45	50.32	61.77
Ti	39.5	18.4	115.5	266.7
V	45.11	20.80	127.7	293.7
Co	29.84	49.42	3.54	0.47
Ni	29.53	49.54	3.82	0.97
Zn	5.52	6.22	9.07	15.96
Ga	6.30	7.06	10.05	17.65
Rb	-	-	-	-
Sr	0.0854	0.267	0.0520	0.113
Y	10.81	5.17	71.45	44.21
Zr	1.59	6.00	20.72	16.19
Nb	0.0108	0.0006	0.0055	-
Ba	0.117	-	0.0071	0.0213
La	0.0030	0.0139	0.0478	0.605
Ce	0.0505	0.127	0.138	0.838
Pr	0.0217	0.0443	0.0554	0.202
Nd	0.249	0.514	0.990	2.81
Sm	0.250	0.638	1.85	3.52
Eu	0.174	0.497	1.04	1.15
Gd	0.736	1.36	5.75	6.71
Tb	0.189	0.231	1.35	1.24
Dy	1.64	1.28	11.09	8.31

Ho	0.398	0.200	2.64	1.69
Er	1.22	0.415	8.37	4.89
Tm	0.177	0.0429	1.22	0.661
Yb	1.21	0.242	8.90	4.69
Lu	0.173	0.0266	1.34	0.667
Hf	0.0156	0.0610	0.300	0.226
Pb	-	0.0076	0.0072	0.0428
Th	0.0003	0.0017	0.0209	0.119
U	0.0064	0.0139	0.0025	0.0410

Table B2 - Part B Averaged trace element concentrations (ppm) for garnet in diamondiferous eclogites. Only primary compositions are averaged, while for metasomatised garnets, the least (meta low) and most (meta high) metasomatised compositions are given.

Sample #	**SGF-003 50036**			**SGF-008 50076**		**SGF-009 50095**	**SGF-020 50138**	**SGF-021 50148**	**SGF-025 50223**	
Mineral	primary	meta low	meta high	primary	meta				primary	meta
n	6	1	1	3	1	10	4	7	12	1
Sc	69.92	64.53	73.60	80.17	93.00	62.19	57.39	75.81	90.74	92.40
Ti	1695.7	1610.0	2986.0	1715.3	2637.0	2757.7	1482.0	1365.7	1882.4	2612.0
V	136.9	121.8	168.3	355.8	408.3	111.2	191.1	330.4	348.1	418.9
Co	67.44	62.70	70.18	56.17	53.03	69.51	74.45	54.25	52.82	55.40
Ni	78.67	73.50	75.00	130.4	116.8	32.26	121.1	65.24	40.55	37.20
Zn	47.47	46.20	48.10	31.03	25.50	90.41	35.15	53.37	31.35	28.30
Ga	9.50	9.27	12.10	8.11	9.52	10.27	12.08	8.56	9.34	11.00
Rb	0.0200	0.2660	0.8900	0.0227	0.0990	0.0130	0.0275	0.0180	0.0388	21.4000
Sr	1.04	4.93	7.06	0.503	2.81	0.948	0.339	0.678	0.586	6.30
Y	11.35	10.56	13.32	31.14	28.38	32.82	7.36	40.90	32.23	33.70
Zr	7.85	15.20	45.00	13.29	26.83	13.84	5.88	9.53	11.78	19.67
Nb	0.267	0.716	1.2500	0.135	0.631	0.0952	0.401	0.153	0.142	0.730
Ba	0.0536	5.30	19.30	0.0135	1.52	0.0132	0.107	0.0318	5.01	9.60
La	0.0449	0.5710	1.11	0.0233	0.4080	0.0266	0.0344	0.0277	0.0193	0.2950
Ce	0.450	1.28	2.51	0.190	0.990	0.274	0.237	0.262	0.179	0.788
Pr	0.141	0.218	0.368	0.0606	0.168	0.0994	0.0598	0.0920	0.0608	0.152
Nd	1.16	1.34	2.32	0.646	1.23	0.982	0.391	0.856	0.603	1.14
Sm	0.605	0.639	1.08	0.477	0.720	0.877	0.249	0.603	0.539	0.797
Eu	0.370	0.369	0.534	0.235	0.321	0.459	0.175	0.273	0.225	0.265
Gd	1.16	1.20	1.90	1.27	1.56	2.21	0.646	1.93	1.57	1.44

Tb	0.248	0.227	0.359	0.376	0.366	0.544	0.162	0.587	0.371	0.336
Dy	1.90	1.92	2.39	3.84	3.47	4.77	1.25	5.80	3.66	3.44
Ho	0.437	0.414	0.524	1.12	1.03	1.22	0.280	1.50	1.14	1.22
Er	1.35	1.26	1.54	4.24	4.05	4.16	0.846	5.03	4.44	5.12
Tm	0.191	0.176	0.209	0.715	0.734	0.644	0.113	0.770	0.669	0.787
Yb	1.35	1.33	1.39	5.67	5.76	4.86	0.800	5.70	5.01	6.10
Lu	0.194	0.189	0.223	0.889	0.917	0.755	0.116	0.848	0.848	1.04
Hf	0.173	0.277	0.983	0.336	0.723	0.257	0.181	0.254	0.294	0.485
Pb	0.0029	0.0550	0.0710	0.0108	0.0128	0.0027	0.0041	0.0055	0.0044	0.0145
Th	0.0064	0.0730	0.134	0.0025	0.0240	0.0020	0.0155	0.0033	0.0051	0.0560
U	0.0165	0.0356	0.0419	0.0064	0.0228	0.0054	0.0249	0.0085	0.0049	0.0147

Table B2 - Part B continued

Sample #	SGF-025 50224-1	SGF-025 50224-2	SGF-025 50224-3			SGF-025 50225	SGF-025 50226	SGF-034	SGF-039 50443-1	SGF-039 50443-2
Mineral			primary	meta low	meta high					
n	4	2	2	1	1	5	2	8	5	1
Sc	88.23	88.85	96.84	93.10	94.20	81.86	89.31	113.5	34.45	56.91
Ti	2327.3	2399.5	2447.0	2702.0	3102.0	2161.0	2450.0	1024.3	1999.4	3001.0
V	393.8	406.1	429.7	455.5	525.2	362.4	411.9	443.8	127.3	117.9
Co	53.25	56.65	55.53	49.95	48.65	52.12	59.23	51.88	66.52	61.17
Ni	41.44	51.40	45.65	43.00	44.60	47.32	53.83	58.04	87.38	42.54
Zn	29.70	46.10	30.10	25.10	25.90	34.72	38.55	68.48	39.52	93.10
Ga	9.77	19.98	10.89	11.09	12.36	9.86	11.41	9.51	9.84	12.01
Rb	0.0110	0.3350	0.0070	0.0940	0.0860	0.0140	0.0110	0.0089	0.0082	0.0050
Sr	0.499	3.06	0.489	0.990	1.01	0.466	0.499	0.561	0.905	1.39
Y	33.15	36.07	30.30	26.50	24.24	30.55	28.52	48.55	7.96	29.63
Zr	17.75	17.65	9.67	10.87	11.41	9.22	16.60	7.10	15.79	14.26
Nb	0.161	0.358	0.174	0.261	0.346	0.150	0.141	0.230	0.567	0.0720
Ba	0.1163	176.5	0.0735	1.14	1.22	0.0530	0.0140	0.0045	0.0020	0.0074
La	0.0244	0.1790	0.0385	0.0830	0.128	0.0191	0.0212	0.0198	0.0747	0.0378
Ce	0.232	0.488	0.293	0.422	0.476	0.191	0.197	0.339	0.771	0.350
Pr	0.0833	0.102	0.0990	0.133	0.140	0.0631	0.0633	0.137	0.239	0.117
Nd	0.849	0.790	0.908	1.05	1.04	0.611	0.695	1.08	1.92	1.20
Sm	0.595	0.535	0.651	0.820	0.790	0.477	0.512	0.674	0.785	1.18
Eu	0.256	0.231	0.137	0.162	0.174	0.146	0.212	0.339	0.358	0.599
Gd	1.42	1.45	1.36	1.53	1.42	1.25	1.14	2.16	1.13	2.78
Tb	0.357	0.421	0.178	0.188	0.167	0.233	0.267	0.776	0.212	0.582

Dy	3.91	4.48	2.14	2.02	1.75	2.69	3.03	7.52	1.50	4.66
Ho	1.21	1.34	0.993	0.850	0.794	1.04	0.978	1.84	0.312	1.10
Er	4.89	4.97	5.19	4.56	4.35	4.71	4.18	6.11	0.842	3.38
Tm	0.774	0.820	0.715	0.617	0.595	0.657	0.722	1.02	0.105	0.496
Yb	6.07	6.37	4.90	4.35	4.33	4.75	5.54	7.90	0.6702	3.73
Lu	1.01	0.996	1.10	1.01	0.998	0.938	0.938	1.16	0.0824	0.549
Hf	0.451	0.454	0.231	0.262	0.285	0.226	0.442	0.160	0.414	0.279
Pb	0.0039	0.0088	0.0037	0.0106	0.0035	0.0046	0.0037	0.0036	0.0030	-
Th	0.0054	0.0249	0.0124	0.0140	0.0240	0.0044	0.0018	0.0013	0.0205	0.0024
U	0.0065	0.0131	0.0030	0.0025	0.0039	0.0028	0.0059	0.0198	0.0448	0.0026

Table B2 - Part B continued

Sample #	SGF-039 50446		SGF-040 50455	SGF-040 50461	SGF-042 50495			SGF-048 50655			SGF-066 51152	SGF-140 37430
Mineral	primary	meta			primary	meta low	meta high	primary	meta low	meta high		
n	4	1	4	3	4	1	2	4	1	1	4	8
Sc	92.88	94.11	104.4	39.10	60.14	73.79	52.48	91.75	102.0	110.6	59.79	95.34
Ti	1915.3	1912.0	3021.8	1705.0	2585.8	3972.0	1226.0	1850.8	2256.0	3403.0	2751.5	1492.9
V	374.9	366.3	442.2	126.8	202.6	307.3	124.4	343.7	382.7	388.4	115.5	153.1
Co	53.93	53.52	54.04	66.38	49.51	53.19	44.27	59.68	62.60	71.70	65.68	58.34
Ni	64.90	66.90	48.48	101.2	8.36	12.46	5.31	49.86	47.30	63.60	26.96	38.69
Zn	36.80	36.60	27.28	40.63	74.32	42.80	109.70	39.58	30.80	34.00	97.60	39.51
Ga	9.70	9.52	11.84	10.13	12.97	15.71	11.15	11.43	11.15	12.33	11.51	5.21
Rb	0.0253	0.0100	0.0580	0.0060	0.0383	0.0100	0.0280	0.0265	0.2290	0.0320	0.0990	0.0105
Sr	0.54	0.61	0.69	0.98	0.43	0.30	0.73	0.53	0.57	0.41	1.32	0.56
Y	44.81	45.11	32.11	6.92	33.86	25.06	46.87	35.53	30.27	32.86	29.99	20.50
Zr	12.60	12.70	31.28	16.18	21.73	35.72	10.68	11.24	21.47	32.98	12.85	8.23
Nb	0.169	0.177	0.267	0.304	0.0696	0.163	0.0075	0.130	0.188	0.133	0.104	0.154
Ba	0.0125	0.0340	4.9778	0.0120	0.0394	0.0890	0.108	0.0147	0.0520	0.0760	0.399	0.0025
La	0.0234	0.0583	0.0605	0.0465	0.0248	0.0660	0.105	0.0206	0.0550	0.0610	0.0611	0.0203
Ce	0.230	0.289	0.394	0.486	0.126	0.253	0.226	0.189	0.286	0.170	0.437	0.217
Pr	0.0803	0.0910	0.120	0.185	0.0478	0.0770	0.0554	0.0653	0.0800	0.0500	0.130	0.0829
Nd	0.791	0.796	1.13	1.55	0.481	0.583	0.630	0.631	0.741	0.466	1.2510	0.756
Sm	0.661	0.602	0.840	0.657	0.893	0.505	1.72	0.490	0.590	0.399	0.971	0.520
Eu	0.305	0.310	0.368	0.329	0.589	0.287	1.08	0.224	0.251	0.170	0.492	0.235
Gd	2.15	2.13	1.67	1.04	2.60	1.48	4.63	1.37	1.28	1.09	2.21	0.919
Tb	0.624	0.636	0.406	0.186	0.631	0.366	1.03	0.419	0.342	0.311	0.526	0.198

Dy	6.13	6.02	4.01	1.34	5.29	3.55	7.83	4.49	3.54	3.59	4.53	2.19
Ho	1.66	1.72	1.19	0.27	1.29	0.95	1.78	1.36	1.13	1.24	1.13	0.766
Er	5.97	5.83	4.72	0.744	4.29	3.62	5.20	5.00	4.60	5.08	3.83	3.39
Tm	0.908	0.950	0.793	0.0970	0.661	0.578	0.732	0.828	0.815	0.884	0.580	0.666
Yb	6.96	6.97	6.43	0.62	4.91	4.62	5.35	6.43	6.26	7.06	4.47	5.93
Lu	1.08	1.09	1.03	0.0850	0.750	0.720	0.756	0.986	0.999	1.19	0.693	1.05
Hf	0.267	0.299	0.873	0.445	0.481	0.880	0.116	0.269	0.529	0.807	0.267	0.129
Pb	0.0078	0.0043	0.0059	0.0045	0.0032	0.0065	0.0084	0.0053	0.0029	0.0097	0.0030	0.0032
Th	0.0032	0.0030	0.0157	0.0089	0.0060	0.0101	0.0055	0.0036	0.0119	0.0360	0.0089	0.0022
U	0.0102	0.0132	0.0186	0.0224	0.0038	0.0036	0.0015	0.0054	0.0079	0.0130	0.0044	0.0076

Table B3 - Part A Averaged major element concentrations (wt%) for garnet (grt) and clinopyroxene (cpx) crystals in barren eclogite xenoliths from Fort à la Corne. Garnets are classified using the G-schematic derived by Grütter et al. 2004. Clinopyroxenes are characterised as omphacite (omph) or diopside (di) based on $0.2 \leq Na/(Na+Ca) < 0.8$ (Coleman et al. 1965; Clark and Papike 1968).

Sample#	**52006-1**			**52006-2**		**52006-3**				**52006-4**		
Mineral	grt	cpx		grt	cpx	grt	cpx			grt	cpx	
Description	G4	Omph	Di	G4	Omph	G3	Omph	Omph	Di	G4	Omph	Di
n	8	9	6	22	4	6	6	1	4	6	7	4
SiO_2	41.89	55.07	54.06	40.39	54.93	39.87	55.44	52.78	52.95	41.73	55.19	54.35
2σ	0.25	0.33	0.72	0.26	0.06	0.25	0.20	-	1.37	0.24	0.20	0.17
TiO_2	0.16	0.33	0.38	0.17	0.23	0.11	0.20	0.46	0.30	0.24	0.33	0.35
2σ	0.01	0.01	0.14	0.05	0.02	0.01	0.01	-	0.06	0.01	0.01	0.09
Al_2O_3	23.87	4.30	2.25	22.81	6.78	22.76	8.77	6.78	5.83	23.43	4.21	1.85
2σ	0.08	0.07	0.49	0.14	0.02	0.11	0.11	-	1.13	0.06	0.09	0.17
Cr_2O_3	0.11	0.14	0.19	0.11	0.12	0.07	0.09	0.13	0.10	0.09	0.14	0.18
2σ	0.03	0.03	0.04	0.01	0.01	0.02	0.02	-	0.03	0.01	0.02	0.02
MnO	0.33	0.06	0.07	0.36	0.04	0.37	0.05	0.06	0.07	0.32	0.06	0.07
2σ	0.01	0.01	0.01	0.01	0.01	0.01	0.01	-	0.04	0.01	0.01	0.03
FeO	9.04	2.82	2.95	16.00	3.71	16.10	3.22	4.27	4.61	9.22	2.84	3.10
2σ	0.10	0.04	0.18	0.26	0.02	0.12	0.04	-	0.95	0.02	0.10	0.29
NiO	0.02	0.05	0.05	0.02	0.06	-	0.03	0.04	0.03	-	0.05	0.05
2σ	-	0.01	0.01	0.00	0.01	-	0.01	-	0.01	-	0.01	0.01
MgO	20.54	14.85	16.86	14.19	12.00	12.18	10.71	12.80	13.42	20.13	14.84	17.22
2σ	0.09	0.10	0.56	0.13	0.06	0.08	0.13	-	0.69	0.08	0.10	0.21
CaO	3.71	18.71	21.51	5.64	16.85	7.61	15.78	18.83	19.66	3.75	18.70	21.39
2σ	0.01	0.06	0.52	0.07	0.03	0.14	0.15	-	0.73	0.02	0.07	0.26
Na_2O	0.05	2.92	1.09	0.06	4.07	0.04	4.82	2.85	2.18	0.05	2.87	0.90
2σ	0.003	0.04	0.44	0.01	0.04	0.01	0.08	-	0.27	0.01	0.05	0.18
K_2O	-	0.002	0.002	-	0.01	-	0.03	0.003	0.01	-	0.003	0.002
2σ	-	0.002	0.001	-	0.003	-	0.002	-	0.01	-	0.002	0.002
P_2O_5	0.03	0.03	0.01	0.05	0.03	0.03	0.02	0.02	0.02	0.03	0.03	0.03
2σ	0.01	0.01	0.00	0.01	0.01	0.00	0.01	-	0.01	0.00	0.01	0.01
Total	99.74	99.27	99.44	99.81	98.85	99.15	99.16	99.02	99.20	98.98	99.27	99.48
2σ	0.39	0.28	0.36	0.45	0.15	0.26	0.26	-	0.44	0.32	0.18	0.34
Mg#	80.19	90.37	91.06	61.26	85.24	57.43	85.55	84.25	83.84	79.56	90.29	90.84

Table B3 continued

Sample#	**52006-5**			**52006-6**			**52006-7**			**52006-9**		
Mineral	grt	cpx		grt	cpx		grt	cpx		grt	cpx	
Description	G3	Omph	Di	G3	Omph	Di	G3	Omph	Omph	G4	Omph	Di
n	7	2	2	8	5	1	6	3	1	7	2	1
SiO_2	39.62	55.24	53.03	39.95	54.51	53.47	39.94	54.24	51.79	41.62	54.91	53.83
2σ	0.18	0.02	0.01	0.17	1.85	-	0.29	0.49	-	0.13	0.10	-
TiO_2	0.18	0.37	0.44	0.09	0.20	0.18	0.13	0.25	0.31	0.18	0.42	0.40
2σ	0.01	0.02	0.01	0.01	0.12	-	0.01	0.04	-	0.01	0.00	-
Al_2O_3	22.29	9.04	4.50	22.43	9.68	5.60	22.64	15.66	13.01	23.16	4.99	2.47
2σ	0.04	0.08	0.18	0.07	0.37	-	0.06	0.74	-	0.09	0.01	-
Cr_2O_3	0.06	0.07	0.10	0.06	0.07	0.10	0.01	0.02	0.03	0.23	0.24	0.31
2σ	0.01	0.00	0.02	0.01	0.01	-	0.01	0.01	-	0.02	0.02	-
MnO	0.36	0.03	0.04	0.31	0.04	0.04	0.24	0.03	0.02	0.34	0.06	0.07
2σ	0.01	0.01	0.01	0.01	0.03	-	0.01	0.00	-	0.01	0.01	-
FeO	17.62	4.79	5.82	15.93	3.19	3.34	11.68	2.42	2.75	10.45	3.65	4.30
2σ	0.11	0.02	0.07	0.05	0.78	-	0.10	0.73	-	0.16	0.00	-
NiO	-	0.06	0.07	0.02	0.06	0.08	-	0.03	0.05	-	0.04	0.04
2σ	-	0.00	0.01	-	0.02	-	-	0.01	-	-	0.00	-
MgO	11.38	9.41	13.37	11.25	10.46	13.28	9.51	6.98	9.75	19.40	13.90	16.61
2σ	0.14	0.01	0.65	0.07	0.88	-	0.07	0.48	-	0.19	0.01	-
CaO	7.25	13.90	19.10	8.95	16.17	20.55	14.91	12.27	16.52	3.52	17.02	20.12
2σ	0.03	0.02	0.38	0.04	1.19	-	0.15	1.00	-	0.02	0.00	-
Na_2O	0.07	5.93	2.42	0.03	4.47	2.34	0.05	7.03	4.60	0.05	3.64	1.13
2σ	0.01	0.01	0.17	0.01	0.96	-	0.01	0.84	-	0.01	0.03	-
K_2O	-	0.005	0.003	-	0.002	0.01	-	0.01	0.01	0.01	0.002	0.002
2σ	-	0.003	0.001	-	0.004	-	-	0.01	-	-	0.0001	-
P_2O_5	0.06	0.02	0.02	0.03	0.01	0.08	0.04	0.02	0.04	0.04	0.03	0.03
2σ	0.01	0.00	0.00	0.01	0.01	-	0.01	0.01	-	0.01	0.02	-
Total	98.89	98.86	98.92	99.04	98.86	99.07	99.13	98.94	98.89	98.99	98.89	99.30
2σ	0.24	0.06	0.05	0.17	0.22	-	0.25	0.30	-	0.18	0.09	-
Mg#	53.50	77.78	80.36	55.72	85.38	87.63	59.21	83.71	86.35	76.80	87.16	87.33

Table B3 continued

Sample#	**52006-11**				**52006-12**			**52006-13**		**52006-14**	
Mineral	grt	cpx			grt	cpx		grt	cpx	grt	cpx
Description	G3	Omph	Di	Di	G4	Omph	Di	G4	Di	G3	Omph
n	8	5	2	2	4	10	1	9	4	7	1
SiO_2	40.17	54.92	53.70	50.83	39.87	55.31	53.60	41.04	54.48	39.41	55.33
2σ	0.28	0.16	0.02	0.91	0.20	0.50	-	0.22	0.10	0.20	-
TiO_2	0.21	0.23	0.25	0.60	0.12	0.21	0.24	0.09	0.63	0.05	0.21
2σ	0.04	0.00	0.03	0.05	0.02	0.01	-	0.02	0.04	0.02	-
Al_2O_3	22.40	7.58	4.46	7.10	22.23	7.54	3.93	23.06	5.49	22.40	11.92
2σ	0.06	0.07	0.18	1.10	0.05	0.39	-	0.10	0.24	0.08	-
Cr_2O_3	0.06	0.06	0.08	0.06	0.13	0.16	0.21	0.07	0.07	0.04	0.05
2σ	0.01	0.02	0.01	0.01	0.01	0.03	-	0.01	0.01	0.02	-
MnO	0.35	0.04	0.05	0.11	0.42	0.05	0.06	0.40	0.04	0.35	0.00
2σ	0.01	0.01	0.01	0.00	0.01	0.01	-	0.01	0.00	0.01	-
FeO	16.50	3.68	4.15	5.46	18.68	4.26	4.69	12.37	2.10	16.15	2.23
2σ	0.07	0.08	0.08	0.13	0.04	0.11	-	0.33	0.02	0.05	-
NiO	-	0.08	0.09	0.06	-	0.03	0.04	-	0.01	-	0.00
2σ	-	0.01	0.01	0.02	-	0.01	-	-	0.01	-	-
MgO	13.12	11.31	14.21	13.18	12.60	11.13	13.92	16.44	13.99	9.35	8.93
2σ	0.09	0.11	0.12	0.62	0.08	0.42	-	0.20	0.26	0.07	-
CaO	6.02	16.19	20.27	19.89	4.62	15.77	19.70	5.42	20.41	10.93	14.50
2σ	0.11	0.05	0.32	0.19	0.06	0.54	-	0.14	0.20	0.07	-
Na_2O	0.06	4.52	1.87	1.72	0.04	4.37	2.21	0.02	2.48	0.03	5.63
2σ	0.01	0.03	0.26	0.03	0.00	0.27	-	0.01	0.12	0.01	-
K_2O	-	0.01	-	0.005	-	0.02	0.001	-	0.002	-	0.005
2σ	-	0.00	-	0.002	-	0.003	-	-	0.004	-	-
P_2O_5	0.03	0.02	0.03	0.02	0.06	0.02	0.02	0.04	0.01	0.06	0.02
2σ	0.01	0.01	0.01	0.02	0.00	0.01	-	0.01	0.01	0.01	-
Total	98.92	98.63	99.16	99.03	98.76	98.87	98.63	98.95	99.72	98.77	98.82
2σ	0.26	0.09	0.09	0.13	0.18	0.29	-	0.29	0.16	0.17	-
Mg#	58.62	84.57	85.92	81.14	54.59	82.32	84.11	70.32	92.23	50.79	87.73

Table B3 continued

Sample#	**52006-15**			**52006-16**		**52006-17**			**52006-18**		
Mineral	grt	cpx		grt	cpx	grt	cpx		grt	cpx	
Description	G4	Omph	Di	G4	Omph	G4	Omph	Di	G4	Omph	Di
n	5	2	3	7	4	6	6	2	7	3	3
SiO_2	40.60	54.54	53.87	41.49	54.95	41.48	55.37	54.73	40.60	54.94	53.84
2σ	0.10	0.07	1.06	0.23	0.11	0.18	0.30	0.53	0.28	0.42	0.54
TiO_2	0.22	0.42	0.28	0.13	0.28	0.21	0.29	0.28	0.16	0.39	0.38
2σ	0.01	0.03	0.22	0.01	0.01	0.01	0.01	0.05	0.01	0.01	0.02
Al_2O_3	22.79	6.31	3.12	22.96	3.51	23.23	3.65	2.10	22.61	6.29	3.54
2σ	0.05	0.30	1.00	0.05	0.06	0.07	0.02	0.29	0.06	0.11	0.27
Cr_2O_3	0.01	0.02	0.14	0.76	0.88	0.13	0.32	0.31	0.08	0.09	0.12
2σ	0.02	0.02	0.19	0.05	0.08	0.01	0.08	0.01	0.01	0.01	0.00
MnO	0.35	0.04	0.08	0.37	0.06	0.33	0.06	0.07	0.35	0.04	0.05
2σ	0.01	0.02	0.03	0.00	0.01	0.01	0.00	0.01	0.01	0.01	0.00
FeO	13.62	3.82	3.96	9.20	3.06	10.16	3.66	3.54	14.79	4.39	4.96
2σ	0.17	0.01	1.15	0.03	0.03	0.07	0.03	0.04	0.17	0.05	0.16
NiO	-	0.05	0.04	-	0.05	-	0.04	0.04	-	0.05	0.07
2σ	-	0.01	0.02	-	0.01	-	0.01	0.001	-	0.01	0.01
MgO	15.17	12.49	15.46	19.88	14.72	19.51	14.75	16.32	14.64	11.98	14.52
2σ	0.25	0.36	0.45	0.06	0.11	0.07	0.06	0.40	0.13	0.16	0.26
CaO	5.95	16.88	20.64	3.91	18.79	3.65	18.39	21.03	5.96	16.51	19.87
2σ	0.17	0.11	0.67	0.03	0.12	0.02	0.08	0.01	0.03	0.07	0.27
Na_2O	0.06	4.19	1.46	0.04	2.84	0.05	2.86	1.19	0.05	4.31	1.81
2σ	0.00	0.15	0.05	0.00	0.07	0.01	0.05	0.16	0.01	0.02	0.08
K_2O	-	0.001	0.002	-	0.00	-	0.002	-	-	0.003	0.01
2σ	-	0.000	0.002	-	0.00	-	0.002	-	-	0.002	0.002
P_2O_5	0.02	0.02	0.02	0.03	0.03	0.03	0.02	0.01	0.04	0.02	0.03
2σ	0.00	0.01	0.01	0.01	0.01	0.01	0.01	0.01	0.01	0.01	0.02
Total	98.81	98.78	99.09	98.77	99.17	98.79	99.42	99.62	99.28	99.03	99.19
2σ	0.12	0.03	0.44	0.17	0.08	0.18	0.24	0.01	0.25	0.28	0.22
Mg#	66.50	85.34	87.43	79.38	89.54	63.83	87.79	89.15	76.25	82.95	83.92

Table B3 continued

Sample#	**52006-19**	**52006-20**	**52006-21**			**52006-22**		**52006-23**		
Mineral	grt	grt	grt	cpx		grt	cpx	grt	cpx	
Description	G4D	G3D	G4	Omph	Di	G4	Omph	G4	Omph	Di
n	8	6	7	7	3	7	6	6	5	5
SiO_2	41.49	40.27	41.35	56.14	54.33	41.32	55.56	41.52	55.81	54.93
2σ	0.33	0.26	0.29	0.31	0.07	0.29	0.13	0.25	0.48	0.32
TiO_2	0.35	0.48	0.13	0.28	0.26	0.14	0.29	0.19	0.39	0.40
2σ	0.01	0.02	0.01	0.03	0.06	0.02	0.01	0.01	0.01	0.04
Al_2O_3	22.85	22.05	23.24	5.89	4.12	23.27	4.03	23.13	4.97	2.79
2σ	0.13	0.03	0.11	1.53	0.99	0.08	0.10	0.10	0.19	0.70
Cr_2O_3	0.07	0.07	0.02	0.06	0.06	0.07	0.21	0.05	0.07	0.07
2σ	0.01	0.01	0.02	0.04	0.03	0.02	0.04	0.01	0.01	0.02
MnO	0.33	0.37	0.35	0.06	0.08	0.40	0.06	0.35	0.05	0.08
2σ	0.01	0.01	0.00	0.01	0.00	0.02	0.01	0.01	0.00	0.01
FeO	10.39	15.54	11.01	4.04	4.29	10.28	3.42	10.73	3.44	3.81
2σ	0.05	0.05	0.22	0.75	0.73	0.06	0.02	0.15	0.03	0.16
NiO	-	0.02	0.02	0.05	0.04	-	0.03	0.02	0.04	0.04
2σ	-	-	-	0.01	0.01	-	0.01	-	0.01	0.01
MgO	18.71	13.18	18.20	12.78	15.09	19.20	14.50	19.44	13.88	16.15
2σ	0.09	0.08	0.27	1.67	0.58	0.08	0.07	0.11	0.16	0.60
CaO	4.88	7.02	4.94	16.93	19.55	4.19	18.64	3.62	17.44	20.18
2σ	0.03	0.03	0.11	2.04	1.02	0.03	0.09	0.03	0.15	0.86
Na_2O	0.08	0.13	0.04	3.79	1.85	0.04	2.92	0.05	3.47	1.47
2σ	0.01	0.01	0.01	0.88	0.37	0.01	0.03	0.01	0.11	0.43
K_2O	-	-	-	0.01	0.004	-	0.01	-	0.002	0.01
2σ	-	-	-	0.01	0.002	-	0.01	-	0.001	0.01
P_2O_5	0.09	0.07	0.04	0.02	0.04	0.04	0.03	0.03	0.02	0.02
2σ	0.00	0.02	0.01	0.01	0.02	0.01	0.01	0.00	0.01	0.01
Total	99.24	99.18	99.33	100.04	99.72	98.94	99.69	99.11	99.59	99.96
2σ	0.50	0.22	0.41	0.72	0.56	0.39	0.15	0.18	0.44	0.56
Mg#	60.18	74.66	76.90	84.94	86.25	76.35	88.32	47.93	87.79	88.31

Table B3 continued

Sample#	**52006-24**			**52006-25**	**52006-26**			**53001-1**	**53001-2**	**17664**	**17672**
Mineral	grt	cpx		grt	grt	cpx		grt	grt	grt	grt
Description	G3	Omph	Di	G4D	G3	Omph	Di	G4	G4	G4	G3
n	8	5	1	2	4	1	1	8	9	22	4
SiO_2	39.38	55.80	54.19	38.80	39.70	54.95	52.48	40.89	41.09	39.11	38.48
2σ	0.19	1.06	-	0.07	0.17	-	-	0.33	0.23	0.23	0.20
TiO_2	0.04	0.15	0.13	0.03	0.18	0.33	0.38	0.03	0.05	0.06	0.08
2σ	0.01	0.02	-	0.01	0.00	-	-	0.00	0.01	0.02	0.01
Al_2O_3	22.22	9.98	6.92	21.91	22.55	7.22	4.36	23.16	23.30	21.71	21.60
2σ	0.05	1.19	-	0.04	0.03	-	-	0.07	0.08	0.22	0.05
Cr_2O_3	0.03	0.06	0.08	0.13	0.06	0.06	0.11	0.14	0.06	0.12	0.04
2σ	0.02	0.01	-	0.01	0.01	-	-	0.02	0.01	0.02	0.01
MnO	0.35	0.02	0.03	0.45	0.34	0.03	0.08	0.36	0.20	0.78	0.56
2σ	0.01	0.00	-	0.01	0.01	-	-	0.01	0.01	0.04	0.01
FeO	17.36	2.82	3.37	22.83	14.60	4.19	5.62	13.84	12.18	23.94	24.03
2σ	0.05	0.24	-	0.09	0.08	-	-	0.05	0.04	1.22	0.06
NiO	-	0.01	0.01	-	-	0.07	0.06	-	0.02	-	-
2σ	-	0.01	-	-	-	-	-	-		-	-
MgO	8.96	10.05	12.50	10.39	12.51	11.24	15.45	16.84	16.73	8.65	7.15
2σ	0.07	1.09	-	0.03	0.09	-	-	0.06	0.07	0.67	0.03
CaO	10.58	16.02	19.64	3.93	8.61	16.44	19.36	3.83	5.68	5.68	6.87
2σ	0.02	1.89	-	0.03	0.04	-	-	0.02	0.06	0.09	0.10
Na_2O	0.02	4.75	2.66	0.00	0.06	4.48	1.13	0.01	0.03	0.00	0.01
2σ	0.01	0.94	-	0.00	0.01	-	-	0.01	0.01	0.01	0.01
K_2O	-	0.004	-	-	-	-	-	-	-	-	-
2σ	-	0.003	-	-	-	-	-	-	-	-	-
P_2O_5	0.04	0.01	0.02	0.05	0.04	0.03	0.03	0.03	0.05	0.05	0.03
2σ	0.01	0.01	-	0.02	0.01	-	-	0.01	0.02	0.01	0.00
Total	98.99	99.67	99.55	98.53	98.65	99.03	99.03	99.13	99.38	100.11	98.85
2σ	0.14	0.21	-	0.01	0.17	-	-	0.40	0.24	0.28	0.20
Mg#	60.42	86.42	86.87	44.80	68.45	82.71	83.06	68.45	71.00	39.16	34.64

Table B3 - Part B Averaged major element chemistry for diamondiferous eclogite and peridotite micro-xenoliths from FALC

Sample#	**SGF-003 50036**				**SGF-008 50076**			**SGF-009 50095**		**SGF-020 50138**
Mineral		grt		cpx		grt		grt	cpx	grt
Description	primary G3D	meta low G3D	meta high G3D	Omph	primary G3D	meta low G4D	meta high G4	G4D	Omph	G4
n	9	-	-	4	7	-	-	15	8	12
SiO_2	41.15	41.24	41.49	55.00	41.44	41.52	41.94	40.27	55.39	41.73
2σ	0.12	-	-	41.44	0.20	-	-	0.12	0.12	0.10
TiO_2	0.25	0.26	0.33	0.19	0.26	0.32	0.38	0.40	0.46	0.22
2σ	0.01	-	-	0.26	0.02	-	-	0.03	0.01	0.01
Al_2O_3	22.70	22.77	22.76	6.36	22.56	22.32	22.63	22.20	10.31	22.42
2σ	0.05	-	-	22.56	0.09	-	-	0.09	0.12	0.07
Cr_2O_3	0.13	0.13	0.15	0.09	0.15	0.30	0.29	0.02	0.05	0.53
2σ	0.01	-	-	0.15	0.04	-	-	0.03	0.01	0.03
MnO	0.23	0.23	0.23	0.05	0.38	0.34	0.31	0.42	0.08	0.19
2σ	0.01	-	-	0.38	0.01	-	-	0.01	0.01	0.01
FeO	9.47	9.49	9.68	3.26	10.48	9.77	8.07	17.93	5.60	9.19
2σ	0.08	-	-	10.48	0.06	-	-	0.26	0.03	0.03
NiO	-	-	-	0.04	0.03	-	-	-	0.02	-
2σ	-	-	-	0.03	0.00	-	-	-	0.01	-
MgO	15.37	15.89	16.51	14.03	17.54	18.75	20.68	12.58	9.49	20.01
2σ	0.27	-	-	17.54	0.13	-	-	0.12	0.04	0.11
CaO	9.85	9.18	8.31	17.42	6.36	5.65	4.88	5.97	12.00	4.78
2σ	0.28	-	-	6.36	0.19	-	-	0.18	0.10	0.10
Na_2O	0.08	0.09	0.08	3.08	0.09	0.08	0.07	0.16	5.98	0.04
2σ	0.01	-	-	0.09	0.01	-	-	0.01	0.11	0.01
K_2O	-	-	-	0.25	-	-	-	-	0.17	-
2σ	-	-	-	-	-	-	-	-	0.04	-
P_2O_5	-	-	0.05	0.02	-	-	-	0.05	0.01	0.04
2σ	-	-	-	-	-	-	-	0.01	0.01	-
Total	99.23	99.28	99.60	99.78	99.26	99.06	99.24	99.96	99.56	99.12
2σ	0.18	-	-	99.26	0.23	-	-	0.14	0.20	0.18
Mg#	74.29	74.90	75.25	88.49	74.89	77.38	82.04	55.57	75.13	74.68

Table B3 - Part B continued

Sample#	**SGF-020 50140**			**SGF-021 50148**			**SGF-025 50223**		
Mineral	grt			grt			grt		
Description	primary G3D	meta low G3D	meta high G1	primary G3D	meta low G3D	meta high G4	primary G3D	meta low G3D	meta high G4
n	63	-	-	12			7	-	-
SiO_2	40.75	41.07	42.24	40.76	41.19	34.03	41.02	41.28	41.79
2σ	0.36	-	-	0.10	-	-	0.07	-	-
TiO_2	0.52	0.59	1.26	0.22	0.30	0.21	0.28	0.36	0.42
2σ	0.08	-	-	0.02	-	-	0.02	-	-
Al_2O_3	22.45	22.63	22.22	22.25	22.32	26.57	22.31	22.26	22.48
2σ	0.22	-	-	0.09	-	-	0.02	-	-
Cr_2O_3	0.15	0.18	0.84	0.15	0.18	0.31	0.11	0.11	0.15
2σ	0.02	-	-	0.01	-	-	0.01	-	-
MnO	0.40	0.41	0.30	0.39	0.38	0.40	0.38	0.37	0.32
2σ	0.01	-	-	0.01	-	-	0.01	-	-
FeO	14.31	14.03	7.77	14.82	12.56	13.16	12.72	12.84	8.62
2σ	0.09	-	-	0.07	-	-	0.19	-	-
NiO	0.02	-	-	-	-	-	-	-	-
2σ	0.00	-	-	-	-	-	-	-	-
MgO	14.58	15.23	20.71	14.55	16.44	21.50	15.26	16.13	20.20
2σ	0.21	-	-	0.08	-	-	0.30	-	-
CaO	6.59	6.60	4.89	6.49	6.24	3.26	7.31	6.31	5.11
2σ	0.09	-	-	0.06	-	-	0.25	-	-
Na_2O	0.09	0.08	0.06	0.10	0.09	0.04	0.09	0.10	0.05
2σ	0.01	-	-	0.01	-	-	0.01	-	-
K_2O	0.01	-	-	-	-	0.01	-	-	-
2σ	0.00	-	-	-	-	-	-	-	-
P_2O_5	0.05	-	0.03	0.05	-	-	0.04	0.05	-
2σ	0.02	-	-	0.01	-	-	0.00	-	-
Total	99.86	100.83	100.33	99.73	99.71	99.49	99.49	99.81	99.13
2σ	0.52	-	-	0.15	-	-	0.17	-	-
Mg#	64.48	65.92	82.62	63.62	70.00	74.44	68.14	69.13	80.68

Table B3 - Part B continued

Sample#	**SGF-025 50224-1**			**SGF-025 50224-2**			**SGF-025 50224-3**		
Mineral	grt			grt			grt		
Description	primary	meta low	meta high	primary	meta low	meta high	primary	meta low	meta high
n	G3D 3	G4D -	G1 -	G3D 4	G4D -	G4 -	G3D 8	G4 -	G1 -
SiO_2	40.92	41.01	41.72	40.96	41.33	41.65	41.15	41.39	41.98
2σ	0.11	-	-	0.03	-	-	0.10	-	-
TiO_2	0.31	0.35	0.44	0.35	0.34	0.40	0.35	0.34	0.43
2σ	0.02	-	-	0.01	-	-	0.01	-	-
Al_2O_3	22.37	22.22	22.60	22.30	22.60	22.51	22.26	22.43	22.52
2σ	0.04	-	-	0.02	-	-	0.06	-	-
Cr_2O_3	0.10	0.14	0.14	0.12	0.13	0.29	0.11	0.12	0.35
2σ	0.01	-	-	0.02	-	-	0.02	-	-
MnO	0.37	0.37	0.31	0.38	0.35	0.30	0.37	0.37	0.28
2σ	0.00	-	-	0.01	-	-	0.01	-	-
FeO	12.41	12.51	8.14	12.56	10.22	8.36	12.12	11.39	7.85
2σ	0.11	-	-	0.01	-	-	0.55	-	-
NiO	-	-	-	-	-	-	-	-	-
2σ	-	-	-	-	-	-	-	-	-
MgO	16.08	16.64	20.74	16.34	18.53	20.39	16.48	18.04	20.71
2σ	0.16	-	-	0.32	-	-	0.37	-	-
CaO	6.66	5.78	4.91	6.18	5.57	4.95	6.34	5.30	5.09
2σ	0.28	-	-	0.44	-	-	0.22	-	-
Na_2O	0.10	0.13	0.05	0.10	0.07	0.06	0.10	0.05	0.06
2σ	0.00	-	-	0.01	-	-	0.01	-	-
K_2O	-	-	-	-	-	-	-	-	-
2σ	-	-	-	-	-	-	-	-	-
P_2O_5	0.04	-	-	0.04	-	0.04	0.04	-	-
2σ	0.01	-	-	-	-	-	0.00	-	-
Total	99.36	99.14	99.04	99.29	99.15	98.94	99.27	99.42	99.27
2σ	0.10	-	-	0.11	-	-	0.17	-	-
Mg#	69.78	70.34	81.96	69.87	76.37	81.30	71.82	73.84	82.46

Table B3 - Part B continued

Sample#	**SGF-025 50225**			**SGF-025 50226**	**SGF-034**	**SGF-039 50443-1**	**SGF-039 50443-2**		**SGF-039 50446**
Mineral	grt			grt	grt	grt	grt	cpx	grt
Description	primary	meta low	meta high	primary	primary	primary	primary		primary
	G3D	G4D	G4	G4D	G3D	G3	G3D	Omph	G3D
n	9	-	-	3	12	5	3	8	9
SiO_2	40.97	41.29	41.64	40.95	40.51	41.06	40.21	55.27	40.58
2σ	0.06	-	-	0.07	0.08	0.13	0.14	0.16	0.19
TiO_2	0.35	0.37	0.38	0.36	0.16	0.29	0.43	0.50	0.29
2σ	0.01	-	-	0.01	0.01	0.01	0.00	0.01	0.02
Al_2O_3	22.22	22.35	22.45	22.22	22.15	22.50	22.22	9.57	22.17
2σ	0.07	-	-	0.02	0.05	0.03	0.03	0.22	0.06
Cr_2O_3	0.11	0.13	0.16	0.12	0.11	0.09	0.02	0.07	0.12
2σ	0.01	-	-	0.01	0.01	0.01	0.04	0.01	0.00
MnO	0.37	0.37	0.32	0.38	0.37	0.20	0.36	0.08	0.38
2σ	0.01	-	-	0.01	0.01	0.00	0.01	0.00	0.01
FeO	12.57	11.30	8.89	12.63	14.44	8.53	15.31	4.55	12.69
2σ	0.06	-	-	0.06	0.06	0.07	0.03	0.03	0.17
NiO	-	-	-	-	-	-	-	0.03	-
2σ	-	-	-	-	-	-	-	0.01	-
MgO	16.43	17.85	19.83	16.74	14.09	15.79	14.28	10.53	15.61
2σ	0.15	-	-	0.07	0.05	0.26	0.03	0.21	0.20
CaO	6.08	5.54	4.98	5.81	7.26	10.18	6.01	13.10	6.86
2σ	0.19	-	-	0.01	0.04	0.40	0.01	0.16	0.09
Na_2O	0.10	0.04	0.05	0.11	0.08	0.07	0.15	5.22	0.10
2σ	0.01	-	-	0.00	0.01	0.01	0.00	0.08	0.01
K_2O	-	-	-	-	-	-	-	0.27	-
2σ	-	-	-	-	-	-	-	0.01	-
P_2O_5	-	-	0.04	-	0.04	0.04	0.05	0.02	0.05
2σ	-	-	-	-	0.00	-	0.01	0.01	0.01
Total	99.22	99.25	98.74	99.32	99.16	98.71	99.00	99.19	98.81
2σ	0.03	-	-	0.12	0.15	0.12	0.13	0.23	0.19
Mg#	69.97	73.79	79.90	70.26	63.50	76.74	62.45	80.51	68.67

Table B3 - Part B continued

Sample#	**SGF-040 50455**					**SGF-040 50461**		**SGF-042 50495**		
Mineral		grt		cpx		grt	cpx		grt	
Description	cpx	meta low	meta high			primary		primary	meta low	meta high
	G3D	G4	G4	Omph	Di	G3D	Omph	G3D	G4D	G4D
n	4	-	-	4	2	4	5	9	-	-
SiO_2	40.27	40.95	41.71	54.23	52.36	40.99	54.51	39.95	40.22	41.46
2σ	0.15	-	-	0.37	1.31	0.08	0.24	0.13	-	-
TiO_2	0.25	0.35	0.35	0.16	0.41	0.25	0.12	0.21	0.27	0.65
2σ	0.01	-	-	0.08	0.02	0.01	0.01	0.02	-	-
Al_2O_3	22.01	22.04	22.64	6.86	6.09	22.53	7.30	22.14	22.15	22.27
2σ	0.05	-	-	0.38	0.66	0.04	0.19	0.09	-	-
Cr_2O_3	0.13	0.12	0.18	0.07	0.07	0.14	0.10	0.00	-	-
2σ	0.01	-	-	0.01	0.00	0.02	0.01	0.00	-	-
MnO	0.40	0.36	0.29	0.05	0.08	0.20	0.03	0.54	0.64	0.35
2σ	0.01	-	-	0.01	0.02	0.01	0.01	0.04	-	-
FeO	14.79	11.19	8.42	3.28	4.09	8.16	2.62	19.23	17.71	11.03
2σ	0.03	-	-	0.20	0.31	0.04	0.31	0.65	-	-
NiO	-	-	-	0.03	0.00	0.03	0.05	-	-	-
2σ	-	-	-	0.01	0.01	-	0.01	-	-	-
MgO	14.45	18.04	20.81	13.23	14.36	15.01	12.97	11.52	12.70	18.78
2σ	0.11	-	-	0.75	0.40	0.15	0.09	0.45	-	-
CaO	6.62	5.62	4.36	17.51	19.14	11.38	17.77	6.20	5.92	4.51
2σ	0.01	-	-	0.16	1.24	0.15	0.15	0.16	-	-
Na_2O	0.09	0.05	0.06	3.23	1.99	0.08	3.32	0.10	0.09	0.11
2σ	0.01	-	-	0.34	0.53	0.00	0.05	0.01	-	-
K_2O	-	-	-	0.16	0.03	-	0.23	-	-	-
2σ	-	-	-	0.06	0.02	-	0.02	-	-	-
P_2O_5	0.04	-	-	0.01	0.01	0.04	0.01	0.09	-	-
2σ	0.00	-	-	0.01	0.01	0.00	0.01	0.01	-	-
Total	99.01	98.72	98.82	98.82	98.61	98.75	99.02	99.89	99.70	99.17
2σ	0.18	-	-	0.06	0.05	0.16	0.34	0.27	-	-
Mg#	63.54	74.19	81.50	87.80	86.22	76.63	89.83	51.06	56.11	75.22

Table B3 - Part B continued

Sample#	**SGF-048 50655**			**SGF-066 51152**		**SGF-067 51188**		**SGF-127 53865**	**SGF-140 37430**	
Mineral		grt		grt	cpx	grt		grt	grt	cpx
Description	primary	meta low	meta high	primary						
	G3D	G4D	G4D	G4D	Omph	G9	G11	G10D	G4D	Omph
n	4	-	-	6	3	12	3	2	11	11
SiO_2	40.88	41.26	41.59	40.42	55.45	40.93	41.09	41.19	41.31	54.97
2σ	0.07	-	-	0.07	0.03	0.07	0.07	0.05	0.07	0.13
TiO_2	0.24	0.35	0.30	0.41	0.52	0.11	0.54	0.17	0.23	0.18
2σ	0.01	-	-	0.01	0.01	0.01	0.02	0.01	0.02	0.01
Al_2O_3	22.13	22.50	22.56	22.22	11.17	16.65	17.12	20.48	22.35	6.95
2σ	0.06	-	-	0.04	0.06	0.11	0.06	0.05	0.09	0.44
Cr_2O_3	0.12	0.13	0.16	0.04	0.09	8.56	7.21	3.75	0.03	0.06
2σ	0.01	-	-	0.03	0.01	0.10	0.06	0.13	0.04	0.01
MnO	0.40	0.39	0.33	0.40	0.08	-	-	0.30	0.42	0.14
2σ	0.00	-	-	0.01	0.00	-	-	0.01	0.01	0.01
FeO	14.10	12.81	10.18	17.58	5.22	6.78	6.72	9.34	13.56	5.86
2σ	0.09	-	-	0.05	0.02	0.06	0.02	0.00	0.05	0.44
NiO	-	-	-	-	0.01	0.08	0.04		0.03	0.03
2σ	-	-	-	-	0.00	0.02	0.00	0.00	-	0.01
MgO	14.98	17.25	18.68	13.50	9.37	19.06	19.74	21.01	17.21	14.10
2σ	0.25	-	-	0.08	0.05	0.06	0.04	0.13	0.07	0.78
CaO	6.51	4.90	5.43	5.28	11.16	6.61	6.20	2.27	4.34	12.79
2σ	0.27	-	-	0.08	0.03	0.05	0.03	0.03	0.04	0.54
Na_2O	0.10	0.08	0.07	0.16	6.00	0.02	0.06	0.09	0.12	4.08
2σ	0.01	-	-	0.01	0.05	0.02	0.01	0.01	0.01	0.34
K_2O	-	-	-	-	0.21	-	-	-	-	0.07
2σ	-	-	-	-	0.00	-	-	-	-	0.01
P_2O_5	0.04	-	-	0.06	0.02	-	-	0.06	0.04	0.01
2σ	-	-	-	0.02	0.01	-	-	0.01	0.01	0.01
Total	99.44	99.66	99.31	100.01	99.28	98.73	98.71	98.58	99.60	99.22
2σ	0.14	-	-	0.12	0.06	0.11	0.05	0.01	0.20	0.14
Mg#	65.44	70.59	76.59	63.26	76.17	83.97	83.37	80.04	69.34	81.08

Table B4 - Part A Averaged oxygen isotope compositions (n=6) of garnets in barren eclogite xenoliths from Fort à la Corne. All values are given in ‰.

Sample #	**52006-1**	**52006-2**	**52006-3**	**52006-4**	**52006-5**	**52006-6**	**52006-7**	**52006-9**	**52006-11**	**52006-12**
$\delta^{18}O$ (SMOW)	4.91	3.89	3.82	4.83	3.91	3.72	4.15	6.04	3.95	3.89
2σ (‰)	0.31	0.31	0.30	0.31	0.30	0.30	0.31	0.31	0.30	0.29

Sample #	**52006-13**	**52006-14**	**52006-15**	**52006-16**	**52006-17**	**52006-18**	**52006-19**	**52006-20**	**52006-21**	**52006-22**
$\delta^{18}O$ (SMOW)	5.04	5.27	3.97	4.84	4.55	4.06	6.14	6.22	4.22	4.52
2σ (‰)	0.31	0.30	0.30	0.31	0.31	0.30	0.31	0.31	0.30	0.29

Sample #	**52006-23**	**52006-24**	**52006-25**	**52006-26**	**53001-1**	**53001-2**	**17664**	**17672**
$\delta^{18}O$ (SMOW)	4.98	5.30	7.89	3.56	5.37	4.66	5.78	6.85
2σ (‰)	0.30	0.31	0.31	0.31	0.31	0.31	0.30	0.30

Table B4 - Part B Oxygen isotope compositions of garnets in diamondiferous eclogite xenoliths from Fort à la Corne. All values are given in ‰

Sample #	**SGF-003**										
$\delta^{18}O$ (SMOW)	5.12	5.37	5.31	4.70	5.31	5.17	4.53	4.62	5.26	5.53	5.32
2σ (‰)	0.27	0.26	0.26	0.27	0.30	0.28	0.28	0.27	0.26	0.26	0.29

Sample #	**SGF-008**							**SGF-009**			
$\delta^{18}O$ (SMOW)	5.44	5.44	5.40	5.85	5.87	5.76	5.62	6.08	6.05	6.14	6.34
2σ (‰)	0.27	0.29	0.28	0.27	0.26	0.26	0.26	0.28	0.30	0.28	0.28

Sample #	**SGF-009**					**SGF-020 50138**					
$\delta^{18}O$ (SMOW)	6.32	6.23	6.08	6.03	6.27	5.59	5.55	5.49	5.40	5.41	5.53
2σ (‰)	0.29	0.26	0.27	0.27	0.27	0.29	0.29	0.29	0.26	0.29	0.26

Sample #	**SGF-020 50138**			**SGF-020 50140**							
$\delta^{18}O$ (SMOW)	5.50	5.51	5.38	6.43	6.53	6.47	5.84	6.50	6.62	6.60	5.89
2σ (‰)	0.26	0.28	0.28	0.32	0.30	0.31	0.29	0.30	0.29	0.28	0.28

Sample #	**SGF-020 50140**						**SGF-021**				
$\delta^{18}O$ (SMOW)	6.58	6.51	6.60	6.55	6.42	6.38	6.45	6.52	6.55	6.55	6.53
2σ (‰)	0.29	0.28	0.28	0.29	0.28	0.28	0.26	0.26	0.27	0.29	0.28

Sample #	**SGF-021**				**SGF-025 50223**						
$\delta^{18}O$ (SMOW)	6.52	6.46	6.58	6.31	6.12	6.19	6.39	6.63	6.58	6.27	6.13
2σ (‰)	0.27	0.28	0.27	0.29	0.28	0.29	0.27	0.27	0.28	0.29	0.27

Table B4 - Part B continued

Sample #	SGF-025 50223		SGF-025 50224-1								
$\delta^{18}O$ (SMOW)	6.28	6.22	6.53	6.17	6.39	5.96	6.40	6.26	6.39	5.72	5.73
2σ (‰)	0.26	0.27	0.27	0.29	0.26	0.30	0.27	0.27	0.26	0.27	0.26

Sample #	SGF-025 50224-1					SGF-025 50224-2					
$\delta^{18}O$ (SMOW)	5.75	5.93	5.91	5.86	6.29	6.40	6.35	6.32	5.98	6.14	6.20
2σ (‰)	0.27	0.27	0.29	0.29	0.27	0.29	0.29	0.30	0.27	0.26	0.27

Sample #	50224-2	SGF-025 50224-3								
$\delta^{18}O$ (SMOW)	6.21	5.87	6.10	6.03	5.86	5.78	6.40	6.33	5.65	5.68	5.86
2σ (‰)	0.28	0.26	0.29	0.28	0.26	0.29	0.28	0.29	0.26	0.29	0.28

Sample #	50224-3	SGF-025 50225								50226
$\delta^{18}O$ (SMOW)	6.83	6.51	6.27	6.28	5.87	6.09	6.32	6.24	6.63	6.46	6.21
2σ (‰)	0.28	0.27	0.27	0.28	0.26	0.28	0.30	0.29	0.28	0.26	0.26

Sample #	SGF-025 50226		SGF-034								
$\delta^{18}O$ (SMOW)	6.08	5.99	6.91	6.86	6.93	6.59	6.90	6.76	6.76	6.68	6.76
2σ (‰)	0.32	0.27	0.29	0.27	0.29	0.28	0.29	0.29	0.28	0.27	0.28

Sample #	SGF-039 50443-1						SGF-039 50443 2				
$\delta^{18}O$ (SMOW)	5.13	4.98	5.08	4.92	5.11	5.05	6.42	6.40	6.15	6.20	6.32
2σ (‰)	0.28	0.26	0.33	0.29	0.29	0.28	0.28	0.27	0.30	0.31	0.27

Table B4 - Part B continued

Sample #	SGF-039 50443 2			SGF-040 50455					SGF-040 50455		
$\delta^{18}O$ (SMOW)	6.27	6.10	6.27	5.67	6.06	5.67	6.60	5.96	5.79	5.50	5.74
2σ (‰)	0.28	0.26	0.27	0.29	0.27	0.33	0.30	0.27	0.30	0.26	0.29

Sample #	SGF-040 50455			SGF-040 50461						SGF-042	
$\delta^{18}O$ (SMOW)	5.59	6.24	6.34	5.26	5.11	4.98	5.20	5.25	5.19	6.64	7.45
2σ (‰)	0.29	0.27	0.26	0.26	0.28	0.27	0.28	0.28	0.31	0.26	0.27

Sample #	SGF-042							SGF-048			
$\delta^{18}O$ (SMOW)	7.40	7.57	7.45	7.38	6.93	7.51	7.49	6.61	6.79	5.87	5.99
2σ (‰)	0.28	0.28	0.27	0.27	0.26	0.27	0.29	0.29	0.26	0.28	0.27

Sample #	SGF-048				SGF-066						SGF-140
$\delta^{18}O$ (SMOW)	7.64	6.49	6.52	6.00	6.15	6.21	6.13	6.03	6.16	6.27	6.46
2σ (‰)	0.27	0.27	0.27	0.30	0.26	0.30	0.30	0.27	0.28	0.28	0.27

Sample #	SGF-140						
$\delta^{18}O$ (SMOW)	6.25	6.37	6.26	6.38	6.47	6.48	6.27
2σ (‰)	0.29	0.29	0.27	0.29	0.29	0.26	0.29

Table B5 Mg-Fe exchange temperatures calculated for garnet-clinopyroxene in diamond-free and diamondiferous eclogites using the thermometer of Krogh (1988). Pressures were derived by projecting the temperatures onto the Fort à la Corne geotherm (from Chapter 2). For the diamondiferous samples averaged primary garnet compositions were used in the calculation.

	Sample #	Paragenesis		$T_{Krogh88}$ (ºC)	$P_{geotherm}$ (kbar)
Diamond-free	**52006-1**	G4	Omph	1039	48
		G4	Di	979	45
	52006-2	G4	Omph	895	40
	52006-3	G3	Omph	909	41
		G3	Omph	964	44
		G3	Di	981	45
	52006-4	G4	Omph	1021	47
		G4	Di	976	44
	52006-5	G3	Omph	1111	51
		G3	Di	1011	46
	52006-6	G3	Omph	944	43
		G3	Di	854	38
	52006-7	G3	Omph	1303	61
		G3	Omph	1165	54
	52006-9	G4	Omph	1127	52
		G4	Di	1116	52
	52006-11	G3	Omph	893	40
		G3	Di	839	37
		G3	Di	1034	47
	52006-12	G4	Omph	811	36
		G4	Di	754	33
	52006-13	G4	Di	735	32
	52006-14	G3	Omph	840	37
	52006-15	G4	Omph	1047	48
		G4	Di	938	42
	52006-16	G4	Omph	1091	50
	52006-17	G4	Omph	1118	52
		G4	Di	1012	46
	52006-18	G4	Omph	1089	50
		G4	Di	1041	48
	52006-21	G4	Omph	1316	62

		G4	Di	1212	56
	52006-22	G4	Omph	1095	50
	52006-23	G4	Omph	1063	49
		G4	Di	1027	47
	52006-24	G3	Omph	830	37
		G3	Di	815	36
	52006-26	G3	Omph	1159	54
		G3	Di	1141	53
Diamondiferous	**SGF-003 50036**	G3D	Omph	1329	62
	SGF-009 50095	G3D	Omph	1194	55
	SGF-039 50443-2	G3D	Omph	1177	55
	SGF-040 50461	G3D	Omph	1394	65
	SGF-066 51152	G4D	Omph	1173	55
	SGF-140 37430	G4D	Omph	1276	60

Table B6 - Part A Averaged major element bulk rock compositions for barren eclogite xenoliths. All values are given in wt%. Bulk rock compositions were calculated for all eclogites with fresh garnet and clinopyroxene.

Sample #	**52006-1**		**52006-2**	**52006-3**			**52006-4**		**52006-5**		**52006-6**		**52006-7**	
Paragenesis	Omph	Di	Omph	Omph	Omph	Di	Omph	Di	Omph	Di	Omph	Di	Omph	Omph
SiO_2	48.5	48.0	47.7	47.7	46.3	46.4	48.5	48.0	47.4	46.3	47.2	46.7	47.1	45.9
TiO_2	0.24	0.27	0.20	0.15	0.28	0.21	0.29	0.30	0.28	0.31	0.14	0.13	0.19	0.22
Al_2O_3	14.1	13.1	14.8	15.8	14.8	14.3	13.8	12.6	15.7	13.4	16.1	14.0	19.1	17.8
Cr_2O_3	0.13	0.15	0.12	0.08	0.10	0.08	0.11	0.13	0.06	0.08	0.06	0.08	0.01	0.02
MnO	0.19	0.20	0.20	0.21	0.22	0.22	0.19	0.20	0.19	0.20	0.17	0.18	0.13	0.13
FeO	5.9	6.0	9.9	9.7	10.2	10.4	6.0	6.2	11.2	11.7	9.6	9.6	7.0	7.2
NiO	0.04	0.04	0.04	0.02	0.02	0.02	0.03	0.03	0.03	0.03	0.04	0.05	0.01	0.02
MgO	17.7	18.7	13.1	11.4	12.5	12.8	17.5	18.7	10.4	12.4	10.9	12.3	8.2	9.6
CaO	11.2	12.6	11.2	11.7	13.2	13.6	11.2	12.6	10.6	13.2	12.6	14.7	13.6	15.7
Na_2O	1.5	0.6	2.1	2.4	1.4	1.1	1.5	0.5	3.0	1.2	2.3	1.2	3.5	2.3
K_2O	0.00	0.00	0.01	0.01	0.00	0.00	0.00	0.00	0.00	0.00	0.00	0.01	0.01	0.01
P_2O_5	0.03	0.02	0.04	0.03	0.03	0.03	0.03	0.03	0.04	0.04	0.02	0.05	0.03	0.04
Total	99.5	99.6	99.3	99.2	99.1	99.2	99.1	99.2	98.9	98.9	99.0	99.1	99.0	99.0

Table B6 - Part A continued

Sample #	52006-9		52006-11			52006-12		52006-13	52006-14	52006-15		52006-16
Paragenesis	Omph	Di	Omph	Di	Di	Omph	Di	Di	Omph	Omph	Di	Omph
SiO_2	48.3	47.7	47.5	46.9	45.5	47.6	46.7	47.8	47.4	47.6	47.2	48.2
TiO_2	0.30	0.29	0.22	0.23	0.41	0.16	0.18	0.36	0.13	0.32	0.25	0.20
Al_2O_3	14.1	12.8	15.0	13.4	14.8	14.9	13.1	14.3	17.2	14.5	13.0	13.2
Cr_2O_3	0.24	0.27	0.06	0.07	0.06	0.14	0.17	0.07	0.05	0.01	0.08	0.82
MnO	0.20	0.21	0.19	0.20	0.23	0.24	0.24	0.22	0.18	0.20	0.22	0.22
FeO	7.0	7.4	10.1	10.3	11.0	11.5	11.7	7.2	9.2	8.7	8.8	6.1
NiO	0.02	0.02	0.04	0.04	0.03	0.01	0.02	0.01	0.00	0.02	0.02	0.02
MgO	16.6	18.0	12.2	13.7	13.1	11.9	13.3	15.2	9.1	13.8	15.3	17.3
CaO	10.3	11.8	11.1	13.1	13.0	10.2	12.2	12.9	12.7	11.4	13.3	11.3
Na_2O	1.8	0.6	2.3	1.0	0.9	2.2	1.1	1.3	2.8	2.1	0.8	1.4
K_2O	0.00	0.00	0.01	0.00	0.00	0.01	0.00	0.00	0.00	0.00	0.00	0.00
P_2O_5	0.03	0.03	0.03	0.03	0.03	0.04	0.04	0.02	0.04	0.02	0.02	0.03
Total	98.9	99.1	98.8	99.0	99.0	98.8	98.7	99.3	98.8	98.8	98.9	99.0

Table B6 - Part A continued

Sample #	**52006-17**		**52006-18**		**52006-21**		**52006-22**	**52006-23**		**52006-24**		**52006-26**	
Paragenesis	Omph	Di	Omph	Di	Omph	Di	Omph	Omph	Di	Omph	Di	Omph	Di
SiO_2	48.4	48.1	47.8	47.2	48.7	47.8	48.4	48.7	48.2	47.6	46.8	47.3	46.1
TiO_2	0.25	0.25	0.28	0.27	0.21	0.20	0.21	0.29	0.29	0.10	0.09	0.26	0.28
Al_2O_3	13.4	12.7	14.4	13.1	14.6	13.7	13.7	14.1	13.0	16.1	14.6	14.9	13.5
Cr_2O_3	0.22	0.22	0.09	0.10	0.04	0.04	0.14	0.06	0.06	0.05	0.05	0.06	0.09
MnO	0.19	0.20	0.19	0.20	0.20	0.22	0.23	0.20	0.21	0.19	0.19	0.18	0.21
FeO	6.9	6.9	9.6	9.9	7.5	7.6	6.8	7.1	7.3	10.1	10.4	9.4	10.1
NiO	0.02	0.02	0.03	0.04	0.03	0.03	0.01	0.03	0.03	0.00	0.00	0.04	0.03
MgO	17.1	17.9	13.3	14.6	15.5	16.6	16.8	16.7	17.8	9.5	10.7	11.9	14.0
CaO	11.0	12.3	11.2	12.9	10.9	12.2	11.4	10.5	11.9	13.3	15.1	12.5	14.0
Na_2O	1.5	0.6	2.2	0.9	1.9	0.9	1.5	1.8	0.8	2.4	1.3	2.3	0.6
K_2O	0.00	0.00	0.00	0.00	0.00	0.00	0.00	0.00	0.00	0.00	0.00	0.00	0.00
P_2O_5	0.03	0.02	0.03	0.03	0.03	0.04	0.03	0.02	0.02	0.03	0.03	0.03	0.03
Total	99.1	99.2	99.2	99.2	99.7	99.5	99.3	99.3	99.5	99.3	99.3	98.8	98.8

Table B6 - Part B Averaged major element bulk rock compositions for diamond-bearing xenoliths. All values are given in wt%. Bulk rock compositions were calculated for all eclogites with fresh garnet and clinopyroxene. In diamondiferous samples assumed primary garnet compositions were used in the calculation.

Sample #	**SGF-003 50036**	**SGF-009 50095**	**SGF-039 50443-2**	**SGF-040 50461**	**SGF-040 50465**		**SGF-066 51152**	**SGF-140 37430**
Paragenesis	Omph	Omph	Omph	Omph	Omph	Di	Omph	Omph
SiO_2	48.1	47.8	47.7	47.8	47.2	46.3	47.9	48.1
TiO_2	0.23	0.43	0.47	0.19	0.21	0.33	0.46	0.20
Al_2O_3	14.5	16.3	15.9	14.9	14.4	14.0	16.7	14.6
Cr_2O_3	0.11	0.03	0.05	0.12	0.10	0.10	0.07	0.04
MnO	0.14	0.25	0.22	0.11	0.23	0.24	0.24	0.28
FeO	6.4	11.8	9.9	5.4	9.0	9.4	11.4	9.7
NiO	0.02	0.01	0.01	0.04	0.02	0.00	0.01	0.03
MgO	14.9	11.0	12.4	14.0	13.8	14.4	11.4	15.7
CaO	13.4	9.0	9.6	14.6	12.1	12.9	8.2	8.6
Na_2O	1.6	3.1	2.7	1.7	1.7	1.0	3.1	2.1
K_2O	0.12	0.09	0.13	0.11	0.08	0.01	0.10	0.03
P_2O_5	0.03	0.03	0.04	0.02	0.02	0.02	0.04	0.03
Total	99.5	99.8	99.1	98.9	98.9	98.8	99.7	99.4

Table B7 Averaged trace element bulk rock compositions for barren clogites. All values are given in ppm. Bulk rock compositions were calculated for all eclogites with fresh garnet and clinopyroxene. Only primary clinopyroxene compositions (omphacite) were used, as diopside from spongy rims was not analysed.

Sample #	52006-1	52006-2	52006-3	52006-4	52006-5	52006-6	52006-7	52006-9
Sc	42.23	37.61	47.87	38.46	31.32	33.15	20.08	34.28
Ti	1592.4	1250.5	1054.1	1853.0	1920.2	876.5	1046.3	1996.1
V	309.0	168.0	210.2	330.8	268.2	180.0	124.3	258.7
Co	37.64	61.50	52.57	39.01	61.68	61.20	49.93	43.45
Ni	243.1	299.5	147.7	249.9	236.4	309.2	147.9	165.3
Zn	15.10	56.61	70.57	15.64	70.88	73.49	31.26	17.83
Ga	10.12	11.81	12.26	11.15	15.17	15.97	12.20	13.61
Rb	0.216	0.0044	-	-	0.0268	0.785	0.148	-
Sr	92.14	141.6	120.7	94.69	93.43	123.9	22.63	160.4
Y	8.37	10.13	9.70	8.06	9.72	5.36	4.82	14.48
Zr	12.00	13.83	14.50	13.08	14.98	7.82	18.86	30.81
Nb	0.214	0.0025	0.6309	0.242	0.375	0.656	1.0316	0.554
Ba	0.631	0.407	-	1.0705	0.114	65.28	-	0.218
La	6.68	2.77	1.68	7.23	1.63	1.17	0.403	7.05
Ce	11.45	6.90	5.18	12.69	5.68	3.42	1.86	19.42
Pr	0.951	0.852	0.780	1.01	0.907	0.493	0.427	2.41
Nd	3.37	3.87	3.94	3.47	4.32	2.39	3.30	10.01
Sm	0.865	1.28	1.35	0.868	1.10	0.699	1.76	2.14
Eu	0.356	0.594	0.576	0.368	0.464	0.415	0.821	0.713
Gd	1.11	1.69	1.70	1.13	1.37	0.8595	1.62	2.22
Tb	0.195	0.282	0.266	0.195	0.242	0.142	0.194	0.370
Dy	1.43	1.91	1.74	1.39	1.73	0.9659	1.02	2.56
Ho	0.312	0.378	0.364	0.309	0.366	0.202	0.175	0.549
Er	1.00	1.10	1.13	0.961	1.10	0.606	0.465	1.66
Tm	0.145	0.146	0.154	0.136	0.149	0.0827	0.0596	0.237
Yb	1.08	1.04	1.12	1.03	1.06	0.615	0.431	1.71
Lu	0.165	0.147	0.149	0.154	0.153	0.0946	0.0583	0.251
Hf	0.440	0.409	0.390	0.469	0.412	0.308	0.602	0.875
Pb	0.399	0.508		0.418	0.165	0.145	0.0251	0.644
Th	0.238	0.0981	0.115	0.253	0.0358	0.0705	0.0104	0.200
U	0.0469	0.0253	0.0248	0.0574	0.0228	0.0230	0.0448	0.0474

Table B7 continued

Sample #	52006-11	52006-12	52006-13	52006-14	52006-15	52006-16	52006-17
Sc	31.15	37.71	69.06	45.22	35.20	49.78	34.04
Ti	1730.9	1112.5	2542.1	872.7	1997.7	847.4	875.5
V	268.9	224.2	311.5	256.2	255.7	275.9	227.5
Co	68.53	59.31	35.28	37.37	50.10	22.76	25.13
Ni	351.2	135.0	54.72	35.42	182.4	169.5	177.1
Zn	61.26	73.27	22.10	77.80	20.72	14.59	19.37
Ga	28.00	14.29	10.43	16.77	12.60	9.52	11.28
Rb	3.24	0.0497	-	-	-	-	0.0826
Sr	137.8	174.0	84.84	162.6	156.8	221.3	182.6
Y	7.81	12.58	19.18	18.08	6.87	18.79	7.50
Zr	14.48	10.02	28.67	16.09	7.33	41.18	33.43
Nb	0.642	0.0225	0.0223	-	0.185	0.617	0.695
Ba	551.2	0.105	0.587	-	0.411	-	1.2937
La	3.87	1.91	1.11	0.169	6.50	8.76	6.94
Ce	10.45	6.40	5.35	1.29	16.97	29.06	26.68
Pr	1.27	0.954	1.08	0.402	1.98	3.93	3.58
Nd	5.23	4.63	6.37	3.31	7.37	17.03	15.69
Sm	1.20	1.32	1.98	1.59	1.05	3.04	2.69
Eu	0.519	0.565	0.760	0.796	0.387	0.900	0.766
Gd	1.27	1.77	2.45	2.30	1.06	2.59	1.86
Tb	0.202	0.316	0.423	0.414	0.179	0.416	0.243
Dy	1.44	2.27	3.18	3.06	1.27	3.05	1.46
Ho	0.299	0.467	0.718	0.675	0.264	0.708	0.286
Er	0.905	1.36	2.34	2.11	0.76	2.32	0.835
Tm	0.129	0.184	0.338	0.296	0.099	0.348	0.114
Yb	0.916	1.27	2.50	2.12	0.695	2.60	0.792
Lu	0.137	0.185	0.371	0.312	0.0973	0.400	0.121
Hf	0.443	0.355	0.888	0.716	0.226	1.12	0.907
Pb	0.299	0.356	0.0912	0.251	0.302	-	0.459
Th	0.0885	0.0250	0.0408	0.0016	0.143	0.174	0.106
U	0.0334	0.0079	0.0102	0.0003	0.0497	0.0476	0.0289

Table B7 continued

Sample #	52006-18	52006-21	52006-22	52006-23	52006-24	52006-26
Sc	30.31	44.12	44.34	34.57	48.01	53.86
Ti	1348.1	1348.7	1297.8	2043.2	575.9	1606.6
V	218.7	221.1	244.1	234.0	229.3	298.1
Co	38.02	50.48	33.00	38.97	37.29	54.09
Ni	283.7	195.4	113.3	155.5	33.18	246.3
Zn	49.28	27.01	12.96	12.12	86.57	29.12
Ga	13.36	16.63	9.35	11.86	16.33	11.20
Rb	-	-	-	-	-	0.0394
Sr	123.4	164.8	213.2	118.8	143.9	121.4
Y	8.94	6.88	10.45	15.07	23.18	4.16
Zr	20.26	16.09	47.66	25.50	16.74	6.94
Nb	0.467	0.501	0.553	1.08	0.0475	0.580
Ba	-	99.1438	0.1036	-	0.0153	-
La	3.09	5.98	7.48	5.21	0.126	3.78
Ce	11.29	16.45	25.71	16.61	1.41	9.12
Pr	1.62	1.95	3.57	2.10	0.507	0.934
Nd	7.50	8.01	15.89	8.71	4.54	3.61
Sm	1.70	1.50	2.89	1.56	2.34	0.792
Eu	0.651	0.520	0.855	0.503	1.00	0.308
Gd	1.78	1.39	2.23	1.54	3.30	0.809
Tb	0.277	0.210	0.315	0.286	0.586	0.126
Dy	1.73	1.35	1.96	2.29	4.09	0.795
Ho	0.343	0.264	0.392	0.564	0.871	0.161
Er	0.970	0.724	1.12	1.91	2.59	0.462
Tm	0.127	0.0939	0.152	0.282	0.361	0.0644
Yb	0.862	0.645	1.08	2.15	2.55	0.466
Lu	0.124	0.0949	0.156	0.342	0.370	0.0716
Hf	0.526	0.371	1.35	0.903	0.736	0.183
Pb	0.213	-	-	0.230	0.194	0.293
Th	0.0643	0.135	0.125	0.126	-	0.0847
U	0.0267	0.0367	0.0307	0.0339	0.0008	0.0535

Appendix C – Geochemical data for diamonds from Fort à la Corne

Data reported in Appendix C are averaged; for the complete dataset see the UAL Dataverse dataset: "Geochemical data for diamonds from Fort à la Corne" at

https://doi.org/10.7939/DVN/AQ2J5V

Table C1 Diamond petrography; Morphology, size, colour, surface features, and inclusions of Fort à la Corne diamonds

Sample#	SGF-003 50036	SGF-008 50076	SGF-009 50095			SGF-020 50138	
	1	1	1	2	3	1	2
Host	Ecl	Ecl	Ecl	Ecl	Ecl	Ecl	Ecl
Type	MC	A	MC	MC	A	A	A
Shape	M	O, A	O	M	M, A	I, A?	I, A?
Colour	Colourless	Brown	Colourless	Colourless	Colourless	Grey	Grey
Weight (g)	0.00093	0	6E-04	0.004	0.01165	0.00039	0.00022
Surface	SG, negTrig	SG, DL, some Res	SG, IG	SG	IG		
CL	Zoned	Homogenous w/ rim	Zoned	Zoned	Zoned	Fractured	Fractured
Inclusion		Graphite incl				Graphite incl Cloudy	Graphite incl Cloudy
Comment	Serpentine on surface						

Eclogite - Ecl, Peridotite - Per, Kimberlite - Kimb, Garnet – Gt
Octahedra - O, Dodecahedron - D, Macle - M, Aggregate - A, Irregular (unknown shape) - I, Dyke - Dy, Inclusions – Incl
Stepped growth - SG, Deformation lines – DL, Imperfect growth – IG, Ribbing - R, Rough surface -RS, Resorption - Res, negative Trigons - negTrig,
All grey diamonds have a brown tint.

Table C1 continued

Sample#	SGF-020 50140					SGF-021 50148	
	1	2	3	4	5	1	2
Host	Ecl	Ecl	Ecl	Ecl	Ecl	Ecl	Ecl
Type	A	A	A	A	A	MC	MC
Shape	Dy	Dy	Dy	Dy	Dy	F	F
Colour	Grey	Grey	Grey	Grey	Grey	Grey	Grey
Weight (g)	0.00227	0.00435	0.00175	4E-04	1.74504	0.00125	0.02511
Surface						RS	RS
CL	Fractured, zoned	Fractured, zoned	Fractured, zoned	Fractured, zoned	Fractured, zoned	Homogenous	Complex
Inclusion	Cloudy	Cloudy	Cloudy	Cloudy	Cloudy	Graphite incl	Cloudy
Comment	Diamond broken out of the dyke	Diamond broken out of the dyke	Diamond broken out of the dyke	Diamond broken out of the dyke	Half sample, including ecl		

Table C1 continued

Sample#	SGF-025 50223		SGF-025 50224-1		SGF-025 50224-2	SGF-025 50224-3	
	1	2	1	2	1	1	2
Host	Ecl	Ecl	Ecl	Ecl	Ecl	Ecl	Ecl
Type	MC	A	A	A	A	A	A
Shape	O, F	O, A	O, A	D, A	O-D, A	O-D, A	O-D, A
Colour	Colourless - Grey/Brown	Colourless - Grey/Brown	Colourless - Grey/Brown	Colourless - Grey/Brown	Colourless - Grey/Brown	Colourless - Grey/Brown	Colourless - Grey/Brown
Weight (g)	0.00378	0.00031	0.00016	0.00059	0.00161	0.00058	0.00121
Surface	SG, negTrig	SG	Lightly graphitised, RS	SG, R, IG of octahedra faces			
CL	Homogenous	Fractured	Fractured	Fractured	Fractured	Fractured	Fractured
Inclusion	Graphite incl	Graphite incl Cloudy		Cloudy	Dark microincl		
Comment							

Table C1 continued

Sample#	SGF-025 50225			SGF-025 50226	SGF-034		SGF-039 50443-1
	1	2	3	1	1	2	1
Host	Ecl	Ecl	Ecl	Ecl	Ecl	Ecl	Ecl
Type	A	A	A	A	MC	MC	MC
Shape	O-D, A	O-D, A	O-D, A	O-D, A	O-D, F	O-D, F	O, F
Colour	Colourless - Grey/Brown	Colourless - Grey/Brown	Colourless - Grey/Brown	Colourless - Grey/Brown	Colourless	Cplourless	Colourless
Weight (g)	0.00026	0.00028	0.00091	0.00051	0.00202	0.00342	0.00052
Surface				RS	SG	SG, negTrig	SG
CL	Fractured	Fractured	Fractured	Fractured	Complex	Homogenous	Homogenous w/ rim
Inclusion				Dark Incl	Graphite incl		
Comment				Cloudy Serpentine/kimb on surface			

Table C1 continued

Sample#	SGF-039 50443-2	SGF-039 50446			SGF-040 50455	SGF-040 50461
	1	1	2	3	1	1
Host	Ecl	Ecl	Ecl	Ecl	Ecl	Ecl
Type	A	A	A	A	A	A
Shape	O, A, F	D, A, F	D, A, F	D, A, F	O, A	O-D, A
Colour	Colourless	Brown	Colourless	Yellow-brown	Brown	Brown
Weight (g)	0.00046	0.00155	0.00049	0.00029	0.00044	0.00064
Surface	SG	SG	SG	SG	SG, minimal Res, negTri	SG
CL	Complex	Fractured	Fractured	Fractured	Homogenous w/ rim	Homogenous w/ rim
Inclusion		Graphite incl				Incl along fracture
Comment	Cloudy Serpentine/kimb on surface	Cloudy Serpentine/kimb on surface	Cloudy Serpentine/kimb on surface	Cloudy Serpentine/kimb on surface	Serpentine/kimb on surface	Cloudy Serpentine/kimb on surface

Table C1 continued

Sample#	SGF-042 50495 1	SGF-048 50655 1	SGF-066 51152 1	SGF-067 51188 1	SGF-127 53865-1 1	 2
Host	Ecl	Ecl	Ecl	Per	Per	Per
Type	A?	A	A	MC	PC	PC
Shape	O-D	O, A	I, A	O	O, A, F	O, A, F
Colour	Colourless	Grey	Grey	Colourless	Grey	Grey
Weight (g)	0.01613	0.00312	0.00191	0.00359	0.00019	0.0005
Surface	SG	SG, R, minimal Res	RS	SG, R (110), minimal Res on edges	Lightly graphitised, RS, SG	Lightly graphitised, RS, SG
CL	Complex	Complex	Zoned	Zoned	Complex	Complex
Inclusion	Incl along fracture			Dark micro-incl (graphite?)	Dark micro-incl (graphite?)	
Comment	Cloudy Serpentine/kimb on surface	Cloudy Serpentine/kimb on surface	Cloudy		Cloudy	Cloudy

Table C1 continued

Sample#	SGF-127 53865-2		SGF-140 37430		
	1	2	1	2	3
Host	Per	Per	Ecl	Ecl	Ecl
Type	PC	PC	A	A	A
Shape	O, A, F	O, A, F	O-D, A	O-D, A	O-D, A
Colour	Grey	Grey	Colourless	Colourless	Colourless
Weight (g)	0.00058	0.00023	0.00093	0.00034	0.00023
Surface	Lightly graphitised, RS, SG	Lightly graphitised, RS, SG	Incomplete growth	Incomplete growth	Incomplete growth
CL	Complex	Complex	Complex	Complex	Complex
Inclusion	Dark micro-incl (graphite?)	Dark micro-incl (graphite?)			
Comment	Cloudy Intergrown w/ purple gt	Cloudy			

Table C2 – Part A Fourier transform infrared spectroscopy (FTIR) data for diamonds from Fort à la Corne. Table is split into three parts (A, B and C). Nitrogen content and aggregation state are reported in ppm and %B, respectively. The location and area of the platelet peak (B') are given in cm^{-1} and cm^{-2}.

Sample#			Diamond Type (N aggregation)	N_A (ppm)	N_B (ppm)	N_T (ppm)	%B	Platelet - B' (1378 - 1358 cm^{-1}) Position (cm^{-1})	Area (cm^{-2})
SGF-003	**50036**	a	IaAB	448	227	674	34	1369	143
		b	IaAB	456	225	681	33	1369	133
		c	IaAB	443	201	644	31	1360	122
		d	IaAB	452	203	654	31	1369	142
SGF-008	**50076**	b	IaB	0	222	222	100		
		c	IaB	0	107	107	100		
SGF-009	**50095-1**	a	IaA	924	11	935	1		
		b	IaA	977	27	1005	3		
	50095-2	a	IaAB	633	175	808	22	1370	26
		b	IaAB	636	167	803	21	1370	29
	50095-3	a	IaAB	523	221	744	30	1370	22
		b	IaAB	679	161	840	19	1374	8
SGF-020	**50138-1**	a	II						
	50138-2	b	II						
	50140-1	a	IaB	0	532	532	100		
		b	IaB	0	549	549	100		
	50140-2	a	IaB	0	779	779	100	1368	7
		b	IaB	0	889	889	100	1368	4
	50140-3	a	IaB	0	238	238	100		
		b	IaB	0	333	333	100	1365	9
	50140-4	a	IaB	0	397	397	100	1367	0.2
		b	IaB	0	286	286	100		
SGF-021	**50148-1**	a	II						
		b	II						
	50148-2	a	-						
		b	-						

Table C2 – Part A continued

Sample#			Diamond Type (N aggregation)	N_A (ppm)	N_B (ppm)	N_T (ppm)	%B	Platelet - B' (1378 - 1358 cm^{-1}) Position (cm^{-1})	Area (cm^{-2})
SGF-025	50223-1	a	II						
		b	II						
	50223-2	a	IaB	1	476	477	100		
		b	IaB	0	397	397	100		
	50224-1-1	a	IaB	0	121	121	100	1366	18
		b	IaB	0	357	357	100		
	50224-1-2	a	IaB	0	381	381	100		
		b	IaB	0	405	405	100		
	50224-2	a	IaB	0	692	692	100		
	50224-3-1	a	IaB	0	99	99	100		
		b	IaB	0	206	206	100		
	50224-3-2	a	-						
	50225-1	a	IaB	0	48	48	100		
		b	IaB	0	56	56	100		
	50225-2	a	IaB	0	194	194	100		
		b	IaB	0	193	193	100		
	50225-3		-						
	50226	a	IaB	0	62	62	100		
		b	IaB	0	43	43	100		
SGF-034	1	a	II						
		b	II						
	2	a	II						
		b	II						

Table C2 – Part A continued

Sample#			Diamond Type (N aggregation)	N_A (ppm)	N_B (ppm)	N_T (ppm)	%B	Platelet - B' (1378 - 1358 cm^{-1}) Position (cm^{-1})	Area (cm^{-2})
SGF-039	50443-1	a	IaAB	10	8	18	45	1369	3
		b	IaAB	5	17	22	77	1361	3
	50443-2	a	IaA	923	13	936	1		
		b	IaA	878	0	878	0		
	50446-1	a	II						
		b	II						
	50446-2	a	II						
		b	II						
	50446-3	a	-						
		b	IaB	0	24	24	100		
SGF-040	50455	a	II						
		b	II						
	50461	a	II						
		b	II						
SGF-042	50495	a	IaAB	78	393	471	83	1360	143
		b	IaAB	78	343	421	81	1360	117
SGF-048	50655	a	II						
		b	II						
SGF-066	51152	a	IaAB	133	302	435	69	1378	19
		b	IaAB	303	139	442	31	1378	17
SGF-067	51188	a	IaAB	23	14	37	38	1359	8
		b	IaAB	22	12	34	35	1360	7

Table C2 – Part A continued

Sample#			Diamond Type (N aggregation)	N_A (ppm)	N_B (ppm)	N_T (ppm)	%B	Platelet - B' (1378 - 1358 cm^{-1}) Position (cm^{-1})	Area (cm^{-2})
SGF-127	53865-1-1	a	IaAB	748	177	925	19	1370	92
		b	IaAB	710	183	892	21	1370	108
	53865-1-2	a	IaAB	792	159	951	17	1370	87
		b	IaAB	792	167	959	17	1370	83
	53865-2-1	a	II						
		b	II						
	53865-2-2	a	II						
		b	II						
SGF-140	37430-1	a	IaAB	750	171	921	19	1369	99
		b	IaAB	639	166	805	21	1369	92
	37430-2	a	IaAB	712	182	894	20	1369	109
		b	IaAB	383	90	473	19	1369	51
	37430-3	a	IaAB	600	144	745	19	1369	77
		b	IaAB	623	140	763	18	1369	80

Table C2 – Part B FTIR data for diamonds from FALC. Area under the hydrogen peak (3107 cm^{-1}), and nitrogen aggregation and platelet peak degradation temperatures (^oC) are listed. Location of carbonate, CO_2 and CH_2 peaks is reported when identified.

Sample#			Hydrogen (3107 cm^{-1}) Area (cm^{-2})	$T_{Nitrogen}$ (2Ga) (^oC)	$T_{Platelet}$(2Ga) (^oC)	Carbonate 870-885, 1420 - 1450 cm^{-1}	CO_2 650-670, 2350-2395cm^{-1}	CH_2 symmetric & asymmetric stretch
SGF-003	**50036**	a	6	1115	1138	-	-	2850, 2920
		b	4	1114	1178	-	-	2850, 2920
		c	3	1113	1170	-	-	2850, 2920
		d	6	1113	-	-	-	2850, 2920
SGF-008	**50076**	b	1	-	-	-	2391	2850, 2920
		c	2	-	-	-	2391	2850, 2920
SGF-009	**50095-1**	a	3	1023	-	-	-	-
		b	2	1041	-	-	-	-
	50095-2	a	1	1096	1251	-	-	-
		b	1	1096	1248	-	-	-
	50095-3	a	2	1108	1257	-	-	-
		b	4	1092	1266	-	-	-
SGF-020	**50138-1**	a	5	1385	-	874, 1420-1450	-	2850, 2920
	50138-2	b	5	-	-	874, 1420-1451	-	2850, 2920
	50140-1	a	38	1280	-	864, 1420-1450	2369	2856, 2924
		b	40	1279	-	864, 1420-1450	-	2856, 2924
	50140-2	a	49	1269	1279	864, 1420-1451	2370	-
		b	49	1265	1284	-	-	-
	50140-3	a	27	1304	-	864, 1420-1451	2378	2852, 2922
		b	34	1294	1272	864, 1420-1452	2380	2848, 2922
	50140-4	a	34	1289	1294	864, 1420-1453	2368	-
		b	27	1299	-	864, 1420-1454	660, 2376	-
SGF-021	**50148-1**	a	-	-	-	864, 1420-1453	-	2850, 2918
		b	-	-	-	864, 1420-1453	-	2850, 2918
	50148-2	a	-	-	-	864, 1420-1453	-	2850, 2918

Table C2 – Part B continued

Sample#			Hydrogen (3107 cm^{-1}) Area (cm^{-2})	$T_{Nitrogen}$ (2Ga) (^oC)	$T_{Platelet}$(2Ga) (^oC)	Carbonate 870-885, 1420-1450 cm^{-1}	CO_2 650-670, 2350-2395cm^{-1}	CH_2 symmetric & asymmetric stretch
SGF-025	50223-1	a	-	-	-	-	-	-
		b	-	-	-	1420-1450	-	2852, 2924
	50223-2	a	29	1311	-	862, 1420-1450	661, 2362	2848, 2916
		b	28	1289	-	862, 1420-1450	660, 2362	2848, 2920
	50224-1-1	a	12	1325	1251	862, 1420-1450	658, 2362	2852, 2924
		b	23	1292	-	862, 1420-1450	660, 2362	2850, 2925
	50224-1-2	a	34	1290	-	862, 1420-1450	658, 2364	2852, 2926
		b	28	1288	-	862, 1420-1450	658, 2362	-
	50224-2	a	32	1272	-	862, 1420-1450	660, 2364	2850, 2918
	50224-3-1	a	11	1332	-	862, 1420-1450	665, 2354	2848, 2922
		b	21	1309	-	862, 1420-1450	665, 2354	2848, 2922
	50224-3-2	a	-	-	-	-	-	-
	50225-1	a	7	1355	-	-	661, 2354	2852, 2916
		b	7	1350	-	-	661, 2362	2852, 2916
	50225-2	a	17	1311	-	862, 1420-1450	660, 2366	2852, 2922
		b	17	1311	-	862, 1420-1450	658, 2366	2856, 2929
	50225-3		-	-	-	-	-	-
	50226	a	9	1347	-	-	661, 2354	2850, 2918
		b	7	1359	-	-	661, 2355	2850, 2918
SGF-034	1	a	0.4	-	-	1450-1471	-	2852, 2926
		b	0.3	-	-	877, 1450-1471	-	2852, 2924
	2	a	-	-	-	1450-1471	-	2852, 2924
		b	-	-	-	1450-1471	-	2852, 2925

Table C2 – Part B continued

Sample#			Hydrogen (3107 cm^{-1}) Area (cm^{-2})	$T_{Nitrogen}$ (2Ga) (^oC)	$T_{Platelet}$(2Ga) (^oC)	Carbonate 870-885, 1420-1450 cm^{-1}	CO_2 650-670, 2350-2395cm^{-1}	CH_2 symmetric & asymmetric stretch
SGF-039	50443-1	a	2	1219	1227	1420-1450	-	2852, 2924
		b	1	1253	1246	1420-1450	-	2850, 2922
	50443-2	a	7	1028	-	-	-	2856, 2926
		b	13	1008	-	-	-	2850, 2922
	50446-1	a	0	-	-	1457, 1540	662, 2391	2858, 2927
		b	2	-	-	866, 1457, 1540	660, 2391	2852, 2921
	50446-2	a	2	-	-	877, 1420-1460	660, 2386	2852, 2929
		b	3	-	-	-	660, 2386	2854, 2927
	50446-3	a	-	-	-	1420-1450	660, 2393	2854, 2923
		b	3	1378	-	875, 1420-1450	660, 2391	2854, 2923
SGF-040	50455	a	-	-	-	862, 1430-1480	660, 2341/2393	2850, 2920
		b	-	-	-	1420-1480	660, 2341/2393	2850, 2922
	50461	a	5	-	-	1420-1480	660, 2341/2395	2852, 2920
		b	-	-	-	1420-1480	660, 2341/2391	2850, 2920
SGF-042	50495	a	42	1181	1226	-	-	-
		b	40	1180	1229	-	-	-
SGF-048	50655	a	-	-	-	-	657, 2337/2391	2848, 2918
		b	-	-	-	875, 1420-1450	660, 2339/2393	2850, 2920
SGF-066	51152	a	42	1163	1263	-	-	2850, 2922
		b	31	1123	1254	-	-	2852, 2924
SGF-067	51188	a	1	1192	-	-	-	2850, 2920
		b	2	1191	1175	-	-	2850, 2920

Table C2 – Part B continued

Sample#			Hydrogen (3107 cm^{-1}) Area (cm^{-2})	$T_{Nitrogen}$ (2Ga) (^oC)	$T_{Platelet}$(2Ga) (^oC)	Carbonate 870-885, 1420-1450 cm^{-1}	CO_2 650-670, 2350-2395cm^{-1}	CH_2 symmetric & asymmetric stretch
SGF-127	53865-1-1	a	3	1090	1202	-	-	2850, 2920
		b	8	1093	1177	-	-	2850, 2920
	53865-1-2	a	5	1085	1194	-	-	2850, 2918
		b	3	1086	1206	-	-	2850, 2824
	53865-2-1	a	16	-	-	-	-	-
		b	18	-	-	-	-	-
	53865-2-2	a	12	-	-	-	-	-
		b	12	-	-	-	-	-
SGF-140	37430-1	a	1	1089	1185	-	-	2850, 2922
		b	1	1095	1192	-	-	2850, 2922
	37430-2	a	1	1092	1175	-	-	2850, 2920
		b	1	1105	1189	-	-	2850, 2920
	37430-3	a	2	1095	1197	-	-	2850, 2922
		b	2	1093	1186	-	-	2852, 2924

Table C2 - Part C FTIR data for diamonds from FALC. List of mineral micro-inclusions identified in the FTIR spectrum.

Sample#			Mineral inclusions
SGF-003	**50036**	a	730-850cm^{-1} (cb/sil), 1014cm^{-1} (sheet sil), 1090cm^{-1} (phl/ap/cb)
		b	730-850cm^{-1} (cb/sil), 1014cm^{-1} (sheet sil), 1090cm^{-1} (phl/ap/cb)
		c	730-850cm^{-1} (cb/sil), 1014cm^{-1} (sheet sil), 1090cm^{-1} (phl/ap/cb)
		d	730-850cm^{-1} (cb/sil), 1014cm^{-1} (sheet sil), 1090cm^{-1} (phl/ap/cb), 3676cm^{-1} (hydrated mica)
SGF-008	**50076**	b	3676cm^{-1} (hydrated mica)
		c	3676cm^{-1} (hydrated mica)
SGF-009	**50095-1**	a	1090cm^{-1} (phl/ap/cb)
		b	1090cm^{-1} (phl/ap/cb)
	50095-2	a	730-850cm^{-1} (cb/sil), 1014cm^{-1} (sheet sil), 1090cm^{-1} (phl/ap/cb)
		b	730-850cm^{-1} (cb/sil), 1014cm^{-1} (sheet sil), 1090cm^{-1} (phl/ap/cb)
	50095-3	a	730-850cm^{-1} (cb/sil), 1014cm^{-1} (sheet sil), 1090cm^{-1} (phl/ap/cb)
		b	730-850cm^{-1} (cb/sil), 1014cm^{-1} (sheet sil), 1090cm^{-1} (phl/ap/cb)
SGF-020	**50138-1**	a	730-850cm^{-1} (cb/sil), 1014cm^{-1} (sheet sil), 1090cm^{-1} (phl/ap/cb), 3676cm^{-1} (hydrated mica)
	50138-2	b	730-850cm^{-1} (cb/sil), 1014cm^{-1} (sheet sil), 1090cm^{-1} (phl/ap/cb), 3676cm^{-1} (hydrated mica)
	50140-1	a	730-850cm^{-1} (cb/sil), 1014cm^{-1} (sheet sil), 1090cm^{-1} (phl/ap/cb), 3676cm^{-1} (hydrated mica)
		b	730-850cm^{-1} (cb/sil), 1014cm^{-1} (sheet sil), 1090cm^{-1} (phl/ap/cb), 3676cm^{-1} (hydrated mica)
	50140-2	a	730-850cm^{-1} (cb/sil), 1014cm^{-1} (sheet sil), 1090cm^{-1} (phl/ap/cb), 3676cm^{-1} (hydrated mica)
		b	730-850cm^{-1} (cb/sil), 1014cm^{-1} (sheet sil), 1090cm^{-1} (phl/ap/cb), 3676cm^{-1} (hydrated mica)
	50140-3	a	730-850cm^{-1} (cb/sil), 1014cm^{-1} (sheet sil), 1090cm^{-1} (phl/ap/cb), 3676cm^{-1} (hydrated mica)
		b	730-850cm^{-1} (cb/sil), 1014cm^{-1} (sheet sil), 1090cm^{-1} (phl/ap/cb), 3676cm^{-1} (hydrated mica)
	50140-4	a	730-850cm^{-1} (cb/sil), 1014cm^{-1} (sheet sil), 1090cm^{-1} (phl/ap/cb), 3676cm^{-1} (hydrated mica)
		b	730-850cm^{-1} (cb/sil), 1014cm^{-1} (sheet sil), 1090cm^{-1} (phl/ap/cb), 3676cm^{-1} (hydrated mica)
SGF-021	**50148-1**	a	730-850cm^{-1} (cb/sil), 1014cm^{-1} (sheet sil), 1090cm^{-1} (phl/ap/cb), 3676cm^{-1} (hydrated mica)
		b	730-850cm^{-1} (cb/sil), 1014cm^{-1} (sheet sil), 1090cm^{-1} (phl/ap/cb), 3676cm^{-1} (hydrated mica)
	50148-2	a	
		b	

Table C2 – Part C continued

Sample#			Mineral inclusions
SGF-025	50223-1	a	-
		b	730-850cm^{-1} (cb/sil), 1014cm^{-1} (sheet sil), 1090cm^{-1} (phl/ap/cb), 3676cm^{-1} (hydrated mica)
	50223-2	a	730-850cm^{-1} (cb/sil), 1014cm^{-1} (sheet sil), 1090cm^{-1} (phl/ap/cb), 3676cm^{-1} (hydrated mica)
		b	730-850cm^{-1} (cb/sil), 1014cm^{-1} (sheet sil), 1090cm^{-1} (phl/ap/cb), 3676cm^{-1} (hydrated mica)
	50224-1-1	a	730-850cm^{-1} (cb/sil), 1014cm^{-1} (sheet sil), 1090cm^{-1} (phl/ap/cb), 3676cm^{-1} (hydrated mica)
		b	730-850cm^{-1} (cb/sil), 1014cm^{-1} (sheet sil), 1090cm^{-1} (phl/ap/cb), 3676cm^{-1} (hydrated mica)
	50224-1-2	a	730-850cm^{-1} (cb/sil), 1014cm^{-1} (sheet sil), 1090cm^{-1} (phl/ap/cb), 3676cm^{-1} (hydrated mica)
		b	730-850cm^{-1} (cb/sil), 1014cm^{-1} (sheet sil), 1090cm^{-1} (phl/ap/cb), 3676cm^{-1} (hydrated mica)
	50224-2	a	730-850cm^{-1} (cb/sil), 1014cm^{-1} (sheet sil), 1090cm^{-1} (phl/ap/cb)
	50224-3-1	a	730-850cm^{-1} (cb/sil), 1014cm^{-1} (sheet sil), 1090cm^{-1} (phl/ap/cb), 3676cm^{-1} (hydrated mica)
		b	730-850cm^{-1} (cb/sil), 1014cm^{-1} (sheet sil), 1090cm^{-1} (phl/ap/cb), 3676cm^{-1} (hydrated mica)
	50224-3-2	a	-
	50225-1	a	730-850cm^{-1} (cb/sil), 1014cm^{-1} (sheet sil), 1090cm^{-1} (phl/ap/cb), 3676cm^{-1} (hydrated mica)
		b	730-850cm^{-1} (cb/sil), 1014cm^{-1} (sheet sil), 1090cm^{-1} (phl/ap/cb), 3676cm^{-1} (hydrated mica)
	50225-2	a	730-850cm^{-1} (cb/sil), 1014cm^{-1} (sheet sil), 1090cm^{-1} (phl/ap/cb)
		b	730-850cm^{-1} (cb/sil), 1014cm^{-1} (sheet sil), 1090cm^{-1} (phl/ap/cb)
	50225-3		-
	50226	a	730-850cm^{-1} (cb/sil), 1014cm^{-1} (sheet sil), 1090cm^{-1} (phl/ap/cb), 3676cm^{-1} (hydrated mica)
		b	730-850cm^{-1} (cb/sil), 1014cm^{-1} (sheet sil), 1090cm^{-1} (phl/ap/cb), 3676cm^{-1} (hydrated mica)
SGF-034	1	a	730-850cm^{-1} (cb/sil), 1014cm^{-1} (sheet sil), 1090cm^{-1} (phl/ap/cb), 3676cm^{-1} (hydrated mica)
		b	730-850cm^{-1} (cb/sil), 1014cm^{-1} (sheet sil), 1090cm^{-1} (phl/ap/cb), 3676cm^{-1} (hydrated mica)
	2	a	3676cm^{-1} (hydrated mica)
		b	3676cm^{-1} (hydrated mica)

Table C2 – Part C continued

Sample#			Mineral inclusions
SGF-039	50443-1	a	730-850cm^{-1} (cb/sil), 1014cm^{-1} (sheet sil), 1090cm^{-1} (phl/ap/cb), 3676cm^{-1} (hydrated mica)
		b	730-850cm^{-1} (cb/sil), 1014cm^{-1} (sheet sil), 1090cm^{-1} (phl/ap/cb), 3676cm^{-1} (hydrated mica)
	50443-2	a	730-850cm^{-1} (cb/sil), 1014cm^{-1} (sheet sil), 1090cm^{-1} (phl/ap/cb), 3676cm^{-1} (hydrated mica)
		b	730-850cm^{-1} (cb/sil), 1014cm^{-1} (sheet sil), 1090cm^{-1} (phl/ap/cb), 3676cm^{-1} (hydrated mica)
	50446-1	a	730-850cm^{-1} (cb/sil), 1014cm^{-1} (sheet sil), 1090cm^{-1} (phl/ap/cb)
		b	730-850cm^{-1} (cb/sil), 1014cm^{-1} (sheet sil), 1090cm^{-1} (phl/ap/cb)
	50446-2	a	730-850cm^{-1} (cb/sil), 1014cm^{-1} (sheet sil), 1090cm^{-1} (phl/ap/cb)
		b	730-850cm^{-1} (cb/sil), 1014cm^{-1} (sheet sil)
	50446-3	a	730-850cm^{-1} (cb/sil), 1014cm^{-1} (sheet sil)
		b	730-850cm^{-1} (cb/sil), 1014cm^{-1} (sheet sil), 1090cm^{-1} (phl/ap/cb)
SGF-040	50455	a	730-850cm^{-1} (cb/sil), 1014cm^{-1} (sheet sil), 1090cm^{-1} (phl/ap/cb)
		b	730-850cm^{-1} (cb/sil), 1014cm^{-1} (sheet sil), 3676cm^{-1} (hydrated mica)
	50461	a	730-850cm^{-1} (cb/sil), 1014cm^{-1} (sheet sil), 3676cm^{-1} (hydrated mica)
		b	730-850cm^{-1} (cb/sil)
SGF-042	50495	a	730-850cm^{-1} (cb/sil), 1014cm^{-1} (sheet sil), 1090cm^{-1} (phl/ap/cb), 3676cm^{-1} (hydrated mica)
		b	730-850cm^{-1} (cb/sil), 1014cm^{-1} (sheet sil), 1090cm^{-1} (phl/ap/cb), 3676cm^{-1} (hydrated mica)
SGF-048	50655	a	-
		b	730-850cm^{-1} (cb/sil), 1014cm^{-1} (sheet sil), 1090cm^{-1} (phl/ap/cb), 3676cm^{-1} (hydrated mica)
SGF-066	51152	a	730-850cm^{-1} (cb/sil), 1014cm^{-1} (sheet sil), 1090cm^{-1} (phl/ap/cb), 3676cm^{-1} (hydrated mica)
		b	730-850cm^{-1} (cb/sil), 1014cm^{-1} (sheet sil), 1090cm^{-1} (phl/ap/cb), 3676cm^{-1} (hydrated mica)
SGF-067	51188	a	1014cm^{-1} (sheet sil), 1090cm^{-1} (phl/ap/cb)
		b	1014cm^{-1} (sheet sil), 1090cm^{-1} (phl/ap/cb)

Table C2 – Part C continued

Sample#			Mineral inclusions
SGF-127	53865-1-1	a	730-850cm^{-1} (cb/sil), 1014cm^{-1} (sheet sil), 1090cm^{-1} (phl/ap/cb)
		b	730-850cm^{-1} (cb/sil), 1014cm^{-1} (sheet sil), 1090cm^{-1} (phl/ap/cb)
	53865-1-2	a	730-850cm^{-1} (cb/sil), 1014cm^{-1} (sheet sil), 1090cm^{-1} (phl/ap/cb)
		b	730-850cm^{-1} (cb/sil), 1014cm^{-1} (sheet sil), 1090cm^{-1} (phl/ap/cb)
	53865-2-1	a	730-850cm^{-1} (cb/sil), 1014cm^{-1} (sheet sil), 1090cm^{-1} (phl/ap/cb), 3676cm^{-1} (hydrated mica)
		b	730-850cm^{-1} (cb/sil), 1014cm^{-1} (sheet sil), 1090cm^{-1} (phl/ap/cb), 3676cm^{-1} (hydrated mica)
	53865-2-2	a	730-850cm^{-1} (cb/sil), 1014cm^{-1} (sheet sil), 1090cm^{-1} (phl/ap/cb), 3676cm^{-1} (hydrated mica)
		b	730-850cm^{-1} (cb/sil), 1014cm^{-1} (sheet sil), 1090cm^{-1} (phl/ap/cb), 3676cm^{-1} (hydrated mica)
SGF-140	37430-1	a	730-850cm^{-1} (cb/sil), 1014cm^{-1} (sheet sil), 1090cm^{-1} (phl/ap/cb)
		b	730-850cm^{-1} (cb/sil), 1014cm^{-1} (sheet sil), 1090cm^{-1} (phl/ap/cb)
	37430-2	a	730-850cm^{-1} (cb/sil), 1014cm^{-1} (sheet sil), 1090cm^{-1} (phl/ap/cb)
		b	730-850cm^{-1} (cb/sil), 1014cm^{-1} (sheet sil), 1090cm^{-1} (phl/ap/cb), 3676cm^{-1} (hydrated mica)
	37430-3	a	730-850cm^{-1} (cb/sil), 1014cm^{-1} (sheet sil), 1090cm^{-1} (phl/ap/cb)
		b	730-850cm^{-1} (cb/sil), 1014cm^{-1} (sheet sil), 1090cm^{-1} (phl/ap/cb), 3676cm^{-1} (hydrated mica)

Table C3 Carbon and nitrogen isotope ratios, as well as nitrogen concentrations of Fort à la Corne diamonds from micro-xenoliths. Isotopic values are given in ‰, while nitrogen concentrations (N) are reported as ppm. Spots in annealing fractures and rims are labelled as secondary.

Sample#		Spots	$\delta^{13}C_{VPDB}$ (‰)	2σ (‰)	N (at. ppm)	2σ (ppm)	$\delta^{15}N_{AIR}$ (‰)*	2σ (‰)	N (at. ppm)	Comment
SGF-003 50036	1	A	-3.16	0.19	879.7	70.8	-1.08	0.84	792	-
		B	-3.00	0.19	841.1	67.7	-0.26	0.76	798	-
		C	-3.19	0.19	880.5	70.9	-1.61	0.90	735	-
SGF-008 50076	1	A	-17.00	0.22	17.4	1.4	-	-	-	-
		B	-19.04	0.18	12.1	1.4	-	-	-	Secondary
		C	-16.93	0.18	16.0	1.3	-	-	-	-
		D	-16.89	0.18	18.3	1.5	-	-	-	-
		E	-17.10	0.19	17.0	1.4	-	-	-	-
		F	-17.55	0.21	1.5	0.3	-	-	-	Secondary
SGF-009 50095	1	A	-4.11	0.19	996.4	79.8	-5.61	0.70	969	-
		B	-3.84	0.20	809.7	64.8	-5.20	0.74	837	-
		C	-4.25	0.19	1006.8	80.8	-5.70	0.73	920	-
		D	-4.39	0.19	829.4	66.4	-5.09	0.76	803	-
		E	-4.32	0.18	904.6	72.4	-5.10	0.71	922	-
	2	A	-4.49	0.20	1006.9	82.9	-4.12	0.74	798	-
		B	-4.78	0.19	1024.5	82.6	-4.18	0.71	915	-
		C	-4.65	0.18	781.4	62.6	-3.39	0.89	709	-
	3	A	-4.40	0.20	939.0	75.7	-4.59	0.75	840	-
		B	-4.67	0.19	926.6	75.4	-5.16	0.72	898	-
		C	-4.83	0.18	940.8	76.6	-2.37	0.71	874	-
		D	-4.62	0.20	788.8	63.1	-3.98	0.77	750	-

* For low N concentrations, typically below 30 molar ppm, δ15NAIR was not analysed, as the errors would be too high.

Table C3 continued

Sample#		Spots	$\delta^{13}C_{VPDB}$ (‰)	2σ (‰)	N (at. ppm)	2σ (ppm)	$\delta^{15}N_{AIR}$ (‰)*	2σ (‰)	N (at. ppm)	Comment
SGF-020	50138	A	-3.33	0.18	51.1	4.2	-	-	-	-
		B	-3.48	0.18	49.0	4.1	-	-	-	-
	1	C	-3.24	0.19	42.1	3.4	-	-	-	-
		D	-3.47	0.21	3.6	0.9	-	-	-	Secondary
		E	-3.59	0.18	47.7	4.0	-	-	-	-
		A	-3.80	0.20	48.9	4.0	-	-	-	-
	2	B	-3.80	0.19	45.9	4.0	-	-	-	-
		C	-3.79	0.20	55.1	4.4	-	-	-	-
		D	-3.71	0.21	35.9	3.0	-	-	-	-
SGF-020	50140	A	-16.39	0.18	348.1	28.1	-0.36	1.24	351	-
		B	-16.01	0.18	283.1	22.7	-2.36	1.22	292	-
	1	C	-16.91	0.19	425.1	34.2	1.41	0.91	516	-
		D	-16.31	0.18	145.3	11.8	0.03	1.41	210	-
		E	-16.12	0.18	39.0	3.5	-	-	-	Secondary
		F	-17.29	0.18	753.7	60.5	0.63	1.20	520	-
		A	-16.40	0.18	243.6	19.6	-2.55	1.34	232	-
	2	B	-16.38	0.20	241.4	19.3	-0.27	1.37	237	-
		C	-16.32	0.21	308.4	24.7	-1.25	1.18	304	-
		D	-16.33	0.20	232.5	18.6	-0.80	1.42	209	-

Table C3 continued

Sample#		Spots	$\delta^{13}C_{VPDB}$ (‰)	2σ (‰)	N (at. ppm)	2σ (ppm)	$\delta^{15}N_{AIR}$ (‰)*	2σ (‰)	N (at. ppm)	Comment
SGF-020	50140	A	-16.01	0.19	228.0	18.3	-1.66	1.42	199	-
		B	-15.99	0.20	283.0	23.0	-0.86	1.41	199	-
		C	-15.91	0.20	39.9	3.6	-	-	-	Secondary
		D	-15.89	0.18	240.3	19.2	-1.58	1.21	275	-
	3	E	-16.37	0.19	1.4	0.1	-	-	-	Secondary
		F	-16.53	0.19	527.6	42.3	-2.29	1.05	476	-
		G	-16.56	0.18	936.7	75.0	-1.55	0.70	939	-
		H	-16.85	0.18	861.2	69.0	-1.57	0.78	877	-
		I	-16.87	0.18	1420.9	113.7	-0.64	0.59	1285	-
		A	-15.99	0.19	385.2	31.1	-1.19	1.11	390	-
		B	-16.26	0.19	465.1	37.2	-2.19	0.95	459	-
		C	-16.38	0.18	1094.5	88.2	-1.47	0.77	1047	-
	4	D	-16.57	0.19	1098.4	87.9	-1.72	0.72	806	-
		E	-16.50	0.18	1343.6	107.8	-0.88	0.56	1441	-
		F	-16.66	0.18	999.1	80.0	0.16	0.71	852	-
SGF-021	50148	A	-13.37	0.18	1.1	0.1	-	-	-	-
		B	-13.37	0.18	0.4	0.0	-	-	-	-
	1	C	-13.23	0.19	0.4	0.0	-	-	-	-
		D	-13.26	0.19	0.7	0.1	-	-	-	-
		E	-13.58	0.20	1.3	0.2	-	-	-	-
		A	-16.52	0.19	1278.3	102.8	-1.70	0.59	1350	-
	2	B	-16.74	0.19	805.7	65.0	-2.02	0.75	816	-
		C	-16.68	0.18	298.5	24.1	0.83	1.53	248	-

Table C3 continued

Sample#			Spots	$\delta^{13}C_{VPDB}$ (‰)	2σ (‰)	N (at. ppm)	2σ (ppm)	$\delta^{15}N_{AIR}$ (‰)*	2σ (‰)	N (at. ppm)	Comment
SGF-025	50223	1	A	-21.86	0.20	1.9	0.4	-	-	-	-
			B	-22.68	0.19	0.8	0.1	-	-	-	-
			C	-21.74	0.19	1.8	0.4	-	-	-	-
			D	-21.58	0.19	1.5	0.3	-	-	-	-
		2	A	-21.72	0.21	561.4	45.0	-0.39	0.89	522	-
			B	-21.86	0.20	604.2	48.5	-1.08	0.81	689	-
			C	-22.08	0.18	2.3	0.3	-	-	-	Secondary
			D	-22.46	0.19	0.7	0.1	-	-	-	Secondary
			E	-21.56	0.22	587.9	47.0	-0.58	0.90	523	-
SGF-025	50224-1-1	1	A	-22.04	0.19	657.1	53.8	-0.36	0.80	662	-
			B	-22.10	0.20	292.4	23.7	1.52	3.63	28	-
			C	-22.01	0.18	153.6	12.7	1.45	1.65	134	-
			D	-21.43	0.19	264.8	22.5	-0.50	0.80	719	-
			E	-21.82	0.19	2.2	0.3	-	-	-	Secondary
		2	A	-21.51	0.19	692.7	55.4	0.77	1.05	489	-
			B	-21.58	0.18	547.5	43.9	1.08	1.04	378	-
			C	-21.49	0.19	416.1	35.4	0.09	1.12	460	-
			D	-21.58	0.19	56.0	5.9	-	-	-	Secondary
			E	-21.57	0.18	4.0	0.3	-	-	-	Secondary
SGF-025	50224-2	1	A	-21.78	0.18	762.8	61.1	-0.90	0.76	723	
			B	-21.71	0.18	796.2	63.7	-1.09	0.84	741	
			C	-21.68	0.19	695.7	55.8	0.43	0.82	743	
			D	-22.79	0.19	4.1	0.3	-	-	-	Secondary
			E	-22.74	0.19	2.2	0.3	-	-	-	Secondary

Table C3 continued

Sample#		Spots	$\delta^{13}C_{VPDB}$ (‰)	2σ (‰)	N (at. ppm)	2σ (ppm)	$\delta^{15}N_{AIR}$ (‰)*	2σ (‰)	N (at. ppm)	Comment
SGF-025	50224-3-1	A	-22.36	0.19	186.0	15.6	1.95	1.76	132	-
		B	-22.15	0.19	140.4	11.8	2.50	1.57	156	-
	1	C	-22.14	0.21	39.1	4.0	-	-	-	Secondary
		D	-22.27	0.19	230.1	19.0	2.81	1.53	194	-
		E	-22.12	0.19	19.8	2.4	-	-	-	Secondary
		A	-22.06	0.18	273.5	21.9	0.57	1.19	288	-
		B	-21.54	0.19	274.8	22.1	0.83	1.22	279	-
	2	C	-22.10	0.19	124.7	11.8	1.38	1.90	120	-
		D	-22.05	0.20	7.0	1.1	-	-	-	Secondary
		E	-22.08	0.19	4.1	0.6	-	-	-	Secondary
SGF-025	50225-1	A	-21.80	0.20	66.2	6.1	-3.26	2.74	61	-
		B	-21.81	0.18	78.3	6.5	-2.87	2.63	68	-
	1	C	-21.32	0.18	130.2	10.6	-1.80	1.87	121	-
		D	-21.21	0.20	2.0	0.2	-	-	-	Secondary
		A	-22.14	0.18	230.7	19.1	2.97	1.09	350	-
	2	B	-22.03	0.19	367.4	29.6	2.77	1.29	260	-
		C	-22.00	0.19	478.0	38.6	1.99	1.07	449	-
		A	-21.98	0.19	34.9	3.8	-	-	-	Secondary
		B	-22.20	0.19	53.5	5.0	-	-	-	-
	3	C	-22.20	0.18	59.1	5.1	-	-	-	-
		D	-21.43	0.19	106.5	9.1	-	-	-	-
		E	-21.50	0.19	30.8	5.1	-	-	-	Secondary

Table C3 continued

Sample#			Spots	$\delta^{13}C_{VPDB}$ (‰)	2σ (‰)	N (at. ppm)	2σ (ppm)	$\delta^{15}N_{AIR}$ (‰)*	2σ (‰)	N (at. ppm)	Comment
SGF-025	50226	1	A	-21.75	0.19	74.6	6.2	-	-	-	-
			B	-21.77	0.20	79.3	6.7	-	-	-	-
			C	-21.32	0.21	76.9	7.1	-	-	-	-
			D	-19.22	0.18	1.7	0.1	-	-	-	Secondary
			E	-21.90	0.19	0.9	0.2	-	-	-	Secondary
SGF-034		1	A	-17.93	0.18	8.9	0.7	-	-	-	-
			B	-18.17	0.20	2.4	0.3	-	-	-	-
			C	-18.23	0.18	2.8	0.3	-	-	-	-
			D	-15.03	0.39	10.8	1.1	-	-	-	-
			E	-18.14	0.20	1.9	0.2	-	-	-	-
		2	A	-17.76	0.19	1.6	0.1	-	-	-	-
			B	-17.67	0.19	0.9	0.1	-	-	-	-
			C	-17.63	0.18	1.0	0.1	-	-	-	-
			D	-17.02	0.20	1.2	0.1	-	-	-	-
			E	-17.35	0.19	21.4	2.2	-	-	-	-
SGF-039	50443	1	A	-3.07	0.18	1.7	0.2	-	-	-	-
			B	-3.23	0.20	17.8	1.7	-	-	-	-
			C	-3.13	0.20	0.8	0.1	-	-	-	-
			D	-3.14	0.18	3.1	0.3	-	-	-	-
			E	-2.98	0.20	0.9	0.1	-	-	-	-
		2	A	-3.96	0.19	1211.3	97.3	-3.20	0.87	828	-
			B	-4.37	0.18	903.1	72.4	-3.90	0.77	712	-
			C	-4.28	0.19	1284.0	106.8	-3.53	0.63	1104	-
			D	-4.34	0.20	1160.6	93.0	-2.88	0.72	913	-

Table C3 continued

Sample#			Spots	$\delta^{13}C_{VPDB}$ (‰)	2σ (‰)	N (at. ppm)	2σ (ppm)	$\delta^{15}N_{AIR}$ (‰)*	2σ (‰)	N (at. ppm)	Comment
SGF-039	50446-1	1	A	-20.97	0.20	21.0	2.1	-	-	-	-
			B	-20.80	0.19	22.6	2.0	-	-	-	-
			C	-20.92	0.19	20.7	1.8	-	-	-	-
			D	-20.76	0.18	16.6	1.5	-	-	-	Secondary
			E	-20.74	0.19	12.3	1.4	-	-	-	Secondary
			F	-21.03	0.18	5.7	0.6	-	-	-	Secondary
			G	-21.49	0.21	23.2	2.0	-	-	-	-
		2	A	-20.54	0.19	6.5	0.7	-	-	-	-
			B	-20.58	0.19	14.0	1.6	-	-	-	-
			C	-20.65	0.18	8.3	0.9	-	-	-	-
			D	-20.77	0.19	0.8	0.3	-	-	-	-
		3	A	-21.09	0.18	24.4	2.0	-	-	-	-
			B	-21.04	0.20	21.4	1.9	-	-	-	-
			C	-21.20	0.18	1.0	0.2	-	-	-	Secondary
			D	-21.19	0.18	1.0	0.4	-	-	-	Secondary
			E	-21.54	0.18	5.0	1.3	-	-	-	Secondary
SGF-040	50455	1	A	-22.31	0.20	15.8	1.4	-	-	-	-
			B	-22.20	0.19	15.6	1.3	-	-	-	-
			C	-22.01	0.20	3.2	0.6	-	-	-	Secondary
			D	-22.37	0.20	22.0	1.8	-	-	-	-

Table C3 continued

Sample#			Spots	$\delta^{13}C_{VPDB}$ (‰)	2σ (‰)	N (at. ppm)	2σ (ppm)	$\delta^{15}N_{AIR}$ (‰)*	2σ (‰)	N (at. ppm)	Comment
SGF-040	50461	1	A	-5.44	0.18	3.2	0.3	-	-	-	-
			B	-5.49	0.18	3.2	0.3	-	-	-	-
			C	-5.65	0.18	2.2	0.2	-	-	-	-
			D	-4.07	0.19	2.4	0.3	-	-	-	-
			E	-5.68	0.19	3.4	0.3	-	-	-	-
			F	-5.68	0.18	3.7	0.3	-	-	-	-
SGF-042	50495	1	A	-17.31	0.19	19.9	2.9	-	-	-	Secondary
			B	-17.56	0.18	473.8	56.6	2.73	1.55	321	-
			C	-17.50	0.18	184.3	16.6	4.88	3.62	50	-
			D	-17.79	0.19	429.1	34.9	-	-	-	-
			E	-17.79	0.19	393.2	32.1	4.62	1.25	363	-
			F	-17.81	0.19	389.7	31.4	5.51	1.14	349	-
			G	-8.98	0.18	1435.3	116.2	6.27	0.71	1319	-
			H	-9.25	0.19	636.4	51.0	3.91	0.88	662	-
			I	-17.48	0.20	418.6	35.4	3.88	1.04	391	-
SGF-048	50655	1	A	-29.10	0.21	4.4	0.4	-	-	-	-
			B	-28.95	0.18	4.4	0.4	-	-	-	-
			C	-28.95	0.18	5.6	0.5	-	-	-	-
			D	-29.16	0.19	4.3	0.4	-	-	-	-
			E	-28.86	0.18	4.9	0.4	-	-	-	-

Table C3 continued

Sample#			Spots	$\delta^{13}C_{VPDB}$ (‰)	2σ (‰)	N (at. ppm)	2σ (ppm)	$\delta^{15}N_{AIR}$ (‰)*	2σ (‰)	N (at. ppm)	Comment
SGF-066	51152	1	A	-8.77	0.20	1274.7	103.2	1.65	0.60	1204	-
			B	-8.65	0.18	1211.4	98.0	1.43	0.60	1252	-
			C	-7.48	0.19	212.1	17.0	0.31	1.75	128	-
			D	-5.61	0.20	60.5	5.0	-0.11	2.81	51	-
			E	-6.23	0.19	0.5	0.1	-	-	-	Secondary
			F	-4.04	0.19	932.8	74.7	-3.76	0.71	879	-
SGF-067	51188	1	A	-6.45	0.19	41.3	3.8	-	-	-	-
			B	-6.58	0.18	110.1	9.4	-	-	-	-
			C	-6.76	0.18	43.9	3.5	-	-	-	-
SGF-127	53865-1	1	A	-20.40	0.20	680.9	57.5	9.44	1.03	492	-
			B	-20.11	0.19	773.0	62.3	9.24	0.96	675	-
			C	-20.12	0.20	1265.0	101.3	5.52	0.72	1112	-
			D	-19.94	0.19	1293.9	103.7	7.84	0.65	1195	-
			E	-19.82	0.21	1249.5	100.2	6.51	0.66	1056	-
		2	A	-20.10	0.20	1311.5	105.0	7.52	0.64	1239	-
			B	-19.98	0.19	1322.6	105.8	7.62	0.62	1217	-
			C	-19.92	0.18	1340.0	109.4	6.39	0.65	1160	-
			D	-20.18	0.19	1338.2	107.1	7.06	0.63	1216	-
			E	-20.26	0.19	676.2	54.2	9.39	0.86	680	-

Table C3 continued

Sample#		Spots	$\delta^{13}C_{VPDB}$ (‰)	2σ (‰)	N (at. ppm)	2σ (ppm)	$\delta^{15}N_{AIR}$ (‰)*	2σ (‰)	N (at. ppm)	Comment
SGF-127 53865-2-1	1	A	-21.19	0.18	23.7	1.9	-	-	-	-
		B	-21.10	0.19	26.0	2.1	-	-	-	-
		C	-21.17	0.19	25.6	2.1	-	-	-	-
		D	-21.40	0.18	23.8	1.9	-	-	-	-
		E	-21.26	0.20	25.5	2.1	-	-	-	-
	2	A	-21.41	0.18	25.6	2.1	-	-	-	-
		B	-21.63	0.20	25.2	2.0	-	-	-	-
		C	-21.53	0.20	22.8	1.8	-	-	-	-
		D	-21.51	0.19	27.2	2.2	-	-	-	-
SGF-140 37430-1	1	A	-4.57	0.19	826.6	66.2	-4.15	0.83	721	-
		B	-4.40	0.20	32.3	2.9	-	-	-	-
		C	-4.48	0.20	391.0	32.6	-2.53	0.82	598	-
		D	-4.70	0.19	1153.9	92.4	-3.30	0.67	1005	-
		E	-4.80	0.19	1147.5	91.8	-3.66	0.71	1007	-
	2	A	-4.40	0.19	83.0	7.4	1.52	1.96	101	-
		B	-4.55	0.18	1181.9	94.7	-3.88	0.76	1038	-
		C	-4.64	0.18	1177.6	94.6	-4.26	0.67	1042	-
		D	-4.49	0.18	518.5	41.7	-2.46	1.11	504	-
		E	-4.48	0.18	566.2	45.6	-2.51	0.81	645	-
	3	A	-4.77	0.19	866.4	69.6	-2.63	0.77	840	-
		B	-4.82	0.21	849.8	68.4	-2.38	0.73	830	-
		C	-4.89	0.18	854.7	68.5	-2.21	0.74	879	-
		D	-4.85	0.18	879.8	71.1	-1.80	0.76	936	-

Table C3 continued

Sample ID		Spots	$\delta^{13}C_{VPDB}$ (‰)	2σ (‰)	N (at. ppm)	2σ (ppm)	$\delta^{15}N_{AIR}$ (‰)*	2σ (‰)	N (at. ppm)	Comment
SGF-020 50140	XS 1	A	-15.96	0.15	400.0	32.1	-1.15	1.01	404	-
		B	-15.83	0.15	317.8	25.5	-0.94	1.08	355	-
		C	-15.74	0.16	336.6	27.0	-2.40	1.13	367	-
		D	-15.99	0.14	366.4	29.3	-1.78	1.08	375	-
		E	-16.43	0.16	812.7	65.1	-1.55	0.85	784	-
		F	-16.22	0.13	1089.6	88.3	-1.13	1.03	981	-
		G	-13.60	0.16	141.2	11.9	-2.63	1.57	178	-
		H	-13.27	0.14	1.2	0.1	-	-	-	Secondary
		I	-13.45	0.14	2.4	0.2	-	-	-	Secondary
		J	-13.39	0.15	1.3	0.2	-	-	-	Secondary
		K	-13.41	0.16	1.2	0.3	-	-	-	Secondary
	XS 1B	A	-13.88	0.14	2.8	0.4	-	-	-	Secondary
		B	-13.55	0.14	1.3	0.1	-	-	-	Secondary
		C	-13.68	0.18	2.6	0.3	-	-	-	Secondary
		D	-16.51	0.15	1390.0	111.3	-0.99	0.62	1380	-
		E	-16.59	0.15	798.1	64.0	-1.81	0.83	850	-
		F	-16.13	0.13	375.8	30.2	-1.67	1.01	399	-
		G	-15.87	0.17	487.7	39.1	-1.72	1.09	478	-
		H	-15.78	0.14	324.2	26.0	-	-	-	-

Table C3 continued

Sample#			Spots	$\delta^{13}C_{VPDB}$ (‰)	2σ (‰)	N (at. ppm)	2σ (ppm)	$\delta^{15}N_{AIR}$ (‰)*	2σ (‰)	N (at. ppm)	Comment
SGF-020	50140	XS 2	A	-13.65	0.13	-	-	-4.11	1.53	171	-
			B	-16.48	0.14	-	-	-0.27	0.59	1342	-
			C	-16.70	0.14	-	-	-1.38	0.73	826	-
			D	-16.49	0.14	-	-	-0.93	0.90	801	-
			E	-16.05	0.16	-	-	-2.20	1.08	357	-
			F	-15.85	0.15	-	-	-0.11	1.47	238	-
			G	-15.75	0.13	-	-	-1.44	1.58	236	-
			H	-15.83	0.13	-	-	-1.50	1.78	155	-
			I	-16.12	0.13	-	-	-	-	-	-
		XS 2B	A	-13.60	0.14	89.0	7.3	-	-	-	-
			B	-16.58	0.13	1292.3	104.9	-	-	-	-
			C	-16.78	0.15	802.9	64.4	-	-	-	-
			D	-16.07	0.13	315.6	25.3	-	-	-	-
		XS 3	A	-16.56	0.13	3.4	0.8	-	-	-	Secondary
			B	-16.44	0.13	101.5	8.9	-	-	-	-
			C	-16.35	0.13	7.1	1.5	-	-	-	Secondary
			D	-16.31	0.17	28.6	3.4	-	-	-	-
			E	-16.22	0.13	229.8	37.4	-	-	12	-
			F	-15.82	0.14	204.1	16.4	-0.69	1.48	183	-
			G	-15.78	0.14	166.2	13.4	-	-	27	-
			H	-15.55	0.13	216.3	22.3	-1.44	1.29	247	-
			I	-15.77	0.15	406.3	32.7	-0.89	1.07	409	-
			J	-16.51	0.14	786.7	63.1	-1.11	0.77	827	-

Table C3 continued

Sample#		Spots	$\delta^{13}C_{VPDB}$ (‰)	2σ (‰)	N (at. ppm)	2σ (ppm)	$\delta^{15}N_{AIR}$ (‰)*	2σ (‰)	N (at. ppm)	Comment
	XS 4	K	-16.52	0.14	4.6	1.2	-	-	-	Secondary
		A	-16.41	0.15	23.8	6.1	-	-	-	-
		B	-16.22	0.16	35.2	14.8	-	-	-	-
		C	-16.17	0.14	17.0	1.9	-	-	-	-
		D	-16.07	0.15	10.9	1.2	-	-	-	Secondary
		E	-15.81	0.13	177.4	14.4	-	-	-	-
		F	-15.78	0.14	278.4	22.6	-	-	-	-
		G	-15.54	0.15	194.4	15.9	-	-	-	-
		H	-15.60	0.14	318.3	25.7	-	-	-	-
SGF-020 50140		A	-15.76	0.14	-	-	-	-	-	-
		B	-15.71	0.14	-	-	-	-	-	-
		C	-15.68	0.14	390.0	31.4				-
		D	-15.69	0.13	165.6	13.5				-
		E	-16.21	0.13	889.5	71.2	-1.03	0.80	636	-
		F	-16.40	0.16	1203.6	103.3	-1.15	0.61	1294	-
		G	-13.68	0.13	2.1	0.2	-	-	-	Secondary
		H	-16.54	0.14	815.9	65.8	-	-	-	-
		I	-15.76	0.13	244.5	20.8	-2.01	1.32	227	-
		J	-15.51	0.16	243.7	20.0	-1.22	1.27	242	-
		K	-15.75	0.13	455.5	36.5	-1.54	1.11	477	-
		L	-16.17	0.14	464.0	37.2	-1.78	1.04	493	-
		M	-16.22	0.13	975.2	78.6	-1.66	0.73	1016	-
		N	-16.38	0.14	817.0	65.6	-1.83	0.76	834	-
		O	-15.86	0.14	100.7	8.4	0.42	1.51	179	-

Table C3 continued

Sample#	Spots	$\delta^{13}C_{VPDB}$ (‰)	2σ (‰)	N (at. ppm)	2σ (ppm)	$\delta^{15}N_{AIR}$ (‰)*	2σ (‰)	N (at. ppm)	Comment
	P	-15.96	0.14	196.1	16.6	2.34	1.96	100	-
	Q	-15.78	0.13	258.5	20.9	-0.38	1.39	220	-
	R	-15.96	0.12	101.3	14.3	-3.98	1.81	161	-
	S	-15.91	0.12	231.8	18.6	-2.57	1.33	228	-
	T	-15.74	0.16	197.4	15.9	-1.55	1.29	232	-
	U	-16.21	0.16	85.0	13.1	-3.28	3.36	42	-
	V	-16.50	0.15	827.5	68.0	-0.82	0.73	763	-
	X	-16.47	0.15	385.1	31.0	0.07	0.86	562	-
	Y	-15.72	0.14	206.5	16.7	0.67	1.94	102	-
	Z	-15.50	0.12	168.9	13.6	-0.82	1.13	314	-
SGF-020 50140	AA	-15.51	0.12	232.4	18.8	2.32	1.48	177	-
	AB	-15.52	0.14	303.6	24.6	-0.12	1.22	260	-
	AC	-16.63	0.14	37.0	4.7	-	-	-	-
	AD	-16.11	0.14	14.0	3.6	-	-	-	Secondary
	AE	-16.69	0.13	217.6	17.5	2.89	1.55	174	-
	AF	-16.24	0.14	25.6	4.0	-	-	-	-
	AG	-16.34	0.16	-	-	-	-	-	-
	AH	-16.35	0.14	15.9	2.0	-	-	-	-
	AI	-16.23	0.14	17.1	3.5	-	-	-	-
	AJ	-15.88	0.16	51.6	4.6	-1.11	1.30	231	-
	AK	-15.67	0.13	338.7	27.6	-1.71	1.27	289	-

Table C3 continued

Sample#		Spots	$\delta^{13}C_{VPDB}$ (‰)	2σ (‰)	N (at. ppm)	2σ (ppm)	$\delta^{15}N_{AIR}$ (‰)*	2σ (‰)	N (at. ppm)	Comment
		AL	-16.40	0.14	16.2	2.2	-	-	-	-
		AM	-16.21	0.15	129.8	11.3	-2.42	2.19	82	-
		AN	-16.12	0.14	35.3	4.7	-	-	-	-
		AO	-16.72	0.14	27.5	5.6	-	-	-	-
		AP	-16.42	0.14	9.2	1.9	-	-	-	Secondary
		AQ	-16.30	0.13	19.0	2.7	-	-	-	-
		AR	-16.33	0.15	13.4	3.7	-	-	-	Secondary
SGF-020	50140	AS	-16.35	0.14	11.2	1.2	-	-	-	Secondary
		AT	-16.07	0.13	38.2	4.0	-	-	-	-
		AU	-16.42	0.14	51.8	4.4	-	-	28	-
		AV	-15.85	0.13	237.1	19.1	-2.41	1.43	178	-
		AW	-16.00	0.15	204.3	17.7	0.46	1.26	314	-
		AX	-16.50	0.13	617.3	49.9	0.45	1.26	241	-
		AY	-16.10	0.15	1.3	0.3	-	-	18	Secondary
		AZ	-16.45	0.12	75.2	16.2	-	-	-	-